








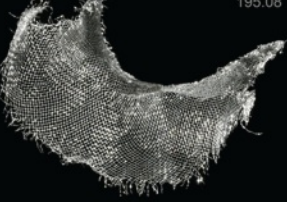

Конденсированные среды и межфазные границы

РЕЦЕНЗИРУЕМЫЙ НАУЧНЫЙ ЖУРНАЛ

Condensed Matter and Interphases

PEER-REVIEWED SCIENTIFIC JOURNAL

Том
Vol. 25, No. 2
2023

<p>Co 27 58.933</p>  <p>Cobalt</p>	<p>Ni 28 58.693</p>  <p>Nickel</p>	<p>Cu 29 63.546</p>  <p>Copper</p>
<p>Rh 45 102.91</p>  <p>Rhodium</p>	<p>Pd 46 106.42</p>  <p>Palladium</p>	<p>Ag 47 107.87</p>  <p>Silver</p>
<p>Ir 77 192.22</p>  <p>Iridium</p>	<p>Pt 78 195.08</p>  <p>Platinum</p>	<p>Au 79 196.97</p>  <p>Gold</p>

Condensed Matter and Interphases

Kondensirovannye sredy i mezhfaznye granitsy

Peer-reviewed scientific journal

Published since January 1999

Periodicity: Quarterly

Volume 25, No. 2, 2023

Full-text version is available in the Russian language on the website: <https://journals.vsu.ru/kcmf>

Condensed Matter and Interphases (Kondensirovannye Sredy i Mezhfaznye Granitsy) publishes articles in Russian and English dedicated to key issues of condensed matter and physicochemical processes at interfaces and in volumes.

The mission of the journal is to provide open access to the results of original research (theoretical and experimental) at the intersection of contemporary condensed matter physics and chemistry, material science and nanoindustry, solid state chemistry, inorganic chemistry, and physical chemistry, and to share scientific data in the **following sections**: atomic, electron, and cluster structure of solids, liquids, and interphase boundaries; phase equilibria and defect formation processes; structure and physical and chemical properties of interphases; laser thermochemistry and photostimulated processes on solid surfaces; physics and chemistry of surface, thin films and heterostructures; kinetics and mechanism of formation of film structures; electrophysical processes in interphase boundaries; chemistry of surface phenomena in sorbents; devices and new research methods.

The journal accepts for publication: reviews, original articles, short communications by leading Russian scientists, foreign researchers, lecturers, postgraduate and undergraduate students.

FOUNDER AND PUBLISHER:

Voronezh State University

The journal is registered by the Russian Federal Service for Supervision of Communications, Information Technology and Mass Media, Certificate of Registration ПИ № ФЦ77-78771 date 20.07.2020

The journal is included in the List of peer reviewed scientific journals published by the Higher Attestation Commission in which major research results from the dissertations of Candidates of Sciences (PhD) and Doctor of Science (DSc) degrees are to be published. Scientific specialties of dissertations and their respective branches of science are as follows: 1.4.1. – Inorganic Chemistry (Chemical sciences); 1.4.4. – Physical Chemistry (Chemical sciences); 1.4.6. – Electrochemistry (Chemical sciences); 1.4.15. – Solid State Chemistry (Chemical sciences); 1.3.8. – Condensed Matter Physics (Physical sciences).

The journal is indexed and archived in: Russian Scientific Index Citations, Scopus, Chemical Abstract, EBSCO, DOAJ, CrossRef

Editorial Board and Publisher Office:
1 Universitetskaya pl., Voronezh 394018
Phone: +7 (432) 2208445
<https://journals.vsu.ru/kcmf>
E-mail: kcmf@main.vsu.ru

Price – not fixed

Subscription index
in the Catalogue «Russian Post»
is I1H134

When reprinting the materials, a reference to the Condensed Matter and Interphases must be cited

The journal's materials are available under the Creative Commons "Attribution" 4.0 Global License



© Voronezh State University, 2023

EDITOR-IN-CHIEF:

Victor N. Semenov, Dr. Sci. (Chem.), Full Professor, Voronezh State University, (Voronezh, Russian Federation)

VICE EDITORS-IN-CHIEF:

Evelina P. Domashevskaya, Dr. Sci. (Phys.–Math.), Full Professor, Voronezh State University, (Voronezh, Russian Federation)

Polina M. Volovitch, Ph.D. (Chem.), Associate Professor, Institut de Recherche de Chimie (Paris, France)

EDITORIAL BOARD:

Nikolay N. Afonin, Dr. Sci. (Chem.), Voronezh State Pedagogical University (Voronezh, Russian Federation)

Vera I. Vasil'eva, Dr. Sci. (Chem.), Full Professor, Voronezh State University, (Voronezh, Russian Federation)

Aleksandr V. Vvedenskii, Dr. Sci. (Chem.), Full Professor, Voronezh State University, (Voronezh, Russian Federation)

Victor V. Gusarov, Dr. Sci. (Chem.), Associate Member of the RAS, Ioffe Physical-Technical Institute RAS (St. Petersburg, Russian Federation)

Vladimir E. Guterman, Dr. Sci. (Chem.), Full Professor, Southern Federal University (Rostov-on-Don, Russian Federation)

Boris M. Darinskii, Dr. Sci. (Phys.–Math.), Full Professor, Voronezh State University, (Voronezh, Russian Federation)

Vladimir P. Zlomanov, Dr. Sci. (Chem.), Full Professor, Moscow State University, (Moscow, Russian Federation)

Valentin M. Ievlev, Dr. Sci. (Phys.–Math.), Full Member of the RAS, Moscow State University, (Moscow, Russian Federation)

Aleksandr D. Izotov, Dr. Sci. (Chem.), Associate Member of the RAS, Kurnakov Institute of General and Inorganic Chemistry RAS (Moscow, Russian Federation)

Oleg A. Kozaderov, Dr. Sci. (Chem.), Associate Professor, Voronezh State University, (Voronezh, Russian Federation)

Andrey I. Marshakov, Dr. Sci. (Chem.), Full Professor, Frumkin Institute of Physical Chemistry and Electrochemistry RAS (Moscow, Russian Federation)

Irina Ya. Mittova, Dr. Sci. (Chem.), Full Professor, Voronezh State University, (Voronezh, Russian Federation)

Victor V. Nikonenko, Dr. Sci. (Chem.), Full Professor, Kuban State University (Krasnodar, Russian Federation)

Oleg V. Ovchinnikov, Dr. Sci. (Phys.–Math.), Full Professor, Voronezh State University, (Voronezh, Russian Federation)

Sergey N. Saltykov, Dr. Sci. (Chem.), Associate Professor, Novolipetsk Steel (Lipetsk, Russian Federation)

Vladimir F. Selemenev, Dr. Sci. (Chem.), Full Professor, Voronezh State University, (Voronezh, Russian Federation)

Vladimir A. Terekhov, Dr. Sci. (Phys.–Math.), Full Professor, Voronezh State University, (Voronezh, Russian Federation)

Evgeny A. Tutov, Dr. Sci. (Chem.), Associate Professor, Voronezh State Technical University (Voronezh, Russian Federation)

Pavel P. Fedorov, Dr. Sci. (Chem.), Full Professor, Prokhorov General Physics Institute RAS (Moscow, Russian Federation)

Vitaly A. Khonik, Dr. Sci. (Phys.–Math.), Full Professor, Voronezh State Pedagogical University (Voronezh, Russian Federation)

Vladimir A. Shaposhnik, Dr. Sci. (Chem.), Full Professor, Voronezh State University (Voronezh, Russian Federation)

Andrey B. Yaroslavtsev, Dr. Sci. (Chem.), Full Member of the RAS, Kurnakov Institute of General and Inorganic Chemistry RAS (Moscow, Russian Federation)

INTERNATIONAL MEMBERS OF THE EDITORIAL BOARD:

Mahammad Babanly, Dr. Sci. (Chem.), Associate Member of the ANAS, Institute of Catalysis and Inorganic Chemistry ANAS (Baku, Azerbaijan)

Tiziano Bellezze, Dr. Sci. (Chem.), Marche Polytechnic University (Ancona, Italy)

Mane Rahul Maruti, Ph.D. (Chem.), Shivaji University (Kolhapur, India)

Nguyen Anh Tien, Ph.D. (Chem.), Associate Professor, University of Pedagogy (Ho Chi Minh City, Vietnam)

Vladimir V. Pankov, Dr. Sci. (Chem.), Full Professor, Belarusian State University (Minsk, Belarus)

Fritz Scholz, Dr. Sci., Professor, Institut für Biochemie Analytische Chemie und Umweltchemie (Greifswald, Germany)

Mathias S. Wickleder, Dr. Sci., Professor, University of Cologne (Koln, Germany)

Vladimir Sivakov, Dr. rer. nat., Leibniz Institute of Photonic Technology (Jena, Germany)

EXECUTIVE SECRETARY:

Vera A. Logacheva, Cand. Sci. (Chem.), Voronezh State University, (Voronezh, Russian Federation)

CONTENTS

Original articles

Goncharova S. S., Redko Yu. A., Lavlinskaya M. S., Sorokin A. V., Holyavka M. G., Kondratyev M. S., Artyukhov V. G.

Biocatalysts based on papain associates with chitosan nanoparticles

173

Grevtseva I. G., Smirnov M. S., Chirkov K. S., Ovchinnikov O. V.

Trap state and exciton luminescence of colloidal PbS quantum dots coated with thioglycolic acid molecules

182

Gurchenko V. S., Mazinov A. S., Smirnov M. S., Grevtseva I. G., Nesterenko L. P., Ovchinnikov O. V.

Photoelectric response in sandwich structures based on condensed layers of Ag₂S quantum dots passivated with thioglycolic acid

190

Lyapun D. V., Kruzhilin A. A., Shevtsov D. S., Potapov A. Yu., Shikhaliev Kh. S.

A comparison of the inhibitory activity of 3-alkyl- and 3-hydroxyalkyl-5-amino-1H-1,2,4-triazoles against copper corrosion in chloride-containing environments

198

Parinova E. V., Antipov S. S., Sivakov V., Belikov E. A., Chuvenkova O. A., Kakuliia I. S., Trebunskikh S. Yu., Skorobogatov M. S., Chumakov R. G., Lebedev A. M., Artyukhov V. G., Turishchev S. Yu.

Localization of the *E. coli* Dps protein molecules in a silicon wires matrix according to scanning electron microscopy and X-ray photoelectron spectroscopy

207

Perepelitsa A. S., Aslanov S. V., Ovchinnikov O. V., Smirnov M. S., Grevtseva I. G., Latyshev A. N., Kondratenko T. S.

Photosensitising reactive oxygen species with titanium dioxide nanoparticles decorated with PbS quantum dots

215

Samoylov A. M., Kopytin S.S., Ivkov S.A., Ratkov E. A., Tutov E. A.

The effect of the synthesis conditions on the crystal structure of palladium(II) oxide nanofilms

225

Sushkova T. P., Semenova G. V., Proskurina E. Yu.

Phase relations in the Si–Sn–As system

237

Tomina E. V., Vo Quang Mai, Kurkin N. A., Doroshenko A. V., Nguyen Anh Tien, Sinelnikov A. A.

Influence of UV radiation on the catalytic activity of nanosized cobalt ferrite in the oxidative degradation reaction of dinitrophenol

249

Fedorov P. P., Chernova E. V.

Phase diagrams of zirconium dioxide systems with yttrium and scandium oxides

257

Kharina A. Yu., Charushina O. E., Eliseeva T. V.

Organic fouling of anion-exchange and bipolar membranes during the separation of amino acid and sucrose by electrodialysis

268

Chetverikova A. G., Makarov V. N., Kanygina O. N., Seregin M. M., Stroganova E. A.

Specifying the structural formula of kaolinite from the Orenburg Region by means of spectroscopic methods

277

Ashirov G. M., Babanly K. N., Mashadiyeva L. F., Yusibov Y. A., Babanly M. B.

Phase equilibria in the Ag₂S–Ag₈GeS₆–Ag₈SiS₆ system and some properties of solid solutions

292



Original articles

Research article

<https://doi.org/10.17308/kcmf.2023.25/11098>

Biocatalysts based on papain associates with chitosan nanoparticles

S. S. Goncharova¹, Yu. A. Redko¹, M. S. Lavlinskaya^{1,2}, A. V. Sorokin^{1,2}, M. G. Holyavka^{1,2}✉,
M. S. Kondratyev^{1,3}, V. G. Artyukhov¹

¹Voronezh State University,
1 Universitetskaya pl., Voronezh 394018, Russian Federation

²Sevastopol State University,
33 Universitetskaya st., Sevastopol 299053, Russian Federation

³Institute of Cell Biophysics of Russian Academy of Sciences, 3 Institutskaya st., Pushchino 142290, Russian Federation

Abstract

The research purpose was to develop and study biocatalysts based on papain associates with chitosan nanoparticles. We obtained medium and high molecular weight chitosan nanoparticles, both with and without ascorbic acid.

When the papain-nanoparticles complexes with ascorbic acid were formed, the catalytic activity of the enzyme increased by 3 % for medium molecular weight chitosan and by 16 % for high molecular weight chitosan. After 168 hours of incubation in 0.05 M of Tris-HCl buffer (pH 7.5) at 37 °C, the free enzyme retained 15 % of its catalytic activity, whereas its associates with chitosan nanoparticles exhibited ~ 30 %. The papain complex with chitosan nanoparticles and ascorbic acid exhibited 40 % of the enzyme catalytic activity.

We simulated the bonds and interactions within the chitosan-ascorbic acid-papain complex. The proposed biocatalysts have high prospects for effective use in cosmetology, biomedicine, and pharmacy.

Keywords: Nanoparticles, Papain, Chitosan, Association

Acknowledgements: The study was supported by Russian Science Foundation grant (project No. 21-74-20053, complexation of nanoparticles with enzymes).

For citation: Goncharova S. S., Redko Yu. A., Lavlinskaya M. S., Sorokin A. V., Holyavka M. G., Kondratyev M. S., Artyukhov V. G. Biocatalysts based on papain associates with chitosan nanoparticles. *Condensed Matter and Interphases*. 2023;25(2): 173–181. <https://doi.org/10.17308/kcmf.2023.25/11098>

Для цитирования: Гончарова С. С., Редько Ю. А., Лавлинская М. С., Сорокин А. В., Холявка М. Г., Кондратьев М. С., Артюхов В. Г. Биокатализаторы на основе ассоциатов папаина с наночастицами хитозана. *Конденсированные среды и межфазные границы*. 2023;25(2): 173–181. <https://doi.org/10.17308/kcmf.2023.25/11098>

✉ Marina G. Holyavka, e-mail: holyavka@rambler.ru

© Goncharova S. S., Redko Yu. A., Lavlinskaya M. S., Sorokin A. V., Holyavka M. G., Kondratyev M. S., Artyukhov V. G., 2023



1. Introduction

Nanoparticles are highly dispersed, usually spherical particles with dimensions not exceeding 100 nm. Nanoparticles have unique properties that make them useful for biomedical applications. The use of polymeric nanoparticles as carriers of genes and drugs is promising, as they are capable of controlled release and targeted delivery of biologically active substances [1].

Nanoparticles have different properties from those of macromolecules. They have a high specific surface area, causing an increase in dispersion. It influences the rate and the ability of the drug to be absorbed by the body systems. Due to the large interface area, nanoparticles are characterised by high drug sorption, which contributes to their more efficient use [2, 3]. Nanoparticles are energy-intensive systems: molecules or atoms on the interface lead to excess surface energy. To minimise this, nanoparticles interact effectively with any compounds and bind rapidly to each other.

The properties of nanoparticles are “collective”, they are determined not by a single particle, but by an ensemble of particles distributed in the dispersion medium. Therefore, the characteristics of the microenvironment are a determining factor in the drug delivery properties [4].

One of the promising materials for targeted delivery systems is chitosan. It is a modified natural polyamino- β -glycoside that has biodegradable, antibacterial, and antifungal properties [5–7]. The polymer is highly mucoadhesive and non-immunogenic [8].

Proteases are applied in many industrial processes, for example, in the food and pharmaceutical technologies, as well as in medicine. Papain has a special place among the frequently-used plant proteases [9, 10].

Papain (EC 3.4.22.2) is a proteolytic enzyme isolated from the unripe papaya peel (*Carica papaya*). The enzyme belongs to the cysteine protease family, it is stable under a wide range of conditions, even at high temperatures and pH values of 3–12. Papain has antibacterial, antioxidant, and antitumour properties. Its complexes are used as a pharmaceutical adjuvant [11–14].

The main disadvantage of proteolytic enzyme soluble forms is their rapid inactivation due to

proteolysis. One of the ways for increasing the stability of proteases is their association with nanoparticles.

Therefore, the aim of this work was to develop biocatalysts based on papain associates with chitosan nanoparticles and study their catalytic activity.

2. Experimental

Papain was the focus of the study and azocasein (Sigma, USA) was used as a substrate for hydrolysis. Nanoparticles were obtained from medium molecular weight (200 kDa) and high molecular weight (350 kDa) chitosan (Bioprogress, Russia).

Chitosan nanoparticles were obtained as follows: 300 mg of chitosan was dissolved in 100 ml of a 0.3 % acetic acid solution under mechanical stirring. Then, a 3 % NaOH solution was added until a white precipitate formed and the pH of the medium exceeded 11. The dispersion was passed through a filter (pore size 0.45 μm), the precipitate was washed with distilled water until neutral pH, placed in 100 ml distilled water, and sonicated using a Qsonica Sonicators (Japan) disintegrator for 10 min (40 kHz). To obtain nanoparticles with ascorbic acid, 50 mg of the latter was added to a solution of chitosan in acetic acid before adding the NaOH solution to it. The other procedures were carried out in the same way as described above.

The associates of nanoparticles with papain were obtained according to the method described in [15] and validated in [16–18].

The protease activity of the obtained complexes was measured as described in [19].

To determine the sizes and surface charges of the papain-nanoparticles associates, we used a Nano Zetasizer ZS (Malvern Instruments, UK) equipped with a 4 mW He/Ne laser with $\lambda = 632.8 \text{ nm}$, the scattering angle was 173° .

In silico studies of the bonds and interactions formed within the chitosan-ascorbic acid-papain complex were performed by flexible molecular docking in the Autodock Vina software (<https://sourceforge.net/projects/autodock-vina-1-1-2-64-bit/>) using the three-dimensional structure of papain (PDB ID: 9PAP, <https://www.rcsb.org/structure/9PAP>). The enzyme structure model

was developed and the carrier polymer matrix was optimised as described in [20].

3. Results and discussion

In the first series of experiments, we evaluated the sizes and zeta potentials of chitosan nanoparticle before and after association with papain. The parameters of the papain associates with nanoparticles are presented in Table 1. The median zeta potential of all nanoparticles was 0 mV. It was found that papain associates with medium and high molecular weight chitosan nanoparticles obtained with ascorbic acid differed significantly in size from the ones produced without ascorbic acid. When medium molecular weight chitosan nanoparticles interacted with papain, the size of the associates exceeded the size of free nanoparticles to a greater extent, 42 times for the particles formed without ascorbic acid and 13 times for those obtained with it. On the other hand, for high molecular weight chitosan nanoparticles associated with papain, the size of complexes was only 6 and 8 times larger, respectively, than that of empty nanoparticles. Based on the obtained sizes of papain-chitosan nanoparticles associates, we could assume that the protein adsorption on the surface of nanoparticles was followed by the formation of multilayer structures.

When papain formed complexes with medium and high molecular weight chitosan nanoparticles, obtained without ascorbic acid, the activity of the associates was 94 and 97 % of

the values for the native enzyme, respectively. When the papain-nanoparticles complexes with ascorbic acid were formed, the proteolytic activity of the enzyme increased by 3 % for medium molecular weight chitosan and by 16 % for high molecular weight chitosan (Fig. 1). The higher residual papain activity in the complex with chitosan nanoparticles formed with ascorbic acid is probably due to the antioxidant properties of this compound over the biocatalyst [21, 22].

The active site of papain is known to contain a cysteine residue. Its sulphhydryl group attacks on the substrate during its hydrolysis. In addition, the SH-group is an effective reducing agent. Therefore, it is easily oxidised by the air oxygen. There are sources reporting on the activation of papain by the introduction of various reducing agents, such as cysteine [23] and other SH-containing compounds [24]. Thus, the fact that papain associates with chitosan nanoparticles and ascorbic acid have higher activity may be attributed to the reducing effect of the acid on the active site SH-group. Moreover, there are reports on the effect of ascorbic acid [25] or its combination with Fe²⁺ [26] or Cu²⁺ [27] ions on the proteolytic activity of native papain. It should also be noted that ascorbic acid has low toxicity and is widely applied for medical purposes. So, it is possible to use enzyme preparations containing it in biomedicine and pharmacy.

We carried out experiments to evaluate the residual activity of papain at 37 °C and pH 7.5

Table 1. Characteristics of medium and high molecular weight chitosan nanoparticles and papain associates with them

Studied sample	Average size, nm	Size range, nm
Chitosan nanoparticles		
Medium molecular weight chitosan	12	7–21
Medium molecular weight chitosan with ascorbic acid	21	14–59
High molecular weight chitosan	33	18–79
High molecular weight chitosan with ascorbic acid	38	28–79
Papain associates with chitosan nanoparticles		
Medium molecular weight chitosan	499	164–1281
Medium molecular weight chitosan with ascorbic acid	267	91–712
High molecular weight chitosan	200	105–396
High molecular weight chitosan with ascorbic acid	321	105–825

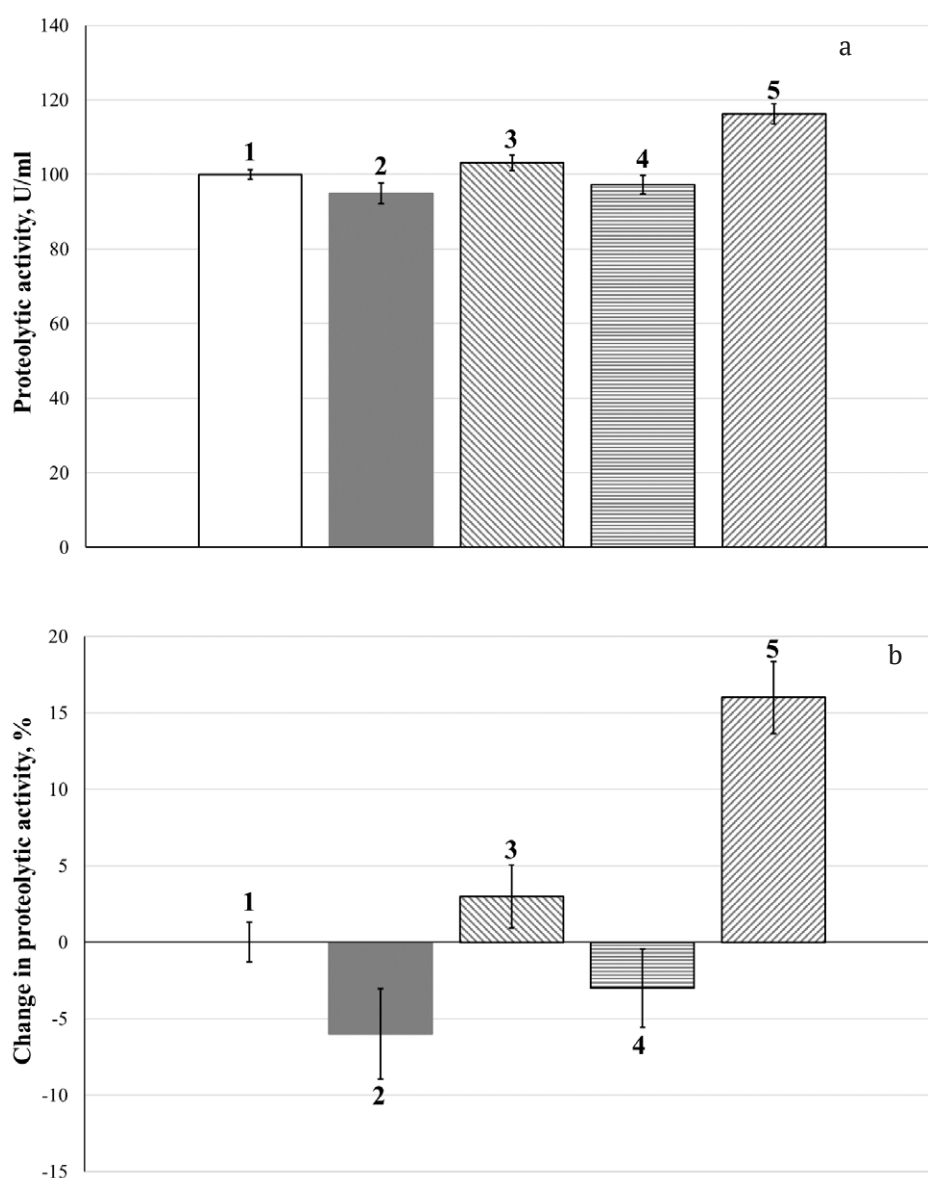


Fig. 1. Catalytic activity of papain, units/ml (A) and its change, % (B): soluble papain (1); papain associated with medium molecular weight chitosan nanoparticles (2); papain associated with medium molecular weight chitosan nanoparticles with ascorbic acid (3); papain associated with high molecular weight chitosan nanoparticles (4); and papain associated with high molecular weight chitosan nanoparticles with ascorbic acid (5). The activity of free papain under optimum hydrolysis conditions was taken as 100 %

in 0.05 M Tris-HCl buffer for free papain and its associates with medium and high molecular weight chitosan nanoparticles obtained with ascorbic acid and without it. All the samples showed a decrease in their activity within 7 days.

After incubation for 168 hours, native papain solution retained 15 % of its initial proteolytic activity. Its complexes with medium and high molecular weight chitosan nanoparticles, retained, respectively, 29 and 34 % of their ability

to hydrolyse azocasein. The associates with medium and high molecular weight chitosan nanoparticles prepared with ascorbic acid kept 40 and 43 %, respectively, of their proteolytic activity (Fig. 2).

Papain associates with both types of chitosan nanoparticles, obtained both with ascorbic acid and without it, were more stable than the free enzyme following 4 hours of incubation in 0.05 M Tris-HCl buffer with pH 7.5 at 37 °C. Thus, complexation with chitosan nanoparticles

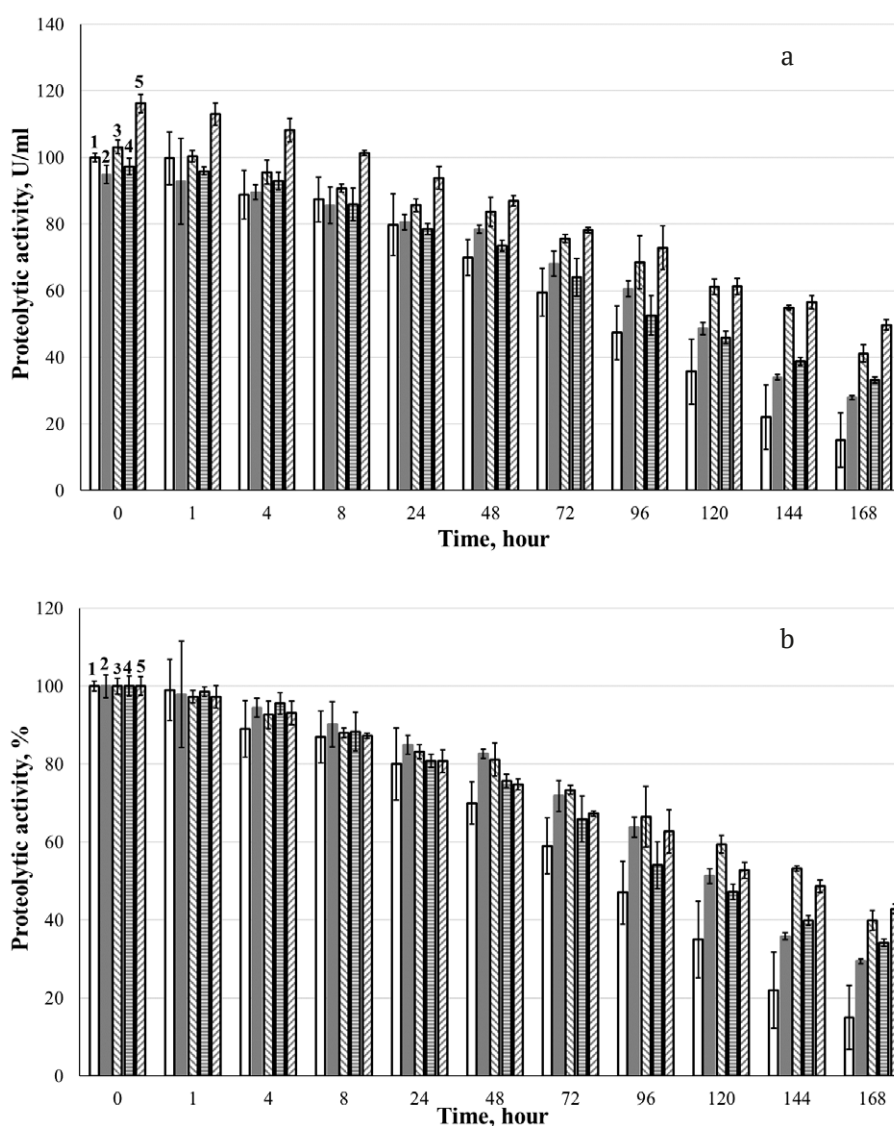


Fig. 2. Residual catalytic activity of papain after incubation of the samples at 37 °C (A: in units/ml of solution or suspension, B: % of the initial value): 1 – soluble papain; 2 – papain associated with medium molecular weight chitosan nanoparticles; 3 – papain associated with medium molecular weight chitosan nanoparticles with ascorbic acid; 4 – papain associated with high molecular weight chitosan nanoparticles; and 5 – papain associated with high molecular weight chitosan nanoparticles with ascorbic acid. The proteolytic activity of the samples without pre-incubation and under optimum hydrolysis conditions was taken as 100 %

increases the stability of papain more effectively than its association with chitosan microparticles under similar conditions. In the case of chitosan microparticles, proteolytic activity stabilisation effects were observed only after 96 hours of incubation in 0.05 M of Tris-HCl buffer with pH 7.5 at 37 °C [16].

To explain the higher residual activity of papain in the complexes with chitosan nanoparticles and ascorbic acid, as well as the increased stability of the enzyme in

this complex during incubation at 37 °C, we simulated the bonds and interactions within the chitosan-ascorbic acid-papain conjugate (Fig. 3). From the results of an *in silico* study of the interactions within the chitosan-ascorbic acid-papain system it also appears that ascorbic acid does not interact directly with cysteine, which is part of the active site (Cys25). However, it interacts hydrophobically with a catalytically-valuable histidine residue (His159) via the carbon skeleton. This fact indicates

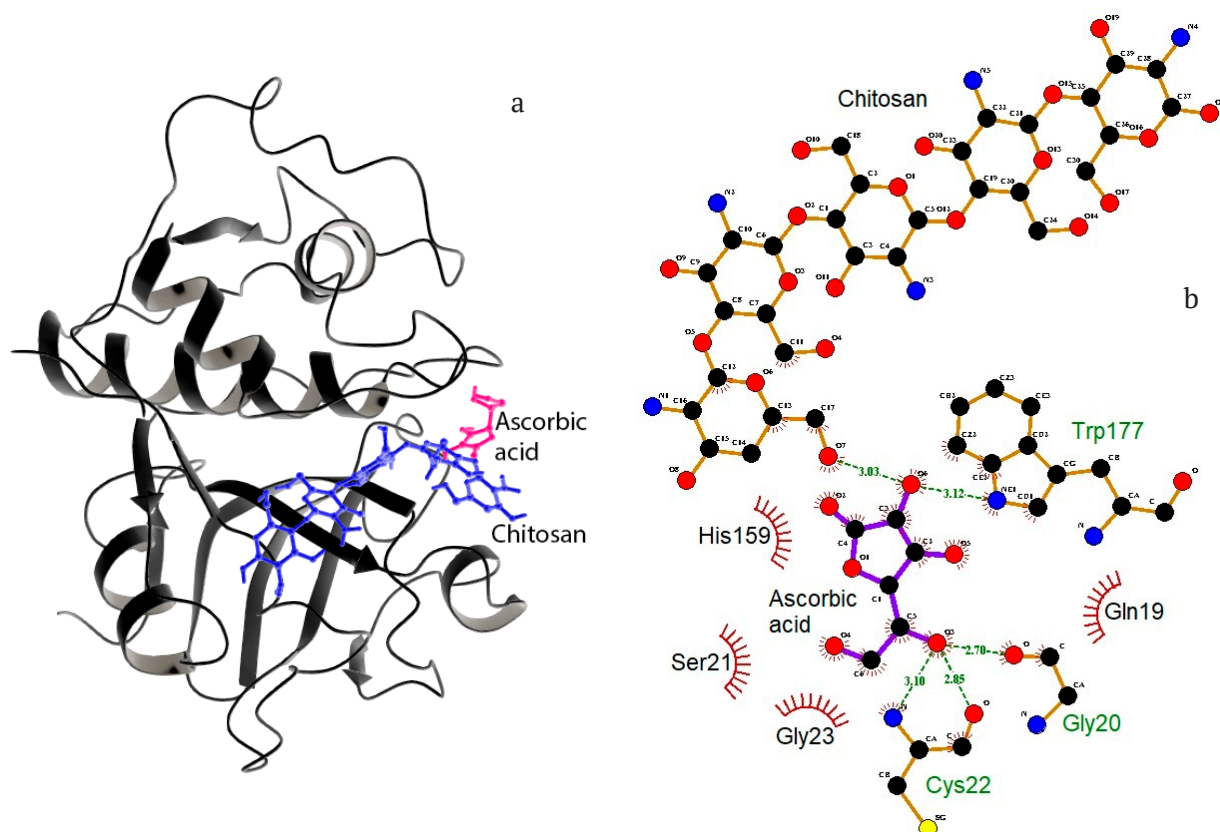


Fig. 3. Topology of the chitosan-ascorbic acid-papain complex (A), and the bonds and interactions between the components of the above system (the dotted lines indicate hydrogen bonds, their lengths are measured in Å (B))

the proximity of the potential reducing agent to the sulphhydryl group and also confirms the hypothesis of a reducing effect of ascorbic acid against the active site of papain. Moreover, ascorbic acid has some advantages over other types of reducing agents for cosmetology, biomedicine, and pharmacy: it is a cofactor for a number of enzymes involved in collagen biosynthesis, is necessary for wound healing and bone repair [28], is involved in thyroxine synthesis and amino acid metabolism [21], plays an important role in the antioxidant system, immune competence, and in the resistance to infections [29]. It prevents DNA mutations, and may be an important element in the treatment of some types of cancer and chronic diseases [29]. Chitosan ascorbate is known to have higher antibacterial activity against *Staphylococcus aureus* and *Escherichia coli* than chitosan, which probably inhibits microbial degradation of papain under physiological conditions (37 °C, pH 7.5) [30].

4. Conclusions

Thus, we obtained papain associates with medium and high molecular weight chitosan nanoparticles with and without ascorbic acid. The samples obtained with ascorbic acid exhibited higher proteolytic activity against azocasein.

It was found that papain associates with both types of chitosan nanoparticles and with ascorbic acid significantly differ in size from the associates with particles formed without it. Papain complexes with medium molecular weight chitosan particles exceed the size of free nanoparticles to a greater extent than the enzyme associates with the particles of high molecular weight chitosan.

While determining the stability of the complexes of chitosan and papain nanoparticles, we noticed a decrease in the proteolytic activity of the samples within seven days. The association with chitosan nanoparticles, especially those obtained with ascorbic acid, increased the stability of papain.

To explain the preserved activity of papain in the complexes with chitosan nanoparticles, we analysed *in silico* the interactions within the chitosan-ascorbic acid-papain system. It was determined that ascorbic acid does not bond directly with Cys25 in the papain active site, but involves into hydrophobic interactions with catalytically important amino acid residue His159. This proves the proximity of the potential reducing agent to the sulphhydryl group and confirms the hypothesis about the reducing effect of ascorbic acid on the active site of papain.

Contribution of the authors

The authors contributed equally to this article.

Conflict of interests

The authors declare that they have no known competing financial interests or personal relationships that could have influenced the work reported in this paper.

References

- Hillaireau H., Couvreur P. Nanocarriers' entry into the cell: relevance to drug delivery. *Cellular and Molecular Life Sciences*. 2009;66: 2873–2896. <https://doi.org/10.1007/s00018-009-0053-z>
- Ashurov N. S., Yugai S. M., Shakhobutdinov S. S., Atakhanov A. A. Physicochemical studies of the structure of chitosan and chitosan ascorbate nanoparticles. *Russian Chemical Bulletin*. 2022;71: 227–231. <https://doi.org/10.1007/s11172-022-3401-x>
- Medvedeva I. V., Medvedeva O. M., Studenok A. G., Studenok G. A., Tseytlin, E. M. New composite materials and processes for chemical, physico-chemical and biochemical technologies of water purification. *Izvestiya Vysshikh Uchebnykh Zavedenii Khimiya Khimicheskaya Tekhnologiya (ChemChemTech)*. 2022;66(1): 6–27. <https://doi.org/10.6060/ivkkt.20236601.6538>
- Egebro Birk S., Boisen A., Hagner Nielsen L. Polymeric nano- and microparticulate drug delivery systems for treatment of biofilms. *Advanced Drug Delivery Reviews*. 2021;174: 30–52. <https://doi.org/10.1016/j.addr.2021.04.005>
- Maevskaya E. N., Dresvyanina E. N., Shabunin A. S., ... Zinoviev E. V. *Preparation and study of the properties of hemostatic materials based on chitosan and chitin nanofibrils**. *Rossiiskie Nanotekhnologii*. 2020;15(4): 493–504. (In Russ.). <https://doi.org/10.1134/S199272232004007X>
- Kolesov S. V., Gurina M. S., Mudarisova R. K. Specific features of the formation of aqueous nanodispersions of interpolyelectrolyte complexes based of chitosan and chitosan succinamide. *Russian Journal of General Chemistry*. 2018;88: 1694–1698. <https://doi.org/10.1134/S1070363218080224>
- Cheung R., Ng T., Wong J., Chan W. Chitosan: an update on potential biomedical and pharmaceutical applications. *Marine Drugs*. 2015;13: 5156–5186. <https://doi.org/10.3390/md13085156>
- Popova E. V., Tikhomirova V. E., Beznos O. V., Grigoriev Yu. V., Chesnokova N. B., Kost O. A. Chitosan nanoparticles – the drug delivery system to the anterior segment of the eye. *Moscow University Chemistry Bulletin*. 2023;64(2): 141–151. <https://doi.org/10.55959/MSU0579-9384-2-2023-64-2-141-151>
- Silva-López R. E., Gonçalves R. N. Therapeutic proteases from plants: biopharmaceuticals with multiple applications. *Journal of Applied Biotechnology & Bioengineering*. 2019;6(2): 101–109. <https://doi.org/10.15406/jabb.2019.06.00180>
- Pankova S. M., Sakibaev F. A., Holyavka M. G., Artyukhov V. G. A possible role of charged amino-acid clusters on the surface of cysteine proteases for preserving activity when binding with polymers. *Biophysics*. 2022;67(1): 8–14. <https://doi.org/10.1134/S0006350922010146>
- Hu R., Chen G., Li Y. Production and characterization of antioxidative hydrolysates and peptides from corn gluten meal using papain, ficin, and bromelain. *Molecules*. 2020;25(18): 4091. <https://doi.org/10.3390/molecules25184091>
- Koroleva V. A., Olshannikova S. S., Holyavka M. G., Artyukhov V. G. Thermal inactivation of cysteine proteases: the key stages. *Biophysics*. 2021;66(3): 364–372. <https://doi.org/10.1134/S0006350921030088>
- Kong Y. R., Jong Y. X., Balakrishnan M., ... Khaw K. Y. Beneficial role of *Carica papaya* extracts and phytochemicals on oxidative stress and related diseases: a mini review. *Biology*. 2021;10(4): 20. <https://doi.org/10.3390/biology10040287>
- Semashko T. A., Lysogorskaya E. N., Okse-noit E. S., Bacheva A. V., Filipova I. Yu. Chemoenzymatic synthesis of new fluorogenous substrates for cysteine proteases of the papain family. *Russian Journal of Bioorganic Chemistry*. 2008;34(3): 339–343. <https://doi.org/10.1134/S1068162008030151>
- Szeto Y. S., Hu Z. *Method for preparing chitosan nano-particles*. Patent no US2008/0234477 A1. Publ. 25.09.2008.
- Olshannikova S. S., Redko Yu. A., Lavlinskaya M. S., Sorokin A. V., Kholyavka M. G., Artyukhov V. G. Preparation of papain complexes with chitosan microparticles and evaluation of their stability using the level of enzyme activity. *Khimiko-Farmatsevticheskii Zhurnal*. 2021;55(11): 51–55. (In

Russ., abstract in Eng.). <https://doi.org/10.30906/0023-1134-2021-55-11-51-55>

17. Koroleva V. A., Holyavka M. G., Olshannikova S. S., Artyukhov V. G. Formation of ficine complexes with chitozan nanoparticles with a high level of proteolytic activity. *Russian Journal of Biopharmaceuticals*. 2018;10(4): 36–40. (In Russ., abstract in Eng.). Available at: <https://elibrary.ru/item.asp?id=36834674>

18. García-Carreño F. L. The digestive proteases of langostilla (*pleuroncodes planipes*, decapoda): their partial characterization, and the effect of feed on their composition. *Comparative Biochemistry and Physiology Part B: Comparative Biochemistry*. 1992;103: 575–578. [https://doi.org/10.1016/0305-0491\(92\)90373-Y](https://doi.org/10.1016/0305-0491(92)90373-Y)

19. Sabirova A. R., Rudakova N. L., Balaban N. P., ... Sharipova M. R. A novel secreted metzincin metalloproteinase from *Bacillus intermedius*. *FEBS Letters*. 2010;584 (21): 4419–4425. <https://doi.org/10.1016/j.febslet.2010.09.049>

20. Olshannikova S. S., Malykhina N. V., Lavlinskaya M. S., ... Artyukhov V. G. Novel immobilized biocatalysts based on cysteine proteases bound to 2-(4-acetamido-2-sulfanilamide) chitosan and research on their structural features. *Polymers*. 2022;14: 3223. <https://doi.org/10.3390/polym14153223>

21. Burri B., Jacob R. *Human metabolism and the requirement for vitamin C*. In: *Vitamin C in health and disease*. Packer L., Fuchs J. (eds.). New York: Marcel Dekker Inc., 1997; 25–58.

22. Arrigoni O., De Tullio M. C. Ascorbic acid: much more than just an antioxidant. *Biochimica et Biophysica Acta*. 2002;1569: 1–9. [https://doi.org/10.1016/s0304-4165\(01\)00235-5](https://doi.org/10.1016/s0304-4165(01)00235-5)

23. Homaei A. A., Sajedi R. H., Sariri R., Seyfzadeh S., Stevanto R. Cysteine enhances activity and stability of immobilized papain. *Amino Acids*. 2010;38: 937–942. <https://doi.org/10.1007/s00726-009-0302-3>

24. Storer A. C., Menrad R. Chapter 419 – Papain. In: *Handbook of Proteolytic Enzymes*. Rawlings N. D., Salvesen G. (eds.). Academic Press; 2013. Vol. 2, pp. 1858–1861. <https://doi.org/10.1016/b978-0-12-382219-2.00418-x>

25. Kyoichi O., Ohnishi T., Tanaka S. Activation and inhibition of papain. *The Journal of Biochemistry*. 1962;51(5): 372–374. <https://doi.org/10.1093/oxfordjournals.jbchem.a127547>

26. Purr A. The activation phenomena of papain and cathepsin. *Biochemical Journal*. 1935;29(1): 13–20. <https://doi.org/10.1042/bj0290013>

27. Kanazawa H., Fujimoto S., Ohara A. On the mechanism of inactivation of active papain by ascorbic acid in the presence of cupric ions. *Biological and Pharmaceutical Bulletin*. 1994;17(6): 789–793. <https://doi.org/10.1248/bpb.17.789>

28. Rebouche C. J. Ascorbic acid and carnitine biosynthesis. *The American Journal of Clinical Nutrition*. 1991;54(6): 1147S–1152S. <https://doi.org/10.1093/ajcn/54.6.1147s>

29. Carr A. C., Frei B. Toward a new recommended dietary allowance for vitamin C based on antioxidant and health effects in humans. *The American Journal of Clinical Nutrition*. 1999;69(6): 1086–1107. <https://doi.org/10.1093/ajcn/69.6.1086>

30. Gegel N. O., Zudina I. V., Malinkina O. N., Shipovskaya A. B. Effect of ascorbic acid isomeric forms on antibacterial activity of its chitosan salts. *Microbiology*. 2018;87(5): 732–737. <https://doi.org/10.1134/S0026261718050107>

Information about the authors

Svetlana S. Goncharova, Junior Researcher, department of biophysics and biotechnology, Voronezh State University (Voronezh, Russian Federation).

<https://orcid.org/0000-0003-3381-2008>

Olshannikovas@gmail.com

Yulia A. Redko, master student, department of biophysics and biotechnology, Voronezh State University (Voronezh, Russian Federation).

<https://orcid.org/0009-0008-8318-8833>

redkoju@yandex.ru

Maria S. Lavlinskaya, Cand. Sci. (Chem.), Senior Researcher, Department of Biophysics and Biotechnology, Voronezh State University; Senior Researcher of Bioresource Potential of the Seaside Territory Laboratory, Sevastopol State University (Sevastopol, Russian Federation).

<https://orcid.org/0000-0001-9058-027X>

maria.lavlinskaya@gmail.com

Andrey V. Sorokin, postgraduate student, Department of Macromolecular Compounds and Colloidal Chemistry, Voronezh State University, Junior Researcher, Department of Biophysics and Biotechnology, Voronezh State University, Junior Researcher of Bioresource Potential of the Seaside Territory Laboratory, Sevastopol State University (Sevastopol, Russian Federation).

<https://orcid.org/0000-0001-5268-9557>

andrew.v.sorokin@gmail.com

Marina G. Holyavka, Dr. Sci. (Biology), Professor, Department of Biophysics and Biotechnology, Voronezh State University (Voronezh, Russian Federation), Professor of Physics Department, Sevastopol State University (Sevastopol, Russian Federation).

<https://orcid.org/0000-0002-1390-4119>

holyavka@rambler.ru

Maxim S. Kondratyev, Cand. Sci. (Phys.–Math.), Head of the Laboratory of Structure and Dynamics of Biomolecular Systems, Institute of Cell Biophysics of the Russian Academy of Sciences (Pushchino, Russian Federation).

<https://orcid.org/0000-0001-6717-4206>
ma-ko@bk.ru

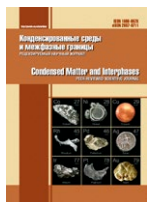
Valery G. Artyukhov, Dr. Sci. (Biology), Professor, Head of the Biophysics and Biotechnology Department, Voronezh State University (Voronezh, Russian Federation)

<https://orcid.org/0000-0002-5872-8382>
artyukhov@bio.vsu.ru

Received 03.10.2022; approved after reviewing 23.11.2022; accepted for publication 15.12.2022; published online 25.06.2023.

Translated by Anastasiia Ananeva

Edited and proofread by Simon Cox



Original articles

Research article

<https://doi.org/10.17308/kcmf.2023.25/11099>**Trap state and exciton luminescence of colloidal PbS quantum dots coated with thioglycolic acid molecules**

I. G. Grevtseva, M. S. Smirnov, K. S. Chirkov, O. V. Ovchinnikov✉

Voronezh State University,
1 Universitetskaya pl., Voronezh 394018, Russian Federation**Abstract**

This work presents the results of studying the IR luminescence of colloid PbS quantum dots coated with molecules of thioglycolic acid.

Luminescence of the sample was recorded using the InGaAs image sensor PDF 10C/M (Thorlabs Inc., USA) and a diffraction monochromator with 600 mm^{-1} grating. To study the temperature dependence of luminescence, the sample was cooled in a nitrogen cryostat down to 80 K. A redistribution of the luminescence intensity between two peaks (1100 and 1280 nm) was identified upon a decrease in temperature. It was shown that an exciton absorption peak was present in the excitation spectrum for the short-wave luminescence peak, and the Stokes shift was $\Delta E_{\text{Stokes}} \sim 0.1 \text{ eV}$. On the contrary, the exciton peak was absent in the luminescence excitation spectrum of the long-wave band, and its red boundary was shifted towards the short-wave region, that provided the Stokes shift of more than 0.3 eV.

It was concluded that the short-wave luminescence band appeared as a result of the radiative annihilation of an exciton, while the long-wave band appeared due to the recombination of charge carriers at trap states. Trap state luminescence was effectively excited upon direct absorption of the radiation by the luminescence centre. A three-level diagram was suggested that determined the IR luminescence of colloid PbS quantum dots coated with thioglycolic acid molecules.

Keywords: Lead sulphide quantum dots, Luminescence spectra, Excitation spectra

Funding: The study was supported by Russian Science Foundation grant No. 22-12-00232, <https://rscf.ru/project/22-12-00232/>

Acknowledgements: The results of transmission electron microscopy using a Libra 120 microscope were obtained with the help of the equipment of the Centre for Collective Use of Voronezh State University.

For citation: Grevtseva I. G., Smirnov M. S., Chirkov K. S., Ovchinnikov O. V. Trap state and exciton luminescence of colloidal PbS quantum dots coated with thioglycolic acid molecules. *Condensed Matter and Interphases*. 2023;25(2): 182–189. <https://doi.org/10.17308/kcmf.2023.25/11099>

Для цитирования: Гревцева И. Г., Смирнов М. С., Чирков К. С., Овчинников О. В. Рекомбинационная и экситонная люминесценция коллоидных квантовых точек PbS, покрытых молекулами тиогликолевой кислоты. *Конденсированные среды и межфазные границы*. 2023;25(2): 182–189. <https://doi.org/10.17308/kcmf.2023.25/11099>

✉ Oleg V. Ovchinnikov, e-mail: ovchinnikov_o_v@rambler.ru

© Grevtseva I. G., Ovchinnikov O. V., Smirnov M. S., Chirkov K. S., 2023



The content is available under Creative Commons Attribution 4.0 License.

1. Introduction

Semiconductor colloid quantum nanocrystals (quantum dots or QDs) attract interest due to their wide range of potential application in various optoelectronic devices and systems. QDs can be used in optic sensors and laser emitters and as non-linear media for controlling intensity, radiation phase, etc. [1–4]. It is possible to use QDs in various devices as their spectral and transport properties can be easily adjusted due to the quantum size effect.

A detailed understanding of the photoprocesses regularities that determine the size-dependent spectral-luminescent properties is required for the practical application of QDs. In case of non-stoichiometric compounds, photoprocesses are also significantly complicated by the participation of Defect trap states. PbS is one of the typical representatives of non-stoichiometric semiconductors [5]. The increased interest in PbS is associated with the possibility of its use in the IR range as the band gap of a bulk crystal is 0.41 eV [6] and the exciton Bohr radius is approximately 20 nm. The absorption bands from IR to the visible range can be controlled by varying the crystal sizes in the range of 1–20 nm due to the quantum size effect [7–13].

Controlling the position of luminescence peaks is an individual large task. Together with a change in the energy structure of exciton states due to variation in the QD size, there is also a possibility to obtain new luminescence bands determined by optical transitions on trap states of charge carriers [15–17].

Still, in each specific case it is necessary to establish the photoprocesses regularities and luminescence mechanisms for different types of semiconductors. At the present time for PbS QDs, the observed experimental regularities turn out to be very contradictory [7–13].

In [9], it was shown for PbS QDs dispersed in polyvinyl films that upon a temperature increase from 10 to 250 K the width of the effective band gap decreased ($\Delta E_g/\Delta T = -1.1 \cdot 10^{-4}$ eV/K). On the contrary, the width of the band gap increased for massive PbS upon a temperature increase ($\Delta E_g/\Delta T = +4.7 \cdot 10^{-4}$ eV/K) [18]. Based on the temperature dependences, the complex band in the QD luminescence spectra was decomposed into three peaks [9] with the Stokes shift (0.47,

0.25, and 0.17 eV). All three peaks were correlated with the recombination of charge carriers on trap states. However, in [7,8,12,13,19], an exciton luminescence mechanism was assumed for luminescence peaks with a Stokes shift regarding the exciton absorption peak in the range from 0 to 0.6 eV.

In [10], two luminescence peaks were discovered for PbS QD films coated with ethanethiol. Based on the data of femtosecond transient absorption spectroscopy, the process of thermal release of localized charge carriers was shown. The increase in the short-wave luminescence peak and decrease in the long-wave peak were observed under an increase in temperature. The increase in the short-wave luminescence peak and decrease in the long-wave peak were observed under an increase in temperature. It was concluded that the short-wave luminescence peak corresponded to radiative exciton annihilation, while the long-wave peak corresponded to the recombination on trap states.

In [20], the complex luminescence band for PbS QDs was also represented by the total of three individual components. Based on the analysis of the data of time-resolved luminescence, it was concluded that the short-wave luminescence peak was determined by the radiative exciton annihilation. As for the other two peaks, the authors associated them with phonon repetitions, although there was a strong difference in the luminescence kinetics of all three bands.

Therefore, the existing experimental data on the regularities of the PbS QD luminescence are very contradictory.

In this work we present the results of studies of the luminescence regularities of colloidal PbS QDs coated with thioglycolic acid molecules (PbS/TGA QDs).

2. Experimental

1.1. Synthesis method

Colloidal PbS/TGA QDs were synthesised in water using thioglycolic acid (TGA) molecules as a passivator of the QD surface. The synthesis method was based on the techniques that we used previously to obtain colloidal solutions of silver and cadmium sulphide QDs [14, 17].

The synthesis of PbS QDs was based on the reaction of substitution of thioglycolic acid

molecules for sulphur atoms in the Pb:TGA precursor. At first, 1.5 mmol of $\text{Pb}(\text{NO}_3)_2$ were dissolved in 50 ml of distilled water, and thioglycolic acid (3 mmol) was added. After that, the pH level was increased up to 9 by the addition of NaOH (1 M), which allowed obtaining the $\text{Pb}(\text{SCH}_2\text{COONa})_2$ precursor. The addition of an aqueous solution of Na_2S (0.85 mmol) was accompanied by a change in colour to brown, which indicated the formation of PbS/TGA QDs. The obtained solution of colloidal QDs was precipitated with acetone (which was added by volume to a concentration of 50%) and centrifugation. The precipitate was gathered and dissolved again in distilled water. The process of purification was repeated twice. Thus, the studied samples were a colloidal solution of PbS/TGA QDs in water.

2.2. Experimental techniques

Structural studies of the sample were conducted using transmission electron spectroscopy (TEM) with a Libra 120 microscope (CarlZeiss, Germany) and a digital analysis of TEM images and X-ray diffraction. The size dispersion of QDs was determined in the sample using TEM images.

Absorption spectra were recorded on a USB2000+ spectrometer (Ocean optics) with a USB-DT radiation source (Ocean optics). Luminescence spectra in the IR region were recorded on a

PDF 10C/M image sensor (ThorlabsInc., USA) with the built-in amplifier and a diffraction monochromator with a 600 mm^{-1} grating. The luminescence spectra were corrected for the spectral characteristics of the devices which was measured using a reference incandescent tungsten lamp with a known colour temperature.

We used the 400 W incandescent lamp and a second monochromator with a 1200 mm^{-1} grating in order to obtain the luminescence excitation spectra, which resulted in an excitation region from 500 to 1300 nm.

We placed the sample in a nitric cryostat and cooled it down to 80 K in order to record the luminescence spectra of the studied sample at low temperatures.

3. Results and discussion

Figure 1a shows a TEM image of the studied samples of PbS/TGA QDs with a histogram of the QD size distribution. It can be seen that the suggested synthesis method allowed obtaining individual nanoparticles with an average size of about 3 nm. The size dispersion was approximately 25–30 %.

Figure 1b shows X-ray diffraction from a PbS QD sample for $\text{CuK}\alpha$ radiation with a 1.056 \AA length, and there are well-distinguished reflections at 25.9° , 30.1° , and 43.05° , corresponding to the cubic modification of the PbS crystal. All

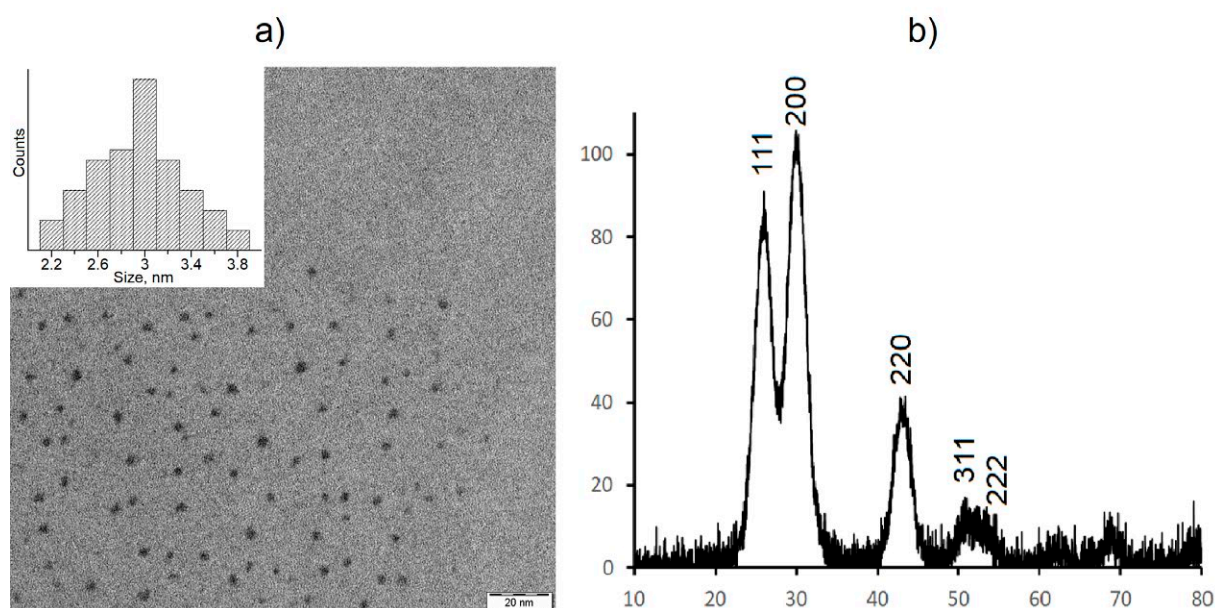


Fig. 1. TEM image of PbS/TGA QDs with size distribution histogram (a). X-ray diffraction from a sample (b)

reflections were significantly broadened. The size of the crystallites was assessed using the Scherrer equation:

$$d = \frac{0.9\lambda}{\beta \cos\theta}, \quad (1)$$

where d is the size, nm, λ is the wavelength of the X-ray emission 0.15405 nm, β is the width of the diffraction peak at half height (the (220) peak was used as it did not overlap with other reflections), θ is the Bragg angle. The size value was of about 3–3.5 nm, which correlated well with the TEM data. Therefore, the synthesized sample was a set of PbS nanocrystals with an average size of about 3 nm.

Figure 2 shows the optical absorption spectrum of PbS/TGA QDs. The edge of the absorption spectrum located in the region of about 1000 nm was shifted towards the short-wave region in relation to the absorption edge of bulk PbS (0.41 eV or 3025 nm), which indicated the quantum limitation of charge carriers. The exciton structure was absent for the absorption spectrum, which is typical for QDs from semiconductors with a high degree of non-stoichiometry [14]. In this case, the shape of the absorption spectrum can be determined not only by transitions between the quantum size states of the nanocrystal but also by transitions with the participation of trap states. A significant contribution to the absence of an exciton

structure was also determined by the considerable size dispersion of QDs in the sample.

Intensive IR luminescence emerged upon the excitation with the wavelength of 462 nm, its spectrum is also presented in Fig. 2. The luminescence spectrum was not elementary and there were at least two peaks, a short-wave peak with the maximum of about 1100 nm and a long-wave peak with the maximum of about 1280 nm. The half width at half-maximum (HWHF) of both luminescence peaks was estimated to be within the range of 0.1–0.2 eV. Narrow luminescence peaks for QDs are usually attributed to radiative exciton annihilation, but luminescence peaks with a HWHF not more than 0.2 eV can also be some semiconductor compounds, even in case of trap-state luminescence [14]. In our case, the absence of an exciton structure in the absorption spectrum did not allow determining the Stokes shift for the identified luminescence peaks. To establish the luminescence mechanisms, we need to consider the luminescence excitation spectra.

As opposed to the absorption spectra that are determined by the absorption of each nanocrystal in the sample, only the QDs emitting in the wavelength of emission recording participate in the formation of the excitation spectra. This allowed achieving selectivity by the wavelength in the luminescence excitation spectra through a change in the wavelength of emission recording.

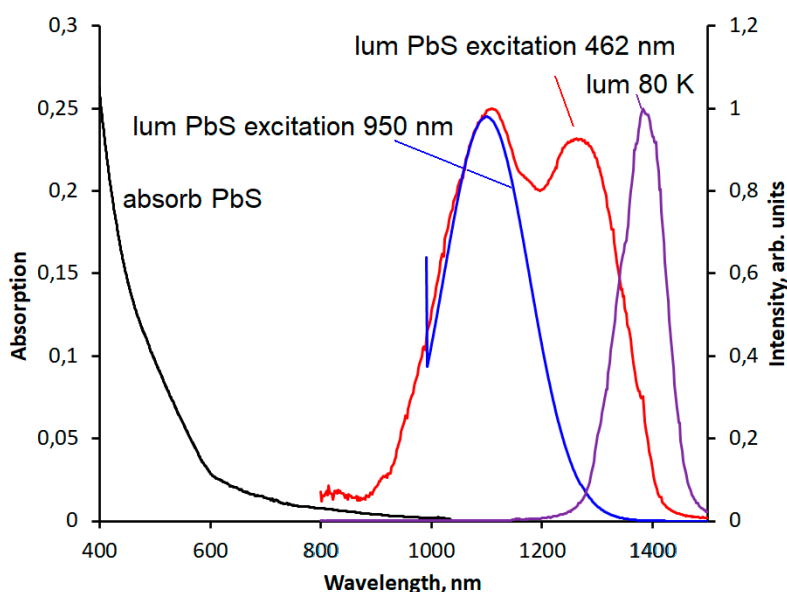


Fig. 2. Spectra of absorption and luminescence of colloidal solutions of PbS/TGA QDs in a quartz cuvette

Figure 3 presents the luminescence excitation spectra recorded at the peak of the observed bands. Narrow intense peaks in the region of 1100 and 1280 nm with a HWHF of approximately 15 nm were associated with the scattering of the excitation radiation, when its wavelength was the same as the wavelength of the luminescence recording. A specific feature was observed with a peak at 990 nm in the luminescence excitation spectrum in the short wavelength band (1100 nm). According to the position and shape of this peak, it was associated with absorption into the ground state of the exciton. In this case, the Stokes shift of the luminescence peak in relation to the exciton absorption peak was 0.125 eV. This value is typical for the PbS QDs exciton luminescence with an average size of about 3–3.5 nm. On the contrary, no exciton structure was found in the luminescence excitation spectrum with a peak at 1280 nm. The excitation band edge was located in the region of 950 nm while the Stokes shift value increased up to 0.33 eV. This allowed associating the long-wave luminescence band with the radiative recombination of charge carriers on trap states. It should be noted that the excitation of the recombination band from the exciton absorption peak was not effective enough (the exciton

absorption peak was absent from the excitation spectrum). Indeed, the intensity of the long-wave band was significantly lower as compared to the short-wave band upon excitation with a wavelength of 950 nm (Fig. 2). The strong absorption by trap states was also shown in [10] as compared to its own exciton absorption for PbS QDs.

If the suggested luminescence mechanisms of colloidal PbS/TGA QDs (recombination and exciton bands) are correct, and both luminescence peaks belong to each QD in the sample, not to individual nanocrystals, there must be some relationship between the intensity of the luminescence bands. And in fact, there is. When the PbS/TGA colloidal QD sample was cooled down to 80 K, the luminescence band with a peak at 1100 nm disappeared, and the radiation in the long-wave band became more intense (Fig. 2). As it cooled down, the long-wave luminescence peak gradually shifted towards the long-wave region from 1280 to 1380 nm, by 0.07 eV.

The dependence of the relative intensity of the luminescence bands on temperature showed that both bands belonged to each nanocrystal in the sample and allowed creating a diagram of energy levels and the transitions between them (Fig. 4). The diagram includes a non-excited

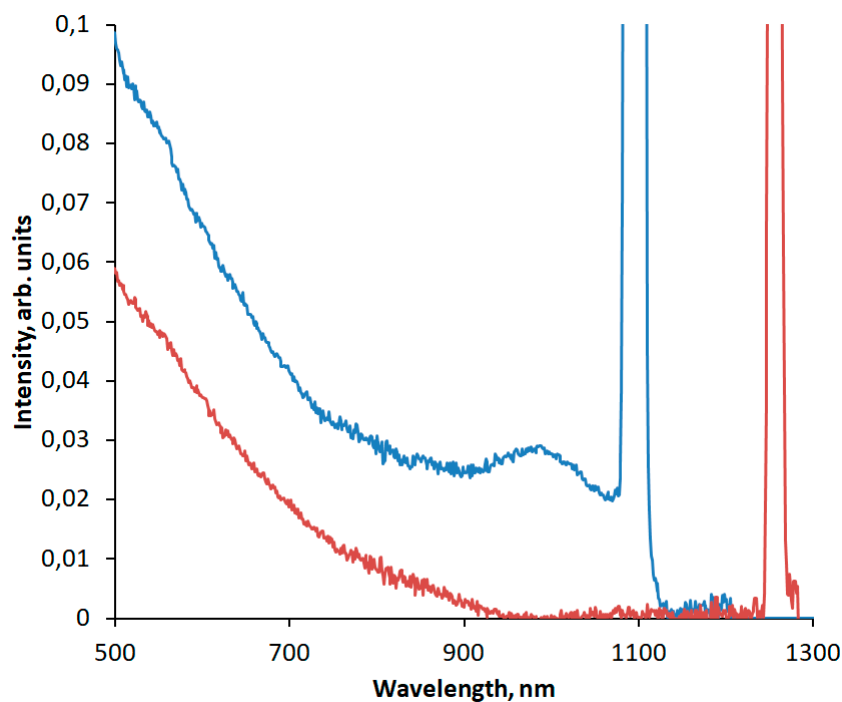


Fig. 3. Luminescence excitation spectra

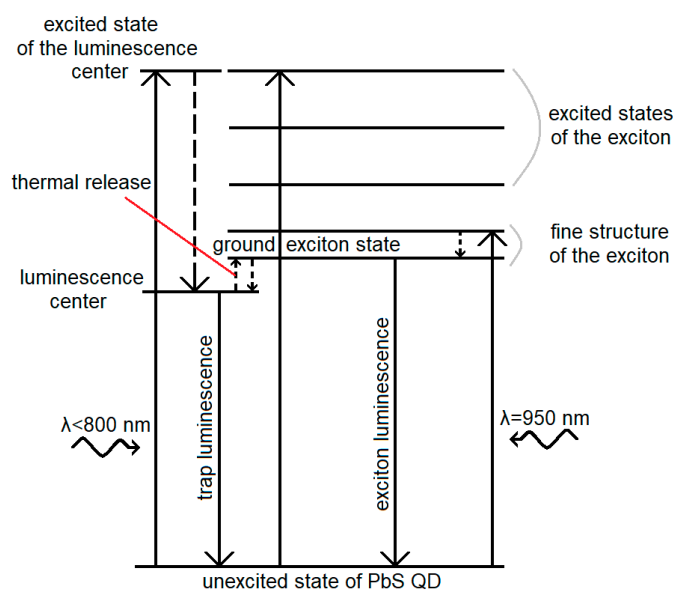


Fig. 4. Diagram of energy transitions in PbS/TGA QDs

state and several excited states of the exciton determine by the ground and the excited state of the electron and the hole at the quantum size levels of the nanocrystal. There were also several levels of the excited state of the trap state luminescence centre.

The observation of two peaks in the luminescence spectrum at room temperature can be explained by the fact that charge carriers are mainly captured by the excited state of the trap when QDs are excited by radiation with a wavelength of 462 nm. After that, charge carriers can move to the exciton level as a result of thermal activation. Therefore, charge carriers are able to recombine both from the trap and from the exciton levels. The thermal activation of the transition to the exciton level also explains the absence of an exciton peak in the spectrum upon cooling the sample down to a temperature of 80 K. When QDs are excited by radiation with a wavelength of 950 nm, the exciton is excited directly. In this case, the capture of charge carriers by the trap state luminescence centre was less efficient as compared to the radiative exciton annihilation, which can explain the weakening of the peak associated with the luminescence from the trap. Thermal excitation of charge carriers from the luminescence centre to the exciton state contributed to the increase in the population of the latter and the increase in the exciton

luminescence with increasing temperature. Excitation of the exciton state with the lowest energy (the wavelength of about 950 nm) apparently corresponded to non-resonant low-efficiency excitation of the luminescence centre. The capture of charge carriers from the exciton state to the luminescence centre was also a slow process. The low capture rate contributed to the dominance of exciton luminescence upon direct excitation by radiation with a wavelength of 950 nm, which corresponded to the region of the exciton absorption peak (Fig. 3).

Therefore, the intense IR luminescence identified for PbS/TGA QDs in two bands corresponded to radiative exciton annihilation at 1100 nm and to recombination on trap states in the long-wave region.

4. Conclusions

In this work we presented new regularities in the IR luminescence of colloid quantum dots of lead sulphide coated with the molecules of thioglycolic acid. Two luminescence peaks with peaks at 1100 nm and 1280 nm were found. A temperature decrease down to 80 K was accompanied by the decrease in luminescence intensity in the short-wave band and simultaneous increase in the intensity of the long-wave luminescence peak. In addition, fundamental differences were found between the photoluminescence excitation

spectra for two peaks. The exciton structure was present in the excitation spectrum of the short-wave luminescence peak while the Stokes shift was about 0.1 eV. On the contrary, no exciton structure was found in the excitation spectrum for the long-wave luminescence peak, while the Stokes shift in the luminescence peak in relation to the long-wave edge of the excitation spectrum was approximately 0.3 eV. It was concluded that the nature of the short-wave peak (1100 nm) was associated with the radiative exciton annihilation, and the long-wave peak emerged as a result of the recombination of charge carriers on trap states. We proposed an empirical diagram of photoprocesses that takes into account the thermal redistribution of the populations of the exciton state and trap state luminescence centre together with the special features of direct excitation of trap state luminescence.

Author contributions

I. G. Grevtseva – methodology development, text writing and editing. M. S. Smirnov – research concept, conducting research, review writing, and text editing. K. S. Chirkov – conducting research, review writing. O. V. Ovchinnikov – scientific supervision, research concept, methodology development, text writing, final conclusions.

Conflict of interests

The authors declare that they have no known competing financial interests or personal relationships that could have influenced the work reported in this paper.

References

1. Shehab M., Ebrahim S., Soliman M. Graphene quantum dots prepared from glucose as optical sensor for glucose. *Journal of Luminescence*. 2017;184: 110–116. <http://dx.doi.org/10.1016/j.jlumin.2016.12.006>
2. Chen F., Lin Q., Shen H., Tang A. Blue quantum dot-based electroluminescent light-emitting diodes. *Materials Chemistry Frontiers*. 2020;4: 1340–1365. <https://doi.org/10.1039/D0QM00029A>
3. Bai Z., Ji W., Han D., Chen L., ... Zhong H. Hydroxyl-terminated CuInS₂ based quantum dots: toward efficient and bright light emitting diodes. *Chemistry of Materials*. 2016;28(4): 1085–1091. <https://doi.org/10.1021/acs.chemmater.5b04480>
4. Peng Y., Wang G., Yuan C., He J., Ye S., Luo X. Influences of oxygen vacancies on the enhanced non-linear optical properties of confined ZnO quantum

- dots. *Journal of Alloys and Compounds*. 2018;739: 345–352 <https://doi.org/10.1016/j.jallcom.2017.12.250>
5. Sadovnikov S. I., Rempel A. A. Nonstoichiometric distribution of sulfur atoms in lead sulfide structure. *Doklady Physical Chemistry*. 2009;428(1): 167–171. <https://doi.org/10.1134/S0012501609090024>
6. Scanlon W. W. Recent advances in the optical and electronic properties of PbS, PbSe, PbTe and their alloys. *Journal of Physics and Chemistry of Solids*. 1959;8: 423–428. [https://doi.org/10.1016/0022-3697\(59\)90379-8](https://doi.org/10.1016/0022-3697(59)90379-8)
7. Warner J. H., Thomsen E., Watt A. R., Heckenberg N. R., Rubinsztein-Dunlop H. Time-resolved photoluminescence spectroscopy of ligand-capped PbS nanocrystals. *Nanotechnology*. 2005;16: 175–179. <https://doi.org/10.1088/0957-4484/16/2/001>
8. Torres-Gomez N., Garcia-Gutierrez D. F., Lara-Canche A. R., Triana-Cruz L., Arizpe-Zapata J. A., Garcia-Gutierrez D. I. Absorption and emission in the visible range by ultra-small PbS quantum dots in the strong quantum confinement regime with S-terminated surfaces capped with diphenylphosphine. *Journal of Alloys and Compounds*. 2021;860: 158443–158454. <https://doi.org/10.1016/j.jallcom.2020.158443>
9. Kim D., Kuwabara T., Nakayama M. Photoluminescence properties related to localized states in colloidal PbS quantum dots. *Journal of Luminescence*. 2006;119–120: 214–218. <https://doi.org/10.1016/j.jlumin.2005.12.033>
10. Gilmore R. H., Liu Y., Shcherbakov-Wu W., ... Tisdale W. A. Epitaxial dimers and auger-assisted Detrapping in PbS Quantum Dot Solids. *Matter*. 2019;1(1): 250–265. <https://doi.org/10.1016/j.matt.2019.05.015>
11. Nakashima S., Hoshino A., Cai J., Mukai K. Thiol-stabilized PbS quantum dots with stable luminescence in the infrared spectral range. *Journal of Crystal Growth*. 2013;378: 542–545. <https://doi.org/10.1016/j.jcrysgr.2012.11.024>
12. Loiko P. A., Rachkovskaya G. E., Zacharevich G. B., Yumashev K. V. Wavelength-tunable absorption and luminescence of SiO₂-Al₂O₃-ZnO-Na₂O-K₂O-NaF glasses with PbS quantum dots. *Journal of Luminescence*. 2013;143: 418–422. <https://doi.org/10.1016/j.jlumin.2013.05.057>
13. Kolobkova E., Lipatova Z., Abdrshin A., Nikonorov N. Luminescent properties of fluorine phosphate glasses doped with PbSe and PbS quantum dots. *Optical Materials*. 2017;65: 124–128. <https://doi.org/10.1016/j.optmat.2016.09.033>
14. Smirnov M. S., Ovchinnikov O. V. IR luminescence mechanism in colloidal Ag₂S quantum dots. *Journal of Luminescence*. 2020;227: 117526. <https://doi.org/10.1016/j.jlumin.2020.117526>
15. Smirnov M. S., Ovchinnikov O. V. Luminescence decay characteristics of CdS quantum dots doped with

europium ions. *Journal of Luminescence*. 2019;213: 459–468. <https://doi.org/10.1016/j.jlumin.2019.05.046>

16. Kondratenko T. S., Zvyagin A. I., Smirnov M. S., Perepelitsa A. S., Ovchinnikov O. V. Luminescence and nonlinear optical properties of colloidal Ag₂S quantum dots. *Journal of Luminescence*. 2019;208: 193–200. <https://doi.org/10.1016/j.jlumin.2018.12.042>

17. Kondratenko T. S., Smirnov M. S., Ovchinnikov O. V., ... Vinokur Y. A. Size-dependent optical properties of colloidal CdS quantum dots passivated by thioglycolic acid. *Semiconductors*. 2018;52(9): 1137–1144. <https://doi.org/10.1134/S1063782618090087>

18. Dalven R. Electronic structure of PbS, PbSe, and PbTe. *Solid State Physics*. 1974;28: 179–224. [https://doi.org/10.1016/S0081-1947\(08\)60203-9](https://doi.org/10.1016/S0081-1947(08)60203-9)

19. Yin Q., Zhang W., Zhou Y., Wang R., Zhao Z., Liu C. High efficiency luminescence from PbS quantum dots embedded glasses for near-infrared light emitting diodes. *Journal of Luminescence*. 2022;250: 119065 <https://doi.org/10.1016/j.jlumin.2022.119065>

20. Yue F., Tomm J. W., Kruschke D. Experimental observation of exciton splitting and relaxation dynamics from PbS quantum dots in a glass matrix. *Physical Review B*. 2014;89: 081303(R). <https://doi.org/10.1103/PhysRevB.89.081303>

Information about the authors

Irina G. Grevtseva, Cand. Sci. (Phys.–Math.), Lecturer at the Department of Optics and Spectroscopy, Voronezh State University (Voronezh, Russian Federation).

<https://orcid.org/0000-0002-1964-1233>
grevtseva_ig@inbox.ru

Mikhail S. Smirnov, Dr. Sci. (Phys.–Math.), Associate Professor, Department of Optics and Spectroscopy, Voronezh State University (Voronezh, Russian Federation).

<https://orcid.org/0000-0001-8765-0986>
smirnov_m_s@mail.ru

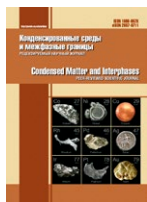
Kirill S. Chirkov, postgraduate student, Department of Optics and Spectroscopy, Voronezh State University (Voronezh, Russian Federation).

<https://orcid.org/0000-0003-0387-0733>
kirill200598@mail.ru

Oleg V. Ovchinnikov, Dr. Sci. (Phys.–Math.), Professor at the Department of Optics and Spectroscopy, Voronezh State University (Voronezh, Russian Federation).

<https://orcid.org/0000-0001-6032-9295>
ovchinnikov_o_v@rambler.ru

Received 13.09.2022; approved after reviewing 29.09.2022; accepted for publication 15.11.2022; published online 25.06.2023.



Condensed Matter and Interphases

Kondensirovannye Sredy i Mezhfaznye Granitsy
<https://journals.vsu.ru/kcmf/>

Original articles

Research article

<https://doi.org/10.17308/kcmf.2023.25/11100>

Photoelectric response in sandwich structures based on condensed layers of Ag_2S quantum dots passivated with thioglycolic acid

V. S. Gurchenko¹, A. S. Mazinov¹, M. S. Smirnov^{2✉}, I. G. Grevtseva², L. P. Nesterenko²,
O. V. Ovchinnikov²

¹V. I. Vernadsky Crimean Federal University,
4 prospekt Vernadskogo, Simferopol 295007, Republic of Crimea, Russian Federation

²Voronezh State University,
1 Universitetskaya pl., Voronezh 394018, Russian Federation

Abstract

The study is aimed at developing a technique for forming a structure with a Schottky barrier in the form of a multilayer Al- Ag_2S -ITO sandwich structure, which includes a condensate of colloidal Ag_2S quantum dots passivated with thioglycolic acid molecules ($\text{Ag}_2\text{S}/\text{TGA}$ QDs).

The spectral properties were studied using a USB2000+ spectrometer (Ocean Optics, USA) with a USB-DT light source (Ocean Optics, USA). Electrophysical and photoelectric properties of the structures were studied using a Keysight B1500A semiconductor device analyzer (Keysight tech, USA). The study of the temperature dependences of the properties in the temperature range from 300 to 360 K was carried out in a Shielded room (Faraday cage) placed in a muffle furnace. It was found that the conductivity of the Al- Ag_2S -ITO structure is mostly governed by the Schottky barrier at the Al-condensed Ag_2S QDs film junction.

At the junction between the condensed Ag_2S QDs film and Al, signs of the formation of a rectifying contact were found.

Under the action of the optical radiation with a wavelength of 650 nm and less, which corresponds to the most probable exciton transition in the UV-Vis absorption of $\text{Ag}_2\text{S}/\text{TGA}$ QDs, an increase in the current was found for the negative branch of the J-V curve.

Keywords: Silver sulfide, Activation energy, Charge carrier mobility, Conduction mechanisms, Schottky barrier

Funding: The work was supported by a grant Russian Science Foundation № 22-12-00232

For citation: Gurchenko V. S., Mazinov A. S., Smirnov M. S., Grevtseva I. G., Nesterenko L. P., Ovchinnikov O. V. Photoelectric response in sandwich structures based on condensed Ag_2S quantum dots passivated with thioglycolic acid. *Condensed Matter and Interphases*. 2023;25(2): 190–197. <https://doi.org/10.17308/kcmf.2023.25/11100>

Для цитирования: Гурченко В. С., Мазинов А. С., Смирнов М. С., Гревцева И. Г., Нестеренко Л. П., Овчинников О. В., Фотоэлектрический отклик в сэндвич-структурах на основе конденсированных слоев квантовых точек Ag_2S , пассивированных тиогликолевой кислотой. *Конденсированные среды и межфазные границы*. 2023;25(2): 190–197. <https://doi.org/10.17308/kcmf.2023.25/11100>

✉ Smirnov Mikhail Sergeevich, e-mail: smirnov_m_s@mail.ru

© Gurchenko V. S., Mazinov A. S., Ovchinnikov O. V., Smirnov M. S., Grevtseva I. G., Nesterenko L. P., 2023



The content is available under Creative Commons Attribution 4.0 License.

1. Introduction

In recent years, optical and transport properties of nanostructures based on semiconductor colloid quantum dots (QDs) have been of particular interest. Due to the existence of QDs in the form of ensembles in colloid solutions, it is possible to obtain thin condensate layers required for the implementation of practical applications using various methods, such as spin coating, dip coating, the Langmuir–Blodgett method, etc. [1–4]. The issue of transport properties comes to the fore in such condensates and their connection with energetic and electrophysical properties of the components (substrates, electrodes, etc.) as well as optical properties of QDs condensates [5, 6].

Optical, electrophysical, and recombination properties in addition to the fabricability of QDs condensates are important for the development of new photodetectors [2] and other photonics devices. The advantages of the use of QDs in photovoltaic devices are related to the ability of fine adjustment of energy levels of the element, modification of the surface in order to increase the efficiency of light absorption, including near-infrared light range [7–9]. The correct choice of the surface ligand of QDs has a positive effect on the transport properties of condensates [6, 7, 10]. To date, it has been established that the use of shorter ligands provides the formation of concentrated layers of QDs condensates, in which the effectiveness of charge diffusion between neighbouring QDs is significantly facilitated. Thiocarboxylic acids are highly promising and can be effectively used to solve these issues [11]. However, there are few studies of the electrophysical photovoltaic properties of QDs passivated with this ligand [12]. Condensates of Ag_2S QDs, in their turn, are of particular interest as model photosensitive media. There are known approaches and technologies for the efficient passivation of interfaces with thiocarboxylic acids for them [13–26].

The possibilities of creating new thin-film systems based on condensates of Ag_2S QDs were mentioned in certain works [27–29]. For example, the addition of silver sulphide as an isolating layer in a Schottky diode improved its characteristics and increased the rate of rectification [29]. However, currently there are no available systematic studies of the conductive

properties, photoresponse, and photoprocess patterns that determine them in systems based on Ag_2S QDs condensates passivated with short-chain molecules of thiocarboxylic acids.

This work partially fills this gap and is dedicated to the analysis of the electrophysical properties and photoresponse in multilayer structures of the Al- Ag_2S -ITO type, which include a condensate of colloidal Ag_2S quantum dots passivated with thioglycolic acid molecules (abbreviated as $\text{Ag}_2\text{S}/\text{TGA}$ QDs) as a photosensitive element.

2. Experimental

2.1. Samples

Electric parameters and photoresponse were studied on Al- Ag_2S QDs-ITO sandwich structures [30]. The initial colloid solution $\text{Ag}_2\text{S}/\text{TGA}$ QDs in the volume of 0.4 ml was applied to the conductive indium tin oxide (ITO) or aluminium substrates obtained using magnetron sputtering. Surface resistance of the substrates did not exceed 20 Ohm/sq, and geometric parameters were 10×10 mm.

The samples of colloid $\text{Ag}_2\text{S}/\text{TGA}$ QDs were synthesised as part of water colloid synthesis. It was based on mixing aqueous solutions of AgNO_3 and TGA with a molar ratio of 1:1 with the aqueous solution of Na_2S the concentration of which corresponded to the molar ratio of $\text{AgNO}_3:\text{TGA}:\text{Na}_2\text{S}$ which was 1:1:0.33. High purity reagents by Sigma-Aldrich were used for the synthesis.

2.2. Methods of experimental studies

Morphology of $\text{Ag}_2\text{S}/\text{TGA}$ QDs was studied using Libra 120 (Carl Zeiss, Germany) and JEOL 2000FX (JEOL Ltd., Japan) transmission electron microscope with high resolution. The surface morphology of thin films of $\text{Ag}_2\text{S}/\text{TGA}$ QDs condensates was evaluated using reflection and transmission microscopy on a MII-4M (LOMO, Russia) micro interferometer.

The absorption properties were studied on a USB2000+ spectrometer (Ocean Optics, USA) with a USB-DT light source (Ocean Optics, USA).

The electrophysical and photoelectric properties of the studied structures were measured using a B1500A semiconductor analyser (Keysight tech, USA). The temperature dependences of

these properties in the range from 300 to 360 K were investigated in a screened chamber (Faraday cage) placed in a muffle furnace. As for the source of monochromatic radiation, we used an incandescent lamp together with an MDR-41 monochromator with a diffraction grating of 1200 mm⁻¹. The operational spectral range was 500–1300 nm, and the power of radiation on the sample was 200 μW.

3. Results and discussion

3.1. Structural and optical properties of samples

An analysis of TEM images demonstrated the formation of ensembles of individual Ag₂S/TGA QDs with an average size of 2.5 nm and a dispersion of 20% (Fig. 1a). The studies of TEM imaging with high resolution showed the formation of Ag₂S nanocrystals in a monoclinic lattice (space group P2₁/c) (Fig. 1b). The thickness of films determined by the interferometric method for Ag₂S/TGA QDs

was 280–300 nm (Fig. 1c).

The optical absorption band of the initial colloidal solutions of Ag₂S/TGA QDs caused by the most probable exciton transition had a maximum in the region of 1.9 eV (650 nm). This value of energy exceeded the width of the band gap for Ag₂S crystals with a monoclinic crystal structure equal to 1.0–1.1 eV (Fig. 1d) [31]. This specific feature is the expression of the size effect. Using the Kayanuma formula [32]:

$$\Delta E = \frac{\hbar^2 \pi^2}{2\mu R^2} - 1.8 \frac{e^2}{\epsilon R} - 0.248 \frac{\mu e^4}{2\epsilon^2 \hbar^2},$$

where $\epsilon = 5.95$ is the dielectric constant of bulk Ag₂S [33], R is the radius of Ag₂S QDs in cm, $\Delta E = E_{\text{exc}} - E_{\text{mass}}$ is the value of a quantum size effect in absorption spectra in erg, $\mu = \frac{m_e \cdot m_h}{m_e + m_h}$,

$m_e = 0.42m_0$ and $m_h = 0.81m_0$ are the effective mass

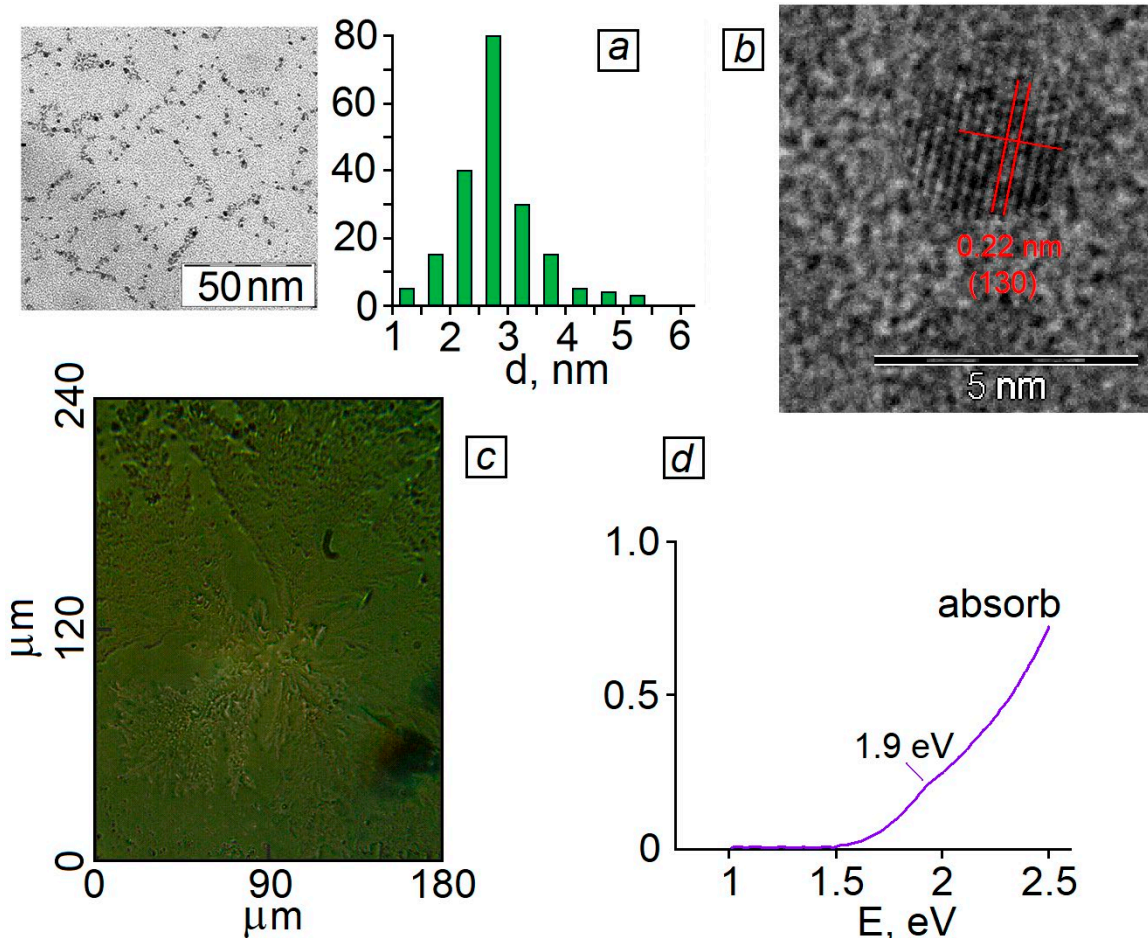


Fig. 1. TEM image, size distribution histogram of Ag₂S/TGA QDs (a). High resolution TEM (b). Optical photograph of an Ag₂S/TGA QD film (c). Optical absorption spectra of Ag₂S/TGA QDs (d)

of the electron and the hole, and the size of nanocrystals was 1.9 nm.

3.2. Electrophysical properties

Figure 2 presents the logarithmic dependence of the current on the applied voltage upon reversed bias for the studied sandwich structures Al-Ag₂S QDs-ITO. In Fig. 3 the current/voltage diagram (J-V curve) was asymmetric in relation to the zero field, which indicated the barrier structure. It should be noted that the currents were of the same magnitude, both with forward and reversed bias.

Based on the estimated value of the work function of electrons in the components of the investigated sandwich structure (4.2–4.8 eV for ITO [34, 35]; 4.1–4.9 eV was the estimated work function for the Ag₂S QDs film [31, 36], 4.25 eV was the electron work function for Al [37]) and their ratio, it can be expected that an ohmic contact will be formed in the sandwich structure at the ITO-Ag₂S QDs film interface and a Schottky barrier at the Ag₂S QDs-Al film interface.

We also formed an Al-Ag₂S QDs-Al sandwich structure to confirm the dominant role of Schottky barrier at the contact with Al-Ag₂S QDs in the formation of conductivity of the Al-Ag₂S QDs-ITO sandwich structure. A J-V curve for this structure also demonstrated the formation of a barrier, and the currents in both directions were similar while the J-V curve was symmetric in relation to the zero field. This indicated that the conductivity

of the Al-Ag₂S QDs-ITO structure was mainly determined by Schottky barrier emerging at the Al-Ag₂S QDs interface. Thus, a rectifying contact was formed at the Al-Ag₂S QDs film interface due to lower work function of Al [38, 39]. J-V curves of the studied films were exponential, therefore, the conductivity mechanism was apparently implemented according to Schottky emission [40,41].

To determine the conductivity mechanism, the J-V curve were replotted on a logarithmic scale [42], which allowed determining the dominant conductivity mechanism. Experimental dependencies of current on the applied voltage (Fig. 3) could be described in three regions by the power law $I \sim U^m$ [43], where m is the value of the slope for each region of the applied voltage. The value m showed the kinetics of charge carriers and the type of conductivity [42].

The resistive conductivity mechanism is typically [42] observed for the lowest voltage applied to the investigated structure, when the concentration of charge carriers injected into the QDs film is significantly lower than the concentration of intrinsic carriers. In this case, the coefficient m must be equal or close to one. Experimentally determined value m_1 for the region of voltages up to 0.2 V was equal to 0.2. As the voltage increased, the regions from 0.2 to 0.7 V could also be identified, where the value m_2 was 2.3, and the range of voltages more than 0.7 V, where m_3 was 5.49. The region of

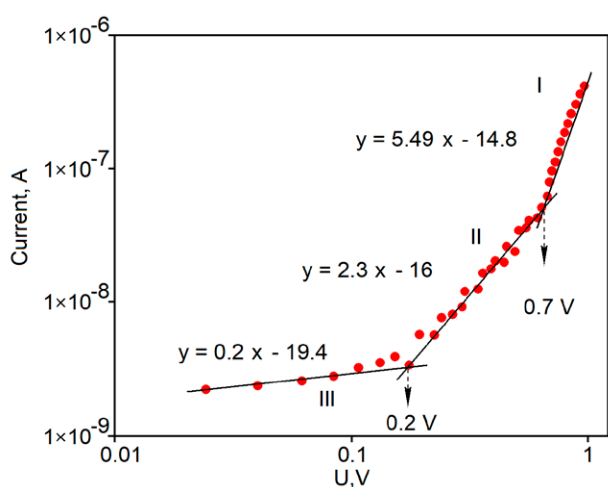


Fig. 2. Logarithmic dependence of the current on the applied voltage at a negative bias at $T = 300$ K for thin-film sandwich structures based on Ag₂S/TGA QDs

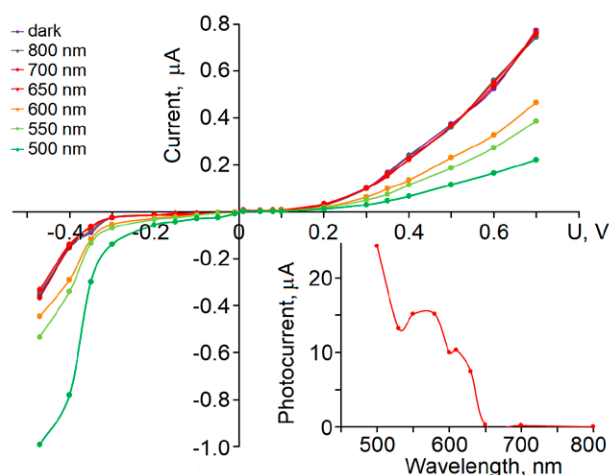


Fig. 3. J-V curve for sandwich structures based on Ag₂S/TGA QDs. The inset shows the photosensitivity spectrum of sandwich structures based on Ag₂S/TGA QDs

low voltages (<0.2 V) showed slightly strange behaviour, which was apparently due to the heterogeneous structure of the Ag₂S QDs film and the contribution of several processes to the conductivity. These processes will be described in detail in a different work.

A current mode with a space charge limited conduction (SCLC) was observed in the range of applied voltages from 0.2 to 0.7 V. The third range corresponded to the charge transfer due to the trap charge limited conduction mechanism (TCLC) [45]. Localised states of recombination luminescence centres seemed to participate in the formation of this third section of J-V curve (Fig. 1). Shallow localised states that we previously discovered for similar samples of colloidal Ag₂S QDs using thermally stimulated luminescence can also have a considerable effect [46].

3.3. Photoelectric response

Figure 3 presents the J-V curves for Al-Ag₂S QDs-ITO sandwich structures both in the absence of radiation and in the presence of illumination for the film structure with monochromatic radiation. It can be seen that there are no changes in the negative branch of J-V curve for the optical wavelength of more than 700 nm (1.77 eV). When comparing to the optical absorption spectra of Ag₂S QDs films, for which an exciton absorption peak was observed in the region of 1.9 eV (650 nm), and the long-wave absorption edge is approximately 700 nm, we can state that the absorption of light by Ag₂S QDs condensates is the primary act in the formation of the photoresponse of sandwich structures based on Ag₂S/TGA QDs. The form of the photocurrent spectrum measured for the negative shift (0.2 V) reiterated the long-wave edge of the absorption spectra of the Ag₂S/TGA QDs film. The forward J-V curve branch shows the changes that occurred under the influence of the radiation with a wavelength of less than 700 nm, which also proves the dominant role of the absorption process in the Ag₂S/TGA QDs film for the formation of a photoresponse.

4. Conclusions

As a result of studying the electrophysical properties of the Al-Ag₂S QDs-ITO sandwich structure, where the main working component was a condensate of colloidal Ag₂S QDs passivated

with thioglycolic acid (TGA) molecules, we established new patterns that indicate the formation of photosensitive systems with a Schottky barrier. The obtained experimental data showed that the conductivity of such structures was determined by Schottky barrier at the Al-Ag₂S QDs interface. Spectral area of photosensitivity of these structures coincided with the region of absorption of Ag₂S QDs condensates. The obtained results indicate that model objects can be developed for photodiode structures based on condensates of colloid Ag₂S/TGA QDs.

Contribution of the authors

The authors contributed equally to this article.

Conflict of interests

The authors declare that they have no known competing financial interests or personal relationships that could have influenced the work reported in this paper.

References

1. Alharthi S. S., Alzahrani A., Razvi M. A. N., Badawi A., Althobaiti M. G. Spectroscopic and electrical properties of Ag₂S/PVA nanocomposite films for visible-light optoelectronic devices. *Journal of Inorganic and Organometallic Polymers and Materials*. 2020;30: 3878–3885. <https://doi.org/10.1007/s10904-020-01519-4>
2. Chand S., Sharma E., Sharma P. Phase change induced quantization in NIR emitting Ag₂S nanocrystals: Structural and optical response for solar energy applications. *Journal of Alloys and Compounds V*. 2019;770: 1173–1180. <https://doi.org/10.1016/j.jallcom.2018.08.133>
3. Cotta M. A. Quantum dots and their applications: what lies ahead? *ACS Applied Nano Materials*. 2020;3(6): 4920–4924. <https://doi.org/10.1021/acsanm.0c01386>
4. Lei Y., Xu S., Ding M., Li L., Sun Q., Wang Z. L. Enhanced photocatalysis by synergistic piezotronic effect and exciton–plasmon interaction based on (Ag-Ag₂S)/BaTiO₃ heterostructures. *Advanced Functional Materials*. 2020;30(51): 2005716. <https://doi.org/10.1002/adfm.202005716>
5. Gao H., Wang F., Wang S., Wang X., Yi Z., Yang H. Photocatalytic activity tuning in a novel Ag₂S/CQDs/CuBi₂O₄ composite: Synthesis and photocatalytic mechanism. *Materials Research Bulletin*. 2019;115: 140–149. <https://doi.org/10.1016/j.materresbull.2019.03.021>
6. Tretyakov I., Svyatodukh S., Perepelitsa A., ... Goltsman G. Ag₂S QDs/Si Heterostructure-Based

- Ultrasensitive SWIR Range Detector. *Nanomaterials*. 2020;10(5):861. <https://doi.org/10.3390/nano10050861>
7. Smirnov M. S., Ovchinnikov O. V. IR luminescence mechanism in colloidal Ag₂S quantum dots. *Journal of Luminescence*. 2020; 227: 117526. <https://doi.org/10.1016/j.jlumin.2020.117526>
8. Mir W. J., Swarnkar A., Sharma R., Katti A., Adarsh K. V., Nag A. Origin of unusual excitonic absorption and emission from colloidal Ag₂S nanocrystals: ultrafast photophysics and solar cell. *The Journal of Physical Chemistry Letters*. 2015;6: 3915–3922. <https://doi.org/10.1021/acs.jpcclett.5b01692>
9. Ruiz D., del Rosal B., Acebron M., ... Juarez B. H. Ag/Ag₂S Nanocrystals for high Sensitivity near-infrared luminescence nanothermometry. *Advanced Functional Materials*. 2016;27: 1604629. <https://doi.org/10.1002/adfm.201604629>
10. Zamiri R., Abbastabar Ahangar H., Zakaria A., Zamiri G., Shabani M., Singh B., Ferreira J. M. F. The structural and optical constants of Ag₂S semiconductor nanostructure in the Far-Infrared. *Chemistry Central Journal*. 2015;9(1): 1–6. <https://doi.org/10.1186/s13065-015-0099-y>
11. Lesnyak V., Gaponik N., Eychmüller A. Colloidal semiconductor nanocrystals: the aqueous approach. *Chemical Society Reviews*. 2013;42: 2905–2929. <https://doi.org/10.1039/c2cs35285k>
12. Gilmore R. H., Liu Y., Shcherbakov-Wu W., ... Tisdale W. A. Epitaxial dimers and Auger-assisted detrapping in PbS quantum dot. *Solids Matter*. 2019;1: 250–265. <https://doi.org/10.1016/j.matt.2019.05.015>
13. Zhang Y., Xia J., Li C., ... Li Q. Near-infrared-emitting colloidal Ag₂S quantum dots excited by an 808 nm diode laser. *Journal of Materials Science*. 2017;52(16): 9424–9429. <https://doi.org/10.1007/s10853-017-1131-5>
14. Kondratenko T. S., Zvyagin A. I., Smirnov M. S., Grevtseva I. G., Perepelitsa A. S., Ovchinnikov O. V. Luminescence and nonlinear optical properties of colloidal Ag₂S quantum dots. *Journal of Luminescence*. 2019;208: 193–200. <https://doi.org/10.1016/j.jlumin.2018.12.042>
15. Wu Q., Zhou M., Shi J., Li Q., Yang M., Zhang Z. Synthesis of water-soluble Ag₂S Quantum dots with fluorescence in the second Near-Infrared window for turn-on detection of Zn(II) and Cd(II). *Analytical Chemistry*. 2017;89(12): 6616–6623. <https://doi.org/10.1021/acs.analchem.7b00777>
16. Ovchinnikov O. V., Grevtseva I. G., Smirnov M. S., ... Matsukovich A.S. Effect of thioglycolic acid molecules on luminescence properties of Ag₂S quantum dots. *Optical and Quantum Electronics*. 2020;52: 198-1-23. <https://doi.org/10.1007/s11082-020-02314-8>
17. Kondratenko T., Ovchinnikov O., Grevtseva I., ... Tatianina E. Thioglycolic acid FTIR spectra on Ag₂S quantum dots interfaces. *Materials*. 2020;13: 909-1-15. <https://doi.org/10.3390/ma13040909>
18. Vardara D. O., Aydin S., Hocaoglu I., Acar F. H. Y., Basaran N. Effects of silver sulfide quantum dots coated with 2-mercaptopropionic acid on genotoxic and apoptotic pathways in vitro. *Chemico-Biological Interactions*. 2018;291: 212–219. <https://doi.org/10.1016/j.cbi.2018.06.032>
19. Jiang P., Wang R., Chen Z. Thiol-based non-injection synthesis of near-infrared Ag₂S/ZnS core/shell quantum dots. *RSC Advances*. 2015;5: 56789–56793. <https://doi.org/10.1039/C5RA08008H>
20. Duman F. D., Erkisa M., Khodadust R., Ari F., Ulukaya E., Acar H. Y. Folic acid-conjugated cationic Ag₂S quantum dots for optical imaging and selective doxorubicin delivery to HeLa cells. *Nanomedicine (Lond)*. 2017;12(19): 2319–2333. <https://doi.org/10.2217/nnm-2017-0180>
21. Liu Q., Pu Y., Zhao Z., Wang J., Wang D. Synthesis of silver sulfide quantum dots via the liquid-liquid interface reaction in a rotating packed bed reactor. *Transactions of Tianjin University*. 2020;26: 273–282. <https://doi.org/10.1007/s12209-019-00228-5>
22. Ovchinnikov O. V., Aslanov S. V., Smirnov M. S., Grevtseva I. G., Perepelitsa A. S. Photostimulated control of luminescence quantum yield for colloidal Ag₂S/2-MPA quantum dots. *RSC Advances*. 2019;9: 37312–37320. <https://doi.org/10.1039/C9RA07047H>
23. Borovaya M., Horiunova I., Plokhovska S., Pushkarova N., Blume Y., Yemets A. Synthesis, properties and bioimaging applications of silver-based quantum dots. *International Journal of Molecular Sciences*. 2021;22: 12202 (1-23). <https://doi.org/10.3390/ijms222212202>
24. Tang R., Xu B., Shen D., Sudlow G., Achilefu S. Ultrasmall visible-to-near-infrared emitting silver-sulfide quantum dots for cancer detection and imaging. *ACS Nano*. 2015;9(1): 220–230. <https://doi.org/10.1021/nn5071183>
25. Ding C., Huang Y., Shen Z., Chen X. Synthesis and bioapplications of Ag₂S quantum dots with Near-Infrared fluorescence. *Advanced Materials*. 2021;33: 2007768. <https://doi.org/10.1002/adma.202007768>
26. Ovchinnikov O., Aslanov S., ... Grevtseva I. Colloidal Ag₂S/SiO₂ core/shell quantum dots with IR luminescence. *Optical Materials Express*. 2021;11(1): 89–104. <https://doi.org/10.1364/OME.411432>
27. Kang M. H., Kim S. H., Jang S., ... Park J. K. Synthesis of silver sulfide nanoparticles and their photodetector applications. *RSC Advances*. 2018;8(50): 28447–28452. <https://doi.org/10.1039/C8RA03306D>
28. Feng J., Li X., Shi Z., ... Zhu L. 2D ductile transition metal chalcogenides (TMCs): novel high-per-

- formance Ag₂S nanosheets for ultrafast photonics. *Advanced Optical Materials*. 2019;8(6): 1901762. <https://doi.org/10.1002/adom.201901762>
29. Badali Y., Azizian-Kalandaragh Y., Akhlaghi E. A., Altindal S. Ultrasound-assisted method for preparation of Ag₂S nanostructures: fabrication of Au/Ag₂S-PVA/n-Si Schottky barrier diode and exploring their electrical properties. *Journal of Electronic Materials*. 2020;49(1): 444–453. <https://doi.org/10.1007/S11664-019-07708-3>
30. Gusev A. N., Mazinov A. S., Shevchenko A. I., Tyutyunik A. S., Gurchenko V. S., Braga E. V. Research of heterojunctions based on the system of fullerene and hydrazine. *Applied Physics*. 2019;6: 48–53. (In Russ., abstract in Eng.). Available at: <https://applphys.orion-ir.ru/appl-19/19-6/PF-19-6-48.pdf>
31. Lin S., Feng Y., Wen X. et. al. Theoretical and experimental investigation of the electronic structure and quantum confinement of wet-chemistry synthesized Ag₂S nanocrystals. *The Journal of Physical Chemistry C*. 2015;119(1): 867–872. <https://doi.org/10.1021/jp511054g>
32. Kayanuma Y. Quantum-size effects of interacting electrons and hHoles in semiconductor microcrystals with spherical shape. *Physical Review B*. 1988;38(14): 9797–9805. <https://doi.org/10.1103/PhysRevB.38.9797>
33. Lu X., Li L., Zhang W., Wang C. Preparation and characterization of Ag₂S nanoparticles embedded in polymer fibre matrices by electrospinning. *Nanotechnology*. 2005;16(10): 2233–2237. <https://doi.org/10.1088/0957-4484/16/10/043>
34. Sugiyama K., Ishii H., Ouchi Y., Seki K. Dependence of indium–tin–oxide work function on surface cleaning method as studied by ultraviolet and x-ray photoemission spectroscopies. *Journal of Applied Physics*. 2000;87(1): 295–298. <https://doi.org/10.1063/1.371859>
35. Kim S. Y., Lee J.-L., Kim K.-B., Tak Y.-H. Effect of ultraviolet–ozone treatment of indium–tin–oxide on electrical properties of organic light emitting diodes. *Journal of Applied Physics*. 2004;95(5): 2560–2563. <https://doi.org/10.1063/1.1635995>
36. Tubtimtae A., Cheng K.-Y., Lee M.-W. Ag₂S quantum dot-sensitized WO₃ photoelectrodes for solar cells. *Journal of Solid State Electrochemistry*. 2014;18: 1627–1633. <https://doi.org/10.1007/s10008-014-2385-3>
37. Lide D. R., Weast R. C. *CRC handbook of Chemistry and physics*. CRC Press, Boca Raton, FL, 1986.
38. Chen H., Lei Y., Yang X., Zhao C., Zheng Z. Using a CdS under-layer to suppress charge carrier recombination at the Ag₂S/FTO interface. *Journal of Alloys and Compounds*. 2021;879: 160348. <https://doi.org/10.1016/j.jallcom.2021.160348>
39. Tyutyunik A. S., Gurchenko V. S., Mazinov A. S. Investigation of temperature dependences of current-voltage characteristics of hybrid organic materials based on zinc complexes. *Applied Physics*. 2021;5: 81–87. (In Russ., abstract in Eng.). <https://doi.org/10.51368/1996-0948-2021-5-81-87>
40. Lengyel G. Schottky emission and conduction in some organic insulating materials. *Journal of Applied Physics*. 1966;37(2): 807–810. <https://doi.org/10.1063/1.1708261>
41. Matsumura M., Jinde Y., Akai T., Kimura T. Analysis of current-voltage characteristics of organic electroluminescent devices on the basis of Schottky emission mechanism. *Japanese Journal of Applied Physics*. 1996;35(11): 5735–5739. <https://doi.org/10.1143/jjap.35.5735>
42. Zhu Y. B., Geng K., Cheng Z. S., Yao R. H. Space-charge-limited current injection into free space and trap-filled solid. *IEEE Transactions on Plasma Science*. 2021;49(7): 2107–2112. <https://doi.org/10.1109/TPS.2021.3084461>
43. Gupta R. K., Ghosh K., Kahol P. K. Fabrication and electrical characterization of Au/p-Si/STO/Au contact. *Current Applied Physics*. 2009;9(5): 933–936. <https://doi.org/10.1016/j.cap.2008.09.007>
44. Dhifaoui H., Aloui W., Bouazizi A. Optical, electrochemical and electrical properties of p-N,N-dimethyl-amino-benzylidene-malononitrile thin films. *Materials Research Express*. 2020;7(4): 045101. <https://doi.org/10.1088/2053-1591/ab7dfb>
45. Gusev A., Braga E., Tyutyunik A., ... Linert W. Synthesis, photoluminescence and electrical study of pyrazolone-based azomethine ligand Zn(II) complexes. *Materials*. 2020;13(24): 5698–1–12. <https://doi.org/10.3390/ma13245698>
46. Perepelitsa A. S., Smirnov M. S., Ovchinnikov O. V., Latyshev A. N., Kotko A. S. Thermostimulated luminescence of colloidal Ag₂S quantum dots. *J. of Luminescence*. 2018; 198: 357–363. <https://doi.org/10.1016/j.jlumin.2018.02.009>

Information about the authors

Vladimir S. Gurchenko, postgraduate student of the Department of Radiophysics and Electronics, Institute of Physics and Technology, V. I. Vernadsky Crimean Federal University (Simferopol, Republic of Crimea, Russian Federation).

<https://orcid.org/0000-0002-8270-3820>
gurchenko_v@mail.ru

Alim S. Mazinov, Dr. Sci. (Phys.–Math.), Associate Professor, Head of the Department of Radiophysics and Electronics, Institute of Physics and Technology, V. I. Vernadsky Crimean Federal University (Simferopol, Republic of Crimea, Russian Federation).

<https://orcid.org/0000-0003-0834-2390>
mazinovas@cfuv.ru

Mikhail S. Smirnov, Dr. Sci. (Phys.–Math.), Associate Professor, Department of Optics and Spectroscopy, Voronezh State University (Voronezh, Russian Federation).

<https://orcid.org/0000-0001-8765-0986>

smirnov_m_s@mail.ru

Irina G. Grevtseva, Cand. Sci. (Phys.–Math.), Senior Lecturer at the Department of Optics and Spectroscopy, Voronezh State University, Voronezh, Russian Federation.

<https://orcid.org/0000-0002-1964-1233>

e-mail: grevtseva_ig@inbox.ru

Lolita P. Nesterenko, Cand. Sci. (Phys.–Math.), Associate Professor, Department of Experimental Physics, Voronezh State University (Voronezh, Russian Federation).

lolita122@mail.ru

Oleg V. Ovchinnikov, Dr. Sci. (Phys.–Math.), Full Professor, Head of the Department of Optics and Spectroscopy, Voronezh State University (Voronezh, Russian Federation).

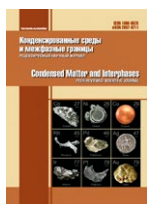
<https://orcid.org/0000-0001-6032-9295>

ovchinnikov_o_v@rambler.ru

Received 08.11.2022; approved after reviewing 22.11.2022; accepted for publication 25.11.2022; published online 25.06.2023.

Translated by Marina Strepetova

Edited and proofread by Simon Cox



Original articles

Research article

<https://doi.org/10.17308/kcmf.2023.25/11101>

A comparison of the inhibitory activity of 3-alkyl- and 3-hydroxyalkyl-5-amino-1*H*-1,2,4-triazoles against copper corrosion in chloride-containing environments

D. V. Lyapun, A. A. Kruzhillin, D. S. Shevtsov, A. Yu. Potapov, Kh. S. Shikhaliev✉

Voronezh State University,
1 Universitetskaya pl., Voronezh 394018, Russian Federation

Abstract

Copper is widely used as a material for technical solutions in microelectronics, as well as for the manufacture of various heat exchange equipment used in aggressive environments. Corrosion inhibitors are used for the reduction of the corrosive activity of the environment. This article presents the results of a study of the anticorrosion activity of a number of derivatives of the class 3-alkyl- and 3-hydroxyalkyl-5-amino-1*H*-1,2,4-triazole with respect to copper corrosion in chloride-containing environment. Over the course of the study, 3-alkyl- and 3-hydroxyalkyl-5-amino-1*H*-1,2,4-triazoles with different lengths of the alkyl substituent were synthesized. The structure of these compounds was confirmed using NMR spectroscopy and HPLC/MS analysis. Based on the results of electrochemical and direct corrosion tests, regularities were established for the inhibitory activity of the obtained compounds in acidic (1% HCl solution) and neutral (borate buffer solution, pH = 7.4) chloride-containing media.

In a neutral media, the greatest protective effect was obtained for 3-propyl-5-amino-1*H*-1,2,4-triazole **I**, which has the shortest alkyl radical without modification by an OH group. As the concentration increased in the range from 0.01 to 10.0 mmol/L, the inhibitory activity increased. With an increase in the length of the alkyl radical and/or the introduction of an OH group, a decrease or absence of a protective effect was observed. At the same time, in an acidic medium, the introduction of a hydroxyl group into the alkyl substituent of 5-amino-1*H*-1,2,4-triazole increased anti-corrosion efficiency only with sufficient length of the carbon chain.

The highest protection degree was obtained for 17-(5-amino-1*H*-1,2,4-triazol-3-yl)heptadecan-7-ol **IV** at a concentration of 10.0 mmol/l and it reached a value of 97%.

Keywords: Metal corrosion, Copper, Corrosion inhibitors, Heterocyclic compounds, Aminotriazoles, Physico-chemical research methods

Funding: The study was supported by the Ministry of Science and Higher Education of the Russian Federation within the framework of state order to higher education institutions in the sphere of scientific research for 2023-2025 (project No. FZGU-2022-0003).

Acknowledgements: Analytical and electrochemical studies were performed using the equipment of the Centre for Collective Use of Scientific Equipment of Voronezh State University.

For citation: Lyapun D. V., Kruzhillin A. A., Shevtsov D. S., Potapov A. Yu., Shikhaliev Kh. S. A comparison of the inhibitory activity of 3-alkyl- and 3-hydroxyalkyl-5-amino-1*H*-1,2,4-triazoles against copper corrosion in chloride-containing environments. *Condensed Matter and Interphases*. 2023;25(2): 198–206. <https://doi.org/10.17308/kcmf.2023.25/11101>

Для цитирования: Ляпун Д. В., Кружиллин А. А., Шевцов Д. С., Потапов А. Ю., Шихалиев Х. С. Сравнение ингибирующей активности 3-алкил- и 3-гидроксиалкил-5-амино-1*H*-1,2,4-триазолов в отношении коррозии меди в хлоридсодержащих средах. *Конденсированные среды и межфазные границы*. 2023;25(2): 198–206. <https://doi.org/10.17308/kcmf.2023.25/11101>

✉ Khidmet S. Shikhaliev, e-mail: shikh1961@yandex.ru

© Lyapun D. V., Kruzhillin A. A., Shevtsov D. S., Potapov A. Yu., Shikhaliev Kh. S., 2023



The content is available under Creative Commons Attribution 4.0 License.

1. Introduction

The widespread use of copper in microelectronics and technological equipment is usually associated with its high electrical and thermal conductivity and general corrosion resistance. In addition, it has additional specific properties, for example, it prevents fouling by marine microscopic organisms, since its ions are detrimental to algae and molluscs [1]. This allows the use of copper in shipbuilding, fisheries and other areas that involve the long-term operation of metals in such environments [2]. However, like most metals, copper is subject to corrosion damage, and it is characterized by local types of corrosion (pitting corrosion) that occur when a solid phase comes into contact with a liquid medium containing, for example, chloride ions. One of the most common ways to reduce the rate of destruction during its use in various environments is the use of special organic corrosion inhibitors [3].

Among organic copper corrosion inhibitors, heterocyclic azole-based compounds have the greatest practical application [4, 5]. This is due to the presence of several properties: good solubility in water, high thermal stability, environmental friendliness, economy, etc. The inhibitory properties of azoles [6–10] are due to the fact that the hydrogen atoms that are directly bonded to the nitrogen atom in the azole ring are highly mobile. As a result, it is possible for the inhibitor to interact with the surface of metals, which is accompanied by adsorption on it and the formation of protective films [11].

Despite the extensive list of already known compounds for which an inhibitory effect has been proven, the task of searching for and studying the properties of new corrosion inhibitors both for one metal in a specific environment and universal inhibitors for a number of metals and alloys used under various conditions is still relevant [12, 13].

The most studied copper corrosion inhibitor of the azole class is 1,2,3-benzotriazole [14–16], which is currently widely used to protect non-ferrous metals. However, not only benzotriazole derivatives, but also some other, more hydrophilic triazoles [17], attract the attention of researchers for the protection of copper and its alloys [18–19]. Thus, 3-amino-1,2,4-triazole is more effective than benzotriazole in preventing the formation

of pitting on a copper–nickel alloy in an ammonia buffer solution containing chlorides or sulphates [20]. The effectiveness of such inhibitors is often increased by introducing a hydrophobic substituent into the triazole ring. However, this reduces their solubility in water and can lead to disruption of the equipment, including due to the formation of particle agglomerates with subsequent clogging of the conductive channels [21, 22]. Obtaining corrosion inhibitors with high protective properties and satisfactory solubility is an important scientific and practical task.

The purpose of this study was the synthesis of 3-alkyl- and 3-hydroxyalkyl-5-amino-1H-1,2,4-triazoles compounds, study and comparison of their inhibitory activity against copper corrosion in neutral and acidic solutions containing chloride ions.

2. Experimental

2.1. Spectral methods of analysis

¹H NMR spectra were obtained using Bruker DRX-500 (operating frequency 500 MHz) in a pulsed Fourier mode in DMSO-d₆. Proton chemical shifts are given in parts per million (ppm) relative to the residual proton signals of the deuterium solvent or tetramethylsilane as an internal standard. Chromatographic analysis of the purity of the obtained compounds was carried out on an Agilent 1260 Infinity liquid chromatograph with UV and mass detection (Agilent 6230 TOF LC/MS high-resolution time-of-flight mass detector, electrospray ionization). Chromatography conditions: Gemini C18 column (4.6×50 mm); sorbent particle diameter 5 μm; linear gradient elution; mobile phase: eluent A – MeCN–H₂O, 2.5: 97.5, 0.1% CF₃COOH, eluent B – MeCN, 0.1% CF₃COOH, mobile phase flow rate 3.75 ml/min; column temperature 40 °C; injection volume 1.5 μl.

2.2. General procedure for the synthesis of 3-substituted 5-amino-1H-1,2,4-triazoles (I–IV) in pyridine

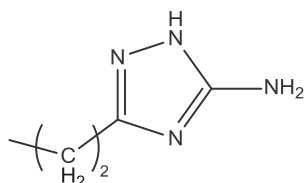
A mixture of 0.1 mol of aminoguanidine bicarbonate, 0.1 mol of the corresponding carboxylic acid ester and 200 ml of pyridine was boiled under reflux for 6–12 hours. The mixture was cooled, pyridine was distilled off on a rotary evaporator, and the residue was recrystallized from a mixture of petroleum ether and isopropyl

alcohol. The formed precipitate was filtered off, washed with petroleum ether, and dried at 60°C.

2.3. General procedure for the synthesis of 3-substituted 5-amino-1H-1,2,4-triazoles (I-IV) in butanol

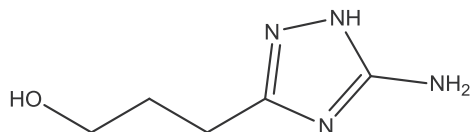
Butanol (100 ml) was added to 0.21 mol of aminoguanidine, then 0.21 mol of the corresponding carboxylic acid was added in portions with stirring. The mixture was carefully heated to 50°C and, after the carbon dioxide evolution ceased, it was boiled with a Dean-Stark apparatus. After the separation of water in the trap ceased, the reaction mass was cooled and butanol was distilled off on a rotary evaporator. The residue was recrystallized from a mixture of petroleum ether and isopropyl alcohol. The precipitate formed after cooling was filtered off, washed with petroleum ether, and dried at 60°C.

3-Propyl-5-amino-1H-1,2,4-triazole I.



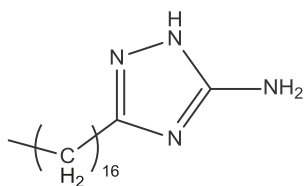
Yield 58-63%, MP 134-136 °C. White powder. ¹H NMR spectrum: 0.88 (t, J=7.5, 3H, CH₃); 1.52–1.57 (m, 2H, CH₂); 2.36 (t, J=7.3, 2H, CH₂); 5.70 (s, 2H, NH₂); 11.45 (s, H, NH). Determined, m/z: 127.0984 [M+H]⁺. C₅H₁₀N₄+H⁺. Calculated, m/z: 127.0979 [M+H]⁺.

3-(5-Amino-1H-1,2,4-triazol-3-yl)propan-1-ol II.



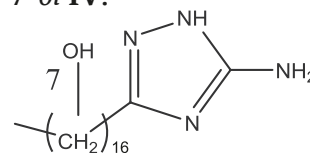
Yield 40-45%, MP 128-130 °C. White powder. ¹H NMR spectrum: 1.48–1.55 (m, 2H, CH₂); 2.38 (t, J=7.3, 2H, CH₂); 3.41 (m, 2H, CH₂); 4.44 (br. s, 1H, OH); 5.67 (s, 2H, NH₂); 11.49 (s, H, NH). Determined, m/z: 143.0821 [M+H]⁺. C₅H₁₀N₄O+H⁺. Calculated, m/z: 143.0855 [M+H]⁺.

3-Heptadecyl-5-amino-1H-1,2,4-triazole III.



Yield 41-49%, MP 99-103 °C. White powder. ¹H NMR spectrum: 0.85 (t, J=7.5, 3H, CH₃); 1.21–1.30 (m, 28H, 14CH₂); 1.52–1.59 (m, 2H, CH₂); 2.37 (t, J=7.3, 2H, CH₂); 5.54 (s, 2H, NH₂); 11.54 (s, H, NH). Determined, m/z: 323.3180 [M+H]⁺. C₁₉H₃₈N₄+H⁺. Calculated, m/z: 323.3171.

17-(5-Amino-1H-1,2,4-triazol-3-yl)heptadecan-7-ol IV.



Yield 42-51%, MP 102-103 °C. White powder. ¹H NMR spectrum: 0.85 (t, J=7.5, 3H, CH₃); 1.24–1.39 (m, 12H, 6CH₂); 1.53–1.60 (m, 2H, CH₂); 1.77–1.81 (m, 4H, 2CH₂); 2.38 (t, J=7.3, 2H, CH₂); 2.73–2.78 (m, 4H, 2CH₂); 3.79–3.83 (m, 1H, CH); 4.44 (br. s, 1H, OH); 5.54 (s, 2H, NH₂); 11.54 (s, H, NH). Determined, m/z: 339.3220 [M+H]⁺. C₁₉H₃₈N₄O+H⁺. Calculated, m/z: 339.3220.

2.4. Electrochemical studies in a neutral environment

Electrochemical measurements were carried out in an aerated borate buffer solution (pH = 7.40) in the presence of an activating additive of 0.01 mol/L NaCl. Studies in this solution allow to obtain information about the passivating effect of triazoles and their ability to stabilize the passive state of copper under conditions of competitive adsorption of an organic inhibitor and chloride.

Polarization curves were recorded on an M1 copper electrode reinforced with epoxy resin (area 0.75 cm²) in an electrochemical cell with undivided electrode spaces using an IPC-PRO potentiostat. The working electrode was preliminarily cleaned with K2000 sandpaper, washed with distilled water, and degreased with ethanol (reagent grade). Electrode potentials (*E*) was measured relative to the silver chloride electrode, connecting the space of the electrochemical cell and the reference electrode by electrolytic bridge based on agar-agar and sodium nitrate, and recalculated to the scale of a standard hydrogen electrode (potential +201 mV relative to SHE). The auxiliary electrode was a platinum grid.

After the reduction of the copper oxide film formed in air at *E* = -0.60 V for 15 min, the polarization was turned off until the open-circuit potential (*E*_{cor}) was established. The time

to the onset of the steady state ranged from 3 to 5 minutes. Next, with stirring, a NaCl solution with a concentration (C_{Cl^-}) 0.01 mol/l and test inhibitors was added. After the new E_{cor} value was established, the anodic and cathodic polarization curves were recorded within 3–5 minutes with a potential scan rate of 0.2 mV/s from E_{cor} in the anodic and cathodic directions, respectively.

Measurements for each concentration of the substance were made at least 5 times until reproducible data were obtained, followed by statistical processing of the measurement results.

2.5. Salt spray testing (neutral environment)

Corrosion tests were carried out on copper plates (20×50 mm, thickness 0.2 mm), which were preliminarily cleaned with K2000 sandpaper, washed with distilled water, and degreased with ethanol (chemically pure). A protective film of inhibitors was obtained by incubation the plates in an aqueous solution with the addition of inhibitors with concentrations of $C_{inh} = 1.0, 5.0,$ and 10.0 mmol/l for 60 minutes at room temperature. The samples were dried and placed in a salt spray cabinet. As a solution (GOST R 52763-2007), we used a 5% NaCl solution (pH = 6.5–7.2), which was sprayed as a mist inside the cabinet with the test samples. The samples were irrigated with a solution at intervals of 1 hour at room temperature and a constant relative humidity of 95–100% in the cabinet. Inspection of the samples was carried out 3 times per day to determine the time of appearance of the first corrosion damage (τ_{cor}).

2.6. Gravimetric tests in acidic environment

The tests were carried out in accordance with GOST 9.905-82 “Methods of corrosion tests”, 9.907-83 “Methods for removing products after corrosion tests” on copper plates (20×50 mm, thickness of 0.2 mm). The plates were cleaned with K2000 sandpaper, washed with distilled water, degreased with ethanol (reagent grade) and dried with filter paper. The experiments were carried out in a 1% HCl solution (pH = 0.55) for 7 days under natural aeration without stirring for three samples simultaneously (for each inhibitor concentration). The study of anticorrosion activity was carried out for systems with an inhibitor concentration of $C_{in} = 1.0, 5.0,$ and 10.0 mmol/l.

The corrosion rate was determined based on the weight loss of the samples and was calculated using the formula:

$$k_{inh} = \frac{\Delta m}{S \cdot t},$$

where $\Delta m = m_0 - m$ (m_0 is the weight of the sample before the start of the experiment; m is the weight of the sample after testing, g; S – plate area, m²; t – time of the experiment, days).

For each solution, the corrosion rate k_0 was determined without inhibitor additive (k_0 (1% HCl solution) = 44 g/m²days). The effectiveness of the inhibitory action of aminotriazole derivatives was evaluated based on the value of the inhibition coefficient $\gamma = k_0/k_{inh}$ and degree of protection:

$$Z = \left[\frac{k_0 - k_{inh}}{k_0} \right] \cdot 100 \%,$$

where k_0 and k_{inh} are the corrosion rates in the background solution and in the solution with the inhibitor, respectively.

3. Results and discussion

3.1. Electrochemical studies in a neutral environment

Based on the results of electrochemical measurements, data were compared for a solution without the addition of inhibitors (control experiment) and in the presence of substances I–IV. The influence of C_{inh} on the E_{cor} , as well as the change in current density (i) in the initial segments of the anodic (APC) and cathodic (CPC) polarization curves were analysed.

Introduction of 3-propyl-5-amino-1H-1,2,4-triazole I in the concentration range $C_{inh} = 0.01$ – 1.00 mmol/l resulted in a shift of E_{cor} by 39–66 mV into the cathodic region relative to the control experiment (Table 1). On APC and CPC in the presence of 3-propyl-5-amino-1H-1,2,4-triazole I there was a decrease in the current density relative to the control experiment (Fig. 1a). With an increase in the concentration of a substance, the CPC did not change, and the current density decreased on the APC.

According to [23], in the initial sections of the APC, copper is oxidized with the formation of complexes according to the scheme:

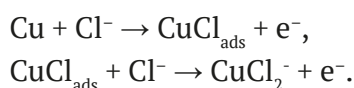
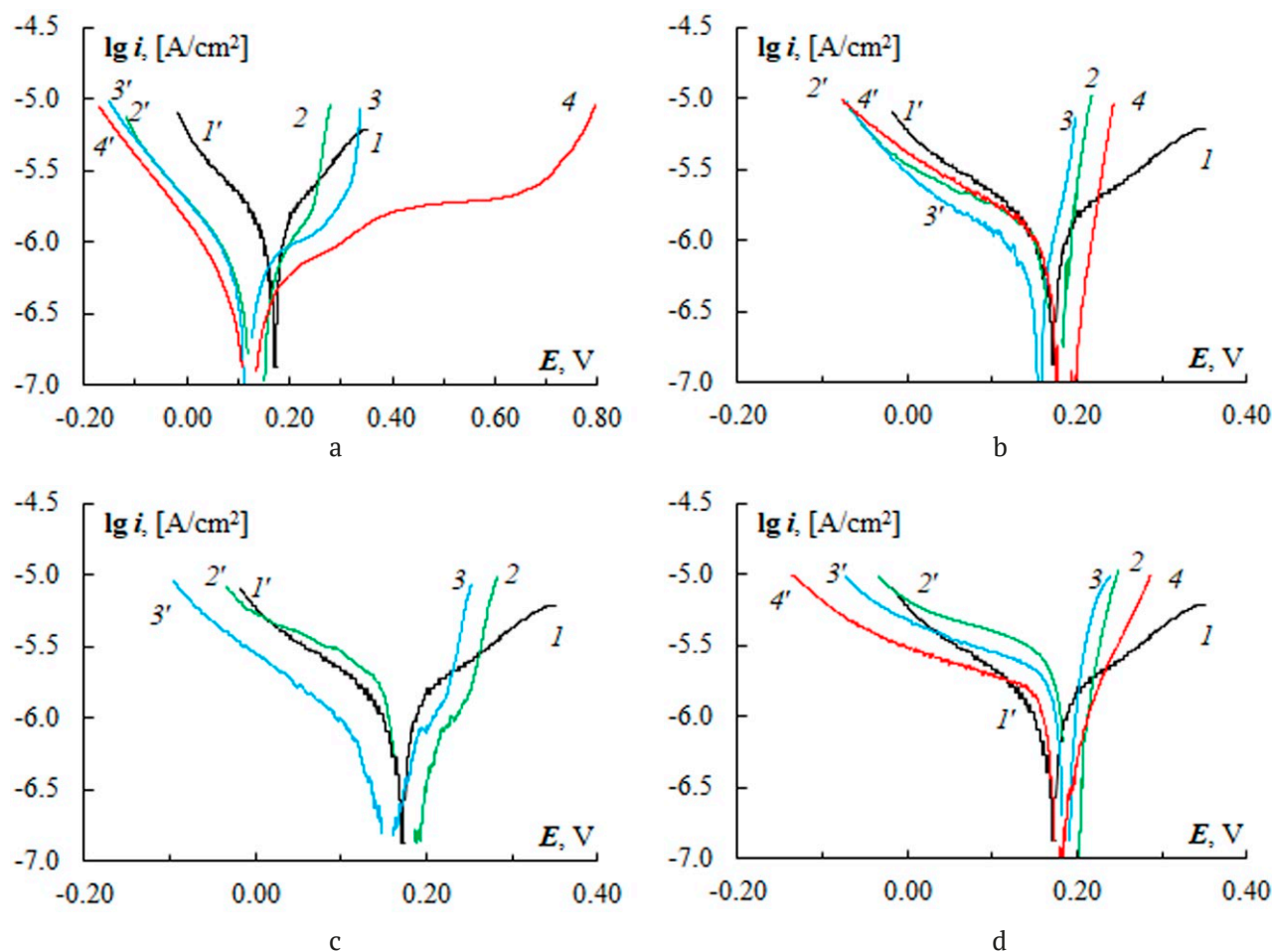
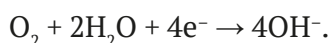


Table 1. Stationary values of copper E_{cor} in borate buffer solution (pH = 7.40) in the presence of 0.01 M NaCl and I-IV inhibitors of various concentrations

Inhibitor	Inhibitor concentration, C_{inh} , mmol/l			
	0.00	0.01	0.10	1.00
I	+176	+135	+110	+120
II		+181	+154	+181
III		+177	+151	–
IV		+200	+186	+175


Fig. 1. Anodic (1–4) and cathodic (1'–4') polarization curves obtained on copper in a borate buffer (pH = 7.40) with of 0.01 M NaCl and 3-propyl-5-amino-1*H*-1,2,4-triazole I (a), 3-(5-amino-1*H*-1,2,4-triazol-3-yl)propane-1-ol II (b), 3-heptadecyl-5-amino-1*H*-1,2,4-triazole III (c), 17-(5-amino-1*H*-1,2,4-triazol-3-yl)heptadecan-7-ol IV (d) with a concentration of C_{in} (mmol/l): 1, 1' – without additive; 2, 2' – 0.01; 3, 3' – 0.10; 4, 4' – 1.00

At the same time, the reduction of the oxidizing agent (air oxygen) proceeds at the cathode:



Thus, the introduction of 3-propyl-5-amino-1*H*-1,2,4-triazole I suggests an inhibitory effect on copper corrosion in a neutral solution in the presence of chlorides with a predominant effect

on the anodic metal oxidation process. In the concentration range $C_{\text{inh}} = 0.01\text{--}1.00$ mmol/l, an increase in inhibitory activity was observed.

When 3-(5-amino-1*H*-1,2,4-triazol-3-yl)propan-1-ol II and 3-heptadecyl-5-amino-1*H*-1,2,4-triazole III were added, the change of E_{cor} relative to the control experiment was observed only when $C_{\text{inh}} = 0.10$ mmol/l at –22 and –25 mV, respectively (Table 1). Current density on APC

with 3-(5-amino-1*H*-1,2,4-triazol-3-yl)propan-1-ol **II** for all studied concentrations increased faster than in the solution without an additive (Fig. 1b). On a CPC at $C_{inh} = 0.10$ mmol/l reduction of i was obtained. That is, a slight inhibitory effect can occur for a given substance only when $C_{inh} = 0.10$ mmol/l by reducing the reduction rate of the oxidant (air oxygen).

Current density in the initial sections of APC with 3-heptadecyl-5-amino-1*H*-1,2,4-triazole **III** decreased relative to the control experiment (Fig. 1c), the difference was obtained on the CPC at $C_{inh} = 0.10$ mmol/l. Thus, the introduction of 3-heptadecyl-5-amino-1*H*-1,2,4-triazole **III** suggests an inhibitory effect on copper corrosion in a neutral solution in the presence of chlorides with a predominant effect on the anodic metal oxidation process. In the concentration range $C_{inh} = 0.01$ – 0.10 mmol/l, there was an increase in inhibitory activity, which was less pronounced, relative to 3-Propyl-5-amino-1*H*-1,2,4-triazole **I**.

The introduction of 17-(5-amino-1*H*-1,2,4-triazol-3-yl)heptadecan-7-ol **IV** with the minimum studied concentration $C_{inh} = 0.01$ mmol/l caused a shift of $E_{cor} + 24$ mV relative to the solution without an additive. With increasing C_{inh} up to 1.00 mmol/l, the E_{cor} value coincided with the result of the control experiment. The initial sections of the CPC were indistinguishable from the control experiment. On the APC, the current density increased faster. According to the results of electrochemical measurements, it was

not possible to predict the inhibitory effect of 17-(5-amino-1*H*-1,2,4-triazol-3-yl)heptadecan-7-ol **IV** in relation to copper in a neutral solution in the presence of chlorides.

Thus, in the series of studied derivatives of 3-alkyl-5-amino-1*H*-1,2,4-triazoles, according to the results of electrochemical measurements in a neutral aerated solution (pH = 7.4) in the presence of 0.01 mol/L NaCl, an increase in inhibitory activity in the absence of OH groups and a decrease in the length of the hydrocarbon radical was obtained. The decrease in inhibitory activity with an increase in the length (volume) of substituents, despite an increase in surface activity, was explained by the authors of [24] as steric hindrances in the process of adsorption and the formation of complex compounds with copper. The introduction of an OH group increased the hydrophilicity of the molecule.

3.2. Salt spray testing (neutral environment)

On the one hand, the results of salt spray testing (periodic spraying with a neutral chloride solution) tend to be similar to the results of electrochemical measurements in a solution (Table 2). The highest τ_{cor} value was obtained for 3-propyl-5-amino-1*H*-1,2,4-triazole **I**. Parameter τ_{cor} increased relative to the control experiment by 10 times at $C_{inh} = 1.0$ mmol/l and by 12.5 times at $C_{inh} = 10.0$ mmol/l. For copper plates after incubation in 3-(5-amino-1*H*-1,2,4-triazol-3-yl)propan-1-ol **II** and 3-heptadecyl-5-amino-1*H*-

Table 2. Comparative results of direct tests of 3-substituted 5-amino-1*H*-1,2,4-triazoles **I–IV**

Inhibitor	C_{inh} , mmol/l	1% HCl solution			Salt spray
		k , g/m ² -day	γ	Z, %	τ_{cor} , hour
without	0.0	44.0	1.0	–	4
I	1.0	43.9	1.0	3.3	40
	5.0	41.9	1.0	1.4	44
	10.0	37.3	1.1	12.2	50
	1.0	23.0	1.0	–0.7	21
II	5.0	22.1	1.0	2.9	30
	10.0	21.2	1.1	7.0	30
	1.0	52.7	0.8	–24.0	20
III	5.0	49.4	0.9	–16.2	22
	10.0	14.6	2.9	65.6	27
	1.0	1.5	16.0	93.8	15
IV	5.0	7.9	3.1	68.2	17
	10.0	0.7	35.3	97.2	24

1,2,4-triazole **III** solutions at $C_{inh} = 1.0$ mmol/l, the time to the formation of corrosion lesions increased by 5.2 and 5 times, respectively, at $C_{inh} = 10.0$ mmol/l by 7.5 and 6.8 times. For 17-(5-amino-1*H*-1,2,4-triazol-3-yl)heptadecan-7-ol **IV** τ_{cor} increased from 3.8 to 6 times in the considered range C_{inh} .

On the other hand, the manifestation of an inhibitory effect with a trend towards an increase in inhibitory activity with an increase in C_{inh} was obvious. This can be explained by differences in the preparation procedure for the experiment: for electrochemical measurements, potential inhibitors **I–IV** were injected simultaneously with the activator (chlorides), and for salt spray testing, copper plates were kept in a solution with additives **I–IV** and after exposure, they were exposed to a chloride solution.

3.3. Gravimetric tests in acidic environment

The highest degree of protection (> 68%) in 1% HCl solution was obtained for 17-(5-amino-1*H*-1,2,4-triazol-3-yl)heptadecan-7-ol **IV**. At $C_{inh} = 1.0$ and 10.0 mmol/L, this parameter reached 93 and 97%, respectively. For 3-heptadecyl-5-amino-1*H*-1,2,4-triazole **III** only for $C_{inh} = 10.0$ mmol/l, an inhibitory effect was established with a degree of protection of 65%. At lower concentrations, corrosion was intensified by 16–24%.

For substances **I**, **II** with a short alkyl substituent, the degree of protection was from 0 to 12%, i.e., they did not possess an inhibitory effect on copper corrosion in the test solution.

Thus, among the studied derivatives of 3-alkyl-5-amino-1*H*-1,2,4-triazoles, according to the results of gravimetric tests in an acidic aerated 1% HCl solution (pH = 0.55), an increase in inhibitory activity was obtained with the inclusion of an OH group and an increase in the length of the hydrocarbon radical. This agrees with the data of [25], where in HCl solution, aminotriazole and its short-chain modifications exhibited low protective properties at concentrations up to 10 mmol/L.

4. Conclusions

The synthesis was carried out and the structure of 3-alkyl- and 3-hydroxyalkyl-5-amino-1*H*-1,2,4-triazoles with different lengths of the alkyl substituent was proved. For a neutral chloride-

containing medium, the highest protective effect out of all studied substances was obtained for 3-propyl-5-amino-1*H*-1,2,4-triazole with a short alkyl substituent. The inhibitory activity increased with the increase in concentration. With an increase in the length of the hydrocarbon radical and with the introduction of an OH group into the structure, the inhibitory activity decreased. The data of potentiodynamic and full-scale measurements in the salt spray cabinet were consistent. For an acidic environment (1% HCl solution) the highest inhibitory effect according to the results of gravimetric measurements was obtained for 17-(5-amino-1*H*-1,2,4-triazol-3-yl)heptadecan-7-ol with long alkyl substituent with a protection degree of 97% at a concentration of 10.0 mmol/l. When decreasing the length of the hydrocarbon radical and the absence of an OH group, the degree of protection is reduced.

Author contributions

All authors made an equivalent contribution to the preparation of the publication.

Conflict of interests

The authors declare that they have no known competing financial interests or personal relationships that could have appeared to influence the work reported in this paper.

References

1. Isei M. O., Stevens D., Kamunde C. Temperature rise and copper exposure reduce heart mitochondrial reactive oxygen species scavenging capacity. *Comparative Biochemistry and Physiology Part C: Toxicology & Pharmacology*. 2021;243: 108999. <https://doi.org/10.1016/j.cbpc.2021.108999>
2. Korshunova T. *Copper and copper alloys**. Moscow: Infa-Inzheneriya Publ.; 2020. 156 p. (In Russ.)
3. Tasić Ž. Z., Petrović Mihajlović M. B., Radovanović M. B., Antonijević M. M. New trends in corrosion protection of copper. *Chemical Papers*. 2019;73: 2103–2132. <https://doi.org/10.1007/s11696-019-00774-1>
4. Kear G., Barker B. D., Walsh F. C. Electrochemical corrosion of unalloyed copper in chloride media – a critical review. *Corrosion Science*. 2004;46: 109–135. [https://doi.org/10.1016/s0010-938x\(02\)00257-3](https://doi.org/10.1016/s0010-938x(02)00257-3)
5. Finsgar M., Milosev I. Inhibition of copper corrosion by 1,2,3-benzotriazole: A review. *Corrosion Science*. 2010;52: 2737–2749. <https://doi.org/10.1016/j.corsci.2010.05.002>

6. Kuznetsov Yu. I., Kazanskiy L. P. Physicochemical aspects of metal protection by azoles as corrosion inhibitors. *Russian Chemical Reviews*. 2008;77(3): 219–232. <https://doi.org/10.1070/RC2008v077n03ABEH003753>
7. Kuznetsov Yu. I. Triazoles as a class of multifunctional corrosion inhibitors. Review. Part V. 1H-1,2,4-triazole and its derivatives. Copper and its alloys. *International Journal of Corrosion and Scale Inhibition*. 2022;11(3): 965–979. <https://doi.org/10.17675/2305-6894-2022-11-3-5>
8. Schapira J., Vincent J., Lovy Aime L. R. *New application of aminotriazole, composition containing it and process for its use*. Patent FR No. 2656630, Publ. 05.07.1991
9. Kuznetsov Yu. I., Avdeev Y. G., Zel O. O. *Inhibitor of acid metal corrosion**. Patent RF, no. 2539129. Publ. 10.01.2015, bull. no. 1. (In Russ.)
10. Kuznetsov Yu. I., Frolova L. V., Avdeev Y. G., Andreev N. N., Zel O. O. *Inhibitor of sulphide corrosion and hydrogenation of metal hardware**. Patent RF, No. 2539132. Publ. 10.01.2015, bull. no. 1. (In Russ.)
11. Makarychev Yu. B., Arkhipushkin I. A., Karpukhina T. A., Shikhaliev Kh. S., Kazanskiy L. P. Formation of protective nanolayers by some azoles on the surface of zinc from aqueous solutions. Part 1*. *Korroziya: materialy, zashchita*. 2016; 2: 20–27. (In Russ.). Available at: <https://elibrary.ru/item.asp?id=25501817>
12. Khiati Z., Othman A. A., Sanchez-Moreno M., Bernard M.-C., Joiret S., Sutter E. M. M., Vivier V. Corrosion inhibition of copper in neutral chloride media by a novel derivative of 1,2,4-triazole. *Corrosion Science*. 2011;53: 3092–3099. <https://doi.org/10.1016/j.corsci.2011.05.042>
13. Finšgar M. EQCM and XPS analysis of 1, 2, 4-triazole and 3-amino-1,2,4-triazole as copper corrosion inhibitors in chloride solution. *Corrosion Science*. 2013;77: 350–359. <https://doi.org/10.1016/j.corsci.2013.08.026>
14. Skrypnikova E. A., Kaluzhina S. A., Agafonova L. E. Inhibition of copper pitting corrosion in alkaline sulphate media by benzotriazole at elevated temperatures. *International Journal of Corrosion and Scale Inhibition*. 2014;3(1): 59–65. <https://doi.org/10.17675/2305-6894-2014-3-1-059-065>
15. Dugdale I., Cotton J. B. An electrochemical investigation on the prevention of staining of copper by benzotriazole. *Corrosion Science*. 1963;2(1): 69–75. [https://doi.org/10.1016/s0010-938x\(63\)80001-3](https://doi.org/10.1016/s0010-938x(63)80001-3)
16. Poling G. W. Reflection infra-red studies of films formed by benzotriazole on Cu. *Corrosion Science*. 1970;10: 359–370. [https://doi.org/10.1016/s0010-938x\(70\)80026-9](https://doi.org/10.1016/s0010-938x(70)80026-9)
17. Goncharova O. A., Luchkin A. Yu., Andreev N. N., Andreeva N. P., Vesely S. S. Triazole derivatives as chamber inhibitors of copper corrosion. *International Journal of Corrosion and Scale Inhibition*. 2018;7(4): 657–672. <https://doi.org/10.17675/2305-6894-2018-7-4-12>
18. Kuznetsov Yu. I. New possibilities of metal corrosion inhibition by organic heterocyclic compounds. *International Journal of Corrosion and Scale Inhibition*. 2012;1(1): 3–15. <https://doi.org/10.17675/2305-6894-2012-1-1-003-015>
19. Kuznetsov Y. I., Shikhaliev K. S., Agafonkina M. O., Andreeva N. P., Arkhipushkin I. A., Potapov A. Y., Kazansky L. P. Effect of substituents in 5-R-3-amino-1,2,4-triazoles on the chemisorption on copper surface in neutral media. *Corrosion engineering science and technology*. 2021;56(1): 50–60. <https://doi.org/10.1080/1478422X.2020.1807087>
20. Es-Salah K., Keddami M., Rahmouni K., Srhiri A., Takenouti H. Aminotriazole as corrosion inhibitor of Cu-30Ni alloy in 3% NaCl in presence of ammoniac. *Electrochimica Acta*. 2004;49 (17–18): 2771–2778. <https://doi.org/10.1016/j.electacta.2004.01.038>
21. Moussa M. N. H., El-Far A. A., El-Shafei A. A. The use of water-soluble hydrazones as inhibitors for the corrosion of C-steel in acidic medium. *Materials Chemistry and Physics*. 2007;105: 105–113. <https://doi.org/10.1016/j.matchemphys.2007.04.007>
22. Rivera-Grau L. M., Casales M., Regla I., Ortega Toledo D. M., Ascencio-Gutierrez J. A., Porcayo Calderon J., Martinez-Gomez L. Effect of organic corrosion inhibitors on the corrosion performance of 1018 carbon steel in 3% NaCl solution. *International Journal of Electrochemical Science*. 2013;8: 2491–2503. Available at: <http://electrochemsci.org/papers/vol8/80202491.pdf>
23. Lee H. P. Nobe K. Kinetics and mechanisms of Cu electrodisolution in chloride media. *Journal of the Electrochemical Society*. 1986;133(10): 2035. <https://doi.org/10.1149/1.2108335>
24. Kuznetsov Yu. I. Triazoles as a class of multifunctional corrosion inhibitors. Review. Part V. 1H-1, 2, 4-Triazole and its derivatives. Copper and its alloys. *International Journal of Corrosion and Scale Inhibition*. 2022;11: 965–979. <https://doi.org/10.17675/2305-6894-2022-11-3-5>
25. El Issami S. Inhibition de la corrosion du cuivre en milieu HCl 0.5 M par les composés organiques de type triazole. Inhibition of copper corrosion in HCl 0.5 M medium by some triazolic compounds. *Annales de Chimie Science Des Matériaux*. 2002;27(4): 63–72. [https://doi.org/10.1016/s0151-9107\(02\)80019-8](https://doi.org/10.1016/s0151-9107(02)80019-8)

* Translated by author of the article

Информация об авторах

Denis V. Lyapun, Engineer, Department of Organic Chemistry, Voronezh State University (Voronezh, Russian Federation).

<https://orcid.org/0000-0002-5187-124X>
dshef@yandex.ru

Alexey A. Kruzhilin, Cand. Sci. (Chem.), Researcher, Laboratory of Organic Additives for the Processes of Chemical and Electrochemical Deposition of Metals and Alloys Used in the Electronics Industry, Voronezh State University (Voronezh, Russian Federation).

<https://orcid.org/0000-0003-2262-0131>
kruzhilin.alexey@gmail.com

Dmitry S. Shevtsov, Junior Researcher, Laboratory of Organic Additives for the Processes of Chemical and Electrochemical Deposition of Metals and Alloys Used in the Electronics Industry, Voronezh State University (Voronezh, Russian Federation).

<https://orcid.org/0000-0003-4480-787X>
shevtsov@chem.vsu.ru

Andrey Yu. Potapov, Dr. Sci. (Chem.), Head of the Laboratory of Organic Additives for the Processes of Chemical and Electrochemical Deposition of Metals and Alloys Used in the Electronics Industry, Voronezh State University (Voronezh, Russian Federation).

<https://orcid.org/0000-0001-8084-530X>
pistones@mail.ru

Khidmet S. Shikhaliev, Dr. Sci. (Chem.), Full Professor, Head of the Department of Organic Chemistry, Voronezh State University (Voronezh, Russian Federation).

<https://orcid.org/0000-0002-6576-0305>
shikh1961@yandex.ru

Received 10.01.2023; approved after reviewing 30.01.2023; accepted for publication 15.02.2023; published online 25.06.2023.



Condensed Matter and Interphases

Kondensirovannye Sredy i Mezhfaznye Granitsy
<https://journals.vsu.ru/kcmf/>

Original articles

Research article

<https://doi.org/10.17308/kcmf.2023.25/11102>

Localization of the *E. coli* Dps protein molecules in a silicon wires matrix according to scanning electron microscopy and X-ray photoelectron spectroscopy

E. V. Parinova¹✉, S. S. Antipov^{1,2}, V. Sivakov³, E. A. Belikov¹, O. A. Chuvenkova¹, I. S. Kakuliia¹, S. Yu. Trebunskikh¹, M. S. Skorobogatov¹, R. G. Chumakov⁴, A. M. Lebedev⁴, V. G. Artyukhov¹, S. Yu. Turishchev¹

¹Voronezh State University,
1 Universitetskaya pl., Voronezh, 394018, Russian Federation

²Institute of Cell Biophysics of the Russian Academy of Sciences,
3 Institutskaya st., Pushchino, 142290, Russian Federation

³Leibniz Institute of Photonic Technology, Department Functional Interfaces,
9 Albert Einstein st., Jena, 07745, Germany

⁴National Research Center “Kurchatov Institute”,
1 Akademika Kurchatova pl., Moscow, 123182, Russian Federation

Abstract

The work is related to the study of the morphological features of silicon wires arrays combined with a nanomaterial of natural origin, a bacterial ferritin-like protein Dps, and their relationship with the composition of the surface and interior. A silicon wires array was formed by metal-assisted wet chemical etching. To obtain recombinant protein, *Escherichia coli* BL21*(DE3) cells were used as producers, and purification was carried out by the chromatography method. The combination of silicon wires with protein molecules was carried out by layering under laboratory conditions, followed by drying. The resulting hybrid material was studied by scanning electron microscopy and X-ray photoelectron spectroscopy.

The initial silicon wires array had sharp boundaries on the surface. The diameter of the silicon wires was about 100 nm, while the distances between the wires can vary widely, reaching several hundred nanometres or be less than 100 nanometres, depending on the formation conditions, in the absence of noticeable transition layers. The pores formed in this way are available for filling with protein during deposition.

The effectiveness of using the scanning electron microscopy method to study the morphology of the hybrid material “silicon wires – bacterial protein Dps” as well as X-ray photoelectron spectroscopy method together with ion etching for the investigation of the composition and physico-chemical of the hybrid material was demonstrated. Complementary results have shown that the molecular culture, which is a solution of oligomers of the recombinant Dps protein of *E. coli* bacterial cells, can penetrate deep into the pores of the silicon wires array with an extremely developed surface. The possibility of the control of the filling of silicon wires arrays by varying the pore morphology and other modes of formation of structures and their surface has been demonstrated.

The obtained data can be used to study the possibilities of the functionalization of the developed surface of silicon wires by their driven coating with controlled delivery of biohybrid material.

Keywords: Nanostructures, Biomolecules, Hybrid materials, Developed surface, Recombinant ferritin-like protein Dps, Silicon wires, Scanning Electron Microscopy, X-ray Photoelectron Spectroscopy

✉ Elena V. Parinova, e-mail: parinova@phys.vsu.ru

© Parinova E. V., Antipov S. S., Sivakov V., Belikov E. A., Chuvenkova O. A., Kakuliia I. S., Trebunskikh S. Yu., Skorobogatov M. S., Chumakov R. G., Lebedev A. M., Artyukhov V. G., Turishchev S. Yu., 2023



The content is available under Creative Commons Attribution 4.0 License.

Funding: The study was supported by Russian Science Foundation (Project 19-72-20180). The work on silicon wire array formation and the methodology of work with protein molecules from *E. coli* cell material was supported under scholarship of the President of Russian Federation SP-189.2021.1 for young scientists.

For citation: Parinova E. V., Antipov S. S., Sivakov V., Belikov E. A., Chuvenkova O. A., Kakuliia I. S., Trebunskikh S. Yu., Skorobogatov M. S., Chumakov R. G., Lebedev A. M., Artyukhov V. G., Turishchev S. Yu. Localization of the *E. coli* Dps protein molecules in a silicon wires matrix according to scanning electron microscopy and X-ray photoelectron spectroscopy. *Condensed Matter and Interphases*. 2023;25(2): 207–214. <https://doi.org/10.17308/kcmf.2023.25/11102>

Для цитирования: Паринаова Е. В., Антипов С. С., Сиваков В., Беликов Е. А., Чувенкова О. А., Какулия Ю. С., Требунских С. Ю., Скоробогатов М. С., Чумаков Р. Г., Лебедев А. М., Артюхов В. Г., Турищев С. Ю. Локализация молекул белка Dps *E. coli* в матрице нитевидного кремния по данным растровой электронной микроскопии и рентгеновской фотоэлектронной спектроскопии. *Конденсированные среды и межфазные границы*. 2023;25(2): 207–214. <https://doi.org/10.17308/kcmf.2023.25/11102>

1. Introduction

One of the modern and relevant directions of technologies development for the formation of new functional nanomaterials of high scientific and practical interest is the creation and study of structures based on the combination of well-known and well-technologically developed inorganic nanomaterials and biopolymers, including those of natural origin [1, 2]. The well-known silicon wires (Si-NW) remain an attractive material for researchers because of their simple, well-developed and economical production technology, their ability to photoluminescence in the visible spectral region at room temperature [3, 4] and the possibility of using such structures to generate hydrogen [5]. The presence of an extremely developed surface in Si-NW is an important characteristic that enhances the attractiveness of this material. Targeted delivery of nanoparticles, including nano-biohybrid ones, and their controlled distribution during the functionalization of 3D-developed surfaces is a real example of how silicon wires can be applied [6–8].

One of the characteristic examples of a natural functional nano-biohybrid material formation is the accumulation of inorganic nanoparticles inside a natural protein molecule [7, 9]. The Dps protein (DNA-binding protein of starving cells) is a representative of bacterial ferritins [10]. The size of the outer shell of the bacterial protein Dps is about 9 nm. The protein part includes 12 identical subunits with a homododecamer structure [9, 10]. Dps protein molecules are capable of accumulating (depositing) iron ions. The accumulation of iron occurs in the form of inorganic nanoparticles of the iron-oxygen system [9] inside the hollow part of the protein with a diameter of up to 5 nm [9, 10]. Thus, the

Dps dodecamer is a potential container of natural origin, which can serve for the accumulation, storage, and targeted delivery of nanomaterials, including into various matrices with a developed 3D surface. Therefore, the issue of studying the result of combining Si-NW arrays with oligomers of recombinant Dps protein obtained from *E. coli* cells is relevant for the development and application of new hybrid materials combining inorganic structures with desired properties with functional nanomaterials of natural origin.

Previously, by scanning electron microscopy (SEM), we showed the potential possibility of filling the developed and available for functionalization surface of silicon wires with *E. coli* Dps protein molecules [6, 8]. In this study, the morphology data are supplemented by the results of the X-ray photoelectron spectroscopy application - XPS method, sensitive to the surface composition and physico-chemical state of the studied object, together with focused ion etching, in order to establish the possibility of filling the space between Si-NW with a recombinant protein molecular culture.

2. Experimental

Silicon wires were formed by metal-assisted wet chemical etching [3, 4]. Crystalline silicon substrates of *p*- and *n*-types (specific conductivity $\sim 1\text{--}5 \text{ }\Omega/\text{cm}$ and $< 0.02 \text{ }\Omega/\text{cm}$, respectively) were washed for 10 seconds in a solution of 2 % hydrofluoric acid (HF). Deposition of silver nanoparticles on the silicon wafers surface was carried out by immersion in a solution of AgNO_3 (0.01 M) and HF (5 M) at 15 sec (*p*-type substrates) and 45 sec (*n*-type substrates). Then etching was carried out in a 30 % solution of H_2O_2 and HF (5 M) for 180 sec, followed by removal of silver nanoparticles by washing in a solution of HNO_3

(65 %) in water for 10 minutes. The structures formed in this way were dried in air under laboratory conditions.

Cells of *Escherichia coli* BL21*(DE3) bacteria, hereinafter *E. coli*, transformed by pGEM_ *dps*, were used as producers to obtain recombinant Dps protein. Detailed information on the preparation of the recombinant protein, the method of its isolation and purification, removal of inorganic components by stepwise hydrolysis and dialysis are provided in [9]. The protein solution had a concentration of 2 mg/ml in a buffer containing 10 mM NaCl, 50 mM Tris-HCl (pH 7.0) and 0.1 mM EDTA. The sizes of protein molecules were controlled by dynamic light scattering [11]. A single layering of 10 ml protein molecules solution on the surface of Si-NW arrays was performed, followed by drying under laboratory conditions.

The morphology of the initial Si-NW array surfaces and the hybrid structure based on it with a layered protein were studied by Scanning Electron Microscopy. The Carl Zeiss ULTRA 55 microscope was used in the mode of secondary electrons registration with a low accelerating voltage of 2 kV, which is necessary for working with structures of biological origin. To estimate the areas occupied by the wires array and pores, as well as the degree of arrays filling with molecular culture, the Image J software package was used.

XPS studies was carried out using the NANOFES beamline ESCA module of the Kurchatov synchrotron ultrahigh vacuum experimental end-station (National Research Center Kurchatov Institute, Moscow), equipped with an electron energy analyzer SPECS Phoibos 150 [12]. Monochromatized AlK α radiation of an X-ray tube (1486.61 eV) was used, the depth of the informative layer was \sim 2–3 nm [13]. Survey spectra were recorded in the range of binding energies 0–850 eV. To normalize and calibrate the data, a standard approach was used based on the independent recording of the pure gold foil (Au 4f) signal. To identify the main features of the survey spectra, well-known databases were used, from which the actual and most accurate (monochromatic) spectra were selected [13–15]. A focused source of surface etching with argon ions was used at an accelerating voltage of 3 kV

with an etching duration of 20 minutes. The area of the etching site was selected with an excess of the surface area from which the XPS data were recorded.

3. Results and discussion

The SEM data obtained for the initial arrays of *p*- and *n*-type substrates silicon wires are shown in Fig. 1 (a, c) and, on the same scale, for arrays of silicon wires after layering of a molecular protein culture obtained from *E. coli* bacteria (Fig. 1 (b, d)), respectively. For *p*-type substrates, taking into account their significantly higher specific conductivity (\sim 1–5 Ω /cm) compared to *n*-type substrates ($<$ 0.02 Ω /cm), a shorter silver deposition time was chosen according to [3]. This led to the formation of smaller Ag nanoparticles on the surface of *p*-type crystalline silicon and for other equal parameters, to a more pronounced formation of wires during etching. Arrays of *p*-type substrates silicon wires were characterized by a more uniform distribution of submicron size \sim 200–500 nm pores (voids) between the wires, along with generally uniform wall sizes. At the same time, for *n*-type substrates, large pores of similar size were observed together with much smaller ones, about 10–100 nm in size. The formed characteristic upper parts of the wires are indicated by arrow 1, and the pores are indicated by arrow 2 in Fig. 1 (a, c). All observed pores of silicon wires arrays appear to be available for filling as a result of the layering of Dps protein molecules with a size of up to 10 nm.

The morphology of the surface changed after layering the molecular culture of the recombinant bacterial protein Dps from *E. coli* and subsequent drying. Fig. 1 shows the SEM data for *p*-type (Fig. 1b) and *n*-type substrates (Fig. 1d). These data indicate a clear overflow of pore volumes of the wires array of the *p*-type substrate in the presence of Dps molecules (Fig. 1b). Individual small sections most likely represent the uppermost parts of the wires (arrow 1). There were also quite large submicron-sized formations on the surface, which presumably represent a residual salt from the culture medium, or, more likely, a buffer solution used to maintain the conformation of the Dps dodecamer, in which the molecular culture was directly layered. According to the protocol of experiments this salt is NaCl. However, traces

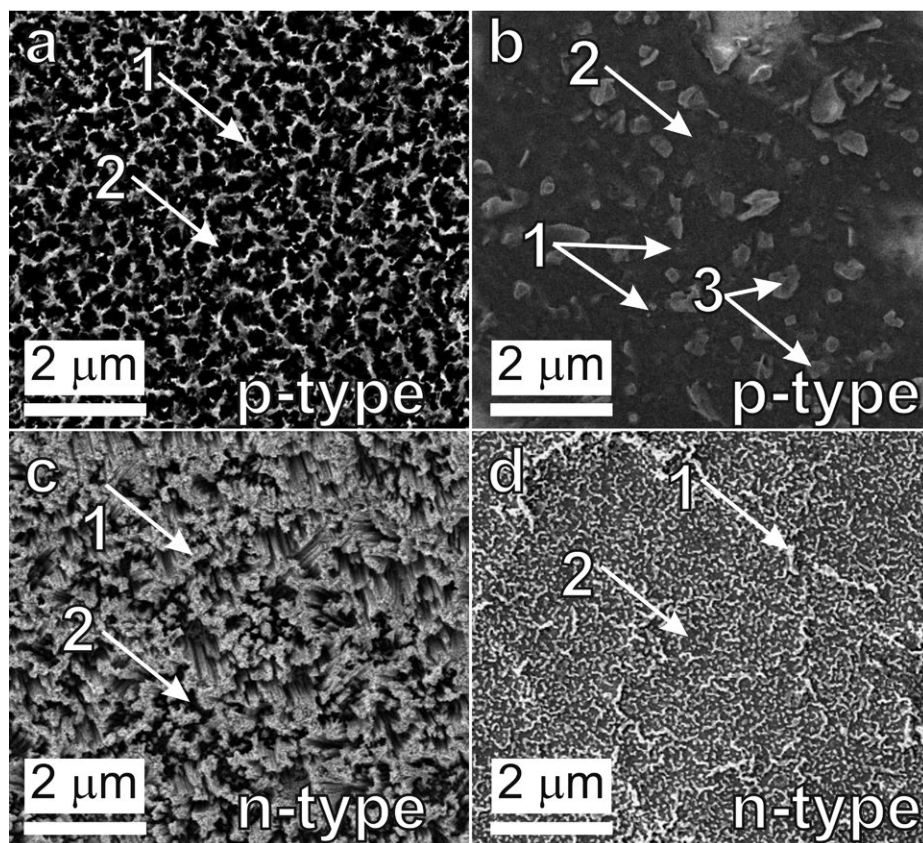


Fig. 1. Scanning electron microscopy of the initial samples of silicon wires array surfaces formed from *p*-type (a) and *n*-type (c) substrates, as well as after layering of the Dps protein molecular culture (b) and (e), respectively. 1 – tops of wires (walls of pores), 2 – pores between wires, 3 – NaCl salt particles after drying

of salt release were not noted for silicon wires formed on *n*-type substrates (Fig. 1d). Here, the filling of pores was also noted (arrow 2), however, a much larger number of uncovered vertices of silicon wires was observed. As the uniform experimental conditions were maintained, we associate this observation with the large volume of formed wires array pores available for filling with molecular culture. The three-fold increase in time of silver deposition on the surface (the size of silver nanoparticles, according to [3] was larger) with a much lower resistivity of *n*-type substrates compared to *p*-type led to a more pronounced “etching” and, as a consequence, large volumes of space between them were available for filling, which is in good agreement with [3, 6, 8]. The absence of NaCl formations on the surface can presumably be explained by the penetration of salt deep into the pores, before the formation of large particles as a result of drying.

The XPS survey spectra are shown in Fig. 2 for *p*-type silicon wire substrates after layering

of the molecular culture. It should be noted that we do not provide XPS survey spectra for both types of the initial substrates and arrays of wires before filling with protein due to their almost complete identity. The exception is the intensities redistribution for the 2s and 2p silicon lines relative to the 1s oxygen line intensity which was obviously associated with an increase in the amount of the wires array surfaces available for oxidation. For the wires arrays, after the layering of *E. coli* Dps cells, all lines corresponded to the biological component of the studied sample were noted. First of all, the 1s carbon line had most significant in intensity, 1s nitrogen and oxygen lines were also present. A weak set of sodium and chlorine lines in combination with the observation of a noticeable Na KLL Auger line indicated some presence of salt on the surface. A comparison with the SEM results may imply the NaCl particles could be observed microscopically with a layer of residual Dps molecular culture covering them. In addition, the presence of barely

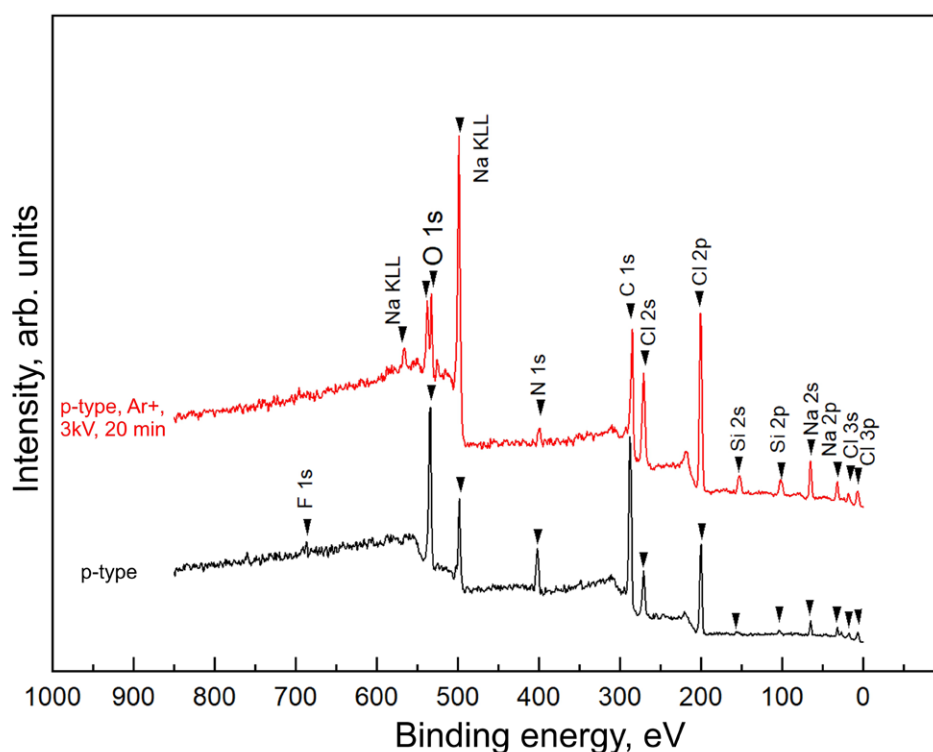


Fig. 2. XPS survey spectra of a silicon wires sample formed on a *p*-type substrate before (black) and after (red) ion beam etching (Ar^+ 3 kV 20 min). The characteristic elements that make up the studied sample surface are noted

noticeable 2s and 2p silicon lines should be noted, confirming the assumption that wire arrays formed on a *p*-type substrate overflow, according to the SEM data.

Unlike the studies published earlier, where “soft” modes were used for etching [16, 7], in the present study we used a relatively high accelerating voltage of argon ions (3 kV) for the removal of the significant part of the surface in 20 minutes of etching. The estimation of the etching rate used at the NANOFES station module, along with calibration measurements, showed the removal rate for silicon atoms of ~ 2.5 nm/min. For the residual part of the molecular culture, this rate may differ by several times [17]. The removal of more than 50 nm of the surface by an ion beam led to significant changes. NaCl lines became the most intense, confirming the assumption made above about the salt particles coverage by the residual protein. The intensities of the silicon lines also became more pronounced, which also implies the removal of a significant amount of protein from the part of the surface subjected to ion etching.

Finally, it should be noted that after the removal of the part of the surface, the intensity

of the oxygen 1s line practically did not change, but the peak became two-component. The preservation of intensity may be associated with the preservation of pores filling with molecular culture. The appearance of the second component of the oxygen peak may be due to the contribution of natural silicon oxide from the wires array “opened” after ion etching. The preservation of the position and relative intensity of the carbon line, obviously the main for the molecular culture, confirms the penetration and filling of pores with Dps protein under the selected method and modes of formation.

XPS spectra survey for *n*-type silicon wire substrates after layering of molecular culture are shown in Fig. 3. It should be noted that the silicon lines were among the most intense, confirming the observations of SEM, indicating the not so pronounced filling of pores in comparison with *p*-type substrates. The two-component oxygen line had the highest intensity here. This result was undoubtedly obtained by the cumulative contribution of oxygen atoms of naturally oxidized silicon wires and protein in the pores of the wires matrix.

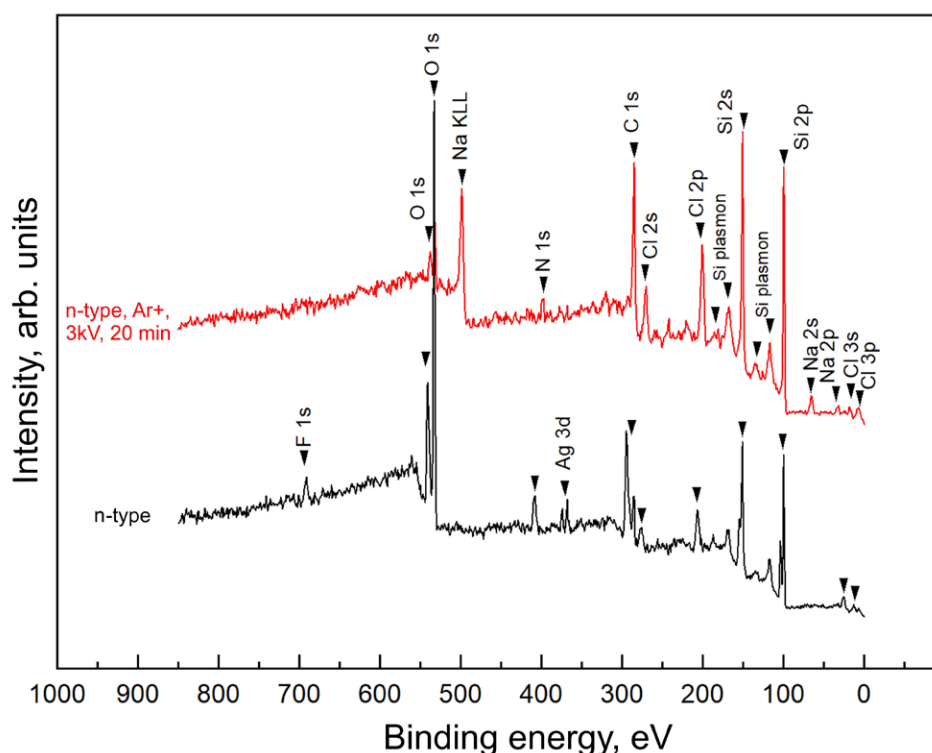


Fig. 3. XPS survey spectra of a silicon wires sample formed on a *p*-type substrate before (black) and after (red) ion beam etching (Ar+ 3 kV 20 min). The characteristic elements that make up the studied sample surface are noted

The intense carbon line as well as nitrogen line, also indicated the presence of a significant amount of protein in the matrix pores of wires. The weak contribution of chlorine lines to the survey spectrum, together with the absence of sodium lines, may indicate insignificant, residual traces of salt in the most superficial layers (~ 3 nm). An interesting observation was the presence of an Ag 3*d* doublet line. This finding is explained by the three times longer deposition time of silver on the silicon surface for *n*-type wafers compared to *p*-type with identical washing time after the formation of a wires array.

As in the previous case, ion etching led to a change in the physicochemical state of the studied structure. The silicon line became one-component after etching. Together with a significant decrease in the intensity of the two-component 1s oxygen line, this observation confirmed the noticeable removal of natural silicon oxide from the developed (including SEM data, Fig 1) surface of the wires array. The 1s oxygen line remained two-component indicating that the Dps protein molecules were

also preserved in the pores. The increase in the intensity of 1s carbon line also confirmed this observation. The appearance of all the lines characteristic of NaCl observed for structures on *p*-type substrates confirmed the assumption made during the analysis of SEM data about the presence of residual culture medium salts or buffer solutions after drying in the depth of pores for wire arrays of *n*-type substrates.

Finally, the presence of fluorine atoms on the studied structures surface after protein layering and the decreased intensity of the nitrogen line after ion etching of the structures formed on the both types of substrates can be considered as the subject of separate studies. Additionally the issue of the removal of residual salts of buffer solutions and the culture medium of *E. coli* cells producers of Dps deserves separate consideration.

4. Conclusions

The possibility of the effective filling of silicon wires array pores with bacterial ferritin Dps molecules of *E. coli* cells has been demonstrated

for the first time using X-ray photoelectron spectroscopy and scanning electron microscopy.

It was shown that the morphology of the initial silicon wires array has a significant effect on the characteristics of pores filling with a molecular culture of the Dps protein. The possibility of the controlled filling of silicon wires arrays by varying the morphology of pores and other modes of structure formation was established: the resistivity of the initial crystalline silicon wafers, etching time, layering characteristics, and salt concentrations of working solutions.

The obtained self-complementary data of the SEM and XPS methods can be used to study the possibilities of the silicon wires developed surface functionalization by driven coating under the controlled delivery of biohybrid material.

Author contributions

All authors made an equivalent contribution to the preparation of the publication.

Conflict of interests

The authors declare that they have no known competing financial interests or personal relationships that could have appeared to influence the work reported in this paper.

References

1. Osminkina L. A., Gongalsky M. B., Motuzuk A. V., Timoshenko V. Y., Kudryavtsev A. A. Silicon nanocrystals as photo- and sono-sensitizers for biomedical applications. *Applied Physics B*. 2011;105: 665–668. <https://doi.org/10.1007/s00340-011-4562-8>
2. Harrison P. M., Arosio P. The ferritins, molecular properties, iron storage and cellular regulation. *Biochimica et Biophysica Acta (BBA) - Bioenergetics*. 1996;1275(3): 161–203. [https://doi.org/10.1016/0005-2728\(96\)00022-9](https://doi.org/10.1016/0005-2728(96)00022-9)
3. Sivakov V. A., Brönstrup G., Pecz B., Berger A., Radnoczi G. Z., Krause M., Christiansen S. H. Realization of vertical and zigzag single crystalline silicon nanowire architectures. *The Journal of Physical Chemistry C*. 2010;114: 3798–3803. <https://doi.org/10.1021/jp909946x>
4. Lo Faro M. J., Leonardi A. Al., D'Andrea C., ... Irrera A. Low cost synthesis of silicon nanowires for photonic applications. *Journal of Materials Science: Materials in Electronics*. 2020;31: 34–40. <https://doi.org/10.1007/s10854-019-00672-y>
5. Ming T., Turishchev S., Schleusener A., ... Sivakov V. Silicon suboxides as driving force for

efficient light-enhanced hydrogen generation on silicon nanowires. *Small*. 2021;17(8): 2007650. <https://doi.org/10.1002/smll.202007650>

6. Parinova E. V., Antipov S. S., Sivakov V., ... Turishchev S. Yu. Dps protein localization studies in nanostructured silicon matrix by scanning electron microscopy. *Condensed Matter and Interphases*. 2021;23(4): 644–648. <https://doi.org/10.17308/kcmf.2021.23/3741>

7. Parinova E. V., Antipov S. S., Belikov E. A., Chuvankova O. A., Kakuliia I. S., Koyuda D. A., Trebunskikh S. Yu., Skorobogatov M. S., Chumakov R. G., Lebedev A. M., Sineelnikov A. A., Artiuhov V. G., Ovchinnikov O. V., Smirnov M. S., Turishchev S. Iu. TEM and XPS studies of bio-nanohybrid material based on bacterial ferritin-like protein Dps. *Condensed Matter and Interphases*. 2022;24(2): 265–272. <https://doi.org/10.17308/kcmf.2022.24/9267>

8. Parinova E. V., Antipov S. S., Belikov E. A., Kakuliia I. S., Trebunskikh S. Y., Turishchev S. Y., Sivakov V. Localization of DPS protein in porous silicon nanowires matrix. *Results in Physics*. 2022;35: 105348. <https://doi.org/10.1016/j.rinp.2022.105348>

9. Antipov S., Turishchev S., Purtov Yu., ... Ozoline O. The oligomeric form of the Escherichia coli Dps 3 protein depends on the availability of iron ions. *Molecules*. 2017;22(11): 1904. <https://doi.org/10.3390/molecules22111904>

10. Zhang Y., Fu J., Chee S. Y., Ang E. X., Orner B. P. Rational disruption of the oligomerization of the mini-ferritin *E. coli* DPS through protein–protein interface mutation. *Protein Science*. 2011;20(11): 1907–1917. <https://doi.org/10.1002/pro.731>

11. Turishchev S. Yu., Antipov S. S., Novolokina N. V., ... Domashevskaya E. P. A soft X-ray synchrotron study of the charge state of iron ions in the ferrihydrite core of the ferritin Dps protein in Escherichia coli. *Biophysics*. 2016;61(5): 705–710. <https://doi.org/10.1134/s0006350916050286>

12. Lebedev A. M., Menshikov K. A., Nazin V. G., Stankevich V. G., Tsetlin M. B., Chumakov R. G.. NanoPES photoelectron beamline of the Kurchatov Synchrotron Radiation Source. *Journal of Surface Investigation: X-ray, Synchrotron and Neutron Techniques*. 2021;15(5): 1039–1044. <https://doi.org/10.1134/s1027451021050335>

13. John F. Moulder *handbook of X-ray photoelectron spectroscopy*. Published by Perkin-Elmer Corporation Physical Electronics Division 6509 Flying Cloud Drive Eden Prairie, Minnesota 55344 United States of America; 1992.

14. *Handbook of the elements and native oxide*. XPS International, Inc.; 1999. srdata.nist.gov/xps

16. Turishchev S. Yu., Chuvankova O. A., Parinova E. V., ... Sivakov V. XPS investigations of MOCVD tin oxide thin layers on Si nanowires array. *Results in*

Physics. 2018;11: 507-509. <https://doi.org/10.1016/j.rinp.2018.09.046>

17. Hüfner S. Very high resolution photoelectron spectroscopy. In: *Lecture Notes in Physics*. Berlin Heidelberg: Springer; 2007. <https://doi.org/10.1007/3-540-68133-7>

Information about the authors

Elena V. Parinova, Cand. Sci. (Phys.-Math.), Assistant Professor, General Physics Department, Voronezh State University (Voronezh, Russian Federation).

<https://orcid.org/0000-0003-2817-3547>
parinova@phys.vsu.ru

Sergey S. Antipov, Dr. Sci. (Biology), Associate Professor, Biophysics and Biotechnology Department, Voronezh State University (Voronezh, Russian Federation).

<https://orcid.org/0000-0003-3244-1428>
ss.antipov@gmail.com

Sivakov Vladimir, PhD, Deputy Head, Leibniz Institute of Photonic Technology (Jena, Germany).

<https://orcid.org/0000-0002-3272-501X>
vladimir.sivakov@leibniz-ipht.de

Evgeny A. Belikov, Engineer of Joint Laboratory “Atomic and Electronic Structure of Functional Materials”, Voronezh State University (Voronezh, Russian Federation).

<https://orcid.org/0000-0001-8336-2231>
belikov@phys.vsu.ru

Olga A. Chuvenkova, Cand. Sci. (Phys.-Math.), Senior researcher of the Joint Laboratory “Atomic and Electronic Structure of Functional Materials”, Voronezh State University (Voronezh, Russian Federation).

<https://orcid.org/0000-0001-5701-6909>
chuvchenkova@phys.vsu.ru

Iuliia S. Kakuliia, Leading Engineer, General Physics Department, Voronezh State University (Voronezh, Russian Federation).

<https://orcid.org/0000-0002-0953-9024>
kakuliia@phys.vsu.ru

Sergey Yu. Trebunskikh, Cand. Sci. (Phys.-Math.), Researcher of the Joint Laboratory “Atomic and Electronic Structure of Functional Materials”, Voronezh State University (Voronezh, Russian Federation).

<https://orcid.org/0000-0002-2481-2797>
trebunskikh@phys.vsu.ru

Matvey S. Skorobogatov, bachelor student, Biophysics and Biotechnology Department, Voronezh State University (Voronezh, Russian Federation).

<https://orcid.org/0000-0003-3244-1428>
ss.antipov@gmail.com

Ratibor G. Chumakov, Cand. Sci. (Phys.-Math.), Senior Researcher of the National Research Center “Kurchatov Institute” (Moscow, Russian Federation).

<https://orcid.org/0000-0002-3737-5012>
ratibor.chumakov@gmail.com

Alexei M. Lebedev, Cand. Sci. (Phys.-Math.), Senior Researcher of the National Research Center “Kurchatov Institute” (Moscow, Russian Federation).

<https://orcid.org/0000-0001-9998-8941>
lebedev.alex.m@gmail.com

Valerii G Artyukhov, Dr. Sci. (Biology), Professor, Head of the Biophysics and Biotechnology Department, Voronezh State University (Voronezh, Russian Federation).

<https://orcid.org/0000-0002-5872-8382>
artyukhov@bio.vsu.ru

Sergey Yu. Turishchev, Dr. Sci. (Phys.-Math.), Associate Professor, Head of the General Physics Department, Voronezh State University (Voronezh, Russian Federation).

<https://orcid.org/0000-0003-3320-1979>
tsu@phys.vsu.ru

Received 23.11.2022; approved after reviewing 05.12.2022; accepted for publication 08.12.2022; published online 25.06.2023.

Translated by Sergey Turishchev

Edited and proofread by Simon Cox



Original articles

Research article

<https://doi.org/10.17308/kcmf.2023.25/11103>

Photosensitising reactive oxygen species with titanium dioxide nanoparticles decorated with PbS quantum dots

A. S. Perepelitsa, S. V. Aslanov, O. V. Ovchinnikov✉, M. S. Smirnov, I. G. Grevtseva,
A. N. Latyshev, T. S. Kondratenko

Voronezh State University,
1 Universitetskaya pl., Voronezh, 394018, Russian Federation

Abstract

The development of new efficient photocatalysts based on nanostructured materials with a wide range of photosensitivity in visible and near-infra-red regions and high efficiency of reactive oxygen species generation is an important task. The purpose of this project was to establish the possibility of photosensitising the process of generating reactive oxygen species (ROs) with TiO₂ nanoparticles (NPs) decorated with colloidal PbS quantum dots (QDs) passivated with 3-mercaptopropionic acid (3MPA) as well as the possibility of increasing the spectral sensitivity of synthesised nanoheterosystems into the red region.

The paper analyses the photocatalytic properties of TiO₂ NPs with an anatase structure and average size of 12 nm decorated with colloidal PbS QDs with an average size of 2.7 nm passivated with 3MPA. It also provides structural and spectral substantiation of the formation of TiO₂ NPs – PbS/3MPA QDs nanoheterostructures. Absorption and luminescence techniques were used to establish the efficiency of generating various ROs by TiO₂ NPs – PbS/3MPA nanoheterostructures and their individual components under excitation in the UV and visible radiation.

It was shown that TiO₂ NPs decoration with PbS QDs extends the spectral range of sensitivity to the generation of reactive oxygen species in the UV to 1;100 nm. The study revealed an increased efficiency of hydrogen peroxide generation by nanoheterostructures as compared to individual PbS QDs and TiO₂ nanoparticles.

Keywords: Nanoparticles, Titanium dioxide, Quantum dots, Lead sulphide, Photosensitisation, Reactive oxygen species, Photocatalysis

Funding: The study was conducted within the framework of the state order to higher education institutions (FZGU-2023-0007) and the Ministry of Science and Higher Education of the Russian Federation under Agreement (N 075-15-2021-1351).

Acknowledgements: The studies of structural properties conducted by the methods of transmission electron microscopy and X-ray diffractometry were carried out using the equipment of the VSU Centre for Collective Use of Scientific Equipment.

For citation: Perepelitsa A. S., Aslanov S. V., Ovchinnikov O. V., Smirnov M. S., Grevtseva I. G., Latyshev A. N., Kondratenko T. S. Photosensitising reactive oxygen species with titanium dioxide nanoparticles decorated with PbS quantum dots. *Condensed Matter and Interphases*. 2023;25(0): 215–224. <https://doi.org/10.17308/kcmf.2023.25/11103>

Для цитирования: Перепелица А. С., Асланов С. В., Овчинников О. В., Смирнов М. С., Гревцева И. Г., Латышев А. Н., Кондратенко Т. С. Фотосенсибилизация активных форм кислорода наночастицами диоксида титана, декорированными квантовыми точками PbS. *Конденсированные среды и межфазные границы*. 2023;25(0): 215–224. <https://doi.org/10.17308/kcmf.2023.25/11103>

✉ Ovchinnikov Oleg Vladimirovich, e-mail: ovchinnikov_o_v@rambler.ru

© Perepelitsa A. S., Aslanov S. V., Ovchinnikov O. V., Smirnov M. S., Grevtseva I. G., Latyshev A. N., Kondratenko T. S., 2023



1. Introduction

The development of effective photocatalysts of various compositions with a wide range of photosensitivity and high efficiency of reactive oxygen species generation is an important scientific and technological task [1]. Traditionally, nanoparticles (NPs) of wide band semiconductors, such as TiO_2 , ZnO, ZnS, etc., are used for photocatalysis [1]. However, despite their high photocatalytic activity and stability, they have a number of drawbacks. The key disadvantage of traditional photocatalysts is that they are not photosensitive to the visible and near-infrared spectral regions [1]. Photosensitivity of nanoparticles of wide band semiconductors can be achieved by doping them with non-metal atoms (S, N, C, etc.) and metal ions (Fe^{3+} , Mo^{5+} , Os^{3+} , Rh^{3+} , etc.), hybrid association with molecules of organic dyes, decorating the surface of the NP with plasmonic nanoparticles (Cu, Au, Ag, Pt) or semiconductor colloidal quantum dots (QDs) (Ag_2S , CdSe, etc.) [1–4]. Decoration of the surface of TiO_2 NPs with colloidal QDs of narrow band semiconductors (Ag_2S , PbS, etc.) is of particular interest. PbS is characterised by the narrow band gap and a large Bohr radius of the Wannier–Mott exciton (~ 18 nm) [5]. These properties allow controlling the position of the exciton absorption peak in the region of 800–2,400 nm [6], and, accordingly, the region of spectral sensitisation of TiO_2 NPs.

[7, 8] demonstrated the possibility of increasing the photocatalytic activity of TiO_2 nanotubes with a size of 90–100 nm when decorating their surface with PbS QDs with a size of 4–5 nm. In this case, PbS nanocrystals were grown directly on the surface of TiO_2 nanotubes. It was shown that decoration of TiO_2 nanotubes increases photocatalytic activity. Other works [9] propose a method for increasing the spectral sensitivity of the TiO_2/Cu heterosystem with a size of ~ 20 nm by the deposition on their surface of PbS QDs with an average size of 3–5 nm dispersed in toluene. This approach increases the spectral sensitivity of the photocatalyst to 610 nm depending on the size of QDs. However, there have been no systematic descriptions of optical and photocatalytic properties of TiO_2 NPs and PbS QDs heterosystems in literature.

The purpose of this work was to establish the possibility of photosensitisation of ROS

in the presence of TiO_2 NPs – PbS/3MPA QDs nanoheterostructures in the visible and near-IR region.

2. Experimental

2.1. Sample synthesis methods

Used reagents are lead nitrate ($\text{Pb}(\text{NO}_3)_2$), 3-mercaptopropionic acid (3MPA), sodium sulphide (Na_2S), sodium hydroxide (NaOH), 2H-1-benzopyranone-2 (coumarin), imidazole, and 4-nitroso-N,N-dimethylaniline (RNO). They were purchased from Sigma-Aldrich and used without further purification. Amplex UltraRed and horseradish peroxidase were purchased from ThermoFisher Scientific.

Colloidal PbS QDs were synthesised in water. 3MPA was used as a passivator. 3MPA (1.5 mmol) was introduced into an aqueous solution of $\text{Pb}(\text{NO}_3)_2$ (1.5 mmol and 200 ml of water) at 30 °C followed by adjustment of the pH level to 10 with NaOH solution. Then, with constant stirring a peristaltic pump was used to add 50 ml of Na_2S solution (0.8 mmol), which served as a source of sulphur. This ratio of reagents provided for the formation of PbS QDs with a concentration of $6 \cdot 10^{-3}$ mol QD/l in water. To remove the by-products of the reaction, PbS QDs were precipitated with acetone, centrifuged, and redispersed in water.

The resulting PbS QDs were used to form nanoheterostructures with TiO_2 NPs. The experimental technique was similar to the one described in detail in [10, 11]. To form the nanoheterostructures, TiO_2 NPs were dispersed in water and sonicated at 60 kHz until a uniform suspension was obtained. The suspension was then mixed with a QDs solution and dried at room temperature. Free QDs were removed from the resulting grey powder.

2.2. Equipment and experimental techniques

Structural studies of the obtained samples were performed by transmission electron microscopy (TEM) using a Libra 120 PLUS transmission electron microscope (Carl Zeiss, Germany) with an accelerating voltage of 120 kV and a THERMO ARL X'TRA X-ray diffractometer (ThermoFisher, Switzerland).

The optical absorption spectra of the colloidal solution of PbS/3MPA QDs and the diffuse reflection spectra of the powders of TiO_2 –

PbS/3MPA nanoheterostructures were recorded with a USB2000+ spectrometer with the combined USB-DT radiation source and IS80 integrating sphere (Ocean Optics, USA). Barium sulphate powder (P.A.) was used as a white standard to measure diffuse reflection spectra. The absorption coefficient was calculated from the experimental diffuse reflection spectra using the Kubelka-Munk function $F(R)$ [12]:

$$F(R) = \frac{k}{s} = \frac{1 - R^2}{2R},$$

where R is the diffuse reflection, k is the absorption coefficient, and s is the scattering coefficient.

A computer-aided spectrometric system based on a MDR-4 diffraction monochromator (LOMO, Russia) with a PDF-10C/M photodiode (ThorLabs, USA) as a radiation receiver were used to record QD luminescence spectra in the range of 800–1,400 nm. An LD PLTB450 semiconductor laser diode (Osram, Germany) with a wavelength of 445 nm and an optical power of 400 mW was used as an excitation source.

Reactive oxygen species were detected by standard absorption and photoluminescence techniques [13]. Production of hydrogen

peroxide (H_2O_2) was controlled with an Amplex UltraRed selective sensor [14] in the presence of peroxidase by measuring the rate of luminescence enhancement of the sensor at a wavelength of 596 nm. The concentration of hydroxyl radical ($\cdot OH$) was determined by the luminescence of 7-hydroxycoumarin (7HC) in the region of 470 nm produced in a coumarin solution in the presence of $\cdot OH$ radicals [15]. The presence of singlet oxygen (1O_2) was monitored by an absorption method using an imidazole solution with the addition of 4-nitroso-N,N-dimethylaniline (RNO) dye at a ratio of 160:1 to reduce the optical density of the RNO absorption band in the region of 445 nm [16].

3. Results and Discussion

3.1. Structural properties of the studied samples

TEM images demonstrated that ensembles of colloidal PbS QDs had been formed with an average size of nanocrystals of ~ 2.7 nm and a dispersion in size of $\sim 25\%$ (Fig. 1).

X-ray diffraction analysis of $K_{\alpha 1}$ emission line of copper (1.54 \AA) revealed the formation of crystallites, the position of reflexes from which corresponded to the cubic FCC lattice of PbS (Fmm) [17] (Fig. 1). Estimates of the average

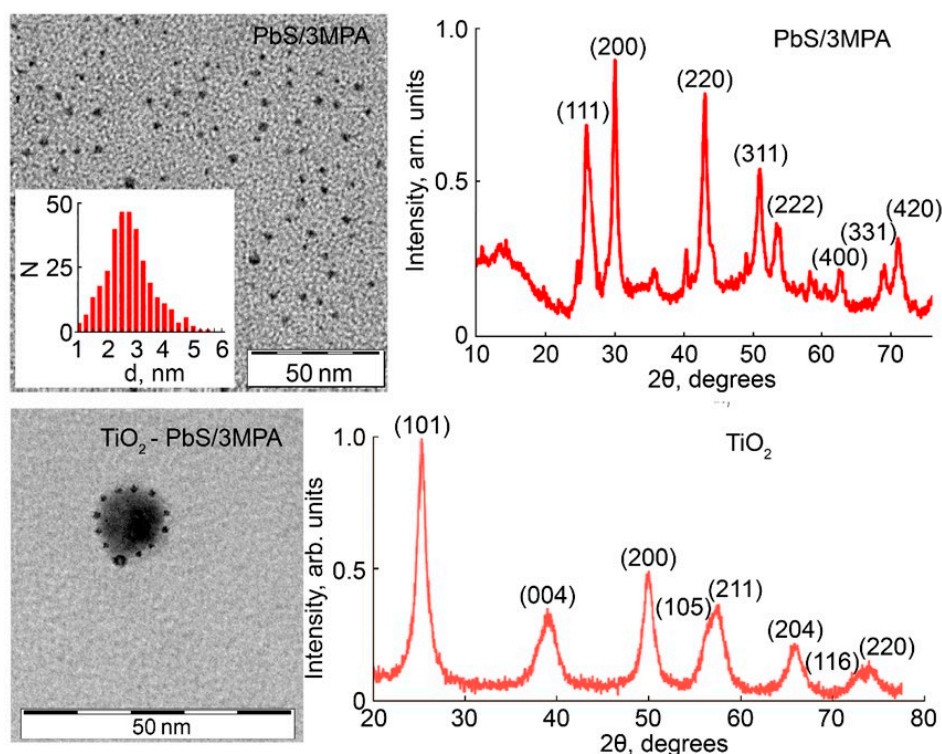


Fig. 1. TEM images and X-ray diffraction patterns of: PbS/3MPA QDs, TiO_2 NPs and $TiO_2 - PbS/3MPA$ nanoheterosystems

size of crystallites performed using the Debye-Scherrer equation [18] had a value of crystallite sizes of ~ 3 nm, which correlated with the TEM data.

X-ray diffraction analysis revealed that TiO_2 NPs had the average size of 12 nm and anatase crystal structure (Fig. 1). TEM images of PbS QDs and TiO_2 NPs mixtures clearly showed nanoparticles with an average size of 10–15 nm on the surface of which there were much smaller NPs with a size of about 2–3 nm (Fig. 1). Comparing the sizes of the detected nanoparticles in mixtures and similar sizes of initial components allows us to assume that the TEM images of mixtures showed TiO_2 NPs with PbS QDs adsorbed on their surfaces.

3.2. Absorption and luminescence properties of the studied samples

The optical absorption spectrum of PbS/3MPA QDs was a broad structureless band with the band edge near 1,300 nm (Fig. 2a) and weak features in the region of 500 and 1,000 nm. The absence of an exciton structure in the PbS QDs optical absorption spectrum can be explained by several factors: 1) size dispersion of QDs, which was detected during the analysis of TEM images; 2) non-stoichiometry of PbS nanocrystals, whose occurrence in PbS nanoscale crystals was indicated in [19]. In this case, optical absorption spectrum for PbS QDs is determined not only by transitions between the quantum size levels in QDs but also by transitions with the participation of trap states.

The intrinsic absorption edge of TiO_2 NPs obtained from the diffuse reflection spectra (Fig. 2a) was located near 3.21 eV and corresponded to the TiO_2 band gap with anatase crystal structure (3.2 eV) [20, 21]. On the long-wavelength side from the intrinsic absorption edge in the region of 3.0–3.2 eV, there was a certain optical density caused by permitted band - trap state transitions. Absorption by trap states in TiO_2 crystals was indicated in [13].

Mixtures of TiO_2 NPs and PbS/3MPA QDs demonstrated transformations of optical absorption spectra. The absorption spectrum of mixtures (Fig. 2a) had a complex structure and was not simply a sum of the spectra of the components. In particular, against the background of strong absorption of TiO_2 NPs (in the quantum energy range above 3.2 eV), there was a broad absorption band in the range of 400–1,100 nm (1–3.1 eV). There were no changes in the absorption region of TiO_2 NPs. Therefore, the transformation of the absorption band structure in the long-wavelength region, for which PbS QDs are accountable in mixtures, and the presence of the absorption band in the region of 200–400 nm, for which TiO_2 NPs are accountable, as well as structural data indicated the formation of TiO_2 NPs – PbS/3MPA nanoheterostructures.

Significant changes were also observed in luminescence when TiO_2 NPs – PbS/3MPA nanoheterostructures were formed. This was accompanied by quenching of PbS QDs luminescence bands in the region of 1,100–

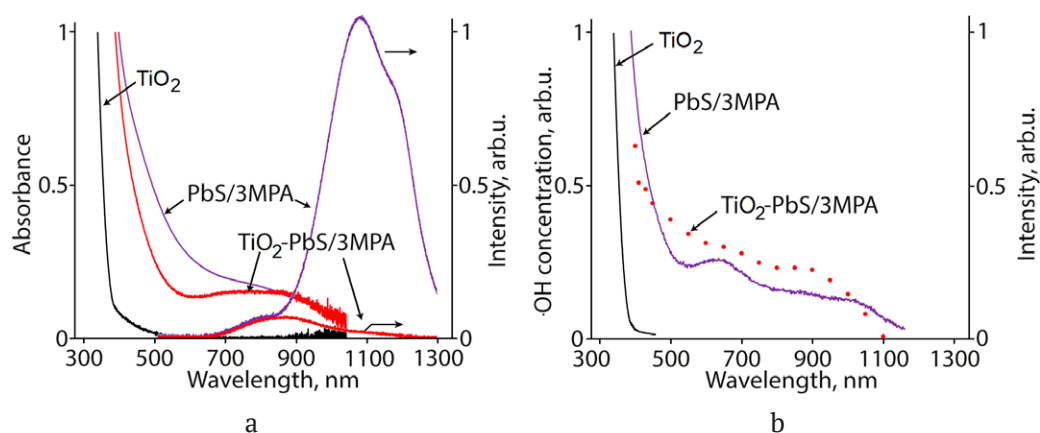


Fig. 2. (a) Optical absorption and photoluminescence spectra of TiO_2 , PbS/3MPA QDs, and TiO_2 – PbS/3MPA nano-heterosystems; (b) photoluminescence excitation spectrum of PbS/3MPA QDs and spectral sensitivity dependences of the $\cdot\text{OH}$ radical production in the suspensions of TiO_2 and TiO_2 – PbS/3MPA nano-heterosystems

1,200 nm. A similar pattern was observed in [10, 11] for TiO₂ NPs decorated with Ag₂S QDs. Quenching of PbS QDs luminescence during their adsorption on the TiO₂ NPs interfaces also indicated that nanoheterostructures had been formed and there had been a transfer of photoexcited charge carriers between the nanostructure components. However, luminescence partially kept in the band with a peak at 890 nm indicated that there was no interaction between PbS QDs with a size of less than 2.5 nm (the smallest) present in the ensembles and surface of TiO₂ NPs, which was due to displacement of the quantum size levels of PbS QDs and states of TiO₂ NPs.

3.3. ROS sensitisation with the obtained samples

Figure 3 shows the results of measurements of ROS generation by TiO₂ NPs – PbS/3MPA QDs nanoheterostructures under excitation by UV radiation and radiation in visible spectral regions. It should be noted that during UV excitation, electrons and holes are generated in both TiO₂ and PbS QDs, while during excitation in the visible range they are mainly generated in PbS QDs. Visible radiation allows establishing

that PbS QDs provide for TiO₂ photosensitisation to this range. On the other hand, selective excitation of components helps to specify the mechanisms of photocatalytic reactions in the TiO₂ NPs – PbS/3MPA QDs heterosystems. The used methods of ROS detection showed that singlet oxygen (¹O₂), hydroxyl radical (·OH) and hydrogen peroxide (H₂O₂) were generated in TiO₂ NPs suspensions exposed to radiation with a wavelength of 365 nm, which is consistent with the data in [22]. In colloidal solutions of PbS/3MPA QDs, we recorded generation of hydrogen peroxide and singlet oxygen (Fig. 4), which had not been previously recorded for PbS QDs in the literature.

The formation of nanoheterostructures led to a change in the efficiency of generation of all types of ROS. Under UV excitation of TiO₂ NPs decorated with PbS/3MPA QDs, in the absorption region of titanium dioxide the efficiency of generation of hydroxyl ·OH radical decreased by 10%, of singlet oxygen by 40%, and the generation of H₂O₂ increased by 3.5 times relative to pure TiO₂ NPs. The efficiency of singlet oxygen and hydrogen peroxide generation by the created nanoheterosystems under excitation

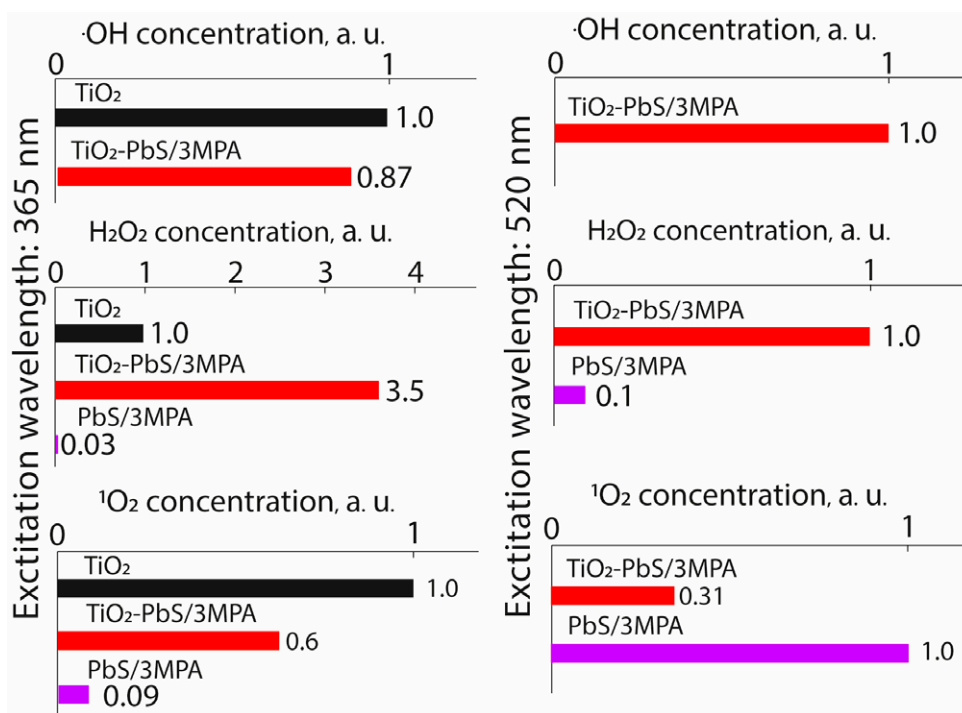


Fig. 3. Histograms of the relative rates of production of hydroxyl radical (·OH), hydrogen peroxide (H₂O₂), and singlet oxygen (¹O₂) in the suspensions of TiO₂, PbS/3MPA QDs, and TiO₂ – PbS/3MPA nanoheterosystems when excited by radiation in the UV and visible region of the spectrum

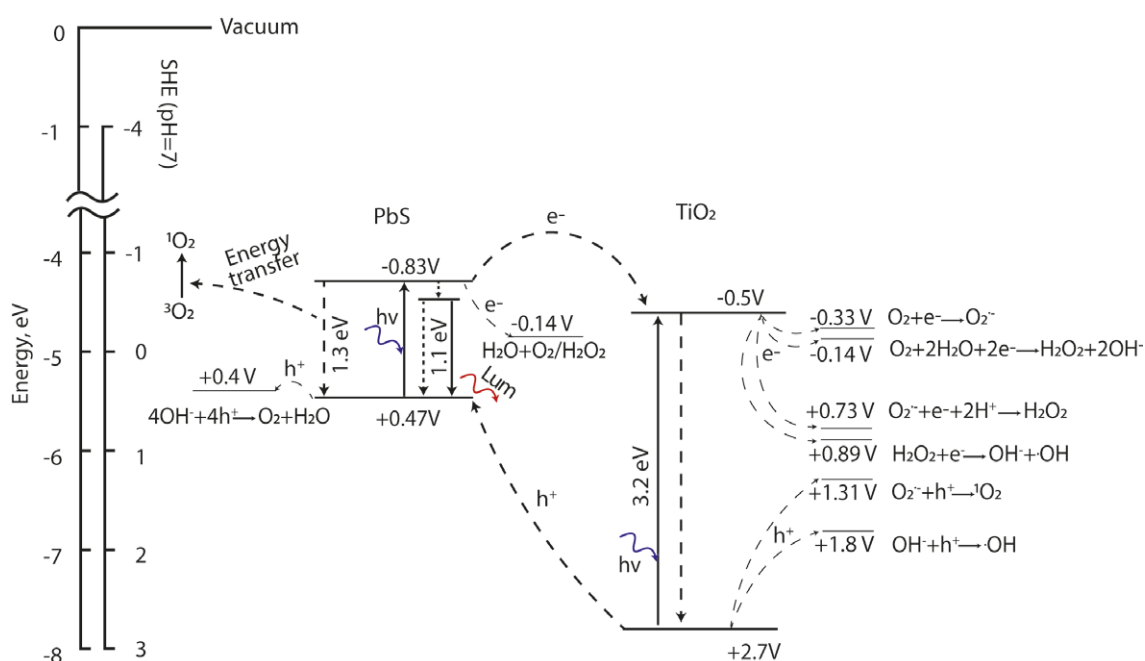


Fig. 4. Scheme of photoprocesses and photocatalytic reactions in the TiO_2 – $\text{PbS}/3\text{MPA}$ nano-heterosystem. The data on redox potentials and the location of bands were taken from [13, 23–28]

in the UV region of the spectrum increased by 6.6 and 120 times, respectively, relative to pure PbS QDs.

When $\text{PbS}/3\text{MPA}$ QDs were excited at a wavelength of 520 nm, hydrogen peroxide and singlet oxygen generation was observed. TiO_2 nanoparticles under 520 nm radiation showed no signs of ROS generation. The formation of TiO_2 NPs – $\text{PbS}/3\text{MPA}$ QDs nanoheterostructures led to the photosensitisation of the $\cdot\text{OH}$ radical, which was not observed in pure PbS QDs, a 10-time increase in hydrogen peroxide generation as compared to the initial $\text{PbS}/3\text{MPA}$ QDs, and a 3-time decrease in the efficiency of singlet oxygen generation. What is more, for the TiO_2 NPs – $\text{PbS}/3\text{MPA}$ QDs nanoheterosystems, a broad band of photosensitivity to the generation of $\cdot\text{OH}$ radical was detected in the range from 300 to 1,100 nm, which was absent in case of the initial components (TiO NPs and $\text{PbS}/3\text{MPA}$ QDs) (Fig. 2b). The shape of the photosensitisation band for $\cdot\text{OH}$ radical qualitatively coincided with the excitation spectrum of $\text{PbS}/3\text{MPA}$ QDs photoluminescence, which, together with the detected quenching of photoluminescence during the formation of nanoheterostructures, indicated the participation of excitons excited in QDs during ROS generation.

3.4. Empirical model of ROS generation in the studied samples

The obtained results allow justifying in general terms the scheme of the mutual arrangement of the energy levels of $\text{PbS}/3\text{MPA}$ QDs and TiO_2 NPs (Fig. 4). It should be noted that the generation of $\cdot\text{OH}$ radical and hydrogen peroxide occurred as a result of a charge carrier transfer reaction [13, 23–28]. On the contrary, the production of singlet oxygen was possible both as a result of the transfer of charge carriers and non-radiative energy transfer from the nanoheterosystem (or one of the components) to the molecule of the unexcited triplet oxygen [31]. The formation of TiO_2 NPs – $\text{PbS}/3\text{MPA}$ QDs nanoheterostructures was accompanied by a pronounced quenching of the PbS QDs luminescence, which was interpreted as the separation of photoexcited charge carriers between the components. Moreover, effective separation of charge carriers was observed both during photoexcitation in the region of strong TiO_2 absorption (UV region) and noticeable PbS QDs absorption (520 nm). Also, the efficiency of ROS production by TiO_2 – $\text{PbS}/3\text{MPA}$ nanoheterostructures redistributed. It is noteworthy that when a nanoheterosystem was photoexcited in the PbS QDs absorption region (520 nm) an $\cdot\text{OH}$ radical was effectively

produced, which indicated the formation of charge phototransfer channels between the components of the system. Indeed, the comparison of the energy of electron affinity for TiO₂ NPs and PbS QDs (taking into account the size effect for the electron and hole levels) allowed us to assume that a second type heterosystem had been formed, i.e. the quantum-size conduction states for PbS QDs were above the bottom of the TiO₂ NPs conduction band. In this case, the most likely was the phototransfer of electrons from PbS QDs to TiO₂ NPs into the conduction band. Then, the holes remained localised in PbS QDs, which blocked the recombination of charge carriers and facilitated their participation in catalytic reactions of ROS generation.

In this case, the electrons in TiO₂ NPs could react with adsorbed H₂O and O₂ molecules, produce the hydroxyl radical ·OH and hydrogen peroxide H₂O₂. The reaction for the production of hydrogen peroxide is known: O₂ + 2e⁻ + 2H⁺ → H₂O₂. This reaction requires a photoelectron from the TiO₂ conduction band [13, 23–28]. In this case, the formation of a heterosystem should contribute to an increase in the efficiency of H₂O₂ generation both when excited in the UV and visible region, which was observed during the experiment. The generation of the ·OH radical in the presence of TiO₂ can be provided for by two reactions: both with the participation of electrons from the conduction band (1) TiO₂ – H₂O₂ + e⁻ → ·OH + OH⁻ [13, 23–28] and holes from the valence band (2) TiO₂ (2) OH⁻ + h⁺ → ·OH. Separation of charge carriers in the heterosystem contributes to the hole localisation in PbS, which blocks reaction (2). In this case, the efficiency of the ·OH radical generation during the heterosystem formation may decrease, which was observed during the experiment under excitation in the UV region. Under the influence of visible radiation, the electron and the hole are generated in PbS QDs. The mutual arrangement of PbS QDs and TiO₂ NPs levels contributes to the transition of the electron to the TiO₂ conduction band. This photo-excited electron from the TiO₂ conduction band can participate in the generation of the ·OH radical by reaction (1). Indeed, under the influence of visible radiation the generation of the ·OH radical was detected for heterosystems, which is not characteristic of individual components.

To close the proposed scheme of the ·OH radical generation under the influence of visible radiation and to let the photocatalyst operate for an unlimited time, reduction of PbS QDs is needed. The study revealed that the generation of the ·OH radical under the influence of visible radiation is not saturated. However, so far the mechanism of PbS QDs reduction has not been established and will be studied separately.

As have been noted, the generation of singlet oxygen is possible both as a result of the charge carrier transfer (electron and hole) and the non-radiative energy transfer from the nanoheterosystem (or one of the components) to the molecule of unexcited triplet oxygen [23–28, 30, 31]. In the case of UV excitation of TiO₂, the following two-stage process is recognised as the main mechanism: (3) O₂ + e → O₂⁻ and (4) O₂⁻ + h⁺ → ¹O₂ [13, 27]. The process of singlet oxygen generation in PbS QDs detected by us cannot proceed by reaction (4) in terms of energy since the level of size quantisation for holes in PbS QDs is located above the oxidative potential O₂⁻/¹O₂. Therefore, the only possible mechanism is the exchange-resonance mechanism of non-radiative transfer of excitation energy from PbS QDs to ³O₂ and excitation of the latter to the singlet state of ¹O₂. This scheme was indirectly confirmed by a sharp decrease in the efficiency of ¹O₂ generation in TiO₂ NPs (UV excitation) when introducing a hole acceptor into the solution, which blocked reaction (4). Introduction of a hole acceptor to the PbS QDs did not change the rate of ¹O₂ generation. In heterosystems, a decrease in the rate of ¹O₂ generation under excitation in the visible radiation as compared to pure PbS QDs is determined by the effective separation of charge carriers between components. It should be noted that we did not find any reports of ¹O₂ photogeneration in PbS QDs. This was observed for carbon, CdS, and ZnS QDs [30, 31].

4. Conclusions

The authors developed a method for decorating the surface of TiO₂ NPs with colloidal PbS QDs with an average size of 2.7 nm obtained in an aqueous solution of 3-mercaptopropionic acid. The following spectral manifestations of the formation of the TiO₂ – PbS/3MPA nanoheterosystem were detected: i) in terms of absorption properties

the study revealed a transformation of PbS QDs absorption bands during adsorption to the surface of TiO₂ NPs; ii) there was quenching of PbS QDs luminescence in the region of 1000-1400 nm during the formation of the TiO₂ – PbS/3MPA QDs nanoheterosystems. Studies were conducted to check the possibility of generating ROS by the obtained nanoheterosystems. The generation of singlet oxygen and hydrogen peroxide in the presence of PbS QDs was detected. It was shown that decorating the surface of TiO₂ NPs resulted in a 10% decrease in the efficiency of hydroxyl radical generation, and a 40% decrease in the efficiency of singlet oxygen generation as compared to pure TiO₂ NPs. The rate of hydrogen peroxide generation increased up to 3.5 times relative to the TiO₂ NPs and up to 150 times relative to PbS/3MPA QDs under excitation by UV radiation. The generation of ROS was detected when excited by radiation in the visible spectrum, which was absent in case of pure TiO₂ NPs. It was determined that the generation of hydrogen peroxide increased by 10 times and the production of singlet oxygen decreased by 3 times relative to pure PbS QDs. The study revealed hydroxyl radical sensitisation absent in case of pure PbS QDs. It also established an expansion of the excitation region of ROS production to 1100 nm. An empirical model for photoprocesses in the studied nanoheterosystems was created.

Author contributions

A. S. Perepelitsa: conducting scientific research, writing of the article, scientific editing of the text; S. V. Aslanov: conducting scientific research, scientific editing of the text; O. V. Ovchinnikov: head of scientific research, scientific editing of the text, discussion of the results of the study; M. S. Smirnov: scientific editing of the text, discussion of the results of the study; I. G. Grevtseva: scientific editing of the text, discussion of the results of the study; A. N. Latyshev: scientific editing of the text, discussion of the results of the study; T. S. Kondratenko: scientific editing of the text, discussion of the results of the study.

Conflict of interests

The authors declare that they have no known competing financial interests or personal

relationships that could have influenced the work reported in this paper.

References

1. *Micro and nano technologies, nanotechnology and photocatalysis for environmental applications*. M. Tahir, M. Rafique, M. Rafique (eds.). Amsterdam: Elsevier Inc. 2020. 244 p.
2. Huang F., Yan A., Zhao H. Influences of doping on photocatalytic properties of TiO₂ photocatalyst. In: *Semiconductor photocatalysis - materials, mechanisms and applications*. <https://doi.org/10.5772/63234>
3. Li R., Li T., Zhou Q. Impact of titanium dioxide (TiO₂) modification on its application to pollution treatment – a review. *Catalysts*. 2020;10(7): 804. <https://doi.org/10.3390/catal10070804>
4. Janczarek M., Kowalska E. On the origin of enhanced photocatalytic activity of copper-modified titania in the oxidative reaction systems. *Catalysts*. 2017;7(11): 317. <https://doi.org/10.3390/catal7110317>
5. Kang I., Wise F. W. Electronic structure and optical properties of PbS and PbSe quantum dots. *Journal of the Optical Society of America B*. 1997;14(7): 1632–1646. <https://doi.org/10.1364/JOSAB.14.001632>
6. Su G., Liu C., Deng Z., Zhao X., Zhou X. Size-dependent photoluminescence of PbS QDs embedded in silicate glasses. *Optical materials express*. 2017;7(7): 2194–2207. <https://doi.org/10.1364/OME.7.002194>
7. Zhang H., Gao Y., Zhu G., Li B., Gou J., Cheng X. Synthesis of PbS/TiO₂ nano-tubes photoelectrode and its enhanced visible light driven photocatalytic performance and mechanism for purification of 4-chlorobenzoic acid. *Separation and Purification Technology*. 2019;227: 115697. <https://doi.org/10.1016/j.seppur.2019.115697>
8. Ratanatawanate C., Tao Y., Balkus K. J. Jr. Photocatalytic activity of PbS quantum dot/TiO₂ nanotube composites. *Journal of Physical Chemistry. C* 2009;113(24): 10755–10760. <https://doi.org/10.1021/jp903050h>
9. Wang C., Thompson R. L., Ohodnicki P., Baltrus J., Matranga C. Size-dependent photocatalytic reduction of CO₂ with PbS quantum dot sensitized TiO₂ heterostructured photocatalysts. *Journal of Materials Chemistry*. 2011;21: 13452. <https://doi.org/10.1039/C1JM12367J>
10. Ovchinnikov O. V., Smirnov M. S., Aslanov S. V., Perepelitsa A. S. Luminescent properties of colloidal Ag₂S quantum dots for photocatalytic applications. *Physics of the Solid State*. 2022;64(13): 12054–2061. <https://doi.org/10.21883/PSS.2022.13.53973.19s>
11. Ovchinnikov O. V., Smirnov M. S., Perepelitsa A. S., ... Hussein A. M. H. Photosensitisation of reactive oxygen species with titanium dioxide nanoparticles decorated with silver sulphide quantum dots. *Condensed Matter and Interphases*. 2022;24(4):

511–522. <https://doi.org/10.17308/kcmf.2022.24/10555>

12. Kubelka P., Munk F. An article on optics of paint layers. *Fuer Tekn. Physik.* 1931;12: 593–609.

13. Nosaka Y., Nosaka A. Y. Generation and detection of reactive oxygen species in photocatalysis. *Chemical Reviews.* 2017;117: 11302–11336. <https://doi.org/10.1021/acs.chemrev.7b00161>

14. Mohanty J. G., Jaffe J. S., Schulman E. S., Raible D. G. A highly sensitive fluorescent micro-assay of H₂O₂ release from activated human leukocytes using a dihydroxyphenoxazine derivative. *Journal of Immunological Methods.* 1997;202(2): 133–141. [https://doi.org/10.1016/S0022-1759\(96\)00244-X](https://doi.org/10.1016/S0022-1759(96)00244-X)

15. Wafi A., Szabó-Bárdos E., Horváth O., Makó E., Jakab M., Zsirka B. Coumarin-based quantification of hydroxyl radicals and other reactive species generated on excited nitrogen-doped TiO₂. *Journal of Photochemistry and Photobiology A: Chemistry.* 2021;404: 112913. <https://doi.org/10.1016/j.jphotochem.2020.112913>

16. Herman J., Neal S. L. Efficiency comparison of the imidazole plus RNO method for singlet oxygen detection in biorelevant solvents. *Analytical and Bioanalytical Chemistry.* 2019;411(20): 5287–5296. <https://doi.org/10.1007/s00216-019-01910-2>

17. Sadovnikov S. I., Kozhevnikova N. S., Pushin V. G., Rempel A. A. Microstructure of nanocrystalline PbS powders and films. *Inorganic Materials.* 2012;48: 21–27. <https://doi.org/10.1134/S002016851201013X>

18. Gusev A. I. *Nanomaterials, nanostructures, nanotechnologies**. Moscow: Fizmatlit Publ.; 2005. 416 p. (In Russ.)

19. Sadovnikov S. I., Rempel A. A. Nonstoichiometric distribution of sulfur atoms in lead sulfide structure. *Doklady Physical Chemistry.* 2009;428(1): 167–171. <https://doi.org/10.1134/S0012501609090024>

20. Kapilashrami M., Zhang Y., Liu Y.-S., Hagfeldt A., Guo J. Probing the optical property and electronic structure of TiO₂ nanomaterials for renewable energy applications. *Chemical Review.* 2014;114: 9662–9707. <https://doi.org/10.1021/cr5000893>

21. Murphy A. B. Band-gap determination from diffuse reflectance measurements of semiconductor films, and application to photoelectrochemical water-splitting. *Solar Energy Materials & Solar Cells.* 2007;91: 1326–1337. <https://doi.org/10.1016/j.solmat.2007.05.005>

22. Nakata K., Fujishima A. TiO₂ photocatalysis: Design and applications. *Journal of Photochemistry and Photobiology C: Photochemistry Reviews.* 2012;13(3): 169–189. <https://doi.org/10.1016/j.jphotochemrev.2012.06.001>

23. Athanasekou C. P., Likodimos V., Falaras P. Recent developments of TiO₂ photocatalysis involving

advanced oxidation and reduction reactions in water. *Journal of Environmental Chemical Engineering.* 2018;6(6): 7386–7394. <https://doi.org/10.1016/j.jece.2018.07.026>

24. Turrens J. F. Mitochondrial formation of reactive oxygen species. *The Journal of Physiology.* 2003;552(2): 335–44. <https://doi.org/10.1113/jphysiol.2003.049478>

25. Fujishima A., Zhang X., Tryk D. A. TiO₂ photocatalysis and related surface phenomena. *Surface Science Reports.* 2008;63(12): 515–582. <https://doi.org/10.1016/j.surfrep.2008.10.001>

26. Kohtani S., Yoshioka E., Miyabe H. Photocatalytic hydrogenation on semiconductor particles. In: *Hydrogenation.* I. Karame (ed.). *IntechOpen.* 2012. 340 p. <https://doi.org/10.5772/45732>

27. Bard A. J., Parsons R., Jordan J. *Standart potentials in aqueous solutions.* Routledge, 1985. 848 p. <https://doi.org/10.1201/9780203738764>

28. Belovolova L.V. Reactive oxygen species in aqueous media (a review). *Optics and Spectroscopy.* 2020;128: 932–951. <https://doi.org/10.1134/S0030400X20070036>

29. Segets D., Lucas J. M., Klupp Taylor R. N., Scheele M., Zheng H., Alivisatos A. P., Peukert W. Determination of the quantum dot band gap dependence on particle size from optical absorbance and transmission electron microscopy measurements. *ACS Nano.* 2012,6(10): 9021–9032. <https://doi.org/10.1021/nn303130d>

30. Ge J., Jia Q., Liu W.,... Wang P. Carbon dots with intrinsic theranostic properties for bioimaging, red-light-triggered photodynamic/photothermal simultaneous therapy in vitro and in vivo. *Advanced Healthcare Materials.* 2016;5(6): 665–675. <https://doi.org/10.1002/adhm.201500720>

31. Bailón-Ruiz S., Perales-Pérez O. J. Generation of singlet oxygen by water-stable CdSe(S) and ZnSe(S) quantum dots. *Applied Materials Today.* 2017;9: 161–166. <https://doi.org/10.1016/j.apmt.2017.06.006>

* Translated by author of the article.

Information about the authors

Aleksey S. Perepelitsa, Cand. Sci. (Phys.–Math.), Associate Professor at the Department of Optics and Spectroscopy, Voronezh State University (Voronezh, Russian Federation).

<https://orcid.org/0000-0002-1264-0107>
a-perepelitsa@yandex.ru

Sergey V. Aslanov, Cand. Sci. (Phys.–Math.), Lecturer of the Department of Optics and Spectroscopy, Voronezh State University (Voronezh, Russian Federation).

<https://orcid.org/0000-0002-3961-2480>
windmaster7@yandex.ru

Oleg V. Ovchinnikov, Dr. Sci. (Phys.–Math.), Full Professor, Dean of the Faculty of Physics, Head of the Department of Optics and Spectroscopy, Voronezh State University (Voronezh, Russian Federation).

<https://orcid.org/0000-0001-6032-9295>
ovchinnikov_o_v@rambler.ru

Mikhail S. Smirnov, Dr. Sci. (Phys.–Math.), Associate Professor, Department of Optics and Spectroscopy, Voronezh State University (Voronezh, Russian Federation).

<https://orcid.org/0000-0001-8765-0986>
smirnov_m_s@mail.ru

Irina G. Grevtseva, Cand. Sci. (Phys.–Math.), Lecturer at the Department of Optics and Spectroscopy, Voronezh State University (Voronezh, Russian Federation).

<https://orcid.org/0000-0002-1964-1233>
grevtseva_ig@inbox.ru

Anatoly N. Latyshev, Dr. Sci. (Phys.–Math.), Full Professor, Department of Optics and Spectroscopy, Voronezh State University (Voronezh, Russian Federation).

<https://orcid.org/0000-0002-7271-0795>
latyshev@phys.vsu.ru

Tamara S. Kondratenko, Dr. Sci. (Phys.–Math.), Associate Professor, Department of Optics and Spectroscopy, Voronezh State University (Voronezh, Russian Federation).

<https://orcid.org/0000-0003-4936-0130>
tamara-shatskikh@rambler.ru

Received 29.10.2022; approved after reviewing 05.12.2022; accepted for publication 20.12.2022; published online 25.06.2023.

*Translated by Irina Charychanskaya
Edited and proofread by Simon Cox*



Original articles

Research article

<https://doi.org/10.17308/kcmf.2023.25/11104>

The effect of the synthesis conditions on the crystal structure of palladium(II) oxide nanofilms

A. M. Samoylov¹✉, S.S. Kopytin¹, S.A. Ivkov¹, E. A. Ratkov¹, E. A. Tutov²¹Voronezh State University,
1 Universitetskaya pl., Voronezh 394018, Russian Federation²Voronezh State Technical University,
84 20 letiya Oktyabrya st., Voronezh, 394006, Russian Federation

Abstract

Nanocrystalline films of palladium(II) oxide obtained by oxidation of the initial metallic Pd layers with a thickness of 35 nm on Si (100) substrates in atmospheric air were studied using XRD analysis, TEM, and RHEED.

PdO/SiO₂/Si (100) heterostructures were synthesised in two stages. First, we obtained finely dispersed layers of metallic Pd on SiO₂/Si (100) substrates with an ~ 300 nm SiO₂ buffer layer using thermal sublimation in a high vacuum. The Pd layers were then oxidised in the temperature range $T_{\text{ox}} = 620 - 1100$ K in atmospheric air (with the partial pressure of oxygen of about 21 kPa). The study determined that the deformation of the tetragonal crystal structure of homogeneous nanocrystalline PdO films is explained by an increase in the values of lattice parameters with the oxidation temperature. The deformation reaches its maximum values at $T_{\text{ox}} \sim 970$ K. Comparison of the obtained results with the earlier data regarding PdO/SiO₂/Si (100) heterostructures synthesised in a dry oxygen atmosphere (with the partial pressure of oxygen of about 101.3 kPa) demonstrated that PdO films synthesized in an oxygen atmosphere are characterized by a higher degree of deformation of the crystal structure.

The effect of the oxidation temperature and O₂ partial pressure on the increase in the tetragonal lattice parameters of the PdO films can be explained by the formation of interstitial oxygen atoms in the octahedral void in the centre of the palladium(II) oxide unit cell.

Keywords: Palladium, Palladium(II) oxide, Heterostructures, Crystal structure, Gas sensors

Funding: The study was supported by the Ministry of Science and Higher Education of the Russian Federation within the framework of state order to higher education institutions in the sphere of scientific research for 2023-2025 (project No. FZGU-2023-0006).

Acknowledgements: Powder diffraction, transmission electron microscopy, and reflection high-energy electron diffraction studies were conducted using the equipment of the Centre for Collective Use of Scientific Equipment of VSU.

For citation: Samoylov A. M., Kopytin S. S., Ivkov S. A., Ratkov E. A., Tutov E. A. The effect of the synthesis conditions on the crystal structure of palladium(II) oxide nanofilms. *Condensed Matter and Interphases*. 2023;25(2): 225–236. <https://doi.org/10.17308/kcmf.2023.25/11104>

Для цитирования: Самойлов А. М., Копытин С. С., Ивков С. А., Ратьков Е. А., Тутов Е. А. Влияние условий синтеза на кристаллическую структуру нанопленок оксида палладия (II). *Конденсированные среды и межфазные границы*. 2023;25(2): 225–236. <https://doi.org/10.17308/kcmf.2023.25/11104>

✉ Alexander M. Samoilov, e-mail: samoylov@chem.vsu.ru

© Samoylov A. M., Kopytin S. S., Ivkov S. A., Ratkov E. A., Tutov E. A., 2023



The content is available under Creative Commons Attribution 4.0 License.

1. Introduction

Creating a global system for monitoring the quality of atmospheric air is one of the most urgent scientific and technical problems of the 21st century [1]. Currently, a number of devices and technologies are used to detect poisonous and explosive gases in air. They include resistive gas sensors based on wide-band metal oxide semiconductors, which are widely used due to their reliability and a relatively low production cost [1–3]. Such devices are necessary for the prevention of technological and household incidents with explosive gases, as well as for security systems in various industrial processes that use poisonous or flammable volatile substances [1–4]. For 50 years, the materials most often used in scientific studies and industrial production of resistive gas sensors have been metal oxide semiconductors with an electronic type of conductivity, specifically tin(IV) oxide SnO_2 [1–6]. Impressive success in the development of gas sensors based on SnO_2 can be explained by the results of studying the physico-chemical patterns that describe and predict the nature of the interaction of the active layer surface with the molecules of detected gases [3, 6, 7]. It was established that *n*-type wide-band semiconductors, particularly SnO_2 , are characterised by a rather narrow homogeneity region [3, 4, 6, 7]. Various authors have proved the nature of point defects, mainly oxygen vacancies, which are responsible for nonstoichiometry and electronic type of conductivity of these compounds [3–7].

Despite the popularity of metal oxide semiconductors with an electronic type of conductivity for the production of gas sensors, materials for the so-called “perfect sensor” with optimal functional parameters have not yet been found [8, 9]. Over the past decade, there has been a considerable increase in the interest in the study of sensor properties of wide-band metal oxide semiconductors with the *p*-type surface and the composites based on them [10].

Recent studies have demonstrated that *p*-type nanostructures with various types of morphological organisation based on palladium(II) oxide are promising materials for the production of gas sensors that can detect even very small concentrations of toxic gases, including ozone and nitrogen oxides, in atmospheric air [11–23].

Prototypes of gas sensors based on nanocrystalline PdO films are characterised by a short recovery period and good reproducibility of the sensor signal when detecting ozone and nitrogen dioxide NO_2 in atmospheric air [17, 20–22]. There is also evidence that sensors based on PdO are highly sensitive to organic compound vapours, carbon monoxide, and hydrogen [24–25], which is of utmost importance for the creation of a strong hydrogen energetics system.

Earlier experiments demonstrated [11–25] that gas sensors based on palladium(II) oxide nanostructures are compatible with similar devices based on metal oxide materials with an electronic type of conductivity [20, 24–25]. However, unlike SnO_2 , a large number of basic physico-chemical properties of palladium(II) oxide have not been thoroughly studied yet. For instance, there is no phase diagram of the palladium-oxygen system, and the nature of point defects responsible for the *p*-type of conductivity of PdO is still a matter of debate [11, 15, 17, 19, 20]. The lack of this information makes it impossible to establish the mechanisms of interaction of the detected gases with the surface of nanostructures of palladium(II) oxide and largely hinders the practical application of gas sensors based on them. A detailed study of the changes in the crystal structure of nanosized PdO films depending on the synthesis conditions will help to get closer to solving the problem of nonstoichiometry of palladium(II) oxide and the nature of point defects [19].

The purpose of our study was to analyse the crystal structure of nanosized Pd films on SiO_2/Si (100) substrates during oxidation in atmospheric air in the temperature range $T_{\text{ox}} = 573\text{--}1148$ K and then compare it to the results of earlier experiments involving oxidation of Pd/ SiO_2/Si (100) heterostructures in a dry oxygen atmosphere [18–19].

2. Experimental

Nanocrystalline films of metallic palladium with a thickness of ~ 35 nm were synthesised using thermal sublimation of palladium foil with the concentration of the main component of 99.998 at.% in a high vacuum (residual pressure $\sim 10^{-10}$ Pa) on SiO_2/Si (100) substrates which were not heated. Since the SiO_2/Si (100) substrates were

not heated, ultradispersed layers were formed with the size of Pd crystallites between 2 and 6 nm. Crystallites of this size ensure uniform oxidation and formation of PdO [17–20]. The thickness of the initial films of metallic palladium determined by studying the cleavages of the Pd/SiO₂/Si(100) heterostructure using scanning electron microscopy was ~ 35 nm (varied within the range of 32–38 nm).

The thickness of the SiO₂ buffer layer was about 300 nm. [18, 19] demonstrated that the SiO₂ buffer layer helps to prevent direct interaction between metallic palladium and the material of the substrate resulting in the formation of palladium silicide Pd₂Si. The oxidation of Pd films grown on Si(100) substrates without a SiO₂ buffer layer in an O₂ atmosphere in the temperature range $T_{\text{ox}} = 970 - 1070$ K resulted in the formation of palladium silicide Pd₂Si [18].

In our study, thermal oxidation of the formed ultradispersed Pd films was performed by heating in air. Pd/SiO₂/Si (100) heterostructures were put into a resistive heating tube furnace at room temperature and then heated to the set temperature at a rate of 250 degrees per hour. After reaching the set temperature, the heterostructures were exposed to isothermal endurance for 120 minutes.

When choosing the oxidation conditions for the ultradispersed Pd layers, we took into account the conditions under which the same process

was conducted in an oxygen atmosphere [18, 19]. The oxidation conditions of the initial films of metallic Pd in air are given in Table 1.

Table 1 demonstrates that in some cases, specifically when the oxidation temperature was $T_{\text{ox}} = 773$ K and $T_{\text{ox}} = 973$ K, the duration of oxidation in air was 120 and 240 minutes. After the isothermal endurance, the samples were cooled together with the furnace.

The phase compositions and the crystal structures of the samples obtained by means of oxidation of the initial metallic Pd layers on SiO₂/Si (100) substrates were analysed using X-ray powder diffraction analysis (XRD) and reflection high-energy electron diffraction (RHEED). DRON-4-07 and Philips PANalytical X'Pert diffractometers with CuK α or CoK α and an ER-100 electronograph were used. X-ray diffraction patterns of the samples were registered with rotation of the samples, while the profiles of X-ray reflections were constructed pointwise with the step of the counter being 0.01°. The most intense reflection (400) of the Si (100) substrate served as an internal standard to prevent accidental errors. Reflections of the Si (100) substrate and Pd and PdO films were identified using an international database [27–28].

Precise determination of the tetragonal crystal lattice period of palladium(II) oxide films was conducted by extrapolating the diffraction

Table 1. Synthesis conditions of nanocrystalline films of palladium(II) oxide by means of oxidation of ~ 35 nm ultradispersed films of metallic palladium in air and in an oxygen atmosphere [18, 19]

Temperature T_{ox} , K	Oxidation in oxygen atmosphere [18, 19]			Oxidation in atmosphere air (this work)		
	Duration τ , minutes	Phase composition of samples	Phase composition of samples	Duration τ , minutes	Phase composition of samples	Phase composition of samples
573	120	Heterogeneous	Pd + PdO	120	Homogeneous	Pd
623	120	Homogeneous	PdO	120	Heterogeneous	Pd + PdO
673	120	Homogeneous	PdO	120	Homogeneous	PdO
773	120	Homogeneous	PdO	120	Homogeneous	PdO
873	120	Homogeneous	PdO	120 и 240	Homogeneous	PdO
923	120	Homogeneous	PdO	120	Homogeneous	PdO
973	120	Homogeneous	PdO	120 и 240	Homogeneous	PdO
1023	120	Homogeneous	PdO	120	Homogeneous	PdO
1073	120	Homogeneous	PdO	120	Homogeneous	PdO
1098	120	Homogeneous	PdO	120	Heterogeneous	Pd + PdO
1123	120	Heterogeneous	PdO + Pd	120	Homogeneous	Pd
1148	120	Heterogeneous	Pd + PdO	120	Homogeneous	Pd

angle to $\theta = 90$ degrees. For this, an extrapolation function $f(\theta)$ was chosen so that the dependence of parameters a and c on the value of $f(\theta)$ was closest to linear. The best results were obtained using the Nelson–Riley extrapolation function [27]:

$$f(\theta) = 0,5 \left(\frac{\cos^2 \theta}{\theta} + \frac{\cos^2 \theta}{\sin \theta} \right), \quad (1)$$

where θ – is the diffraction angle.

The lattice constants a and c of the tetragonal structure of palladium(II) oxide were calculated using a software based on an algorithm for solving a system of quadratic equations with two non-obvious parameters, as well as the UnitCell software. We should note that the results calculated using two different methods correlate with each other within the experimental error. The values of the tetragonal lattice parameters were calculated by means of linear function approximation using the least squares method:

$$a = k \times f(\sin \theta) + a_0, \quad (2a)$$

$$c = k \times f(\sin \theta) + c_0. \quad (2b)$$

3. Results and discussion

Results of the XRD and RHEED analyses of the samples obtained by means of oxidation in air of ultradispersed layers of metallic Pd on SiO_2/Si (100) substrates in the temperature range $T_{\text{ox}} = 573$ –1148 K are presented in Fig. 1 and 2 respectively. A characteristic RHEED pattern of single-phase nanocrystalline PdO films is given in Fig. 1. The XRD patterns of homogeneous Pd layers as well as heterogeneous samples (PdO +

Pd) are given in Fig. 2 in the form of line diagrams of powder pattern. Since the reflections of nanocrystalline Pd and PdO films are 3–4 times less intense than the reflection of the Si (400) substrate, Fig. 2 shows the intensity of X-ray diffraction peaks on a logarithmic scale.

Comparison of the results of earlier experiments involving oxidation of Pd/ SiO_2 /Si (100) heterostructures in an oxygen atmosphere [18, 19] with the analysis of the phase state of the films obtained by means of oxidation of initial layers of metallic Pd in air is given in Table 1 and Fig. 3.

Fig. 2b and Table 1 demonstrate that the XRD analysis did not register any changes in the phase composition after the oxidation of the initial Pd films at $T_{\text{ox}} = 573$ K in atmospheric air. In other words, Pd is not oxidized in air at this temperature, as the PdO phase was not registered.

On the contrary, at the temperatures of $T_{\text{ox}} = 873$ K and $T_{\text{ox}} = 973$ K, the oxidation is fast and complete. When the duration of oxidation was two times longer, the diffraction patterns did not differ from those of the samples oxidised for 120 minutes. Therefore, we can say that 120 minutes is enough to reach the practical thermodynamic conditions required for oxidation.

Fig. 2c shows that after the oxidation in air at $T_{\text{ox}} = 623$ K, heterogeneous samples (Pd + PdO) are formed. The diffraction pattern registered Pd reflections and several most intense PdO reflections. The XRD and RHEED analyses demonstrated that single-phase PdO films are formed after the oxidation in air at $T_{\text{ox}} = 673$ –1073 K (Table 1, Fig. 3). When the oxidation temperature

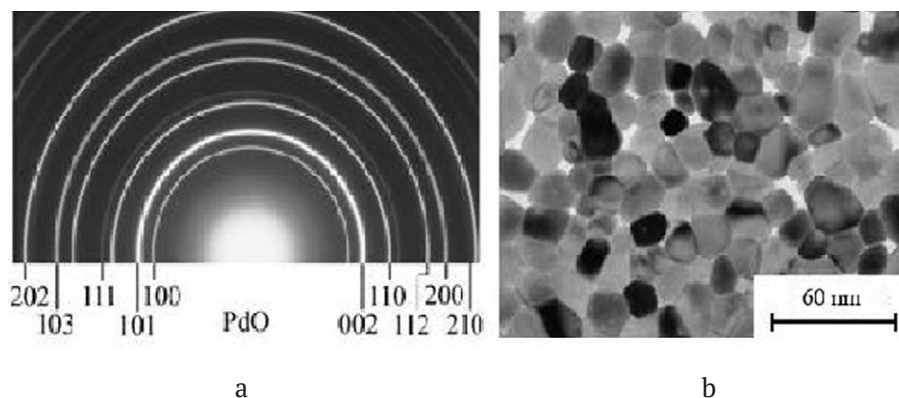


Fig. 1. Reflection high-energy electron diffraction pattern (a) and a bright field TEM image (b) of single-phase (homogeneous) nanocrystalline PdO films obtained by oxidation of the initial ultradispersed palladium layers in atmospheric air at $T_{\text{ox}} = 873$ K

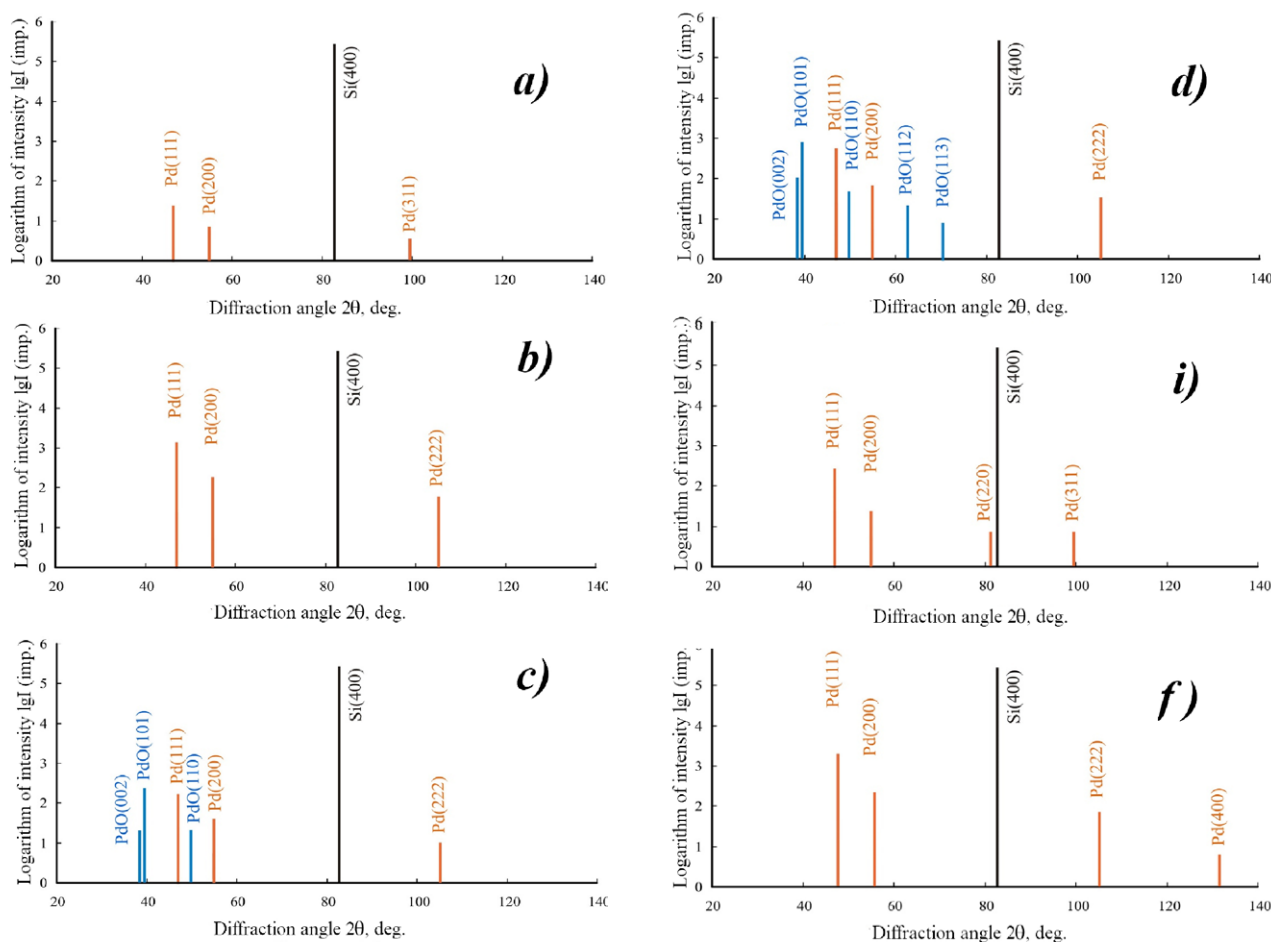


Fig. 2. X-ray diffraction patterns of samples synthesised by oxidation of ultradispersed films of metallic Pd on SiO₂/Si (100) substrates in atmospheric air in the temperature range $T_{ox} = 573 - 1148$ K: a) initial Pd/SiO₂/Si heterostructure; b) $T_{ox} = 573$ K; c) $T_{ox} = 623$ K; d) $T_{ox} = 1098$ K; e) $T_{ox} = 1123$ K; f) $T_{ox} = 1148$ K; CoK α -radiation

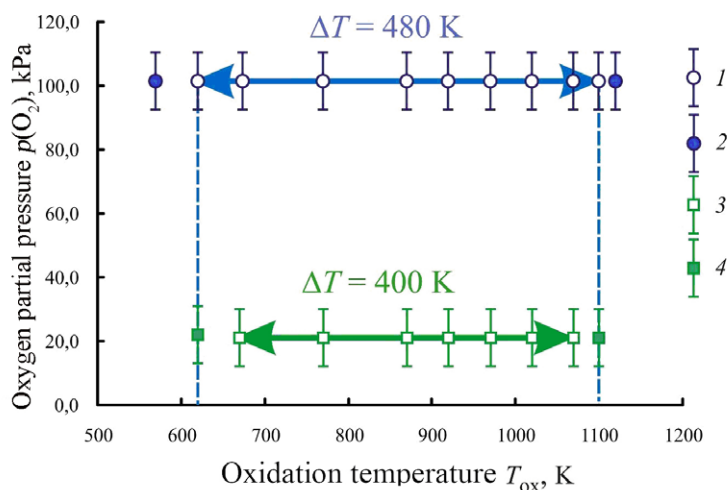


Fig. 3. XRD and RHEED patterns of films obtained by oxidation of the initial ultradispersed layers of metallic Pd on SiO₂/Si (100) substrates in air and in an oxygen atmosphere: 1, 3 – single-phase PdO samples; 2, 4 – heterogeneous samples PdO + Pd; 1, 2 – oxidation in an oxygen atmosphere, data obtained in [18, 19]; 3, 4 – oxidation in air, data obtained in the study

was raised to $T_{\text{ox}} = 1098$ K, heterogeneous samples were formed (Fig. 2d). The diffraction patterns of such samples registered PdO reflections and several metallic Pd reflections. Oxidation in air at $T_{\text{ox}} > 1098$ K results in the complete thermal decomposition of palladium(II) oxide films and the formation of metallic palladium (Fig. 2e and f).

Fig. 3 presents a comparison of the experimental results obtained in our study with the results presented in [18, 19] regarding the phase state of ultradispersed Pd films after oxidation in an oxygen atmosphere. The figure shows that the results obtained in this study are in qualitative agreement with the data presented in [18, 19]. There are only quantitative differences. For instance, homogeneous PdO films were formed after oxidation in an O_2 atmosphere [18, 19] at $T_{\text{ox}} = 623$ K, while during the oxidation in air homogeneous PdO samples were obtained only at $T_{\text{ox}} = 673$ K (Fig. 3). In our study, we also determined that thermal decomposition of homogeneous PdO layers in air followed by the formation of metallic Pd occurs at lower temperatures as compared to oxidation in oxygen. When oxidised in air, heterophase PdO + Pd layers were formed at $T_{\text{ox}} = 1098$ K, while when oxidised in an oxygen atmosphere, thermal decomposition of homogeneous palladium(II) oxide films was only registered at $T_{\text{ox}} = 1123$ K (Fig. 3).

Therefore, we can say that replacing oxygen with atmospheric air for the oxidation process results in a significant reduction (by about 80 K) in the range of oxidation temperatures ensuring the formation of homogeneous PdO films. Taking into account the fact that Pd does not react with nitrogen in the studied temperature range [30], we can say that the oxidation process of Pd resulting in the formation of PdO is largely affected by the partial pressure of oxygen (Fig. 3).

Based on the diffraction patterns of the Pd/SiO₂/Si (100) samples after thermal oxidation in air, we calculated the parameters of the tetragonal crystal lattice of palladium(II) oxide. The comparison of the calculations with the results obtained in [18, 19] is presented in Fig. 4.

Fig. 4 shows that nanocrystalline PdO films on SiO₂/Si(100) substrates demonstrated non-monotonic change in the parameters of the tetragonal crystal lattice depending on the

oxidation temperature. Non-monotonic change in parameters a and c of the tetragonal crystal lattice was registered for PdO films obtained by oxidation both in air and in an oxygen atmosphere (Fig. 4). When the oxidation temperature was increased to $T_{\text{ox}} \sim 973$ K, we observed a monotonous increase in parameters a and c of the tetragonal crystal lattice of single-phase PdO films regardless of the oxidation atmosphere. Further increase in the oxidation temperature at $T_{\text{ox}} > 973$ K was followed by a decrease in the a and c parameters of the tetragonal crystal lattice (Fig. 4). The sharpest decrease in the parameters a and c was registered at $T_{\text{ox}} > 1073$ K.

Despite the similarity of curves $a = f(T_{\text{ox}})$ and $c = f(T_{\text{ox}})$ of PdO films synthesised by means of oxidation of the initial ultradispersed palladium layers in air and in an oxygen atmosphere, there are some quantitative differences. Fig. 4 shows that in order to determine the differences we compared the results of this study and the ones obtained in [18, 19] with the latest data from an international crystallographic database [28]. The figure demonstrates that there are temperature ranges, in which parameters a and c of the tetragonal crystal lattice of nanosized PdO films are larger than those of the reference sample presented in the international crystallographic database [28].

Fig. 4a demonstrates that it is especially noticeable for the parameter a of the tetragonal crystal lattice of palladium(II) oxide films. At the same time, the range of such temperatures for the samples oxidised in an oxygen atmosphere ($\Delta T_{\text{ox}} = 773\text{--}1073$ K) is significantly larger than that of the samples oxidised in air ($\Delta T_{\text{ox}} = 923\text{--}1073$ K). We also calculated the absolute increase in the parameter Δa using the following formula:

$$\Delta a = a_{\text{exp}} - a_{\text{ref}}, \quad (3)$$

where a_{exp} is the experimental value; a_{ref} is the reference value of the ASTM sample.

For the films synthesised in oxygen, parameter Δa was almost three times larger than that of the samples oxidised in air.

Fig. 4b demonstrates that parameter c of the tetragonal crystal lattice of palladium(II) oxide films oxidised in air is lower than that of the ASTM standard sample [28]. At the same time, according to [18, 19], parameter c of the tetragonal crystal

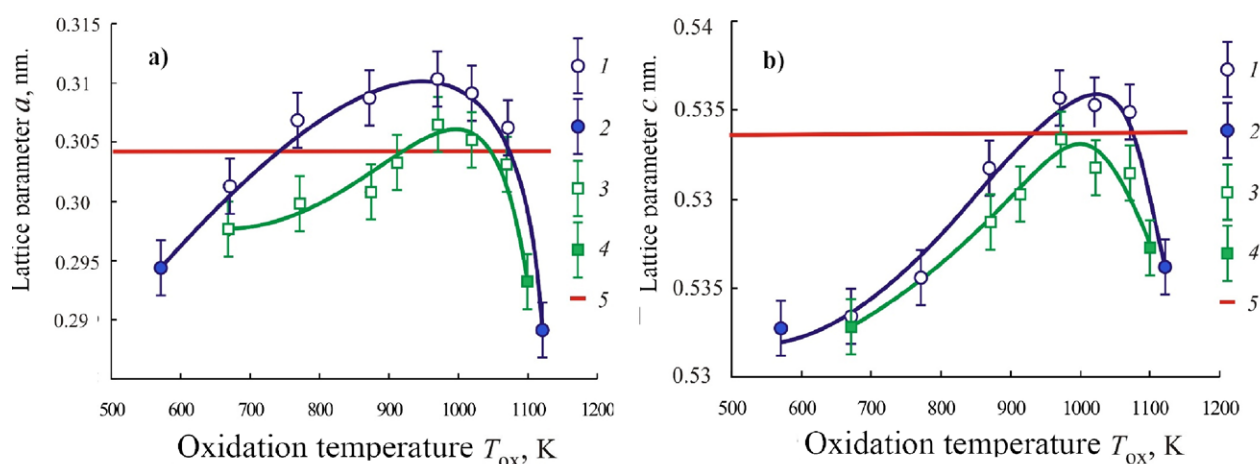


Fig. 4. Dependence of the a and c parameters of the tetragonal crystal lattice of nanosized PdO films synthesised by oxidation of the initial ultradispersed layers of metallic Pd on SiO₂/Si (100) substrates in air and in an oxygen atmosphere on the oxidation temperature T_{ox} : 1, 3 – single-phase PdO samples; 2, 4 – heterogeneous samples PdO + Pd; 1, 2 – oxidation in an oxygen atmosphere, data obtained in [18, 19]; 3, 4 – oxidation in air, data obtained in the study; 5 – ASTM reference sample [28]

lattice of palladium(II) oxide films oxidised in an O₂ atmosphere is higher than the ASTM standard parameter in the range of oxidation temperatures $T_{ox} = 923\text{--}1073$ K.

Therefore, we can say that the distortion of the tetragonal crystal lattice of palladium(II) oxide films obtained by oxidation in air, as compared to the ASTM standard [28], occurs mainly due to an increase in parameter a (Fig. 4a).

In this work, the values of the ratio of the c/a parameters were calculated for a more accurate estimate of the contribution of changes in the a and c parameters to the overall picture of deformation phenomena in the tetragonal lattice of nanocrystalline PdO films. It is known that the c/a ratio is a parametric feature of crystals of the middle category and it reflects the degree of anisotropy of the crystal structure and a number of physical properties.

The change in the c/a values for nanocrystalline PdO films depending on the oxidation temperature T_{ox} is presented in Fig. 5. As the figure shows, the c/a values for all single-phase nanocrystalline PdO films obtained by oxidation in oxygen in the temperature range of $600\text{ K} < T_{ox} < 1050\text{ K}$ [18, 19] are significantly lower than the value calculated for the reference sample from the ASTM database [28]. On the contrary, the c/a values of heterogeneous samples (PdO + Pd) are higher than the similar value of the reference sample.

For the homogeneous PdO films obtained by oxidation in air, the c/a values are higher than the value calculated for the reference sample only in a limited temperature range of $923\text{ K} < T_{ox} < 1050\text{ K}$ (Fig. 5). When oxidised at low temperatures of $673\text{ K} < T_{ox} < 873\text{ K}$ in air, the c/a values were almost the same as the reference.

Curve $c/a = f(T_{ox})$ presented in Fig. 5 demonstrates a flat minimum in the temperature range $800 < T_{ox} < 850\text{ K}$ for PdO films obtained by oxidation in oxygen. For nanocrystalline PdO samples synthesised by oxidation in air, the minimum on curve $c/a = f(T_{ox})$ shifted to higher temperatures $T_{ox} \sim 973\text{ K}$ (Fig. 5).

We should also note that nanosized PdO films obtained by oxidation in an O₂ atmosphere [18, 19] demonstrated greater deformation of the tetragonal lattice as compared to the reference sample in the ASTM database [28] than the samples obtained by oxidation in air (Fig. 5). This is reflected in the absolute values of the change in the parametric ratio $c/a = f(T_{ox})$ as well as in an increase in the range of oxidation temperatures in which the distortions were registered (Fig. 5).

The behaviour of the $c/a = f(T_{ox})$ curves of nanosized PdO films regardless of the synthesis conditions is another evidence proving that an increase in the parameters of the tetragonal lattice of nanocrystalline PdO films is not

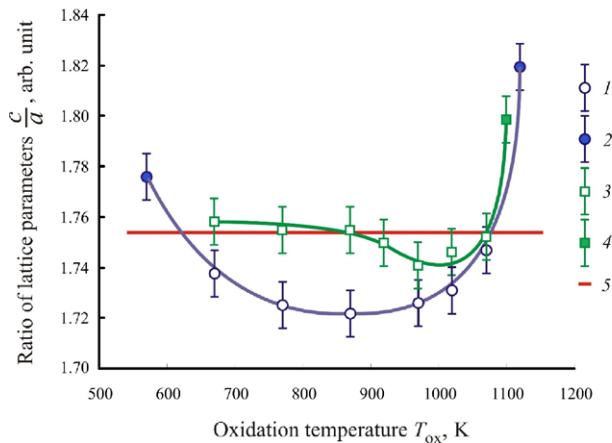


Fig. 5. Dependence of the c/a ratio of the tetragonal crystal lattice of nanosized PdO films synthesised by oxidation of the initial ultradispersed layers of metallic Pd on SiO_2/Si (100) substrates in air and in an oxygen atmosphere on the oxidation temperature T_{ox} : 1, 3 – single-phase PdO samples; 2, 4 – heterogeneous samples PdO + Pd; 1, 2 – oxidation in an oxygen atmosphere, data obtained in [18, 19]; 3, 4 – oxidation in air, data obtained in the study; 5 – ASTM reference sample [28]

uniform. The main contribution to the distortions of the tetragonal crystal structure of palladium(II) oxide occurs mainly due to an increase in the values of the a parameter, which is due to an increase in elementary translations along the Ox and Oy axes.

The above analysis of the transformations of the tetragonal structure of nanocrystalline PdO films depending on the oxidation temperature, demonstrated that the distortion is not uniform mainly due to an increase in the parameter a . This analysis needs to be complemented with the calculations of the unit cell volume of the crystal structure of palladium(II) oxide. Such calculations allow assessing the average degree of distortion of the tetragonal structure of nanocrystalline PdO films.

Based on the experimental data (Fig. 3), we calculated the unit cell volume V_{uc} of the tetragonal structure of nanocrystalline PdO films using the formula:

$$V_{\text{uc}} = a^2c, \quad (4)$$

where V_{uc} – is the unit cell volume; a and c – are parameters of the tetragonal crystal lattice of palladium(II) oxide.

The results of the calculations and their comparison with the data obtained in [18, 19] are given in Fig. 6 as a dependence $V_{\text{uc}} = f(T_{\text{ox}})$. As the figure shows, the unit cell volume V_{uc} of the crystal structure of single-phase nanocrystalline PdO films monotonously grows with an increase in the oxidation temperature from $T_{\text{ox}} = 673$ K to $T_{\text{ox}} = 973$ K regardless of the oxidation atmosphere. The maximum values of V_{uc} are found in the temperature range of $950 < T_{\text{ox}} < 980$ K. At the same time, in the temperature range of $T_{\text{ox}} = 773$ – 1073 K the values of the unit cell volume V_{uc} for PdO films synthesised in oxygen atmosphere exceed the volume of the ASTM reference unit cell [28]. For PdO films obtained by oxidation in air, the range of temperatures in which V_{uc} exceeds the V_{uc} of the reference sample is far below $T_{\text{ox}} = 873$ – 1050 K.

The values of the X-ray density were calculated for a fuller picture of the analysis of the deformations in the structure of nanocrystalline PdO films. The X-ray density $\rho_{\text{Xray}}(\text{PdO})$ was calculated using the formula:

$$\rho_{\text{Xray}}(\text{PdO}) = \frac{2M(\text{PdO})}{V_{\text{uc}} \cdot N_A}, \quad (5)$$

where $M(\text{PdO})$ – is the molar mass of palladium(II) oxide; V_{uc} – is the unit cell volume; N_A – is Avogadro number.

The results calculated using formula (5) for the samples obtained by oxidation in air are presented in Fig.7 as dependence $\rho_{\text{Xray}}(\text{PdO}) = f(T_{\text{ox}})$ in comparison with the data obtained earlier [18, 19]. The figure shows that the values of $\rho_{\text{Xray}}(\text{PdO})$ of PdO films synthesised by oxidation in both oxygen and air monotonously decrease with an increase in the oxidation temperature up to a minimum of $T_{\text{ox}} \sim 970$ K. We should note that the maximum values of density $\rho_{\text{Xray}}(\text{PdO})$ were obtained for heterogeneous samples (PdO + Pd) synthesised at $T_{\text{ox}} = 573$ K and $T_{\text{ox}} = 1123$ K respectively [18, 19].

Comparison of the calculated dependences $\rho_{\text{Xray}}(\text{PdO}) = f(T_{\text{ox}})$ with that of the ASTM reference sample (Fig. 7) demonstrated that homogeneous nanocrystalline PdO films obtained by oxidation in air in the temperature range of $970 < T_{\text{ox}} < 1050$ are characterised by densities lower than those of the reference sample [28]. Minimum values of the X-ray density of PdO samples synthesised

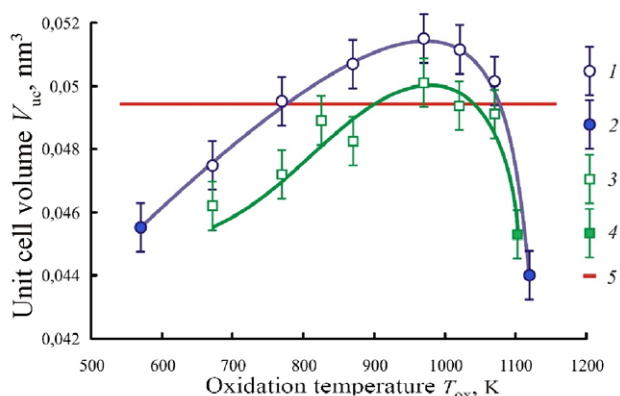


Fig. 6. Dependence of the unit cell volume V_{uc} of the tetragonal crystal lattice of nanocrystalline PdO films synthesised by oxidation of the initial ultradispersed layers of metallic Pd on SiO₂/Si (100) substrates in air and in an oxygen atmosphere on the oxidation temperature T_{ox} : 1, 3 – single-phase polycrystalline PdO samples; 2, 4 – heterogeneous samples (PdO + Pd); 1, 2 – oxidation in an oxygen atmosphere, data obtained in [18, 19]; 3, 4 – oxidation in air, data obtained in the study; 5 – ASTM reference sample [28]

in an O₂ atmosphere were registered in a much larger temperature range of $770 < T_{ox} < 1070$ K. Nanocrystalline PdO films synthesised at lower temperatures ($570 < T_{ox} < 770$), as well as at $T_{ox} > 1070$ K are characterised by a higher X-ray density as compared to the ASTM reference sample [28].

Fig. 7 also shows the density of polycrystalline $\rho(\text{PdO})$ powders of palladium(II) oxide determined by means of hydroscopic weighing [30]. The figure demonstrates that the $\rho_{Xray}(\text{PdO})$ of the ASTM reference sample and $\rho(\text{PdO})$ determined by means of hydroscopic weighing are close to each other.

When analysing the nature of deformations of homogeneous nanocrystalline PdO films (Fig. 4–7), we should point out that the degree of distortion of the crystal lattice of homogeneous nanocrystalline PdO films depends more on the oxidation atmosphere rather than the temperature. The maximum deformation of the tetragonal lattice was observed in PdO films obtained by oxidation in oxygen with the value of partial pressure $p(\text{O}_2) \sim 101\text{--}103$ kPa (Fig. 3).

When discussing the obtained results, it is necessary to take into account the fact that PdO samples are characterised by p-type conductivity [12, 15, 17], which, from the point of view of solid

state chemistry, is explained by the presence of negatively charged interstitial atoms of oxygen. Incorporation of excess oxygen atoms (with regard to the stoichiometric ratio of PdO) confirms a decrease in the density caused by an increase in the portion of a lighter component - oxygen. Therefore, taking into account the unit cell model of palladium(II) oxide suggested in [18], possible ways of incorporation of oxygen atoms into the crystal lattice of palladium(II) oxide are given in Fig. 8.

It is also known [30] that palladium can form compounds with the oxidation state (+4). Palladium(IV) oxide is characterised by a crystal structure of the rutile type TiO₂. The palladium-oxygen coordination number is 6, and the coordination polyhedron is an octahedron. Therefore, oxygen atoms can be incorporated between neighbouring palladium atoms in the crystal structure of palladium(II) oxide as shown in Fig. 8.

Taking into account the unit cell model of palladium(II) oxide [18], interstitial oxygen atoms should be located in the octahedral void in the centre of the cell with coordinates $\left[\begin{matrix} 1 & 1 & 1 \\ 2 & 2 & 2 \end{matrix} \right]$.

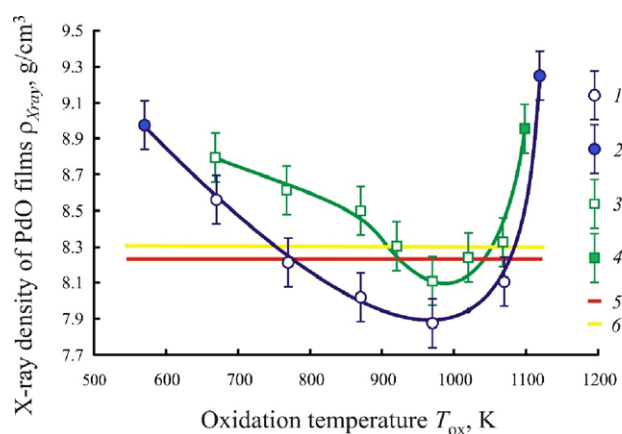


Fig. 7. Dependence of the X-ray density of nanocrystalline PdO films synthesised by oxidation of the initial ultradispersed layers of metallic Pd on SiO₂/Si (100) substrates in air and in an oxygen atmosphere on the oxidation temperature T_{ox} : 1, 3 – single-phase polycrystalline PdO samples; 2, 4 – heterogeneous samples (PdO + Pd); 1, 2 – oxidation in an oxygen atmosphere, data obtained in [18, 19]; 3, 4 – oxidation in air, data obtained in the study; 5 – ASTM reference sample [28]; 6 – data obtained by means of hydrostatic weighing [30]

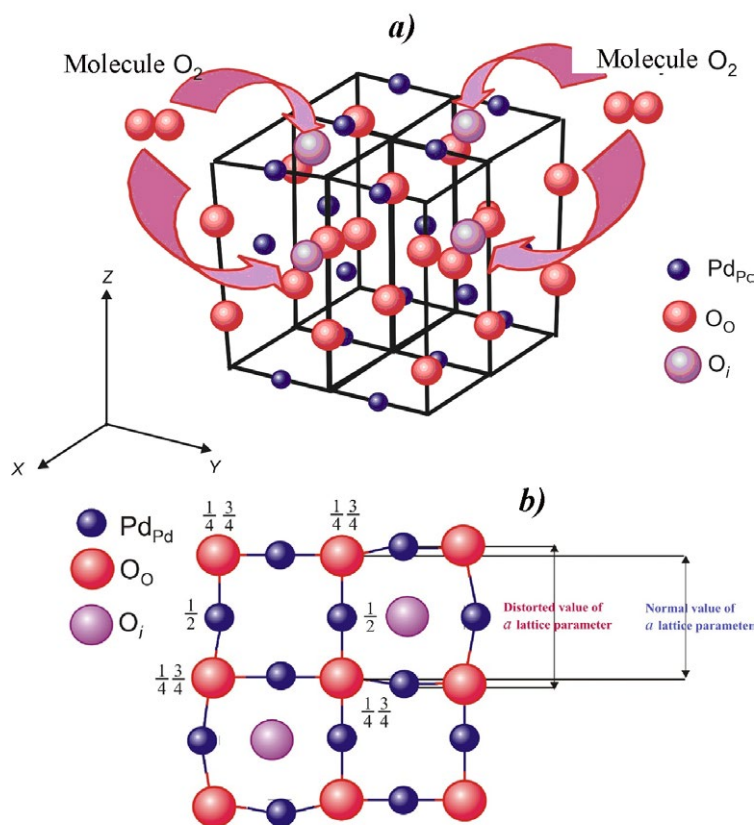


Fig. 8. A scheme explaining the deformations in the tetragonal crystal structure of nanocrystalline PdO films by the incorporation of interstitial oxygen atoms: a) a spatial 3D model of four unit cells of the crystal lattice of palladium(II) oxide; b) a projection of four unit cells of PdO on the plane XOY

4. Conclusions

1. The XRD and RHEED analyses determined that the oxidation of the initial ultradispersed layers of metallic palladium in air results in the formation of homogeneous polycrystalline films of palladium(II) oxide on SiO₂/Si (100) substrates in the temperature range $T_{ox} = 673\text{--}1073$ K. The temperature range is significantly wider, when the oxidation is conducted in an oxygen atmosphere.

2. Based on the calculation of the changes in the parameter ratio of the tetragonal lattice of nanocrystalline PdO films, we demonstrated that the distortions of the crystal lattice are mainly due to an increase in the value of parameter a .

3. The study demonstrated that the degree of distortion of the crystal lattice of homogeneous nanocrystalline PdO films depends on the oxidation atmosphere rather than on the temperature. The maximum deformation of the tetragonal lattice was observed in PdO films obtained by oxidation in oxygen with the value of partial pressure $p(O_2) \sim 101\text{--}103$ kPa.

4. The article suggested a model which explains the distortions in the tetragonal lattice of nanocrystalline films of palladium(II) oxide by the incorporation of excess oxygen atoms into interstitial sites of the unit cell, preferably into the octahedral void in the centre of the cell with coordinates $\left[\left[\frac{1}{2} \frac{1}{2} \frac{1}{2}\right]\right]$.

Contribution of the authors

The authors contributed equally to this article.

Conflict of interests

The authors declare that they have no known competing financial interests or personal relationships that could have influenced the work reported in this paper.

References

1. Yamazoe N. Toward innovations of gas sensor technology. *Sensors and Actuators B*. 2005;108: 2–14. <https://doi.org/10.1016/j.snb.2004.12.075>

2. Seiyama T., Kato A., Fujiishi K., Nagatani M. A new detector for gaseous components using semiconductive thin films. *Analytical Chemistry*. 1962;34: 1502–1503. <https://doi.org/10.1021/ac60191a001>
3. Marikutsa A. V., Rumyantseva M. N., Gaskov A. M., Samoylov A. M. Nanocrystalline tin dioxide: Basics in relation with gas sensing phenomena. Part I. Physical and chemical properties and sensor signal formation. *Inorganic Materials*. 2015;51(13): 1329–1347. <https://doi.org/10.1134/S002016851513004X>
4. Ong C. B., Ng L. Y., Mohammad A. W. A review of ZnO nanoparticles as solar photocatalysts: synthesis, mechanisms and applications. *Renewable and Sustainable Energy Reviews*. 2018;81: 536–551. <https://doi.org/10.1016/j.rser.2017.08.020>
5. Korotcenkov G. Metal oxides for solid-state gas sensors: What determines our choice? *Materials Science and Engineering: B*. 2007; 139: 1–23. <https://doi.org/10.1016/j.mseb.2007.01.044>
6. Marikutsa A. V., Rumyantseva M. N., Gaskov A. M., Samoylov A. M. Nanocrystalline tin dioxide: Basics in relation with gas sensing phenomena. Part II. Active centers and sensor behavior. *Inorganic Materials*. 2016;52(13): 1311–1338. <https://doi.org/10.1134/S0020168516130045>
7. Al-Hashem M., Akbar S., Morris P. Role of oxygen vacancies in nanostructured metal-oxide gas sensors: a review. *Sensors Actuators B*. 2019;301: 126845. <https://doi.org/10.1016/j.snb.2019.126845>
8. Korotcenkov G. *Handbook of gas sensor materials. Properties, advantages and shortcomings for applications. Volume 1: Conventional approaches*. Springer: New York Heidelberg Dordrecht London; 2013. 442 p. <https://doi.org/10.1007/978-1-4614-7165-3>
9. Toda K., Furue R., Hayami S. Recent progress in applications of graphene oxide for gas sensing: A review. *Analytica Chimica Acta*. 2015;878: 43–53. <https://doi.org/10.1016/j.aca.2015.02.002>
10. Kim H.-J., Lee J.-H. Highly sensitive and selective gas sensors using *p*-type oxide semiconductors: Overview. *Sensors and Actuators B*. 2014;192: 607–627. <https://doi.org/10.1016/j.snb.2013.11.005>
11. García-Serrano O., López-Rodríguez C., Andraca-Adame J. A., Romero-Paredes G., Pena-Sierra R. Growth and characterization of PdO films obtained by thermal oxidation of nanometric Pd films by electroless deposition technique. *Materials Science and Engineering B*. 2010;174: 273–278. <https://doi.org/10.1016/j.mseb.2010.03.064>
12. Ryabtsev S. V., Ievlev V. M., Samoylov A. M., Kushev S. B., Soldatenko S. A. Microstructure and electrical properties of palladium oxide thin films for oxidizing gases detection. *Thin Solid Films*. 2017;636: 751–759. <https://doi.org/10.1016/j.tsf.2017.04.009>
13. Ryabtsev S. V., Shaposhnik A. V., Samoylov A. M., Sinelnikov A. A., Soldatenko S. A., Kushev S. B., Ievlev V. M. Thin films of palladium oxide for gas sensors. *Doklady Physical Chemistry*. 2016;470(2): 158–161. <https://doi.org/10.1134/s0012501616100055>
14. Ryabtsev S. V., Ievlev V. M., Samoylov A. M., Kushev S. B., Soldatenko S. A. Real microstructure and electrical properties of palladium oxide thin films for oxidizing gases detecting. In: *Science and Application of Thin Films, Conference & Exhibition (SATF-2016) Çeşme, Izmir, Turkey, September 19–23, 2016. Book of Abstracts: Izmir Institute of Technology*. 2016: 44.
15. Ievlev V. M., Ryabtsev S. V., Shaposhnik A. V., Samoylov A. M., Kushev S. B., Sinelnikov A. A. Ultrathin films of palladium oxide for oxidizing gases detecting. *Procedia Engineering*. 2016;168: 1106–1109. <https://doi.org/10.1016/j.proeng.2016.11.357>
16. Samoylov A. M., Gvarishvili L. J., Ivkov S. A., Pelipenko D. I., Badica P. Two-stage synthesis of pPalladium (II) oxide nanocrystalline powders for gas sensor application. *Research & Development in Material Science*. 2018;8(2). <https://doi.org/10.31031/rdms.2018.08.000682>
17. Ievlev V. M., Ryabtsev S. V., Samoylov A. M., Shaposhnik A. V., Kushev S. B., Sinelnikov A. A. Thin and ultrathin of palladium oxide for oxidizing gases detection. *Sensors and Actuators B*. 2018;255(2): 1335–1342. <https://doi.org/10.1016/j.snb.2017.08.121>
18. Samoylov A. M., Ivkov S. A., Pelipenko D. I., ... Badica P. Structural changes in palladium nanofilms during thermal oxidation. *Inorganic Materials*. 2020;56(10): 1020–1026. <https://doi.org/10.1134/s0020168520100131>
19. Samoylov A. M., Pelipenko D. I., Kuralenko N. S. Calculation of the nonstoichiometry area of nanocrystalline palladium (II) oxide films. *Condensed Matter and Interphases*. 2021;23(1): 62–72. <https://doi.org/10.17308/kcmf.2021.23/3305>
20. Samoylov A. M., Ryabtsev S. V., Popov V. N., Badica P. Palladium (II) oxide nanostructures as promising materials for gas sensors. In: *Novel nanomaterials synthesis and applications*. (George Kyzas ed.). UK, London: IntechOpen Publishing House; 2018. p. 211–229. <https://doi.org/10.5772/intechopen.72323>
21. Ryabtsev S. V., Ghareeb D. A. A., Sinelnikov A. A., Turishchev S. Yu., Obvintseva L. A., Shaposhnik A. V. Ozone detection by means of semiconductor gas sensors based on palladium (II) oxide. *Condensed Matter and Interphases*. 2021;23(1): 56–61. <https://doi.org/10.17308/kcmf.2021.23/3303>
22. Ryabtsev S. V., Ghareeb D. A. A., Turishchev S. Yu., Obvintseva L. A., Shaposhnik A. V., Domashevskaya E. P. Structural and gas-sensitive characteristics of thin semiconductor PdO films of various thicknesses during ozone detection. *Semiconductors*. 2022;56(13): 2057–2062. <https://doi.org/10.21883/SC.2022.13.53898.9684>

23. Samoylov A. M., Pelipenko D. I., Ivkov S. A., Tyulyakova E. S., Agapov B. L. Thermal stability limit of thin palladium(II) oxide films. *Inorganic Materials*. 2022;58(1): 48–55. <https://doi.org/10.1134/S0020168522010095>

24. Choudhury S., Bettya C. A., Bhattacharyya K., Saxenab V., Bhattacharya D. Nanostructured PdO thin film from Langmuir–Blodgett precursor for room temperature H₂ gas sensing. *ACS Applied Materials & Interfaces*. 2016;8(26): 16997–17003. <https://doi.org/10.1021/acsami.6b04120>

25. Yang S., Li Q., Li C., ... Fu Y. Enhancing the hydrogen-sensing performance of p-type PdO by modulating the conduction model. *ACS Appl. Mater. Interfaces*. 2021;13: 52754–52764. <https://doi.org/10.1021/acsami.1c13034>

26. *Phase diagrams of binary metal systems: Handbook: in 3 volumes**. Lyakishev N. P. (ed.) Moscow: Metallurgy Publ.; 1996–2000. (In Russ.)

27. Hammond C. *The basics of crystallography and diffraction*. Fourth edition. International union of crystallography. Oxford University Press; 2015. 519 p.

28. *ASTM JCPDS - International Centre for Diffraction Data*. 1987–2009. JCPDS-ICDD. Newtown Square, PA 19073. USA.

29. Grier D., McCarthy G., North Dakota: State University, Fargo, N. Dakota, USA, ICDD Grant-in-Aid, JCPDS-ICDD, 1991. Card no. 43-1024.

30. Wiberg, E., Wiberg, N., Holleman, A. F. *Inorganic Chemistry*. 1st English Edition. San Diego: Academic Press; Berlin, New York: De Gruyter, USA; 2001. 1884 p.

* Translated by author of the article.

Information about the authors

Alexander M. Samoïlov, Dr. Sci. (Chem.), Associate Professor, Professor at the Department of Materials Science and Industry of Nanosystems, Voronezh State University (Voronezh, Russian Federation).

<https://orcid.org/0000-0003-4224-2203>
samoylov@chem.vsu.ru

Stanislav S. Kopytin, postgraduate student, Department of Materials Science and Industry of Nanosystems, Voronezh State University (Voronezh, Russian Federation).

<https://orcid.org/0000-0001-9353-0219>
kopytin-stanislav@rambler.ru

Sergey A. Ivkov, PhD (Phys.-Math.), Leading Electronics Engineer, Department of Solid State Physics and Nanostructures, Voronezh State University (Voronezh, Russian Federation).

<https://orcid.org/0000-0003-1658-5579>
ivkov@phys.vsu.ru

Egor A. Ratkov, master degree student, Voronezh State University (Voronezh, Russian Federation).

<https://orcid.org/0009-0005-6848-1773>
ratkov1511@gmail.com

Evgeny A. Tutov, Dr. Sci. (Chem.), Associate Professor, Department of Physics, Voronezh State Technical University (Voronezh, Russian Federation).

<https://orcid.org/0000-0002-5481-8137>
tutov_ea@mail.ru

Received 12.12.2022; approved after reviewing 10.01.2023; accepted for publication 15.02.2023; published online 25.06.2023

Translated by Yulia Dymant

Edited and proofread by Simon Cox



Original articles

Research article

<https://doi.org/10.17308/kcmf.2023.25/11110>

Phase relations in the Si–Sn–As system

T. P. Sushkova✉, G. V. Semenova, E. Yu. Proskurina

¹Voronezh State University,
1 Universitetskaya pl., Voronezh 394018, Russian Federation

²Voronezh State Technical University,
84 20 letiya Oktyabrya st., Voronezh, 394006, Russian Federation

Abstract

The goal of this work was to study phase relations in the ternary Si–Sn–As system: to establish cross sections, to construct a scheme of phase equilibria, and to identify the temperature of non-variant transformations.

Ternary alloys were obtained through direct synthesis from simple substances and subjected to long-term solid-phase annealing. Alloys of four polythermal sections of the Si–Sn–As system were examined using X-ray phase and differential thermal analysis. The results of X-ray powder diffraction allowed establishing that the phase subsolidus demarcations was performed by the SnAs–SiAs₂, SnAs–SiAs, Sn₄As₃–SiAs, and Sn₄As₃–Si sections.

As a result of the experiment, taking into account the theoretical analysis, we suggested a scheme of phase equilibria in the system that involved the implementation of eutectic and four peritectic invariant equilibria, and we used differential thermal analysis to determine the temperature of these four-phase transformations.

It was found that extended solid solutions were not formed in the system, and only a substitutional solid solution at least 3 mol % wide was formed based along the SnAs–SiAs₂ section based on tin monoarsenide.

Keywords: Phase diagram, Polythermal section, Si–Sn–As ternary system

Acknowledgements: X-ray powder diffraction studies were performed using the equipment of the VSU Centre for Collective Use of Scientific Equipment.

For citation: Sushkova T. P., Semenova G. V., Proskurina E. Yu. Phase relations in the Si–Sn–As system. *Condensed Matter and Interphases*. 2023;25(2): 237–248. <https://doi.org/10.17308/kcmf.2023.25/11110>

Для цитирования: Сушкова Т. П., Семенова Г. В., Проскурина Е. Ю. Фазовые отношения в системе Si–Sn–As. *Конденсированные среды и межфазные границы*. 2023;25(2): 237–248. <https://doi.org/10.17308/kcmf.2023.25/11110>

✉ Tatiana P. Sushkova, e-mail: sushtp@yandex.ru

© Sushkova T. P., Semenova G. V., Proskurina E. Yu., 2023



1. Introduction

Compounds of the $A^{IV}B^V$ class in the form of bulk single and polycrystals have been actively studied since the 1970s, and the Department of General and Inorganic Chemistry of Voronezh State University also performed such studies [1–4]. Although some of these compounds possess semiconductor properties and electrophysical characteristics that are practically important, they had not been put to good use for a long time. This is mainly associated with the fact that many $A^{IV}B^V$ compounds have a layered structure and can stratify into flakes when crystals are cut and ground, which was considered a significant drawback in the era of wide use of diamond-like semiconductors.

Over the past 20 years, due to the rapid development of 2D technologies, researchers have again turned their attention to this class of compounds. Silicon and germanium monpnictides form a family of two-dimensional layered semiconductors with a possibility of changing the width of the band gap through the variation of the number of layers [5–8]. They can also be used as catalysts and materials for optoelectronic devices [9–11]. The peeling energy of silicon and germanium arsenides and phosphides can be compared to this value for graphene, which suggests a high probability of their successful production using mechanical peeling from bulk crystals [5, 6].

Bulk crystals of $A^{IV}B^V$ compounds also have practical importance as they are capable of interlayer introduction reactions. Tin and silicon arsenides $SnAs$, Sn_4As_3 , $SiAs_2$, and $SiAs$ are suitable materials for the creation of electrodes of alkali-ion batteries [12–14]. For example, Li_2SiAs_2 has a calculated band gap of 1.4 eV, low thermal conductivity at room temperature, and high electrical resistivity, and therefore it is highly promising as a lithium-ion conductor with lithium-ion conductivity at room temperature of $7 \mu\Omega/cm$ [13].

Functional properties of the material can be improved to some extent through doping and the use of solid solutions instead of pure compounds. From this point of view, it is important to study the phase diagrams of multicomponent systems formed by the elements of the IVA and VA groups. The phase diagrams of $A^{IV}-B^V-C^V$ systems with anionic substitution have been studied better

as compared to the diagrams of the systems with cationic substitution [15, 16]. There are no publications on the state diagram of the Si–Sn–As system, which explains the relevance of this work.

The goal of this work was theoretical analysis and experimental study of phase relations in a ternary Si–Sn–As system: establishing cross sections, constructing a scheme of phase equilibria, and identifying the temperature of non-variant transformations.

2. Experimental

2.1. Methods for Sample Synthesis

Due to the high melting point of silicon, which cannot be reached upon synthesis in quartz tubes, as well as the duration of the solid phase reaction and considerable vapour pressure of arsenic at high temperatures, the experimental study of the phase diagram of Si–Sn–As becomes a challenging process.

The samples with the compositions belonging to four polythermal sections of the $SnAs-SiAs_2$, $SnAs-SiAs$, $SnAs-Si$, and $SiAs-Sn$ ternary system were obtained by synthesis in a single zone furnace from simple substances in quartz ampoules vacuumed to the residual pressure of $5 \cdot 10^{-4}$ GPa. KEF 4.5/0.1–43.5 silicon, OVCH-000, and OSCH-9-5 arsenic were used for the synthesis. Arsenic was preliminary purified from oxides using vacuum sublimation. The weighing was performed on AR2140 electronic scales with the measurement error $\pm 1 \cdot 10^{-3}$ g.

Maximum temperature of the furnace heating upon synthesis was 1353 K, which is lower than the melting point of silicon (1683 K). To ensure the possibility of the heterogeneous reaction, the samples were held for six hours at 1353 K and after the synthesis they were subject to solid phase annealing for 250 hours at 753 K (the alloys of the SiAs–Sn section rich in tin were annealed at 473 K).

To make sure that the temperature and the duration of synthesis and annealing are enough for the silicon to react, a binary alloy was prepared in similar conditions, the composition of which $Si_{0.48}As_{0.52}$ corresponded to the eutectic mixture of $SiAs_2$ and $SiAs$ in the Si–As binary system. Peaks of silicon monoarsenide and diarsenide were observed on an X-ray diffraction pattern of this alloy while there were now silicon peaks. Therefore, the temperature and duration of synthesis and

annealing are enough for silicon to react completely in the conditions of our experiment.

2.2. Methodology of X-ray diffraction and differential thermal analysis

The alloys were studied using X-ray diffraction analysis (XRD) and differential thermal analysis (DTA).

X-ray phase analysis was performed using an ARL X'TRA diffractometer with Bragg–Brentano Θ – Θ focusing geometry. The source of radiation was an X-ray tube with a copper anode: $\lambda(\text{Cu-}K_{\alpha 1}) = 0.1541 \text{ nm}$; $\lambda(\text{Cu-}K_{\alpha 2}) = 0.1544 \text{ nm}$. The X-ray patterns were made with a step size of 0.04° and a counting time of 3 seconds per step. The determination error for the interplanar distances d_{hkl} was below $5 \cdot 10^{-4} \text{ nm}$. Parameters of the lattice of the phases were calculated using High Score Plus-305 program and specified using the Pauli principle.

Differential thermal analysis was performed on a DTA device with the programmed furnace heating with a heating rate 5 K/min (7 K/min for the most refractory samples). Heat treated chromel–alumel thermocouples and aluminium oxide were used as a reference. The signal received from the thermocouples was digitized and processed by the MasterSCADA software package. The determination error for the temperature of phase transformations was below $\pm 1 \text{ K}$. The alloys of the studied system had a tendency to overcool, therefore the temperature of phase transitions was determined by the heating curves. In cases where the peak corresponding to the liquidus on a thermogram was stretched and fuzzy, the temperature was determined by the cooling curve with a correction for the overcooling value.

3. Results and discussion

3.1. Results of an X-ray study and a scheme of phase equilibria in a ternary system

As we were studying the Si–Sn–As ternary system for the first time, it was necessary to analyse the possibility of its separation into subsystems using cross sections.

Two intermediate compounds were formed in the Si–As binary system: silicon monoarsenide that had a monoclinic crystal lattice and melted congruently at a temperature of 1386 K, and silicon diarsenide with an orthorhombic lattice,

which decomposed according to the peritectic scheme into SiAs and a melt at 1250 K [17]. Silicon monoarsenide was a one-sided phase shifted towards silicon, while the stoichiometric composition practically coincided with the right border of the homogeneity region. The width of the homogeneity region of SiAs was 0.45 mol % at 1300 K [4,15]. Arsenic dissolves well in silicon, and the maximum solid phase solubility is about 3.5 mol % As at $\sim 1473 \text{ K}$ [17].

In the Sn–As system, two intermediate phases were also formed [18]: tin monoarsenide with a crystal lattice of the NaCl type and Sn_4As_3 which melted congruently at 868 K and crystallised in the trigonal non-centrosymmetrical space group $R\bar{3}m$, while the selected unit cell could be either rhombohedral or hexagonal [19]. Sn_4As_3 had a pronounced homogeneity region ($\sim 3 \text{ mol } \%$) directed towards the excess of tin [18]. In the Si–Sn system [20] there were no intermediate compounds, and a degenerate eutectic near tin was observed with a temperature of 231.9°C , which was similar to the melting point of pure tin. Tin slightly dissolved in silicon, and the maximum solid phase solubility was 0.1 mol % achieved at a temperature of 1339 K.

Therefore, due to the nature of the melting of intermediate phases and the presence of visible regions of homogeneity in some of them, only subsolidus phase separation was possible. Figure 1 shows four possible options for the division of a ternary system by cross sections (below the solidus) into subsystems, each of which had three solid phases coexisting in equilibrium.

Arsenic can participate in equilibria with the closest phases SnAs and SiAs_2 , which means that a part of the concentration triangle with As the apex is separated in the only possible way. As an example, Figure 2a shows the X-ray powder diffraction spectrum of an alloy of the SnAs– SiAs_2 section alloy containing 20 mol % SiAs_2 . Peaks of silicon diarsenide and tin monoarsenide were observed, and the intensity of the peaks of the second phase were higher as it prevailed in this alloy. It should be noted that the $(\text{SnAs})_{0.97}(\text{SiAs}_2)_{0.03}$ sample was single-phase, while $((\text{SnAs})_{0.93}(\text{SiAs}_2)_{0.07})$ was a two-phase sample, which probably indicated the formation of a solid solution based on SnAs with a range of at least 3 mol % along the SnAs– SiAs_2 section.

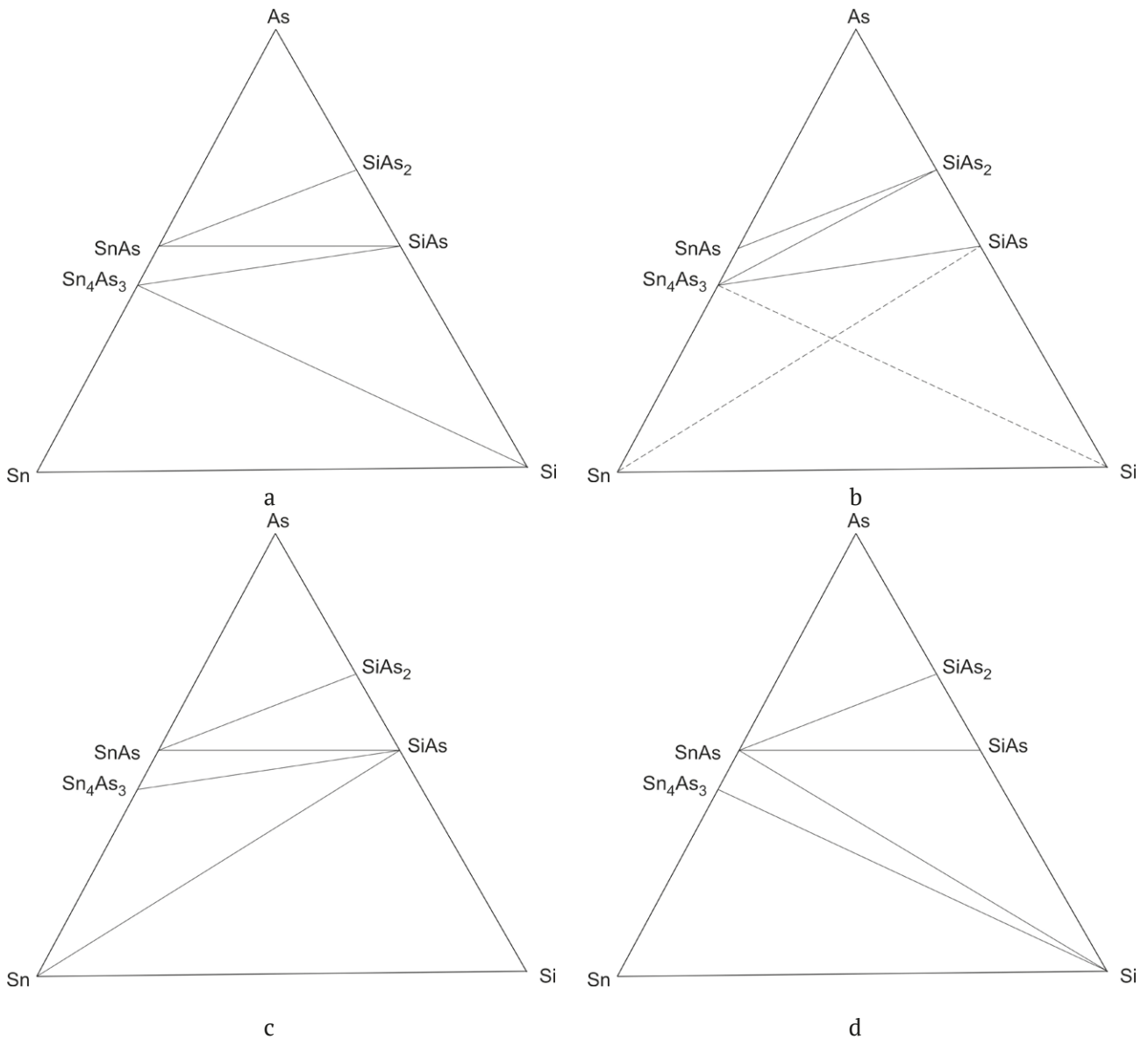


Fig. 1. Schemes of phase equilibria in the Si–Sn–As ternary system

Table 1 shows the cubic lattice parameter (a) and unit cell volume (V) of the SnAs phase which is present in the alloys of the polythermal section SnAs–SiAs₂. Parameters of the lattice were calculated using High Score Plus-305 program and specified using the Pauli principle. Both the lattice parameter and the cell volume were slightly decreased as compared to the data for tin monoarsenide presented in the powder X-ray diffraction catalogue (PDF2-2012 database). This indicated the formation of a solid substitution solution (tin atoms were replaced by smaller silicon atoms). The parameters of the orthorhombic SiAs₂ lattice differed very little from the reference values.

The Sn₄As₃–SnAs–SiAs₂–SiAs trapezium could be divided into triangles corresponding to the equilibrium of three solid phases using two methods: the SnAs–SiAs cross section (Fig. 1a) or the Sn₄As₃–SiAs₂ cross section (Fig. 1b). If the second scheme is correct, the alloys whose compositions belong to the SnAs–SiAs section and are to the right of the crossing point with the Sn₄As₃–SiAs₂ section should not contain tin monoarsenide and should contain Sn₄As₃. X-ray phase analysis showed that, on the contrary, SnAs was present in these alloys, while Sn₄As₃ was not, therefore, the scheme presented in Fig. 1b had to be excluded from consideration.

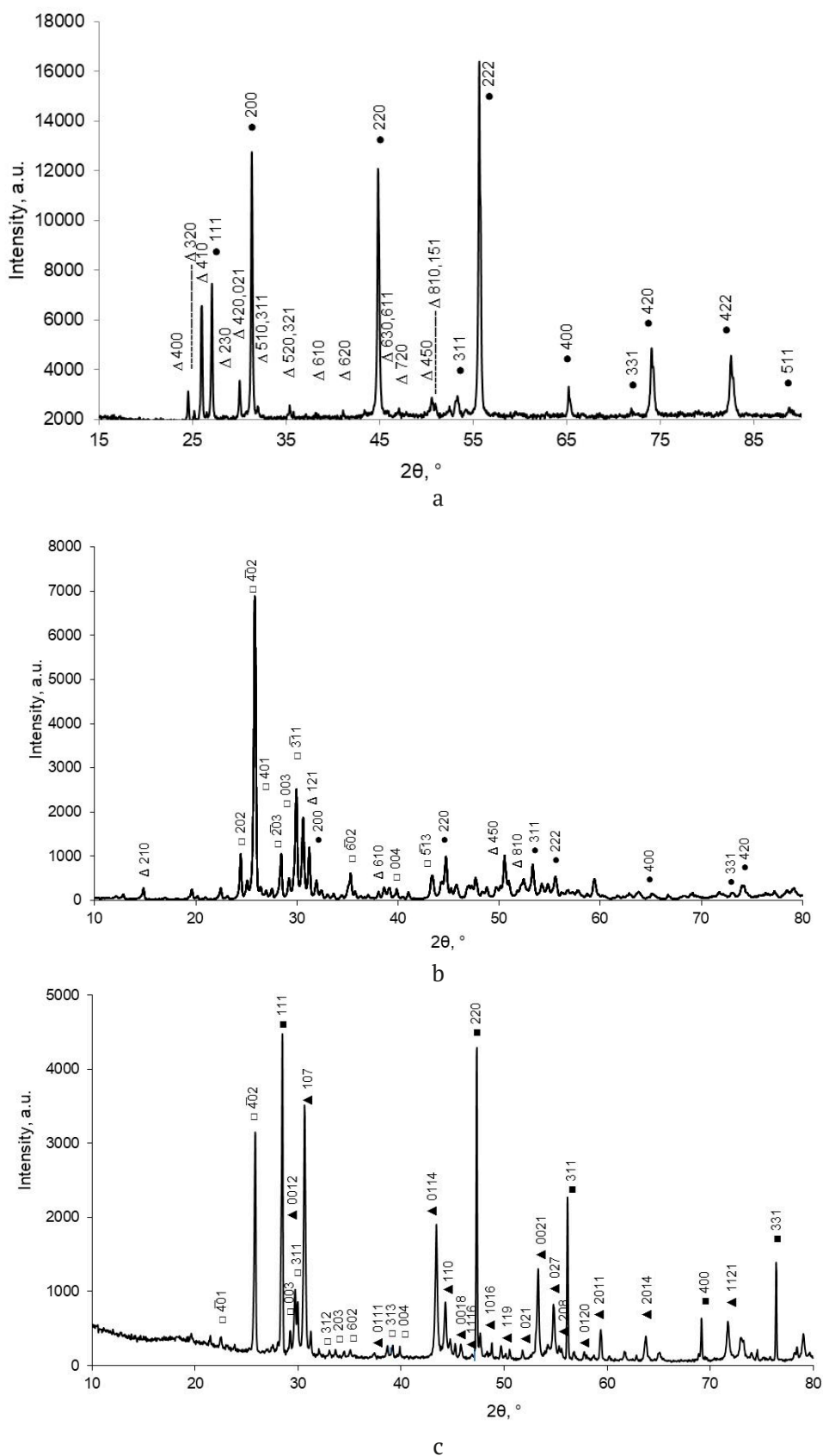


Fig. 2. X-ray powder diffraction patterns of the Si–Sn–As system: a – $(\text{SnAs})_{0.8}(\text{SiAs}_2)_{0.2}$; b – $(\text{SnAs})_{0.4}(\text{SiAs})_{0.6}$; c – $(\text{SnAs})_{0.8}\text{Si}_{0.2}$. Phase symbols: ■ – Si, ● – SnAs, □ – SiAs, Δ – SiAs_2 , ▲ – Sn_4As_3

Table 1. Lattice parameter and unit cell volume of tin monoarsenide present in the alloys of the SnAs–SiAs₂ section

PDF2 data		Composition of the alloys, mol f., SiAs ₂				
SnAs		0.03	0.07	0.2	0.4	0.6
<i>a</i> , Å	5.7248	5.7245	5.7206	5.7225	5.7217	5.7212
<i>V</i> /10 ⁶ pm ³	187.621	187.591	187.208	187.391	187.315	187.268

The cubic phase of SnAs did not have many peaks but almost all of them were observed on diffraction patterns. Fig. 2b shows an X-ray diffraction spectrum of an alloy (SnAs)_{0.4}(SiAs)_{0.6}. Apart from the SnAs and SiAs peaks, several peaks of tin diarsenide could be observed. This is how we explain this fact: the process of crystallisation of the (SnAs)_{0.4}(SiAs)_{0.6} alloy ended at point P₂ (Fig. 3), which corresponded to the four-phase peritectic transformation L + SiAs₂ ↔ SnAs + SiAs. Apparently, the duration of synthesis and annealing was insufficient for this transformation to be fully completed, and there was a certain amount of unreacted silicon diarsenide left. The lattice parameter of tin monoarsenide present in the alloys with the SnAs–SiAs cross section and calculated using XRD data was slightly different from the reference value; the parameters *a* and *b* of the SiAs monoclinic lattice were slightly increased, while the parameter *c* was slightly decreased (Table 2). It can be concluded that the solid-phase solubility along the SnAs–SiAs section was very low.

The Sn–SnAs–SiAs–Si trapezium could be divided into triangles that corresponded to the equilibrium of three solid phases using three

methods (Fig. 1a, c, d). If option (c) is correct, the SiAs–Sn cross section separates silicon, and silicon should not be identified in alloys with the compositions in the concentration triangle (in the plane of the figure, to be precise) located above this cross section. If option (a) is correct, SnAs should not be identified in the alloys with the compositions in the concentration triangle located below the Sn₄As₃–SiAs cross section. The most informative solution to this problem was the study of the samples of the SnAs–Si cross section.

For example, we detected silicon in the (SnAs)_{0.8}Si_{0.2} alloy by XRD, and its peaks were dominating (Fig. 2c), which makes the scheme presented in Fig. 1c incorrect. To choose between schemes (a) and (d), we must examine in more detail the paths of alloy crystallisation of the SnAs–Si polythermal section. Figure 3 shows two possible schemes of phase equilibria in a ternary system, corresponding to situations (a) and (d) in Fig. 1. The crystallisation processes proceeded similarly according to both schemes in the range of compositions rich in arsenic. The field of primary crystallisation of arsenic was limited by monovariant curves e₃P₁ and e₁P₁ along which the eutectic processes L → As + SnAs and

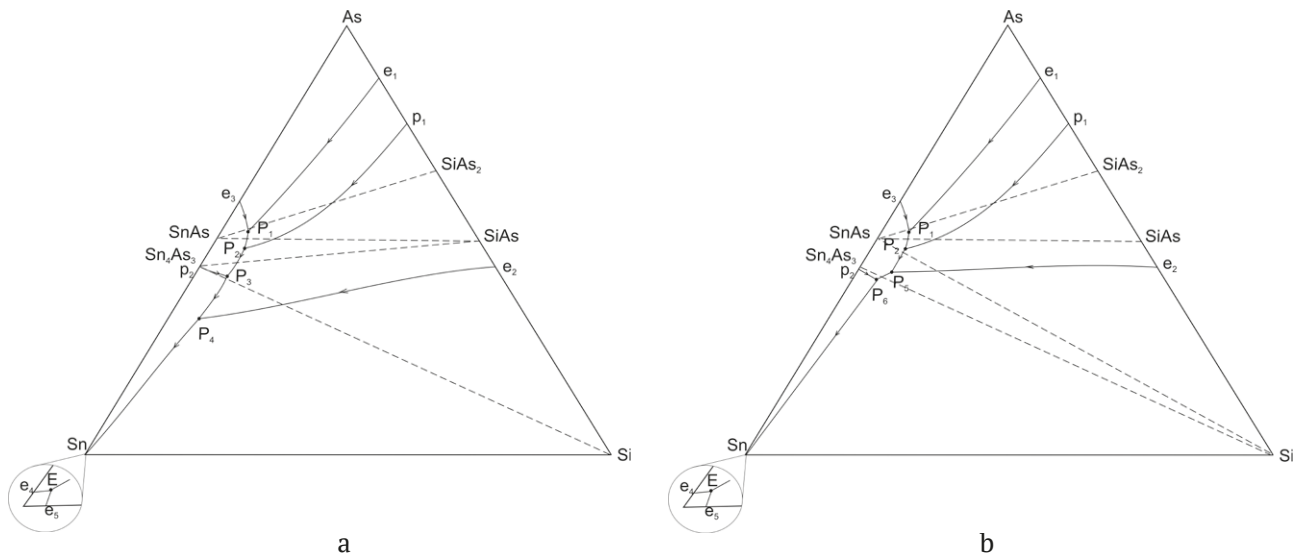

Fig. 3. Schemes of phase equilibria in the Si–Sn–As ternary system

Table 2. Lattice parameters of silicon monoarsenide present in the alloys of the SnAs–SiAs section

PDF2 data		Composition of the alloys, mol f., SiAs				
SiAs		0.2	0.3	0.4	0.6	0.8
<i>a</i> , Å	15.97	15.979	15.980	15.976	15.977	15.979
<i>b</i> , Å	3.668	3.670	3.672	3.669	3.667	3.666
<i>c</i> , Å	9.529	9.520	9.526	9.527	9.526	9.526
β°	106.0	106.1	106.1	106.0	106.0	106.0

$L \rightarrow \text{As} + \text{SiAs}_2$ occurred, respectively. The four-phase peritectic equilibrium $L + \text{As} \leftrightarrow \text{SnAs} + \text{SiAs}_2$ corresponded to point P_1 .

The peritectic process $L + \text{SiAs} \leftrightarrow \text{SiAs}_2$ occurred along the p_1P_2 curve, while the eutectic process $L \rightarrow \text{SnAs} + \text{SiAs}_2$ proceeded along the P_1P_2 curve. Curves e_1P_1 , P_1P_2 , and p_1P_2 limited the field of primary crystallisation of silicon diarsenide. The peritectic point P_2 corresponded to the invariant equilibrium $L + \text{SiAs}_2 \leftrightarrow \text{SnAs} + \text{SiAs}$.

Further processes were different for the two schemes. First, we will consider the option presented in Fig. 3a. Point P_3 corresponded to the four-phase equilibrium with the participation of the melt and solid phases $\text{SnAs} + \text{SiAs} + \text{Sn}_4\text{As}_3$, and it was also peritectic, as it was located outside the triangle connecting the compositions of solid phases coexisting in equilibrium. The $L \rightarrow \text{SiAs} + \text{SnAs}$ process proceeded along the P_2P_3 curve. The p_2P_3 curve separated the primary crystallisation fields of SnAs and Sn_4As_3 .

The P_3P_4 curve separated the primary crystallisation fields of the Sn_4As_3 and SiAs phases. The eutectic process $L \rightarrow \text{SiAs} + \text{Si}$ proceeded along the e_2P_4 line and along the P_4E line: $L \rightarrow \text{Sn}_4\text{As}_3 + \text{Si}$. Point P_4 corresponds to the peritectic process $L + \text{SiAs} \rightarrow \text{Sn}_4\text{As}_3 + \text{Si}$. Point E was located inside the triangle of solid phases and corresponded to the eutectic equilibrium $L \rightarrow \text{Sn}_4\text{As}_3 + \text{Si} + \text{Sn}$. It was degenerate, as the eutectics e_4 and e_5 in binary systems were degenerate.

In the second scheme (Fig. 3b), point P_5 corresponded to the non-variant peritectic process $L + \text{SiAs} \rightarrow \text{SnAs} + \text{Si}$, while point P_6 corresponded

to the peritectic process $L + \text{SnAs} \rightarrow \text{Sn}_4\text{As}_3 + \text{Si}$. The processes similar to the first scheme occurred with a further decrease of temperature (Fig. 3a).

We will consider a possible sequence of crystallisation processes for the $(\text{SnAs})_{0.8}\text{Si}_{0.2}$ alloy in accordance with the first scheme. The figurative point of the melt was located in the field of primary crystallisation of SiAs. Once silicon monoarsenide crystals were separated from the melt, secondary crystallisation occurred along the P_3P_4 curve, and the crystallisation process was completed at point P_4 : $L + \text{SiAs} \rightarrow \text{Sn}_4\text{As}_3 + \text{Si}$. According to the second scheme (Fig. 3b), the $(\text{SnAs})_{0.8}\text{Si}_{0.2}$ composition was in the field of primary silicon crystallisation, and once silicon was separated, the process occurred along the e_2P_5 line and completed with the peritectic process $L + \text{SiAs} \rightarrow \text{SnAs} + \text{Si}$.

Clear intense peaks of silicon and Sn_4As_3 were observed on the diffraction pattern of the $(\text{SnAs})_{0.8}\text{Si}_{0.2}$, while peaks of tin monoarsenide were absent (Fig. 2c). Similar diffraction patterns were also obtained for samples of the SnAs–Si cross section that were richer in silicon, and only the intensity of the peaks changed. This allowed stating that the correct scheme is the one presented in Figs. 1a and 3a, according to which the subsolidus phase separation was performed by the SnAs– SiAs_2 , SnAs–SiAs, Sn_4As_3 –SiAs, and Sn_4As_3 –Si. sections. The lattice parameter of silicon present in the alloys of the section varied within the range of experimental error and without any patterns. The calculated parameters of the rhombohedral lattice of Sn_4As_3 in a hexagonal device (Table 3) also did not allow

Table 3. Lattice parameters of the Sn_4As_3 phase present in the alloys of the SnAs–Si section

PDF2 data		Composition of the alloys, mol f., Si					
Sn_4As_3		0.1	0.2	0.3	0.4	0.6	0.8
<i>a</i> , Å	4.089(1)	4.088	4.086	4.086	4.090	4.078	4.088
<i>c</i> , Å	36.059(6)	36.081	36.0174	36.006	36.140	36.120	36.119

drawing a conclusion that a solid solution of any significant range was formed based on this compound.

We also studied several alloys of the SiAs–Sn polythermal section which did not participate in the subsolidus phase separation. This section crossed the Sn_4As_3 –Si cross section, therefore the alloys with low and high tin content participated in different equilibria. X-ray phase analysis showed the presence of Sn_4As_3 , Si, and SiAs phases in the $(\text{SiAs})_{0.8}\text{Sn}_{0.2}$ alloy (Fig. 4a), and Sn_4As_3 , Si, and Sn phases in the $(\text{SiAs})_{0.4}\text{Sn}_{0.6}$ alloy (Fig. 4b). This indicated that the process of crystallisation of the first alloy ended at point P_4 , while the crystallisation of the second alloy ended at point E (Fig. 3a).

3.2. Results of differential thermal analysis of alloys. Determining the temperatures of four-phase transformations

In this work, differential thermal analysis was performed primarily to determine the temperature of four-phase equilibrium. It was impossible to plot T-x diagrams of polythermal cross sections and the projection of the liquidus surface of the ternary system using experimental data only, as the maximum heating temperature (1273 K) was limited both by the technical properties of the furnace and by the risk of depressurisation of Stepanov's quartz ampoules at high temperatures and arsenic vapour pressure. Therefore, liquidus was not achieved for all samples in the course of DTA.

Figure 5 shows thermograms of some alloys selected so that the temperature of the

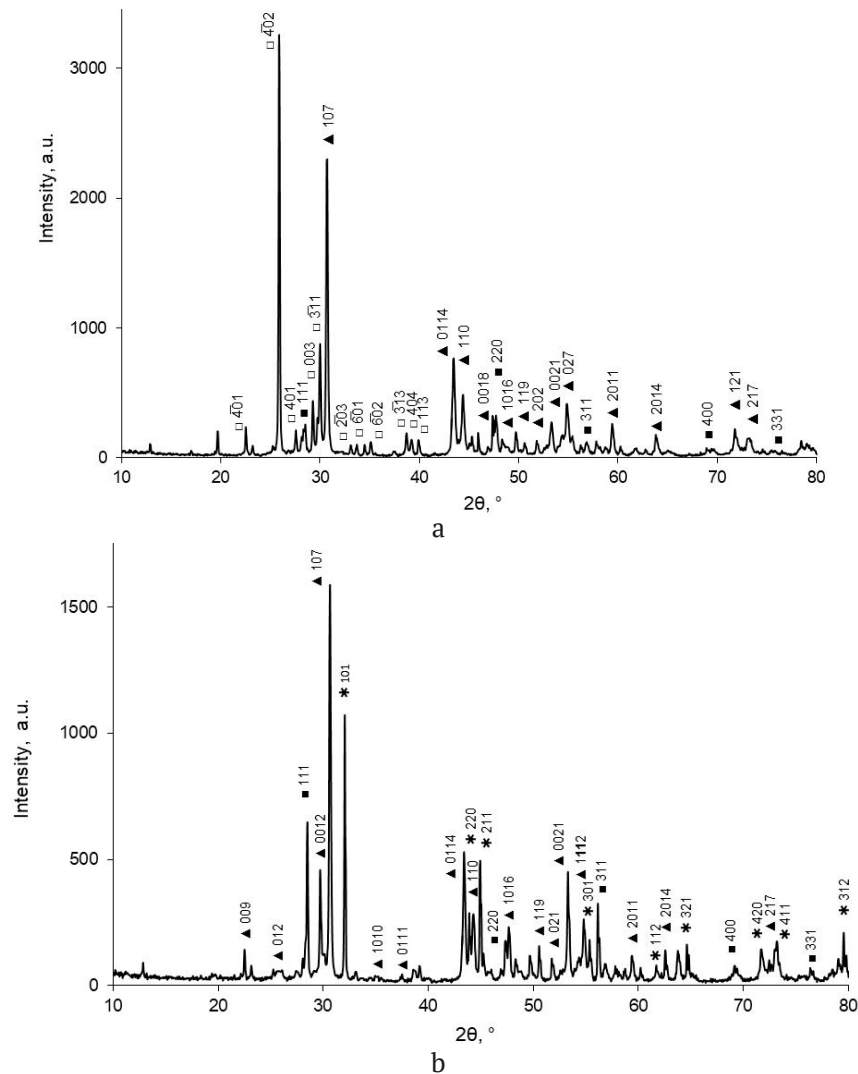


Fig. 4. X-ray powder diffraction patterns of the Si–Sn–As system: a – $(\text{SiAs})_{0.8}\text{Sn}_{0.2}$; b – $(\text{SiAs})_{0.4}\text{Sn}_{0.6}$. Phase symbols: ■ – Si, * – Sn, □ – SiAs, ▲ – Sn_4As_3

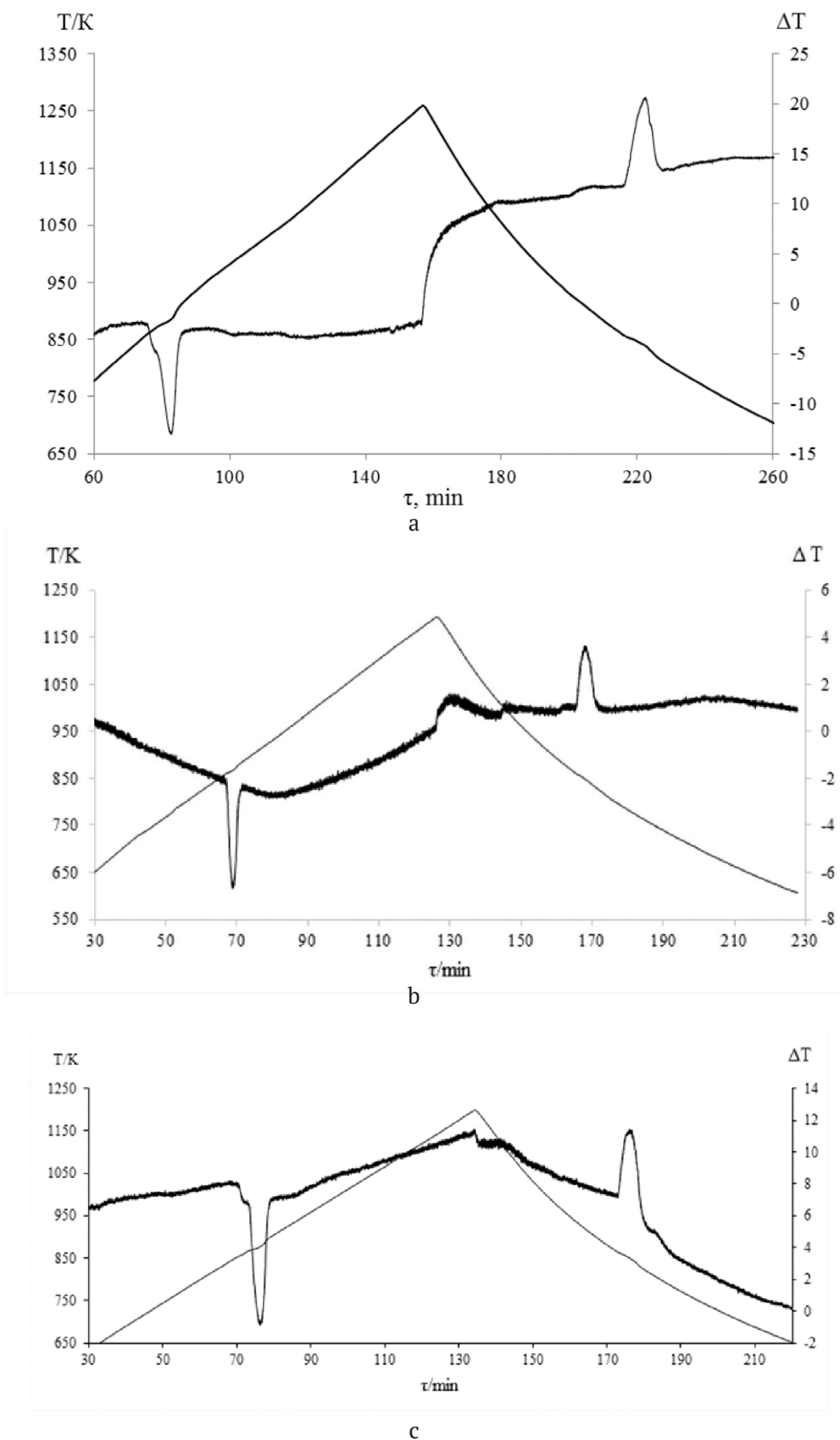
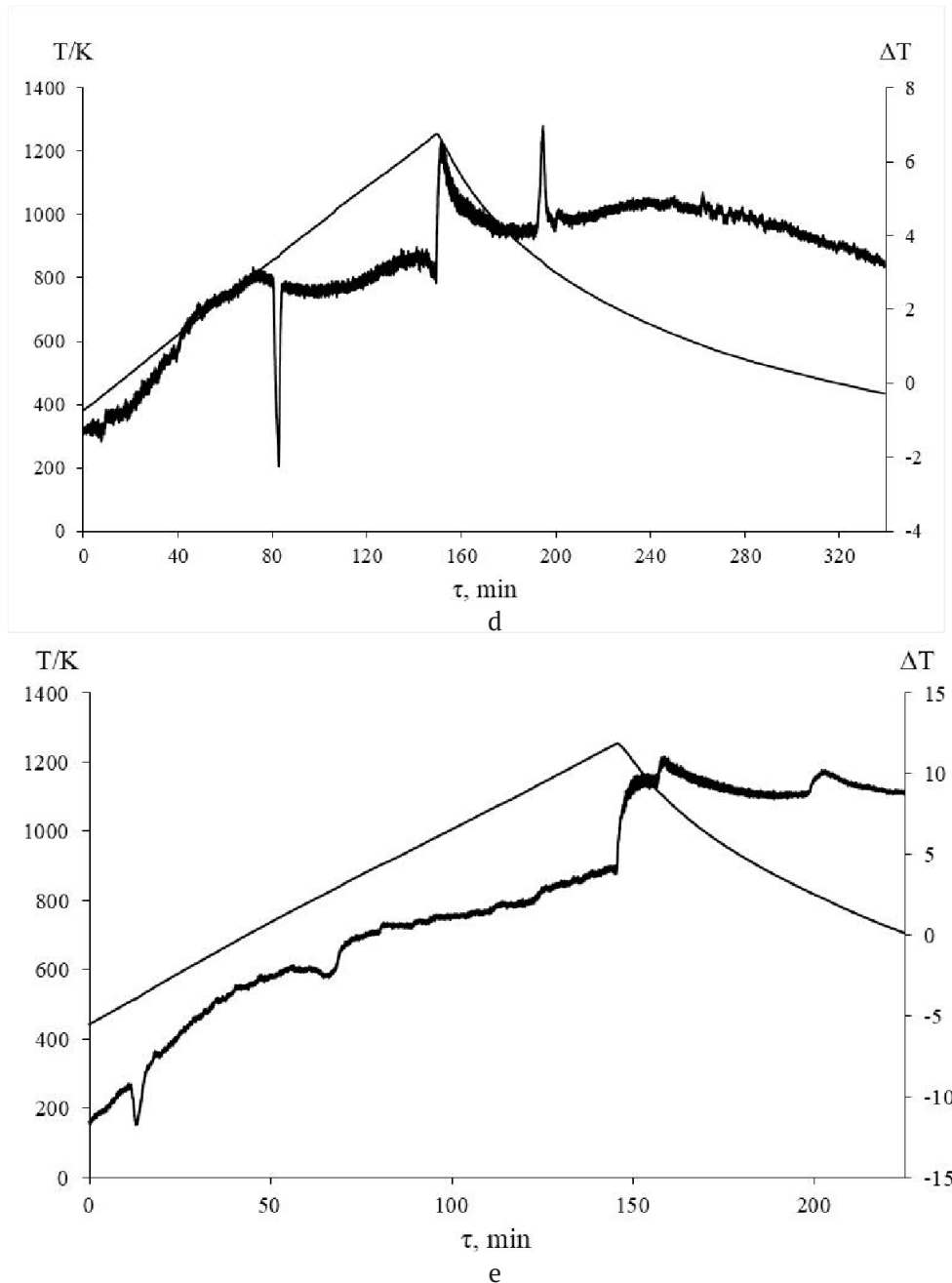


Fig. 5. Thermograms of alloys: a – $(\text{SnAs})_{0.8}(\text{SiAs}_2)_{0.2}$; b – $(\text{SnAs})_{0.4}(\text{SiAs})_{0.6}$; c – $(\text{SnAs})_{0.9}\text{Si}_{0.1}$; d – $(\text{SiAs})_{0.9}\text{Sn}_{0.1}$; e – $(\text{SiAs})_{0.4}\text{Sn}_{0.6}$



End of fig. 5

beginning of the first effect on the heating curve corresponded to the temperature of a certain four-phase invariant equilibrium. For instance, the crystallisation process ended at point P_1 for samples of the SnAs–SiAs₂ section, whose compositions were located to the left of the intersection point of this section with the p_1P_2 curve (Fig. 3a), On the thermogram of the alloy containing 20 mol. % silicon diarsenide, the temperature of the beginning of the first effect was 850 ± 1 K (Fig. 5a), and this temperature

corresponded to the four-phase process $L + As \leftrightarrow SnAs + SiAs_2$.

As for compositions located to the right of the intersection point of the SnAs–SiAs₂ section and the p_1P_2 curve, as well as for all alloys of the SnAs–SiAs section, crystallisation was completed at point P_2 with the process $L + SiAs_2 \leftrightarrow SnAs + SiAs$. For these alloys, we recorded the temperature of the beginning of the first endoeffect at 847 ± 1 K (Fig. 5b shows the thermogram of the (SnAs)_{0.4}(SiAs)_{0.6} sample).

We determined the temperature of the $L + \text{SnAs} \leftrightarrow \text{SiAs} + \text{Sn}_4\text{As}_3$ (p. P₃) peritectic process by thermography of (SnAs)_{0.9}Si_{0.1} alloy. It was 845±1 K (Fig. 5c).

The temperature of peritectic transformation $L + \text{SiAs} \rightarrow \text{Sn}_4\text{As}_3 + \text{Si}$ (p. P₄) could be determined in the course of a thermographic study of the alloys that are rich in silicon of the SnAs–Si section, as well as of the alloys of the Sn–SiAs section with a high content of silicon monoarsenide. Fig. 5d presents a thermogram of the (SiAs)_{0.9}Sn_{0.1} sample, and the determined temperature of the beginning of the first endoeffect was 840±1 K.

The crystallisation of the alloys of the Sn–SiAs section with a high content of tin ended at p. E (Fig. 3a) The temperature of the corresponding eutectic process $L \rightarrow \text{Sn}_4\text{As}_3 + \text{Si} + \text{Sn}$ was determined according to the DTA results of the (SiAs)_{0.4}Sn_{0.6} alloy, and it amounted to 503±1 K (Fig. 5e), which is slightly lower than the temperature of tin melting.

4. Conclusions

We used X-ray diffraction analysis and differential thermal analysis to study the phase relations in the Si–Sn–As ternary system. It was established that the phase subsolidus demarcation was performed by the SnAs–SiAs₂, SnAs–SiAs, Sn₄As₃–SiAs, and Sn₄As₃–Si sections. Taking into account the theoretical analysis and XRD results, we suggested a scheme of phase equilibria in the system that presupposed the existence of one eutectic and four peritectic invariant equilibria with the participation of a melt and three solid phases. Differential thermal analysis allowed identifying the temperatures at which these four-phase equilibrium occurred: $L + \text{As} \leftrightarrow \text{SnAs} + \text{SiAs}_2$ (850±1 K); $L + \text{SiAs}_2 \leftrightarrow \text{SnAs} + \text{SiAs}$ (847±1 K); $L + \text{SnAs} \leftrightarrow \text{SiAs} + \text{Sn}_4\text{As}_3$ (845±1 K); $L + \text{SiAs} \rightarrow \text{Sn}_4\text{As}_3 + \text{Si}$ (840±1 K); $L \rightarrow \text{Sn}_4\text{As}_3 + \text{Si} + \text{Sn}$ (503±1 K). According to the X-ray diffraction analysis, the solid phase solubility along the studied sections was very small, and a solid replacement solution with a range of at least 3 mol % was formed only based on tin monoarsenide along the SnAs–SiAs section. Further examination of the Si–Sn–As system presupposes a more detailed study of this issue as well as a construction of T–x diagrams

of polythermal sections and projections of isotherms of the liquidus surface of the ternary system.

Contribution of the authors

The authors contributed equally to this article.

Conflict of interests

The authors declare that they have no known competing financial interests or personal relationships that could have influenced the work reported in this paper.

References

1. Ugai Ya. A., Miroshnichenko S. N., Goncharov E. G. Study of the P - T - x diagram of the Si–As system*. *Inorganic Materials*. 1974;10(10): 1774–1777. (In Russ.). Available at: <https://www.elibrary.ru/item.asp?id=29085699>
2. Ugai Ya. A., Popov A. E., Goncharov E. G., Lukin A. N., Samoilov A. M. Electrophysical properties and homogeneity region of germanium arsenide*. *Inorganic Materials*. 1983;19(2): 190–192. (In Russ.). Available at: <https://www.elibrary.ru/item.asp?id=29095704>
3. Goncharov E. G., Gladyshev N. F., Ugai Ya. A. Physicochemical nature of intermediate phases in the germanium – arsenic system*. *Russian Journal of Inorganic Chemistry*. 1977;22(7): 1951–1956. (In Russ.). Available at: <https://www.elibrary.ru/item.asp?id=29091830>
4. Goncharov E. G., Popov A. E., Zavrazhnov A. Yu. Semiconducting phosphides and arsenides of silicon and germanium. *Inorganic Materials*. (In Russ.). 1995;31(5): 579–591. Available at: <https://www.elibrary.ru/item.asp?id=29113633>
5. Cheng A-Q., He Z., Zhao J., Zeng H., Chen R-Sh. Monolayered silicon and germanium monophenyl semiconductors: excellent stability, high absorbance, and strain engineering of electronic properties. *ACS Applied Materials & Interfaces*. 2018;10(6): 5133–5139. <https://doi.org/10.1021/acsami.7b17560>
6. Zhou L., Guo Y., Zhao J. GeAs and SiAs monolayers: Novel 2D semiconductors with suitable band structures. *Physica E: Low-dimensional Systems and Nanostructures*. 2018;95: 149–153. <https://doi.org/10.1016/j.physe.2017.08.016>
7. Ramzan M. S., Bacic V., Jing Y., Kuc A. Electronic properties of a new family of layered materials from groups 14 and 15: first-principles simulations. *The Journal of Physical Chemistry C*. 2019;123(41): 25470–25476. <https://doi.org/10.1021/acs.jpcc.9b07068>
8. Barreteau C., Michon B., Besnard C., Giannini E. High-pressure melt growth and transport properties of SiP, SiAs, GeP, and GeAs 2D layered semiconductors.

Journal of Crystal Growth. 2016;443(1): 75–80. <https://doi.org/10.1016/j.jcrysgro.2016.03.019>

9. Reddy P. V. S., Kanchana V., Millichamp T. E., Vaitheeswaran G., Dugdale S. B. Enhanced superconductivity in the high pressure phase of SnAs studied from first principles. *Physica B: Condensed Matter*. 2017;505: 33–40. <https://doi.org/10.1016/j.physb.2016.10.026>

10. Ma Z., Zhuang J., Zhang X., Zhou Zh. SiP monolayers: New 2D structures of group IV–V compounds for visible-light photohydrolytic catalysts. *Frontiers of Physics*. 2018;13(138104). <https://doi.org/10.1007/s11467-018-0760-8>

11. Shojaei F., Mortazavi B., Zhuang X., Azizi M. Silicon diphosphide (SiP₂) and silicon diarsenide (SiAs₂): Novel stable 2D semiconductors with high carrier mobilities, promising for water splitting photocatalysts. *Materials Today Energy*. 2020;16(100377). <https://doi.org/10.1016/j.mtener.2019.100377>

12. Kamali A. R., Fray D. J. Tin-based materials as advanced anode materials for lithium ion batteries: a review. *Reviews on Advanced Materials Science*. 2011;27: 14–24. Available at: <https://www.elibrary.ru/item.asp?id=16869557>

13. Kathleen L. *Synthesis and characterization of tetrel pnictides and compounds in the lithium-tetrel-arsenic system*. University of California. Davis ProQuest Dissertations Publishing: 2016. 136 p. Available at: <https://www.proquest.com/openview/6c5577b9817fa2c2864fdeda33e2acfb/1?cbl=18750&diss=y&loginDisplay=true&pq-origsite=gscholar>

14. Woo K. E., Dolyniuk J. A., Kovnir K. Superseding van der Waals with electrostatic interactions: Intercalation of Cs into the interlayer space of SiAs₂. *Inorganic Chemistry*. 2019;58(8): 4997–5005. <https://doi.org/10.1021/acs.inorgchem.9b00017>

15. Semenova G. V., Goncharov E. G. *Solid solutions with the participation of elements of the fifth group**. Moscow: Izd. MFTI Publ.; 2000. 160 p. (In Russ.) Available at: <https://www.elibrary.ru/item.asp?id=25882424>

16. Kononova E. Y., Sinyova S. I., Semenova G. V., Sushkova T. P. Phase equilibria in the Sn–As–Ge and

Sn–As–P systems. *Journal of Thermal Analysis and Calorimetry*. 2014;117(3): 1171–1177. <https://doi.org/10.1007/s10973-014-3883-3>

17. Olesinski R. W., Abbaschian G. J. The As–Si (arsenic-silicon) system. *Bulletin of Alloy Phase Diagrams*. 1985;6(3): 254–258. <https://doi.org/10.1007/BF02880410>

18. Gokcen N. A. The As–Sn (tin-arsenic) system. *Bulletin of Alloy Phase Diagrams*. 1990;11(3): 271–278. <https://doi.org/10.1007/BF03029298>

19. Kovnir K., Kolen'ko Y. V., ... Shevelkov A. V. Sn₄As₃ revisited: Solvothermal synthesis and crystal and electronic structure. *Journal of Solid State Chemistry*. 2009;182(3): 630–639. <https://doi.org/10.1016/j.jssc.2008.12.007>

20. Olesinski R. W., Abbaschian G. J. The Si–Sn (silicon-tin) system. *Bulletin of Alloy Phase Diagrams*; 1984;5: 273–276. <https://doi.org/10.1007/BF02868552>
* Translated by author of the article

Information about the authors

Tatiana P. Sushkova, Cand. Sci. (Chem.), Associate Professor, Department of General and Inorganic Chemistry, Voronezh State University (Voronezh, Russian Federation).

<https://orcid.org/0000-0003-1969-7082>
sushtp@yandex.ru

Galina V. Semenova, Dr. Sc. (Chem.), Full Professor, Department of General and Inorganic Chemistry, Voronezh State University (Voronezh, Russian Federation).

<https://orcid.org/0000-0003-3877-985X>
semen157@chem.vsu.ru

Elena Yu. Proskurina, Cand. Sci. (Chem.), Assistant Lecturer, Department of General and Inorganic Chemistry, Voronezh State University (Voronezh, Russian Federation).

<https://orcid.org/0000-0002-6149-1398>
helko7@yandex.ru

Received 03.10.2022; approved after reviewing 01.11.2022; accepted for publication 15.11.2022; published online 25.06.2023.

Translated by Marina Strepetova
Edited and proofread by Simon Cox



Condensed Matter and Interphases

Kondensirovannye Sredy i Mezhfaznye Granitsy
<https://journals.vsu.ru/kcmf/>

Original articles

Research article

<https://doi.org/10.17308/kcmf.2023.25/11105>

Influence of UV radiation on the catalytic activity of nanosized cobalt ferrite in the oxidative degradation reaction of dinitrophenol

E. V. Tomina^{1,2✉}, Vo Quang Mai³, N. A. Kurkin¹, A. V. Doroshenko¹,
Nguyen Anh Tien⁴, A. A. Sinelnikov¹

¹Voronezh State University,
1 Universitetskaya pl., Voronezh 394018, Russian Federation

²Morozov Voronezh State University of Forestry and Technologies,
8 Timiryazeva ul., Voronezh 394087, Russian Federation

³Sai Gon University,
273 An Duong Vuong Street, Ward 3, District 5, Ho Chi Minh City, Vietnam

⁴Ho Chi Minh City University of Education,
280 An Duong Vuong Street, Ward 4, District 5, Ho Chi Minh City, Vietnam

Abstract

Due to their multi-functionality, spinel ferrites, both doped and undoped, are promising materials for a wide range of practical applications, including catalysis, sustainable production of hydrogen and CO₂ deposition, electronic and magnet devices, as well as antibacterial agents. Recently, nanosized ferrites have been actively tested as catalysts in Fenton-like processes of deep oxidative degradation of organic substances in order to purify waste waters of different dyes, phenol and its derivatives, and antibiotics. The goal of this work was to establish the catalytic activity of CoFe₂O₄ nanopowder synthesised using citrate combustion in the reaction of oxidative degradation of 2,4-dinitrophenol upon the activation of the process with UV radiation.

Using citrate combustion, we synthesised the impurity-free nanopowder of CoFe₂O₄ cobalt ferrite with the average size of particles of about 70 nm and a pronounced agglomeration of particles. The cobalt spinel was tested as a catalyst of Fenton-like reaction of oxidative degradation of 2,4- dinitrophenol with UV radiation of $\lambda = 270$ nm. This process was differentiated with the sorption of dinitrophenol on a nanosized catalyst.

The degree of degradation of 2,4-dinitrophenol in a Fenton-like reaction without the CoFe₂O₄ catalyst was 14 %, while in the presence of a nanosized catalyst it increased up to 80 %. The effective oxidative degradation of the pollutant was performed in a less acidic environment as compared to a classic Fenton process with a rather large initial concentration of dinitrophenol. This allowed considering the nanosized CoFe₂O₄ as a promising catalyst of Fenton-like of waste waters purification through deep oxidative degradation of toxins.

Keywords: Catalysis, Nanosized ferrites, Wastewater treatment, Ultraviolet radiation

Acknowledgements: The study was supported by Russian Science Foundation grant No. 23-23-00122, <https://rscf.ru/project/23-23-00122/>

The research results were partially obtained using the equipment of the Centre for Collective Use of Scientific Equipment of Voronezh State University. URL: <http://ckp.vsu.ru>.

For citation: Tomina E. V., Vo Quang Mai, Kurkin N. A., Doroshenko A. V., Nguyen Anh Tien, Sinelnikov A. A. Influence of UV radiation on the catalytic activity of nanosized cobalt ferrite in the oxidative degradation reaction of dinitrophenol. *Condensed Matter and Interphases*. 2023;25(2): 249–256. <https://doi.org/10.17308/kcmf.2023.25/11105>

✉ Elena V. Tomina, e-mail: tomina-e-v@yandex.ru

© Tomina E. V., Vo Quang Mai, Kurkin N. A., Doroshenko A. V., Nguyen Anh Tien, Sinelnikov A. A., 2023



The content is available under Creative Commons Attribution 4.0 License.

Для цитирования: Томина Е. В., Во Куанг Май, Куркин Н. А., Дорошенко А. В., Нгуен Ань Тьен, Синельников А. А. Влияние УФ-излучения на каталитическую активность наноразмерного феррита кобальта в реакции окислительной деструкции динитрофенола. *Конденсированные среды и межфазные границы*. 2023;25(2): 249–256. <https://doi.org/10.17308/kcmf.2023.25/11105>

1. Introduction

Today, the pollution of natural water with waste waters of industrial and agricultural productions has a significant antropogenic impact. Among the most widespread toxic agents entering the surface waters from oil refining, wood chemical, coke chemical, aniline dye, textile, and hydrolysis industrial enterprises are phenols and their derivatives. Nitrophenol compounds, such as nitrocece and dinitrophenol, are especially toxic. Nevertheless, dinitrophenols are rather widely used in agriculture due to their pronounced simultaneous herbicidal, fungicidal, and insecticidal effect, and they also act as precursors in the production of dyes and antiseptics for wood. It should be noted that pesticides of the dinitrophenol type have a good cumulation ability, which makes the task of their inactivation even more relevant [1].

It is considered that the most reliable and effective method is the complete oxidative degradation of phenol nitro-derivatives to non-toxic substances. In this regard, Fenton processes are of great interest, in the course of which hydrogen peroxide, by decomposing under the influence of a catalyst, acts as a source of stronger oxidants, primarily hydroxyl radicals with a redox potential from +2.0 to +2.8 V depending on pH [2, 3]. Ferriferrous materials based on mesoporous silicon dioxide, zeolites, and others are used as heterogeneous Fenton catalysts [4, 5].

Nanosized spinel ferrites MeFe_2O_4 [6–10] seem to be promising in this regard as their catalytic activity significantly increases due to a great specific surface area and ability of activation with ultraviolet radiation.

Spinel ferrites are already being used in a number of “green chemistry” technologies, such as wastewater treatment [11–13], carbon deposition [14], and antimicrobial treatment [15]. In case of photochemical processes due to a combination of radiation with the action of different oxidants, the most widespread of which is hydrogen peroxide, and catalysts, the redox potential of the system is considerably increased, and, as a result, the degree of oxidative degradation also rises. Thus,

the goal of this work was to establish the catalytic activity of CoFe_2O_4 nanopowder synthesised using citrate combustion in the reaction of oxidative degradation of 2,4-dinitrophenol upon the activation of the process with UV radiation.

2. Experimental

The synthesis of ferrite-spinel CoFe_2O_4 using the citrate combustion method was carried out according to [16]. Phase composition of the nanopowder was determined by X-ray diffractometry (Empyrean BV diffractometer with Cu anode ($\lambda = 1.54060$ nm)). The scanning was performed within a range of angles $2\theta = 10\text{--}80^\circ$ with a step of 0.0200. The JCPDC database [17] was used to identify the phases. The size and morphology of CoFe_2O_4 particles were determined by transmission electron microscopy (TEM, CarlZeiss Libra-120 transmission electron microscope). Quantitative elemental analysis was performed on a JSM-6380LV JEOL scanning electron microscope with an INCA 250 microanalysis system.

The catalytic activity of the cobalt ferrite nanopowder was studied on a reaction of 2,4-dinitrophenol (DNP) oxidation with hydrogen peroxide. To do this, we prepared a solution containing 0.084 g/l of 2,4-dinitrophenol and 10 wt. % hydrogen peroxide. pH of the solution, which was 4.4, was maintained by an acetate buffer. After that, 0.25 g of cobalt ferrite was added to a series of solution samples with a volume of 15 ml, and the concentration of DNP was measured at certain periods after the beginning of the reaction. Control measurements of the concentrations of DNP solutions without a catalyst were performed in the same manner. The experiment was conducted with daylight and ultraviolet radiation with $\lambda = 270$ nm (Nuobi UV lamp, 20 W). The DNP concentration was determined using photocolourimetry (KFK-3-01 photocolourimeter). The analytical wavelength for 2,4-dinitrophenol was 364 nm. The degree of DNP degradation was calculated by formula (1):

$$W = \frac{C_0 - C_t}{C_0} \cdot 100 \%, \quad (1)$$

where W is the degree of degradation %, C_0 is the concentration of the dye at the initial moment of time, and C_t is the concentration of the dye at the present moment of time.

To differentiate the catalytic oxidative degradation of DNP and its sorption on a nanosized catalyst, we performed an experiment using the above-described method without adding H_2O_2 oxidant to the solutions. In this case, oxidative degradation of DNP was not performed, while decolorisation of the solutions was only determined by the sorption of the pollutant on cobalt ferrite. The duration of static sorption was 2 hours. The sorption capacity of cobalt ferrite was determined using equation (2):

$$A = \frac{(C_0 - C) \cdot V}{m}, \quad (2)$$

where C_0 is the initial concentration of the DNP solution, mol/l; C is the concentration of DNP after a certain time after the beginning of the reaction, mol/l; V is the volume of the adsorbate solution, l; m is the weight of cobalt ferrite, g.

The validity of the results was established using methods of statistical analysis. The law of result distribution was determined using the Kolmogorov-Smirnov test. We determined the statistical significance by the Student's test.

3. Results and discussion

According to XRD results (Fig. 1), cobalt ferrite powder synthesised by citrate combustion did not contain impurities, and all reflections in the diffraction pattern belonged to $CoFe_2O_4$ spinel (JCPDC, card 22-1086).

The average size of coherent scattering regions (CSRs) of $CoFe_2O_4$ particles calculated using the Debye-Scherrer formula [18] was 61 ± 4 nm.

The average values of the weight and atomic percentages of the elements Co, Fe, and O according to the data of energy dispersion analysis are presented in Table 1, and the results correlate with the expected chemical composition.

According to TEM, cobalt ferrite powder (Fig. 2A) was highly agglomerated, which could be associated with specific features of the method of synthesis. Additional ultrasound dispersion of the nanopowder in an ultrasonic bath VU-09-“Ya-FP”-0 for 20 min allowed reducing

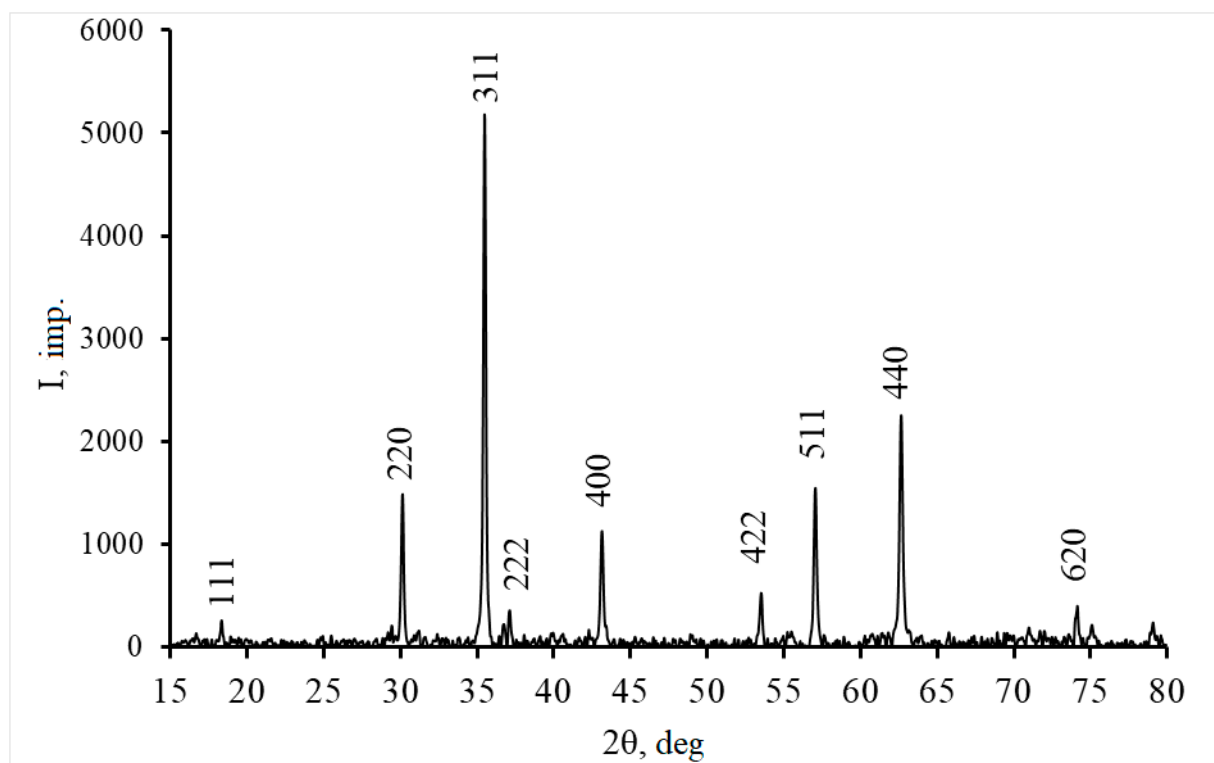


Fig. 1. Diffraction pattern of the $CoFe_2O_4$ powder synthesised by the citrate method

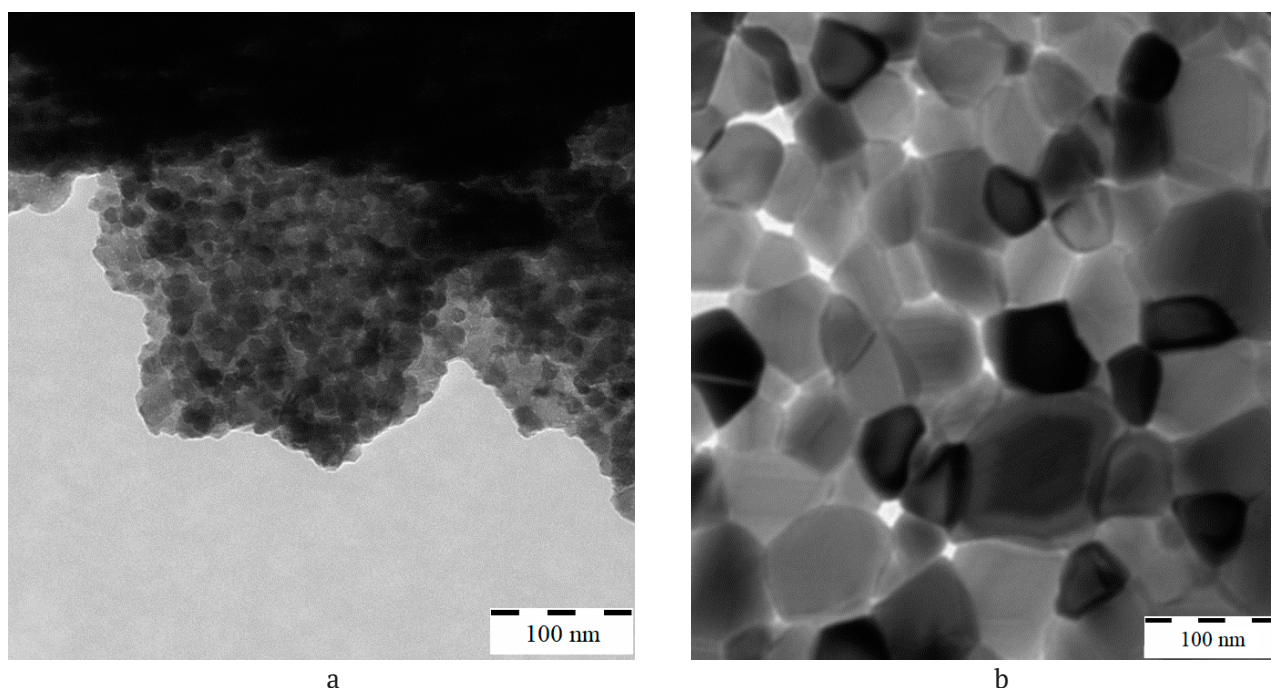


Fig. 2. TEM images of the CoFe_2O_4 sample before (a) and after the ultrasound dispersion (b)

Table 1. Results of energy dispersion analysis of spinel nanopowder

Element	Weight %	Atomic %
O	27.45	56.82
Fe	47.40	28.73
Co	25.15	14.44

the degree of agglomeration, thus making it possible to identify individual nanoparticles on the TEM image and assess their shape and size (Fig. 2b). The CoFe_2O_4 sample was represented by nanoparticles of irregular round shapes, and some particles were faceted. The majority of particles had a size in the range from 50 to 90 nm, while the average size of particles was about 70 nm. According to XRD, the calculated data of CSR values generally correlated with the TEM results.

It was experimentally established that cobalt spinel nanopowder synthesised using the citrate method is an effective heterogeneous catalyst for Fenton-like reactions. Oxidative degradation of DNP under the influence of UV radiation in the presence of the CoFe_2O_4 catalyst proceeded more intensely than in its absence (Fig. 3a). Therefore, the concentration of DNP during catalytic oxidation 2.5 hours after the beginning of the reaction decreased by 5 times. In the absence of a catalyst, after 2.5 hours of reaction, the

concentration of dinitrophenol decreased only by 1.4 times. As for the combination of the H_2O_2 oxidiser with UV radiation, the degradation degree of DNP was 29%, and the degree of degradation increased up to 80% with the introduction of a nanosized decomposition catalyst of hydrogen peroxide into the system.

The shape of kinetic curves of the oxidative degradation of DNP corresponded to the pseudo-first order of the reaction. The rate constant was evaluated by linearisation of the kinetic dependences in logarithmic coordinates (Fig. 3b). The rate constant of the oxidative degradation of DNP in the presence of CoFe_2O_4 with UV radiation was 0.102 min^{-1} , while in the absence of a catalyst, it was an order of magnitude smaller and amounted to 0.0019 min^{-1} . The value of the rate constant of dinitrophenol oxidation was comparable with the values in [19] obtained for a more acidic medium ($\text{pH} \leq 3$) and for the initial DNP concentration 8 times lower as compared to this work. In [10], the calculated constant of photodegradation rate of the methylene blue dye in the presence of nanosized MgFe_2O_4 was 0.0117 min^{-1} with UV radiation by two Xe arc lamps, 35 W each, for two hours. In [20], the rate constant of photodegradation of the same dye with the participation of CoFe_2O_4 as a catalyst and H_2O_2 as an oxidant with daylight but in a

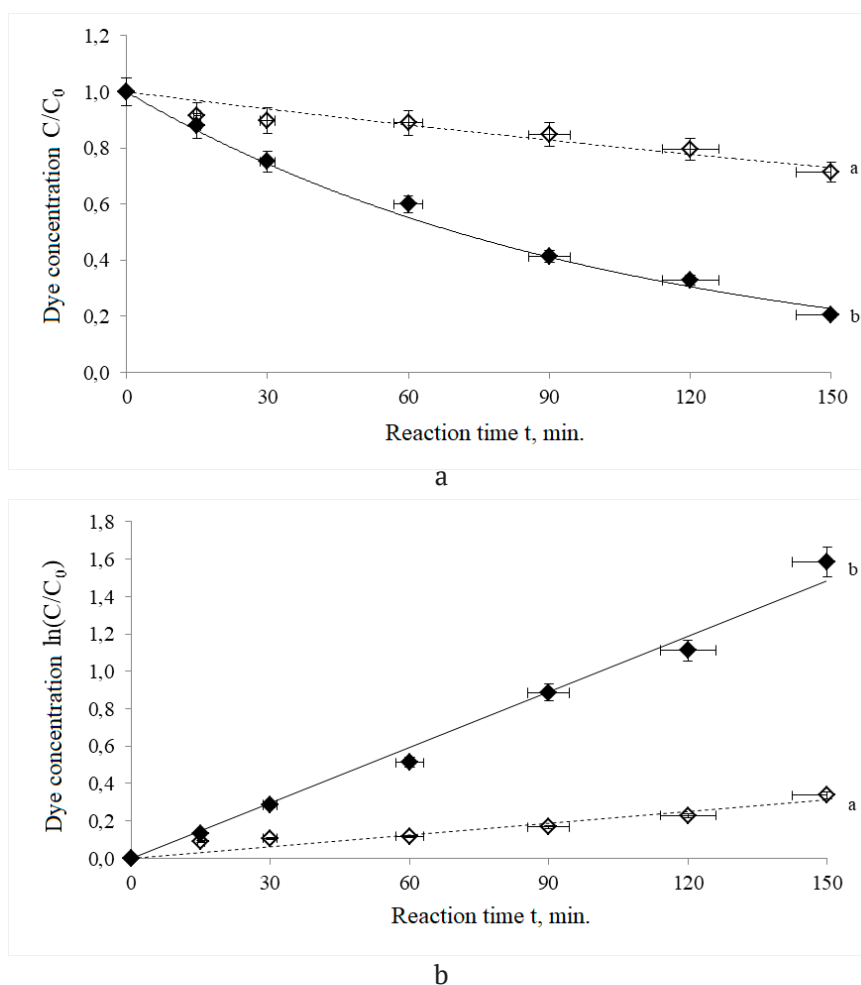


Fig. 3. Change in the concentration of DNP under the influence of UV radiation in the coordinates C/C_0 (a) and $\ln(C/C_0)$ (b) (a – without a catalyst, b – in the presence of the CoFe_2O_4 catalyst.)

considerably more acidic medium ($\text{pH} = 2.5$) was 0.078 min^{-1} . Decomposition of Rhodamine 6 dye in the presence of CoFe_2O_4 in the dark with $\text{pH} = 2$ [21] proceeded much slower (the rate constant was 0.0041 min^{-1}), which allowed concluding that pH of the reaction medium, as well as the type and lighting power were among the most important factors determining the rate of the reaction.

When the reaction proceeded with natural lighting, the catalytic effect of CoFe_2O_4 was feebly pronounced. The degree of DNP degradation was only 14%, although it should be noted that, in the absence of a catalyst, oxidative degradation of 2,4-dinitrophenol hardly occurred (the degradation degree was 0.13%).

The main parameters affecting the course of heterogeneous Fenton-type catalysis were concentration and availability of active catalyst centres, pH , H_2O_2 concentration, and the initial content of organic pollutants and accompanying

ions. As for the classical homogeneous Fenton process, the best pH value is from 2.8 to 3.5 [22]. With higher pH , Fe^{2+} ions become oxidised, thus forming complex hydroxo-compounds, and oxidative activity of H_2O_2 is also reduced.

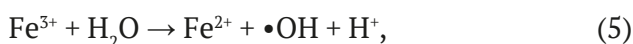
The mechanism of oxidative degradation in heterogeneous Fenton-like reactions consisted in the formation of strong oxidants ($\text{OH}\cdot$) in the course of the reversible transition from Fe^{2+} to Fe^{3+} under exposure to light. It was shown in [23] that tetrahedral centres of Fe^{3+} had electron-withdrawing properties, while the formed Fe^{2+} ions were active centres of Fenton-like processes:

$$\text{Fe}^{2+} + \text{H}_2\text{O}_2 \rightarrow \text{Fe}^{3+} + \cdot\text{OH} + \text{OH}^- \quad (3)$$

In case of cobalt spinel and for cobalt ion (+2), the reaction proceeded with the formation of hydroxyl radicals, which was also confirmed by the data in [24]:



The Fe^{3+} ion is capable of regeneration into Fe^{2+} (especially upon UV radiation) with the formation of an extra amount of hydroxyl and perhydroxyl radicals participating in the oxidation of DNP, which increases the degree of degradation up to 80% as compared to daylight:



It seems that in our case, with daylight, the pH value = 4.4 and the high initial concentration of DNP determined a rather low degree of pollutant degradation.

A series of experiments involving the oxidation of DNP in the combination of H_2O_2 + CoFe_2O_4 + UV and in the presence of CoFe_2O_4 with UV radiation without hydrogen peroxide as an oxidising agent certainly showed that in the first case, the degradation of DNP occurred primarily due to the formation of strong oxidants in the course of the catalytic decomposition of H_2O_2 . The absence of an oxidant revealed a weak sorption capacity of cobalt spinel regarding DNP, and the concentration of the toxic agent decreased only by 5% (Fig. 4). Although under these conditions, Fe^{3+} can be considered as a possible oxidant of dinitrophenol, the data we obtained allowed concluding that this contribution to the overall process was insignificant.

The decrease in the DNP concentration due to sorption was approximately 5% (Fig. 4b), which correlated with the calculated sorption capacity of cobalt ferrite, which was very low, and it may

be associated with the strong agglomeration of the CoFe_2O_4 nanopowder. It should be noted that a small specific surface area was also typical for cobalt spinel synthesised by co-deposition [25]. The sorption capacity of CoFe_2O_4 reached its maximum value (only $0.2 \mu\text{mol/g}$) in 15 min (Fig. 4, insert), and then remained almost unchanged. As a result, it can be concluded that the contribution of sorption to the overall process of DNP degradation in the presence of the CoFe_2O_4 nanosized catalyst in a Fenton-like process was insignificant.

Therefore, the performed assessment of the catalytic activity of nanosized cobalt spinel in the reactions of oxidative degradation of 2,4-dinitrophenol allowed considering CoFe_2O_4 as the basis for creating heterogeneous Fenton catalysts, including composite ones.

4. Conclusions

We synthesised CoFe_2O_4 spinel with an average particle size of about 70 nm using citrate combustion. The strong agglomeration of particles as a result of the selected synthesis method was a specific feature of the nanopowder. We established high catalytic activity of nanodispersed CoFe_2O_4 in Fenton-like reactions of oxidative degradation of 2,4-dinitrophenol upon radiation by ultraviolet $\lambda = 270 \text{ nm}$ in a less acidic medium as compared to a classical Fenton process and with a significantly higher initial pollutant concentration. The degradation degree of DNP without a catalyst was 14%, while in the presence of a nanosized catalyst CoFe_2O_4 it was 80%.

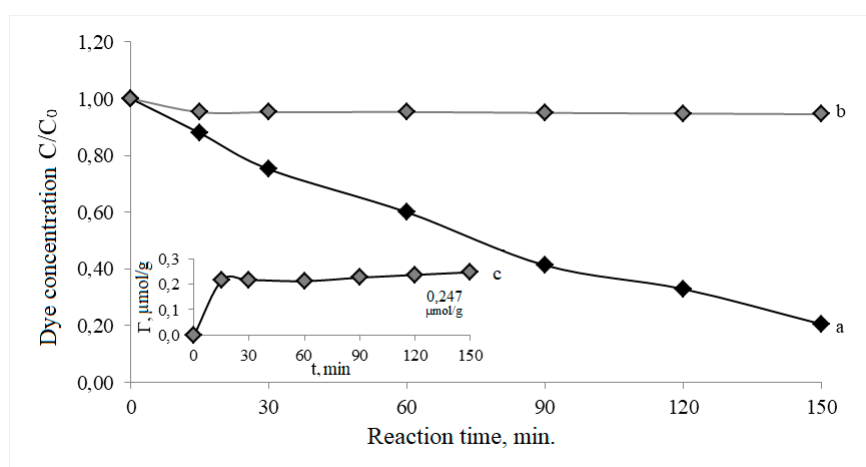


Fig. 4. Curves of catalytic oxidation (a) and sorption (b) of DNP in the presence of CoFe_2O_4 , (c) – sorption capacity of the sample

Contribution of the authors

The authors contributed equally to this article.

Conflict of interests

The authors declare that they have no known competing financial interests or personal relationships that could have influenced the work reported in this paper.

References

1. Ting Li Zhu F., Liang W., ... Guan J. Simultaneous removal of p-nitrophenol and Cr(VI) using biochar supported green synthetic nano zero valent iron-copper: Mechanistic insights and toxicity evaluation. *Process Safety and Environmental Protection*. 2022;146: 629–640. <https://doi.org/10.1016/j.psep.2022.09.049>
2. Zelenskaya E. A., Chernyshev V. M., Shabelskaya N. P., Sulima S. I., Sulima E. V., Semchenko V. V., Vlasenko A. I. The study of catalytic activity of oxides of transition element in the reaction of decomposition of hydrogen peroxide. *Fundamental Research*. 2016;4: 261–265. (In Russ., abstract in Eng.). Available at: <https://www.elibrary.ru/item.asp?edn=vvyjhh>
3. Artemyanov A. P., Zemskova L. A., Ivanov V. V. Catalytic liquid-phase oxidation of phenol in water media using carbon fiber/(iron, iron oxide) catalyst. *ChemChemTech (Izvestiya vysshikh uchebnykh zavedenii. Seriya: khimiya i khimicheskaya tekhnologiya)*. 2017;60(8); 88–95. (In Russ., abstract in Eng.). <https://doi.org/10.6060/tcct.2017608.5582>
4. Ivantsova N. A., Matveeva A. A., Timasheva N. A. Catalytic oxidation of methylene blue dye by air oxygen in the presence of iron shavings and hydrogen peroxide*. *Ekologicheskaya khimiya*. 2012;21(2); 81–85. (In Russ.). Available at: <https://www.elibrary.ru/item.asp?id=22266544>
5. Checherina A. Yu., Stoyanova A. D., Konkova T. V. Investigation of the catalysis efficiency for the purification of aqueous solutions of the azorubin dye in the presence of clay from the Belgorod deposit. *Uspekhi v khimii i khimicheskoi tekhnologii*. 2021;35(6); 122–124. (In Russ.). Available at: <https://www.elibrary.ru/item.asp?id=47194891>
6. Petrova E., Kotsikau D., Pankov V., Fahmi A. Influence of Synthesis Methods on Structural and Magnetic Characteristics of Mg–Zn–Ferrite Nanopowders. *Journal of Magnetism and Magnetic Materials*. 2019;473; 85–91. <https://doi.org/10.1016/j.jmmm.2018.09.128>
7. Somnath S., Indu S., Kotnala R. K., ... Kumar G. Structural magnetic and mössbauer studies of Nd-doped Mg–Mn ferrite nanoparticles. *Journal of Magnetism and Magnetic Materials*. 2017;444; 77–86. <https://doi.org/10.1016/j.jmmm.2017.08.017>
8. Rao K. S., Nayakulu S. V. R., Varma M. C., Choudary G. S. V. R. K., Rao K. H. Controlled phase evolution and the occurrence of single domain CoFe_2O_4 nanoparticles synthesized by PVA assisted sol-gel method. *Journal of Magnetism and Magnetic Materials*. 2018;451(1); 602–608. <https://doi.org/10.1016/j.jmmm.2017.11.069>
9. Mittova I. Ya., Perov N. S., Tomina E. V., Pan'kov V. V., Sladkopezvtsev B. V. Multiferroic nanocrystals and diluted magnetic semiconductors as a base for designing magnetic materials. *Inorganic Materials*. 2021;57(13); 22–48. <https://doi.org/10.1134/S0020168521130033>
10. Lebedev L. A., Tenevich M. I., Popkov V. I. The effect of solution-combustion mode on the structure, morphology and size-sensitive photocatalytic performance of MgFe_2O_4 nanopowders. *Condensed Matter and Interphases*. 2022;24(4): 496–503. <https://doi.org/10.17308/kcmf.2022.24/10645>
11. Rehman F., Sayed M., Khan J. A., ... Khattak R. Degradation of crystal violet dye by Fenton and Photofenton oxidation processes. *Zeitschrift Fur Physikalische Chemie*. 2018;232(12); 1771–1786. <https://doi.org/10.1515/zpch-2017-1099>
12. Oliveira T. P., Rodrigues S. F., Marques G. N., ... Oliveira M. M. Synthesis, characterization, and photocatalytic investigation of CuFe_2O_4 for the degradation of dyes under visible light. *Catalysts*. 2022;12(6): 623. <https://doi.org/10.3390/catal12060623>
13. Tomina, E. V. Kurkin N. A., Konkina D. A. Nanosized ZnFe_2O_4 catalyst for wastewater treatment from dyes by oxidative degradation. *Ecology and Industry of Russia*. 2022;26(5); 17–21. (In Russ., abstract in Eng.). <https://doi.org/10.18412/1816-0395-2022-5-17-21>
14. Chandrasekaran S., Bowen C., Zhang P., Li Z., Yuan Q., Ren X. Spinel photocatalysts for environmental remediation, hydrogen generation, CO_2 reduction and photoelectrochemical water splitting. *Journal of Materials Chemistry A*. 2018;6(24): 11078–11104. <https://doi.org/10.1039/c8ta03669a>
15. Vinuthna C. H., Kadiyala C. B., Chandra S. C., Ravinder D. Magnetic and antimicrobial properties of cobalt-zinc ferrite nanoparticles synthesized by citrate-gel method. *Applied Ceramic Technology*. 2019;16(5); 1944–1953 <https://doi.org/10.1111/ijac.13276>
16. Tomina E. V., Kurkin N. A., Doroshenko A. V. Synthesis of nanosized cobalt ferrite and its catalytic properties in Fenton-like processes. *Inorganic Materials*. 2022;58(7); 701–705. <https://doi.org/10.1134/S0020168522070135>
17. JCPDC PCPDFWIN: A windows retrieval/display program for accessing the ICDD PDF–2 Data base, International Centre for Diffraction Data, 1997.

18. Brandon D., Kaplan U. *Microstructure of materials. Research and control methods*. West Sussex: John Wiley & Sons Ltd; 1999. 384 p.
19. Roshanfekar R. L., Farshi G. B., Irani, M., Sadegh S. M., Haririan, I. Comparison study of phenol degradation using cobalt ferrite nanoparticles synthesized by hydrothermal and microwave methods. *Desalination and Water Treatment*. 2015;56(12); 3393–3402. <https://doi.org/10.1080/19443994.2014.977960>
20. Sharma R. Tailoring the photo-Fenton activity of spinel ferrites (MFe_2O_4) by incorporating different cations ($M = Cu, Zn, Ni$ and Co) in the structure. *RSC Advances*. 2015;5: 6006–6018. <https://doi.org/10.1039/C4RA13692F>
21. Samoila, P., Cojocaru, C., Mahu, E., Ignat, M., Harabagiu, V. Boosting catalytic wet-peroxide-oxidation performances of cobalt ferrite by doping with lanthanides for organic pollutants degradation. *Journal of Environmental Chemical Engineering*. 2021;9(1): 104961. <https://doi.org/10.1016/j.jece.2020.104961>
22. Solovieva A. A., Nemchenko M. N., Lebedeva O. E. Catalytic oxidation of dinitrophenols with hydrogen peroxide in the presence of iron(II) and (III) ions*. *Butlerov Communications*. 2006;9(5); 27–32. (In Russ.). Available at: <https://www.elibrary.ru/item.asp?id=12965471>
23. Tatarchuk T., Shyichuk A., Trawczyńska I., Yaremiy I., Pędziwiatr A. T., Kurzydło P., Bogacz B. F., Gargula R. Spinel cobalt(II) ferrite-chromites as catalysts for H_2O_2 decomposition: Synthesis, morphology, cation distribution and antistructure model of active centers formation. *Ceramics International*. 2020;46: 27517–27530. <https://doi.org/10.1016/j.ceramint.2020.07.243>
24. Ying G., Weihuang Z., Jiawu L., Ping L., Jianfeng Zh., Tinglin H., Kaiqiang L. Mesoporous sulfur-doped $CoFe_2O_4$ as a new Fenton catalyst for the highly efficient pollutants removal. *Applied Catalysis B: Environmental*. 2021;295: 120273. <https://doi.org/10.1016/j.apcatb.2021.120273>
25. Tran Q. A., Tran N. L., Anh D. K. ... Le T. K. Synthesis of magnetic chromium substituted cobalt ferrite $Co(Cr_xFe_{1-x})_2O_4$ adsorbents for phosphate removal. *Condensed Matter and Interphases*. 2022;24(3): 306–314. <https://doi.org/10.17308/kcmf.2022.24/9852>
* Translated by author of the article.

Information about the authors

Elena V. Tomina, Dr. Sci. (Chem.), Head of the Department of Chemistry, Voronezh State University of Forestry and Technologies named after G. F. Morozov (Voronezh, Russian Federation).

<https://orcid.org/0000-0002-5222-0756>
tomina-e-v@yandex.ru

Vo Quang Mai, PhD in Chemistry, Associate Professor, Faculty of Natural Sciences, Saigon University (Ho Chi Minh City, Vietnam).

voquangmai@sgu.edu.vn

Nikolay A. Kurkin, postgraduate student of the Department of Materials Science and Industry of Nanosystems, Voronezh State University (Voronezh, Russian Federation).

<https://orcid.org/0000-0002-0468-8207>
kurkin.nik@yandex.ru

Alyona V. Doroshenko, bachelor of the Department of Materials Science and Industry of Nanosystems, Voronezh State University (Voronezh, Russian Federation).

<https://orcid.org/0000-0001-7487-5078>
al.doroschenko2016@yandex.ru

Nguyen Anh Tien, PhD in Chemistry, Chief of Inorganic Chemistry Department, Ho Chi Minh City University of Education (Ho Chi Minh City, Vietnam).

<https://orcid.org/0000-0002-4396-0349>
tienna@hcmue.edu.vn

Alexander A. Sinelnikov, Cand. Sci. (Phys.–Math.), Head of the Centre for Collective Use of Scientific Equipment Voronezh State University (Voronezh, Russian Federation)

rnileme@mail.ru
<https://orcid.org/0000-0002-0549-4615>

Received 02.03.2023; approved after reviewing 28.03.2023; accepted for publication 15.04.2023; published online 25.06.2023.



Condensed Matter and Interphases

Конденсированные Среды и Межфазные Границы
<https://journals.vsu.ru/kcmf/>

Original articles

Research article

<https://doi.org/10.17308/kcmf.2023.25/11106>

Phase diagrams of zirconium dioxide systems with yttrium and scandium oxides

P. P. Fedorov✉, E. V. Chernova

*Prokhorov General Physics Institute of the Russian Academy of Sciences,
38 Vavilova st., Moscow 119991, Russian Federation*

Abstract

The literature data on the study of phase equilibria in systems zirconia with yttria and scandia are analysed. Possible schemes of low-temperature phase equilibria in ZrO_2 - Y_2O_3 and ZrO_2 - Sc_2O_3 systems are presented taking into account the third law of thermodynamics.

The coordinates of non-variant transformations in these systems are tabulated. A sign of non-equilibrium states is the observation of non-diffusion processes of ordering of solid solutions. The modified cryoscopy method is used to calculate the distribution coefficients of scandia and yttria during the crystallization of the ZrO_2 melt.

The possibilities for the existence of a set of ordered phases in the ZrO_2 - Y_2O_3 system and diffuse phase transition in the cubic modification of zirconia are discussed.

Keywords: Zirconia, Yttria, Scandia, Solid solutions, Ordering, Phase diagrams, Distribution coefficients

Funding: The study was supported by a grant from the Russian Science Foundation No.22-13-00167 <https://rscf.ru/project/22-13-00167>

For citation: P. P. Fedorov, E. V. Chernova. Phase diagrams of zirconium dioxide systems with yttrium and scandium oxides. *Condensed Matter and Interphases*. 2023;25(2): 257–267. <https://doi.org/10.17308/kcmf.2023.25/11106>

Для цитирования: Федоров П. П., Чернова Е. В. Фазовые диаграммы систем диоксида циркония с оксидами иттрия и скандия. *Конденсированные среды и межфазные границы*. 2023;25(2): 257–267. <https://doi.org/10.17308/kcmf.2023.25/11106>

✉ Pavel P. Fedorov, e-mail: ppfedorov@yandex.ru

© P. P. Fedorov, E. V. Chernova., 2023



The content is available under Creative Commons Attribution 4.0 License.

1. Introduction

Phase diagrams are the physical and chemical basis for the synthesis of functional materials. In addition, they allow predicting the behaviour of the material under operating conditions. Solid solutions of oxides of rare earth elements (REE) R_2O_3 in high-temperature cubic modifications of zirconia $Zr_{1-x}R_xO_{2-0.5x}$ are among the most refractory oxides with a melting temperature above 2700°C [1, 2]. Materials based on them are widely used as jewellery crystals (fianites) [3, 4] and refractory and corrosion-resistant ceramics [5–9]. The high anionic conductivity of these solid solutions is combined with a low thermal conductivity [10]. These circumstances determine the use of appropriate materials in electrochemical devices (fuel cells, oxygen sensors) [11–13] and also as thermal barrier coatings [14, 15]. Materials based on zirconia are the basis of nuclear fuel with an inert matrix [16].

A lot of studies were dedicated to the study of phase equilibria in ZrO_2 - R_2O_3 systems, but the result of these studies is not satisfactory. These systems have been studied by various groups of researchers. A summary of the data is provided in [17, 18]. The results obtained for different REE do not fit well with each other. Difficulties are associated both with high melting temperatures and with very long time intervals required to achieve equilibrium in the low-temperature region [19–22]. As in previous studies, we will denote regions of phase diagrams where the time required to establish equilibrium exceeds a year as being low-temperature regions. Cubic solid solutions of $Zr_{1-x}R_xO_{2-0.5x}$ are obviously thermodynamically unstable at low temperatures. However, the negligibly small diffusivity of cations [23] prevent the decomposition of solid solutions, which makes the corresponding materials indefinitely stable at ambient temperatures. The insufficiency of the annealing used in a number of studies was demonstrated by researchers from the Tokyo Institute of Technology [24, 25]. In particular, it turned out that the temperature of the eutectoid decomposition of a solid solution based on the medium-temperature tetragonal modification in the ZrO_2 - Er_2O_3 system, determined in the study [26], was underestimated by about 500 °C [24].

The synthesis of samples under hydrothermal conditions sharply accelerates the processes

of phase formation in refractory oxide systems [2, 27]. However, additional problems arise in this case, associated, in particular, with the contamination of samples with hydroxyl ions, which distort the pattern of phase equilibria [28]. In addition, the resulting nanocrystals of intermediate phases often “get stuck” in metastable states [29–30].

The purpose of this study is a critical analysis of the available data on the study of phase equilibria in key ZrO_2 - Y_2O_3 and ZrO_2 - Sc_2O_3 systems and construction of assumed phase diagrams with extrapolation to absolute zero temperature in accordance with the third law of thermodynamics.

2. Analysis methodology

In this study, we applied the methodology that we used earlier in [31–33]. According to the consequence of the third law of thermodynamics, as the temperature tends to absolute zero in quasi-equilibrium processes, all phases of variable composition should disappear through the decomposition or contraction of compositions to stoichiometric ones [20, 34]. In this case, the limiting solubility curves should have vertical tangents as the temperature approaches absolute zero [33]. The second important thermodynamic condition is the so-called Hume-Rothery rule, according to which, when an ordered phase with a narrow homogeneity region appears, the region of existence of a neighbouring disordered phase should sharply narrow [35].

The corresponding approach using the extrapolation of the most reliable experimental data in the study of phase equilibria allows by extrapolating phase fields to the region of low temperatures, to obtain information for those regions of phase diagrams where an experiment aimed at realizing equilibrium states is complicated or simply impossible. Previously, using this approach, we outlined the scheme of phase equilibria in the ZrO_2 - Er_2O_3 system [22].

An alternative technique is the thermodynamic computer simulation of phase equilibria. The construction of thermodynamic models of the studied systems is an ideal goal to strive for [36–38]. However, there are problems associated, among other things, with the determination of the thermodynamic properties of phases of variable composition and with the choice of

reliable experimental data for their processing [39–42]. The thermodynamic modelling of phase equilibria in ZrO_2 - Y_2O_3 system was performed in [43–46]. The results differ significantly.

3. Results

3.1. ZrO_2 - Y_2O_3 system

The ZrO_2 - Y_2O_3 system is a classic and model system. It has been studied by various groups of researchers [17, 18, 47]. Solid-liquid equilibria were studied by Rouanet [48], Noguchi et al. [49], Lopato et al. [50]. The most detailed studies of phase equilibria in the solid state were carried out by Pascual and Duran [51] and Stubican et al. [52], with an annealing duration of up to 8 months. These studies provided similar results.

Based on the work data Pascual and Duran, see Fig. 1a. In this study the samples were annealed for 3 hours at 2000°C, 10 hours at 1800°C, and 385 hours at 1450°C, which appears acceptable [22]. However, it is obvious that the 8 months used in this study for annealing at 800°C were completely insufficient. The corrected pattern of phase equilibria is shown in Fig. 1b. At the same time, the designations of the phase composition

of the samples annealed and quenched in the study of Pascual and Duran were applied to the figure.

Extensive regions of heterovalent solid solutions based on the high-temperature polymorph of ZrO_2 with fluorite structure (phase F, space group $Fm\bar{3}m$) and low-temperature cubic modification Y_2O_3 (phase C, bixbyite type, space group $Ia\bar{3}$) were formed in the system. Although the bixbyite type is derived from the fluorite type with an ordered arrangement of vacancies [53], the presence of a two-phase F+C region in the phase diagram was reliably recorded as early as by Duwes et al. [36].

Dissolution of yttrium oxide in high-temperature ZrO_2 modification stabilizes the fluorite structure, and a maximum occurs on the liquidus curve. The maximum point on the melting curves of the solid solution is non-variant, and the liquidus and solidus curves merge at it in the presence of a common horizontal tangent. When depicting phase equilibria in this region Pascual and Duran made an unfortunate mistake, which is corrected in Fig. 1b. The course of the liquidus curve in this system was determined using a solar furnace in the studies

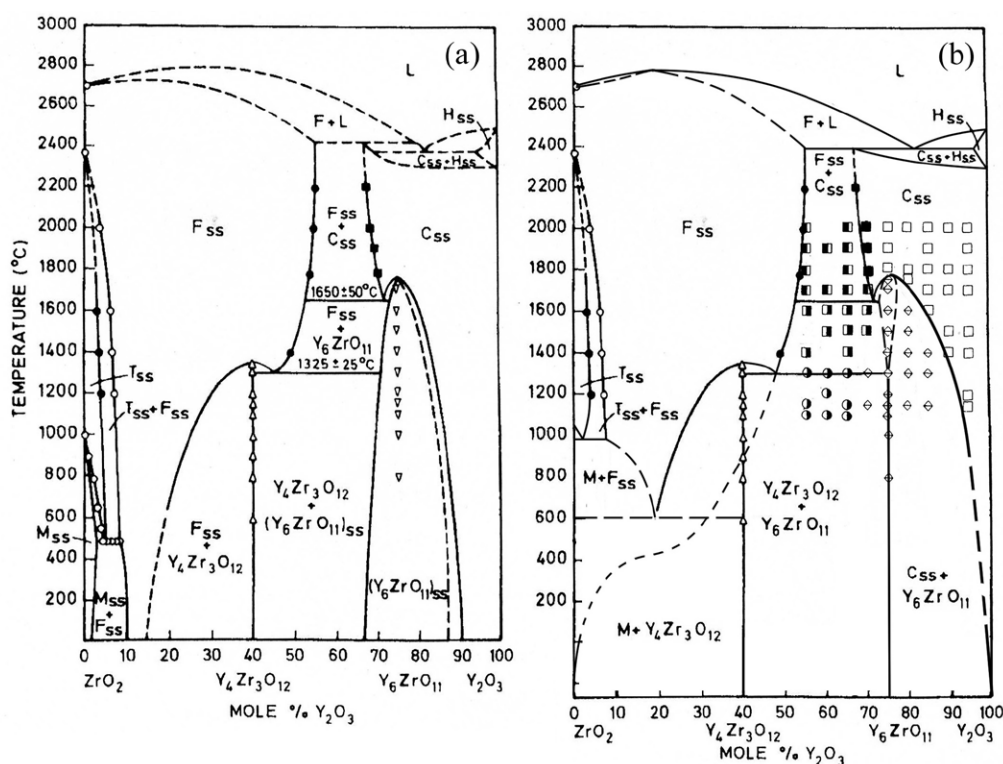


Fig. 1. Phase diagram of the ZrO_2 - Y_2O_3 system according to [51] (a) and its correction taking into account the requirements of the third law of thermodynamics (b)

[48–50], see Fig. 2. When constructing Fig. 1b, we used data of Shevchenko et al. [50].

At a high concentration of yttrium oxide, the melt and three solid phases F, C, and H (a solid solution based on the high-temperature modification of Y_2O_3) should provide two three-phase equilibria, displayed as horizontal segments on the phase diagram. Experimentally, the temperatures of these equilibria are not resolved, and computer simulation [43–46] provides a difference in temperatures within 10–25 degrees. Thus, this system at normal pressure is located in the vicinity of the bifurcation point of A_1II type [54] corresponding to the equilibrium of four condensed phases.

As the temperature decreases, the solid solutions based on the F and C phases undergo ordering with the separation of $Y_4Zr_3O_{12}$ and Y_6ZrO_{11} phases (idealized composition), respectively. The data of [51] and [52] studies agree very well (± 10 °C) in terms of the phase transition temperature $F \leftrightarrow Y_4Zr_3O_{12}$. Our correction in the region of high concentrations of yttrium oxide includes a significant decrease in the region of homogeneity of the ordered phase, which, as the temperature is lowered, must shrink to the ideal Y_6ZrO_{11} composition, as well as the position of the decomposition curve of the solid solution based on the cubic modification of yttrium oxide, which should come to the point of the pure component at $T \rightarrow 0$ K.

Probably, the observation of a wide region of the ordered phase “ Y_6ZrO_{11} ” in the absence of a two-phase region with phase C was caused by the fact that the ordering in this system in

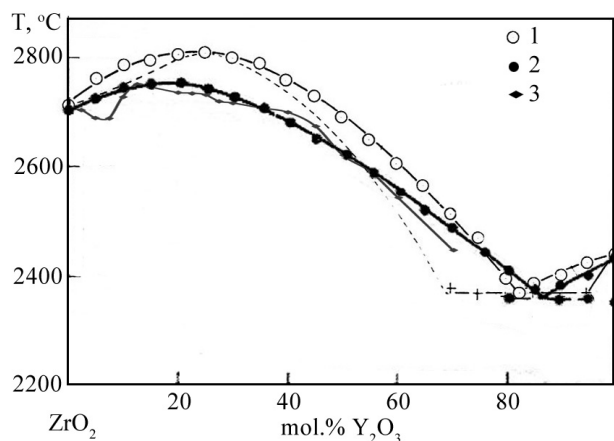


Fig. 2. Liquidus of the ZrO_2 - Y_2O_3 system. 1 – data [48], 2 – data [50], 3 – data [49]

an experimental study [51] occurred according to a non-equilibrium non-diffusion mechanism that does not require overcoming the potential barrier to the nucleation of a new phase in the volume of the old one. A similar phenomenon, as shown by the analysis, was observed during low-temperature ordering in the Ni-Pt system [33], as well as in the HfO_2 - R_2O_3 systems (fluorite-pyrochlore transitions) [22].

The region of low concentrations of yttrium oxide (the decomposition of the tetragonal phase – a solid solution based on the medium-temperature modification of ZrO_2) was corrected by analogy with the data of Yashima and others [24], which, when studying equilibria in a similar ZrO_2 - Er_2O_3 system, annealed samples at 1690 °C for 48 hours and 8 months at 1315 °C. At the same time, the temperature of the eutectoid decomposition of the tetragonal phase was raised by us by several hundred °C in comparison with the variants of the phase diagram presented in [51, 52]).

The dotted line denotes the metastable continuation of the curve of the maximum concentration of this solid solution (the solvus curve of phase F). This curve must pass through the origin of the coordinates and have a vertical tangent at this point. This condition can be fulfilled only if there is a point of inflexion on the solvus curve (in this case, on the metastable part of this curve). It should be noted that the eutectoid corresponding to the decomposition of the fluorite phase should be located above the metastable solvus curve. Accordingly, the temperature of the eutectoid decomposition of the cubic solid solution was presumably targeted at 600 ± 100 °C. This is much higher than is accepted in all studies on phase equilibria in this system, both experimental and calculated.

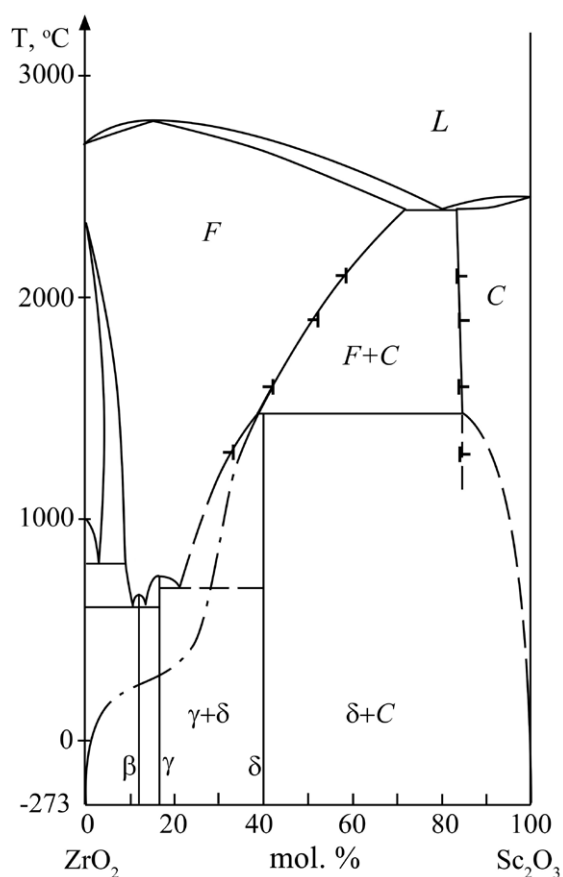
Thus, the proposed version of the phase diagram of the ZrO_2 - Y_2O_3 system (Fig. 1b) is characterized by the following non-variant equilibria, presented in Table 1.

3.2. ZrO_2 - Sc_2O_3 system

Phase equilibria in the ZrO_2 - Sc_2O_3 system have been studied in numerous papers [55–66]. The approximate phase diagram of ZrO_2 - Sc_2O_3 system, plotted in accordance with the data of Spiridonov et al. [57], Shevchenko et al. [60–62] and Fujimori et al. [65, 66] with extrapolation to 0 K is shown in Fig. 3. The coordinates of the non-variant points

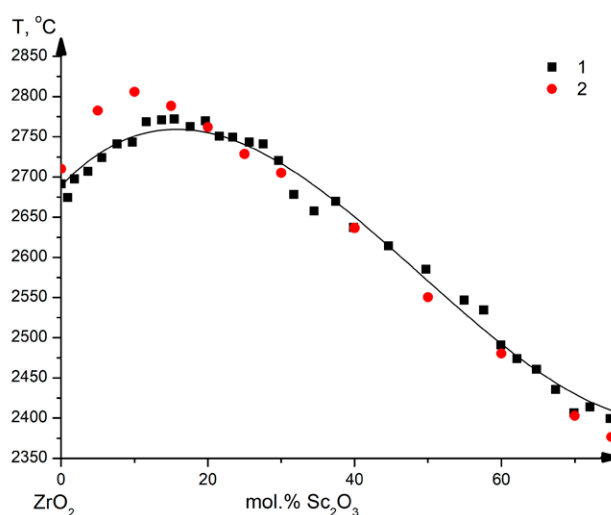
Table 1. Non-variant equilibria in the ZrO_2 - Y_2O_3 system

Name	Phase balance	Composition, mol % Y_2O_3	Temperature, °C	Temperature, K
Dystectics (maximum on the solid solution melting curve)	$L \leftrightarrow F$	20±2	2750±25	3023
A_1 II type bifurcation	$L+F+C+H$	–	2360±50	2633
Distectoid	$F \leftrightarrow Y_4Zr_3O_{12}$	40	1380±10	1653
Distectoid	$C \leftrightarrow Y_6ZrO_{11}$	75	1750±50	2023
Eutectoid	$T \leftrightarrow M + F$	3±1	950±25	1223
Eutectoid	$F \leftrightarrow Y_4Zr_3O_{12} + M$	18±3	600±100	873
Eutectoid	$F \leftrightarrow Y_4Zr_3O_{12} + Y_6ZrO_{11}$	45±3	1350±25	1623
Eutectoid	$C \leftrightarrow Y_6ZrO_{11} + F$	68±2	1650±50	1923


Fig. 3. Summary phase diagram of the ZrO_2 - Sc_2O_3 system

are summarized in Table 2. Wide regions of solid solutions based on scandia (bixbyite type, phase C) and cubic high-temperature modification of zirconia (phase F) were formed in the system. A maximum was formed on the melting curves of the fluorite solid solution. A comparison of the liquidus curves obtained in [58, 60] is shown in Fig. 4.

With decreasing temperature, the fluorite solid solution (phase F) undergoes ordering with the


Fig. 4. Liquidus of the ZrO_2 - Sc_2O_3 system 1 – data [60], 2 – data [58]

release of ordered phases, which were originally assigned the designations β , γ , and δ and $Zr_7Sc_2O_{17}$, $Zr_5Sc_2O_{15}$ and $Zr_3Sc_4O_{12}$ compositions (cubic solid solution, phase F was designated as phase α). The decoding of crystal structures [67–69] allowed refining the composition of the β phase: $Zr_{50}Sc_{12}O_{118}$. Compound $Zr_3Sc_4O_{12}$ was described as a rare mineral found in meteorites [70]. This compound isostructural to the corresponded yttrium phase $Zr_3Y_4O_{12}$ and forms a continuous solid solution with it [63].

The low-temperature phases β , γ , and δ are characterized by the trigonal distortion of the fluorite lattice due to the ordered arrangement of anion vacancies [61]. The differentiation of cations over crystallographic positions practically does not occur due to frozen diffusion [55], although it is energetically favourable [69].

Table 2. Non-variant equilibria in the ZrO_2 - Sc_2O_3 system

Name	Phase balance	Composition, mol % Sc_2O_3	Temperature, °C	Temperature, K
Distectics (maximum on the solid solution melting curve)	$L \leftrightarrow F$	15±5	2800±50	3073
Eutectic	$L \leftrightarrow F + C$	78±2	2400±50	2673
Distectoid	$F \leftrightarrow \beta$		650±50	923
Distectoid	$F \leftrightarrow \gamma$		750±50	1023
Peritectoid	$F + C \leftrightarrow \delta$	40±2	1550±100	1733
Eutectoid	$T \leftrightarrow M + F$	3±1	800±100	1073
Eutectoid	$F \leftrightarrow M + \beta$	11±1	600±50	873
Eutectoid	$F \leftrightarrow \beta + \gamma$	13±1	600±50	873
Eutectoid	$F \leftrightarrow \beta + \delta$	21±2	700±50	973

The transition temperature of the phase β to a disordered state (phase F) is close according to the data of [57, 60–62, 65–66], and is 650 ± 50 °C. Phase disorder temperatures γ and δ indicated in the literature are very different. This may be due to the non-quenchability of the high-temperature disordered cubic phase upon cooling [57]. Data of Zyrin et al. were preferential for the construction of Fig. 4 [61]. In particular, for the transition $\alpha \leftrightarrow \gamma$, Spiridonov et al. [57] and Ruh et al. [59] reported a temperature of ~ 1100 °C. The same group of researchers reported a γ phase disorder temperature equal to 1480 °C [61] and 1650 °C [62]. This region of the phase diagram of ZrO_2 - Sc_2O_3 system requires further research.

It should be noted that the continuation of the line of the maximal concentration of the cubic solid solution (solvus curve of the phase F) to zero coordinates (ZrO_2) subject to the presence of a vertical asymptote is impossible without the assumption of the presence of an inflection point on the metastable continuation of this curve.

3.3. Distribution coefficients

Accurate measurement of the liquidus curve of solid solutions allow calculating the distribution coefficients of the impurity component during the crystallization of the matrix from the melt using the modified cryoscopy method. Previously, such calculations were carried out for a number of ZrO_2 - R_2O_3 systems [71]. The basis of the modified cryoscopy method is the Van't Hoff limit equation:

$$m = [RT_0^2 / \Delta H](k-1), \quad (1)$$

where ΔH and T_0 [K] are enthalpy of melting and melting temperatures of the matrix, R is the universal gas constant, k is the impurity distribution

coefficient, m is the liquidus slope. This equation is valid for infinite dilution.

In the modified cryoscopy method, the value m is not determined based on precision measurements of small values of temperature depression with the introduction of low impurity concentrations, but by approximating liquidus curves in a wide range of concentrations, followed by differentiation of analytical expressions [72, 73].

Previously, this method was used to process the data of [48, 49] using the liquidus curve of the F phase in the ZrO_2 - Y_2O_3 system and study [60] for the ZrO_2 - Sc_2O_3 system. In this study, the data of Shevchenko et al. [50] for the ZrO_2 - Y_2O_3 system and data of Sekiya et al. [58] for the ZrO_2 - Sc_2O_3 system were processed using this method. The points of the liquidus curves in a wide concentration range were processed using the least squares method in the form of a 3rd order polynomial. In this case, the melting point of ZrO_2 (2710 °C) was fixed by the provision of a tenfold weight to this point. Primary data were obtained by digitizing the graph provided in [58].

Data for ZrO_2 - Y_2O_3 [50] and ZrO_2 - Sc_2O_3 [58] systems are well described by third-order polynomials with correlation coefficients of 0.999 and 0.980, respectively. By differentiating the obtained equations for $x = 0$, the values of the liquidus slope (depression) were obtained for an infinitesimal impurity content $m = (\partial T / \partial x)_{x=0}$, namely 594 and 1005 deg/mol, respectively. Hence, according to equation (1) using the enthalpy of ZrO_2 melting, $\Delta H = 16.40$ kcal/mol [74], we obtain the distribution coefficients of Y_2O_3 and Sc_2O_3 during crystallization of the ZrO_2 melt. The obtained value $k_Y = 1.55$ agrees well with

the calculated value obtained from the data of Noguchi et al. [49], but diverges from the value obtained from the data of Rouanet [48], see [22]. The calculated value $k_{sc} = 1.93$ significantly differs from the value $k_{sc} = 2.87$ calculated according to Shevchenko et al. [22]. The discrepancies are determined by the complexity of conducting experiments at temperatures above 2700 °C, see Figs. 2 and 4.

4. Discussion

The wide regions of solid solutions formed in ZrO_2 - R_2O_3 systems are striking examples of the so-called grossly nonstoichiometry [55]. The maxima on the melting curves of these solid solutions are a characteristic feature of heterovalent isomorphism with a variable number of atoms in the unit cell and correlate with high ionic conductivity and low thermal conductivity [9, 75, 76].

The formation of such solid solutions is characterized by the accumulation of defects associated with charge compensation and the formation of ordered phases with decreasing temperature. This effect that is observed in the studied systems and in this case it is weakened and smeared out due to low cationic diffusion. The absence of pronounced differentiation of cations over crystallographic positions during the formation of ordered fluorite-like phases sharply distinguishes oxide systems from analogous fluoride systems. It can be assumed that the complete cationic ordering will change the thermodynamic stability of the corresponding phases and, thus, it will shift the temperature limits of their existence in the phase diagrams of ZrO_2 - R_2O_3 . Probably, the observed pattern of ordering (the formation of only two fluorite-like phases $Y_4Zr_3O_{12}$ and Y_6ZrO_{11} in the ZrO_2 - Y_2O_3 system and three ordered phases in the ZrO_2 - Sc_2O_3 system) is not complete. For comparison, we can refer to the CeO_2 - Ce_2O_3 model system, where the set of ordered phases is much richer [77]. In particular, it can be expected that in the yttrium system the same ordered phases as in the scandium system are formed, and the absence of phases of the β and γ types in the ZrO_2 - Y_2O_3 system associated only with kinetic difficulties [62]. In addition, the existence of the phase $Y_5Zr_2O_{11.5}$, which is isostructural to the erbium analogue can be expected [78].

It should be noted that all thermodynamic models for the ZrO_2 - Y_2O_3 system provide for the presence of only one ordered phase $Y_4Zr_3O_{12}$, which significantly limits their reliability. In this case, the temperature of the eutectoid decomposition of the cubic phase in the ZrO_2 - Y_2O_3 system differs according to the data of different models by hundreds of degrees [43–46], and in [46] it falls below absolute zero, which contradicts the third law of thermodynamics. The diagram constructed by us (Fig. 1b) is closest to the thermodynamic model of Degtyarev and Voronin [43].

The inflection points on the extrapolated solvus curves of the F phases deserve special attention. Such points are characteristic of all binary systems with heterovalent solid solutions based on compounds with the fluorite structure [79], which is associated with diffuse phase transitions in fluorite matrices [80, 81]. In particular, such a behaviour of the solvus line takes place in the system UO_2 - UO_3 [82], and the presence of a diffuse phase transition in uranium dioxide is discussed [80, 83–85]. Thus, the results of low-temperature extrapolation of the solvus curves both in the analysed systems and the corresponding curves in other systems with the participation of zirconia and hafnium oxides [22] suggest the presence of a diffuse phase transition in the cubic ZrO_2 and HfO_2 polymorphs. For zirconium and hafnium oxides, we do not know any indications of its existence.

Conditional estimation of approximate temperature of this transition (since this is diffuse transition, and it is not a phase transition in the thermodynamic sense) based on $T \sim (0.7-0.8)T_{melt}$ [K] ratio provides a value of 1680–2100 °C, i.e. below the temperature of polymorphic transformation between the cubic and tetragonal modifications of ZrO_2 (2170 °C [2]). Thus, probably, all solid solutions of the fluorite structure formed in systems with the participation of zirconia are solid solutions in the disordered initial ZrO_2 form. This creates additional difficulties for constructing the corresponding thermodynamic models.

On numerous published “phase diagrams” of $(Zr,Hf)O_2$ - R_2O_3 systems at temperatures below 1300 °C frozen states are shown instead of equilibrium phase regions. The actual behaviour of materials in these systems upon cooling is

determined mainly not by equilibrium phase transformations, but by non-diffusion phase transitions. Accordingly, on phase diagrams, in some cases, two-phase regions degenerate, and instead of them lines of phase transformations of the martensitic type are present.

A scandium solid solution of optimal concentration is thermodynamically stable at temperatures above 700 °C, i.e., the corresponding products are stable in terms of phase composition for an indefinitely long period of time if they are operated at this temperature without lowering it.

5. Conclusions

Phase equilibria at low temperatures in systems involving zirconia and hafnia are among the unresolved fundamental issues. Since the time of achieving equilibrium controlled by cationic diffusion increases exponentially with decreasing temperature, the study of low-temperature equilibria is a very complicated and often unsolvable problem.

It should be noted that ordering processes in systems with zirconia and hafnium oxides have been very poorly studied. Significant discoveries can be expected here.

Other methods for the investigation of low-temperature phase formation in the discussed systems are required. It can be expected that the use of salt melts will allow progress to be made in solving this problem. It should be noted that salt melts, in contrast to hydrothermal synthesis, contribute to the formation of micron rather than nanoscale powders, which probably less prone to the formation of metastable equilibria.

Author contributions

All authors made an equivalent contribution to the preparation of the publication.

Conflicts of interest

The authors declare that they have no known competing financial interests or personal relationships that could have influenced the work reported in this paper.

References

1. Sabbarao E. C. Zirconia - an overview. In: *Proc. First Int Conf.: Science and Technology of Zirconia*. Cleveland, Ohio; 1981. p. 1–24.
2. Fedorov P. P., Yarotskaya, E. G. Zirconium dioxide. Review. *Condensed Matter and Interphases*.

2021;23(2): 169–187. <https://doi.org/10.17308/kcmf.2021.23/3427>

3. Kuzminov Yu. S., Osiko V. V. *Fianites**. Moscow: Nauka Publ.; 2001. 280 p. (In Russ.)

4. Osiko V. V., Borik M. A., Lomonova E. E. Synthesis of refractory materials by skull melting. In: *Springer Handbook of Crystal Growth*. N.Y.: Springer; 2010. pp. 433–477. https://doi.org/10.1007/978-3-540-74761-1_14

5. Zhigachev A. O., Golovin Yu. I., Umrikhin A. V., ... Dyachek T. A. *Ceramic materials based on zirconium dioxide**. Golovin Yu. I. (ed.). Moscow: Tekhnosfera Publ.; 2018. 357 p. (In Russ.)

6. Kablov E. N. Strategic areas of developing materials and their processing technologies for the period to 2030. *Aviation Materials and Technologies*. 2012;S: 7–17. (In Russ., abstract in Eng.). Available at: <https://www.elibrary.ru/item.asp?id=18084815>

7. Kelly J. R., Denry I. Stabilized zirconia as a structural ceramics: An overview. *Dental Materials*. 2008;24(3): 289–298. <https://doi.org/10.1016/j.dental.2007.05.005>

8. Daou E. E. The zirconia ceramic: strengths and weaknesses. *The Open Dentistry Journal*. 2014;8(1): 33–42. <https://doi.org/10.2174/1874210601408010033>

9. Fedorov P. P., Popov P. A. Principle of equivalency of the disorder sources and heat conductivity of solid. *Nanosystems: Physics, Chemistry, Mathematics*. 2013;4(1): 148–159. (In Russ., abstract in Eng.). Available at: <https://www.elibrary.ru/item.asp?id=18964066>

10. Haering C., Roosen A., Schichl H., Schnoller M. Degradation of the electrical conductivity in stabilized zirconia system. Part. II: Scandia-stabilized zirconia. *Solid State Ionics*. 2005;176(3–4): 261–268. <https://doi.org/10.1016/j.ssi.2004.07.039>

11. Fergus J. F. Electrolytes for solid oxide fuel cells. *Journal of Power Sources*. 2006;162: 30–40. <https://doi.org/10.1016/j.jpowsour.2006.06.062>

12. Mahato N., Banerjee A., Gupta A., Omar S., Balani K. Progress in material selection for solid oxide fuel cell technology: A review. *Progress in Materials Science*. 2015;72: 141–337. <https://doi.org/10.1016/j.pmatsci.2015.01.001>

13. Borik M. A., Bredikhin S. I., Kulebyakin A. V., ... Tabachkova N. Yu. Melt growth, structure and properties of $(ZrO_2)_{1-x}(Sc_2O_3)_x$ solid solution crystals. *Journal of Crystal Growth*. 2016;443: 54–61. <https://doi.org/10.1016/j.jcrysgro.2016.03.004>

14. Clarke D. R., Phillpot S. R. Thermal barrier coatings. *Materials Today*. 2005;8(6): 22–29. [https://doi.org/10.1016/S1369-7021\(05\)70934-2](https://doi.org/10.1016/S1369-7021(05)70934-2)

15. Zhang H., Liu Zh., Yang X., Xie H. Interface failure behavior of YSZ thermal barrier coatings during thermal shock. *Journal of Alloys and Compounds*. 2019;779: 686–697. <https://doi.org/10.1016/j.jallcom.2018.11.311>

16. Degueldre C. Zirconia inert matrix for plutonium utilisation and minor actinides disposition in reactors. *Journal of Alloys and Compounds*. 2007;444-445: 36–41. <https://doi.org/10.1016/j.jallcom.2006.11.203>
17. Andrievskaya E. R. Phase equilibria in the refractory oxide systems of zirconia, hafnia and yttria with rare-earth oxides. *Journal of the European Ceramic Society*. 2008;28(12): 2363–2388. <https://doi.org/10.1016/j.jeurceramsoc.2008.01.009>
18. Andrievskaya E. R. *Phase equilibrium in systems of hafnium, zirconium, yttrium oxides with oxides of rare earth elements**. Kyiv: Naukova Dumka Publ.; 2010. (In Russ.)
19. Fedorov P. P. Determination of the annealing duration in the study of phase equilibrium in the solid state of binary systems*. *Russian Journal of Inorganic Chemistry*. 1992;37(8): 1891–1894. (In Russ.)
20. Fedorov P. P. Third law of thermodynamics as applied to phase diagrams. *Russian Journal of Inorganic Chemistry*. 2010;55: 1722–1739. <https://doi.org/10.1134/S0036023610110100>
21. Fedorov P. P., Alexandrov A. A., Voronov V. V., Mayakova M. N., Baranchikov A. E., Ivanov V. K. Low-temperature phase formation in the SrF_2 – LaF_3 system. *Journal of the American Ceramic Society*. 2021;104(6): 2836–2848. <https://doi.org/10.1111/jace.17666>
22. Fedorov, P. P., Chernova, E. V. The conditions for the solid state synthesis of solid solutions in zirconia and hafnia systems with the oxides of rare earth elements. *Condensed Matter and Interphases*. 2022;24(4): 537–544. <https://doi.org/10.17308/kcmf.2022.24/10558>
23. Sakka Y., Oishi Y., Ando K. Zr-Hf interdiffusion in polycrystalline Y_2O_3 – $(\text{Zr}+\text{Hf})\text{O}_2$. *Journal of Materials Science*. 1982;17: 3101–3105. <https://doi.org/10.1007/bf01203471>
24. Yashima M., Ishizawa N., Nama T., Yoshimura M. Stable and metastable phase relationships in the system ZrO_2 – $\text{ErO}_{1.5}$. *Journal of the American Ceramic Society*. 1991;74(3): 510–513. <https://doi.org/10.1111/j.1151-2916.1991.tb04052.x>
25. Yashima M., Kakihana M., Yoshimura M. Metastable-stable phase diagrams in the zirconia-containing systems utilized in solid-oxide fuel cell application. *Solid State Ionics*. 1996;86: 1131–1149. [https://doi.org/10.1016/0167-2738\(96\)00386-4](https://doi.org/10.1016/0167-2738(96)00386-4)
26. Duran P. The system erbia – zirconia. *Journal of the American Ceramic Society*. 1977;60: 510–513. <https://doi.org/10.1111/j.1151-2916.1977.tb14095.x>
27. Roy R. Aids in hydrothermal experimentation: II, Method of making mixtures for both “dry” and “wet” phase equilibrium studies. *Journal of the American Ceramic Society*. 1956;39(4): 145–146. <https://doi.org/10.1111/j.1151-2916.1956.tb14180.x>
28. Fedorov P. P., Nazarkin M. V., Zakalyukin R. M. On polymorphism and morphotropism of rare-earth sesquioxides. *Crystallography Reports*. 2002;47(2): 281–286. <https://doi.org/10.1134/1.1466504>
29. Almjasheva O. V., Smirnov A. V., Fedorov B. A., Tomkovich M. V., Gusarov V. V. Structural features of ZrO_2 – Y_2O_3 and ZrO_2 – Gd_2O_3 nanoparticles formed under hydrothermal conditions. *Russian Journal of General Chemistry*. 2014;84(5): 804–809. <https://doi.org/10.1134/S1070363214050028>
30. Shuklina A. I., Smirnov A. V., Fedorov B. A., Kirillova S. A., Almjasheva O. V. Structure of nanoparticles in the ZrO_2 – Y_2O_3 system, as obtained under hydrothermal conditions. *Nanosystems: Physics, Chemistry, Mathematics*. 2020;11(6): 729. <https://doi.org/10.17586/2220-8054-2020-11-6-729-738>
31. Fedorov P. P., Volkov S. N. Au–Cu Phase Diagram. *Russian Journal of Inorganic Chemistry*. 2016;61: 772–775. <https://doi.org/10.1134/S0036023616060061>
32. Fedorov, P.P., Shubin, Y.V. & Chernova, E.V. Copper–Palladium Phase Diagram. *Russian Journal of Inorganic Chemistry*. 2021;66: 891–893. <https://doi.org/10.1134/S0036023621050053>
33. Fedorov P. P., Popov A. A., Shubin Yu. V., Chernova E. V. Phase diagram of the nickel-platinum system*. *Russian Journal of Inorganic Chemistry*. 2022;67(12): 1805–1809. (In Russ.). <https://doi.org/10.31857/S0044457X22600748>
34. Abriata J. P., Laughlin D. E. The third law of thermodynamics and low temperature phase stability. *Progress in Materials Science*. 2004;49: 367–387. [https://doi.org/10.1016/s0079-6425\(03\)00030-6](https://doi.org/10.1016/s0079-6425(03)00030-6)
35. Hume-Rothery W., Raynor G. V. *The structure of metals and alloys*. London: The Inst. of metals; 1956.
36. Gusarov V. V., Semin E. G., Suvorov S. A. Calculation of thermodynamic parameters of solid solutions based on metal oxides. *Russian Journal of Applied Chemistry*. 1980;53(8): 1911–1914. (In Russ.)
37. Voronin G. F. New possibilities for thermodynamic calculation and phase diagram construction of heterogeneous systems. *Russian Journal of Physical Chemistry A*. 2003;77(10): 1685–1694. Available at: <https://www.elibrary.ru/item.asp?id=13425953>
38. Suvorov S. A., Semin E. G., Gusarov V. V. *Phase diagrams and thermodynamics of oxide solid solutions*. Leningrad: Leningrad University Publ.; 1986. 140 p.
39. Degtyarev S. A., Voronin G. F. Solution of ill-posed problems in thermodynamics of phase equilibria. The ZrO_2 – Y_2O_3 system. *Calphad*. 1988;12(1): 73–82. [https://doi.org/10.1016/0364-5916\(88\)90031-4](https://doi.org/10.1016/0364-5916(88)90031-4)
40. Degterevev S. A., Voronin G. F. Solution of ill-posed problems of thermodynamics of phase equilibria. I System ZrO_2 – Y_2O_3 *. *Zhurnal Fizicheskoi Khimii*. 1987;61(3): 611–616. (In Russ.)

41. Zaitseva I. A., Skolis Yu. Ya. Partial thermodynamic functions of yttrium-oxide in c.s.s. solutions of the ZrO_2 - Y_2O_3 system*. *Zhurnal Fizicheskoi Khimii*. 1990;64(1): 251–253. (In Russ.)
42. Zaitseva I. A., Dobrokhotova Zh. V. Thermodynamic functions of zirconium oxide in fluorite-like solutions of the ZrO_2 - Y_2O_3 system*. *Inorganic Materials*. 1994;30(7): 955–958. (In Russ.)
43. Degtyarev S.A., Voronin G.F. Calculation of the phase diagram in the ZrO_2 - Y_2O_3 system*. *Zhurnal Fizicheskoi Khimii*. 1987;61(3): 617–622. (In Russ.)
44. Du Y., Jin Z., Huang P. Thermodynamic assessment of the ZrO_2 - $YO_{1.5}$ system. *Journal of the American Ceramic Society*. 1991;74: 1569–1577. <https://doi.org/10.1111/j.1151-2916.1991.tb07142.x>
45. Jacobson N. S., Liu Z.-K., Kaufman L., Zhang F. Thermodynamic modeling of $YO_{1.5}$ - ZrO_2 system. *Journal of the American Ceramic Society*. 2004;87: 1559–1566. <https://doi.org/10.1111/j.1551-2916.2004.01559.x>
46. Chen M., Hallstedt B., Gauckler L. J. Thermodynamic modeling of the ZrO_2 - $YO_{1.5}$ system. *Solid State Ionics*. 2004;170: 255–274. <https://doi.org/10.1016/j.ssi.2004.02.017>
47. Duwez P., Brown F.H., Odell F. The zirconia-yttria system. *Journal of the Electrochemical Society*. 1951;98(9): 356–362. <https://doi.org/10.1149/1.2778219>
48. Rouanet A. Contribution a l'étude des systems zircon-oxyles des lanthanides au voisinage de la fusion. *Revue Internationale Des Hautes Temperatures et Des Refractaires*. 1971;8: 161–180.
49. Noguchi T., Mizuno M., Yamada T. The liquidus curve of the ZrO_2 - Y_2O_3 system as measured by a solar furnace. *Bulletin of the Chemical Society of Japan*. 1970;43: 2614–2616. <https://doi.org/10.1246/bcsj.43.2614>
50. Shevchenko A. V., Tkachenko V. D., Lopato L. M., Ruban A. K., Pasichnyi V. V. A method of determining phase-transition temperatures using solar heating. *Soviet Powder Metallurgy and Metal Ceramics*. 1986;25(1): 79–82. <https://doi.org/10.1007/bf00843028>
51. Pascual C., Duran P. Subsolidus Phase Equilibria and ordering in the system ZrO_2 - Y_2O_3 . *Journal of the American Ceramic Society*. 1983;66: 23–28. <https://doi.org/10.1111/j.1151-2916.1983.tb09961.x>
52. Stubican V. S., Corman G. S., Hellmann J. R., Sent G. Phase relationships in some ZrO_2 system. In: *Advanced in Ceramics*. N. Clausen, A. Ruhle, A. Heuer (eds.). Columbus: American Ceramic Soc Inc; 1984;12: 96–106.
53. Gaboriaud R. J., Paumier F., Lacroix B. Disorder-order phase transformation in a fluorite-related oxide film: in situ diffraction and modeling of the residual stress effects. *Thin Solid Films*. 2016;601: 84–88. <https://doi.org/10.1016/j.tsf.2015.08.030>
54. Fedorov P. P. T - x phase diagrams of binary systems in the condensed state: I. Equilibrium of four phases. *Russian Journal of Physical Chemistry*. 1999;73(9): 1381–1386.
55. Thornber M. R., Bevan D. J. M., Graham J. Mixed oxides of the type MO_2 fluorite- M_2O_3 . III crystal structures of the intermediate phases $Zr_5Sc_2O_{15}$ and $Zr_3Sc_2O_{12}$. *Acta Crystallographica Section B Structural Crystallography and Crystal Chemistry*. 1968;24(9): 1183–1190. <https://doi.org/10.1107/s0567740868003948>
56. Thornber M. R., Bevan D. J. M., Summerville E. Mixed oxides of the type MO_2 Fluorite- M_2O_3 . V. Phase studies in the systems ZrO_2 - M_2O_3 ($M = Sc, Yb, Er, Dy$). *Journal of Solid State Chemistry*. 1970;1: 545–553. [https://doi.org/10.1016/0022-4596\(70\)90140-4](https://doi.org/10.1016/0022-4596(70)90140-4)
57. Spiridonov F. M., Popova L. N., Popil'skii R. Ya. On the phase relations and electrical conductivity in the system ZrO_2 - Sc_2O_3 . *Journal of Solid State Chemistry*. 1970;2(3): 430–438. [https://doi.org/10.1016/0022-4596\(70\)90102-7](https://doi.org/10.1016/0022-4596(70)90102-7)
58. Sekiya T., Yamada T., Hayashi H., Noguchi T. High temperature phase in the ZrO_2 - Sc_2O_3 system. *Nippon Kagaku Kaishi*. 1974;9: 1629–1636 (in Japan). <https://doi.org/10.1246/nikkashi.1974.1629>
59. Ruh R., Garrett H. J., Domagala R. F., Patel V. A. The system zirconia-scandia. *Journal of the American Ceramic Society*. 1977;60(9-10): 399–403. <https://doi.org/10.1111/j.1151-2916.1977.tb15521.x>
60. Shevchenko A. V., Maister I. M., Lopato L. M. Interaction in the HfO_2 - Sc_2O_3 and ZrO_2 - Sc_2O_3 systems at high temperatures. *Izvestiya Akademii Nauk SSSR. Neorganicheskie Materialy*. 1986;23(8): 1320–1324.
61. Zyryin A. V., Red'ko V. P., Lopato L. M., Shevchenko A. V. Ordered phases in the ZrO_2 - Sc_2O_3 and HfO_2 - Sc_2O_3 systems. *Izvestiya Akademii Nauk SSSR. Neorganicheskie Materialy*. 1987;23(8): 1326–1329.
62. Lopato L. M., Red'ko V. P., Gerasimiyuk G. I., Shevchenko A. V. Synthesis of some REE zirconates (hafnates). *Soviet Powder Metallurgy and Metal Ceramics*. 1990;29(4): 318–320. <https://doi.org/10.1007/bf00797236>
63. Maister I. M., Lopato L. M., Zaitseva Z. A., Shevchenko A. V. Interaction in the ZrO_2 - Y_2O_3 - Sc_2O_3 system at 1300–1900 °C. *Izvestiya Akademii Nauk SSSR. Neorganicheskie Materialy*. 1991;27(11): 2337–2340.
64. Sheu T.-S., Xu J., Tien T.-Y. Phase relationships in the ZrO_2 - Sc_2O_3 and ZrO_2 - In_2O_3 systems. *Journal of the American Ceramic Society*. 1993;76(8): 2027–2032. <https://doi.org/10.1111/j.1151-2916.1993.tb08328.x>
65. Fujimori H., Yashima M., Kakihana M., Yoshimura M. Structural changes of scandia-doped zirconia solid solutions: Rietveld analysis and Raman scattering. *Journal of the American Ceramic Society*. 2005;81(11): 2885–2893. <https://doi.org/10.1111/j.1151-2916.1998.tb02710.x>
66. Fujimori H., Yashima M., Kakihana M., Yoshimura M. β -cubic phase transition of scandia-

- doped zirconia solid solution: Calorimetry, X-ray diffraction, and Raman scattering. *Journal of Applied Physics*. 2002;91: 6493–6498. <https://doi.org/10.1063/1.1471576>
67. Rossell H. J. Crystal structure of some fluorite-related M_7O_{12} compounds. *Journal of Solid State Chemistry*. 1976;19(2): 103–111. [https://doi.org/10.1016/0022-4596\(76\)90156-0](https://doi.org/10.1016/0022-4596(76)90156-0)
68. Wurst K., Schweda E., Bevan D. J. M., Mohyla J., Wallwork K. S., Hofmann M. Single-crystal structure determination of $Zr_{50}Sc_{12}O_{118}$. *Solid State Sciences*. 2003;5: 1491–1497. <https://doi.org/10.1016/j.solidstatesciences.2003.09.008>
69. Meyer S., Schweda E., Meta N. J. M., Boysen H., Hoelzel M., Bredow T. Neutron powder diffraction study and DFT calculations of the structure of $Zr_{10}Sc_4O_{26}$. *Zeitschrift für Kristallographie*. 2009;224: 539–543. <https://doi.org/10.1524/zkri.2009.1218>
70. Ma C., Beckett J. R., Rossman G. R. Allendeite ($Sc_4Zr_3O_{12}$) and hexamolybdenum (Mo, Ru, Fe), two new minerals from an ultrarefractory inclusion from the Allende meteorite. *American Mineralogist*. 2014;99(4): 654–666. <https://doi.org/10.2138/am.2014.4667>
71. Fedorov P. P., Chernova E. V. Distribution coefficients of rare-earth oxides in zirconium dioxide melt crystallization. *Inorganic Materials*. 2021;57(9): 901–905. <https://doi.org/10.1134/s0020168521090089>
72. Fedorov P. P., Turkina T. M., Lyamina O. I., Tarasova E. V., Zibrov I. P., Sobolev B. P. Calculation of impurity distribution coefficients from liquidus curves of binary systems MF_2 - RF_3 . *Vysokochistye veshchestva*. 1990;6: 67–72. (In Russ.)
73. Ivanov S. P., Buchinskaya I. I., Fedorov P. P. Distribution coefficients of impurities in cadmium fluoride. *Inorganic Materials*. 2000;36(4): 392–396. <https://doi.org/10.1007/BF02758088>
74. Chase M. W., Davies C. A., Downey J. R., McDonald R. A., Syverud A. N., Valenzuela E. A. JANAF thermochemical tables. *Journal of Physical and Chemical Reference Data*. 1982;11(3): 695–940. <https://doi.org/10.1063/1.555666>
75. Fedorov P. P., Sobolev B. P. Conditions for the formation of maxima on the fusion curves of solid solutions in salt systems. *Russian Journal of Inorganic Chemistry*. 1979;24(4): 572–575.
76. Fedorov P. P. Heterovalent isomorphism and solid solutions with a variable number of ions in the unit cell. *Russian Journal of Inorganic Chemistry*. 2000;45: S268–S291.
77. Zinkevich M., Djurovic D., Aldinger F. Thermodynamic modeling of the cerium-oxygen system. *Solid State Ionics*. 2006;177: 989–1001. <https://doi.org/10.1016/j.ssi.2006.02.044>
78. Pascual C., Duran P. Phase equilibria and ordering in the erbia-zirconia system. *Journal of Materials Science*. 1981;16: 3067–3076. <https://doi.org/10.1007/bf00540314>
79. Fedorov P. P., Alexandrov A. A., Voronov V. V., Mayakova M. N., Baranchikov A. E., Ivanov V. K. Low-temperature phase formation in the SrF_2 - LaF_3 system. *Journal of the American Ceramic Society*. 2021;104(6): 2836–2848. <https://doi.org/10.1111/jace.17666>
80. Bredig M. A. The order-disorder (λ) transition in UO_2 and other solids of the fluorite type of structure. *Colloq. Inter. CNRS*. 1972;205: 183–197.
81. Fossati P. C. M., Chartier A., Boule A. Structural aspects of the superionic transition in AX_2 compounds with the fluorite structure. *Frontiers in Chemistry*. 2021;9: N723507. <http://doi.org/10.3389/fchem.2021.723507>
82. Hoekstra H. R., Siegel S., Gallagher X. The uranium-oxygen system at high pressure. *Journal of Inorganic and Nuclear Chemistry*. 1970;32: 3237–3248. [https://doi.org/10.1016/0022-1902\(70\)80206-8](https://doi.org/10.1016/0022-1902(70)80206-8)
83. Cooper M. W. D., Murphy S. T., Rushton M. J. D., Grimes R. W. Thermophysical properties and oxygen transport in the $(U_xPu_{1-x})O_2$ lattice. *Journal of Nuclear Materials*. 2015;461: 206–214. <https://doi.org/10.1016/j.jnucmat.2015.03.024>
84. Annamareddy A., Eapen J. Disordering and dynamic self-organization in stoichiometric UO_2 at high temperatures. *Journal of Nuclear Materials*. 2017;463: 132–141. <https://doi.org/10.1016/j.jnucmat.2016.10.042>
85. Annamareddy A., Eapen J. Low dimensional string-like relaxation underpins superionic conduction in fluorites and related structures. *Scientific Reports*. 2017; 7:44149. <https://doi.org/10.1038/srep44149>

Information about the authors

Pavel P. Fedorov, Dr. Sci. (Chem.), Full Professor, Chief Researcher, Prokhorov General Physics Institute of the Russian Academy of Sciences (Moscow, Russian Federation).

<https://orcid.org/0000-0002-2918-3926>
ppfedorov@yandex.ru

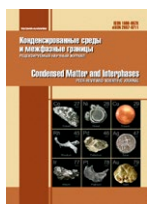
Elena V. Chernova, Junior Researcher, Prokhorov General Physics Institute of the Russian Academy of Science (Moscow, Russian Federation).

<https://orcid.org/0000-0001-7401-5019>
e-chernova@yandex.ru

Received 20.03.20223; approved after reviewing 18.04.2023; accepted for publication 15.05.2023; published online 25.06.2023.

Translated by Valentina Mittova

Edited and proofread by Simon Cox



Original articles

Research article

<https://doi.org/10.17308/kcmf.2023.25/11107>

Organic fouling of anion-exchange and bipolar membranes during the separation of amino acid and sucrose by electrodialysis

A. Yu. Kharina[✉], O. E. Charushina, T. V. Eliseeva

Voronezh State University,
1 Universitetskaya pl., Voronezh 394018, Russian Federation

Abstract

The article presents a study of the behaviour of the MA-41 anion-exchange membrane and MB-2 bipolar membrane during the electrodialysis of a solution containing tyrosine and sucrose. It establishes changes in current-voltage, transport, and structural characteristics of ion-exchange membranes. The study of the evolution of membrane characteristics during a prolonged contact with solutions containing an aromatic amino acid and disaccharide is aimed at providing a deeper understanding of and finding solutions to the problem of organic fouling of membranes, which complicates the electromembrane separation of components of the solution during microbiological synthesis of amino acids.

It was found that the fluxes of tyrosine and sucrose through the MA-41 membrane measured after its operation during 50-hour electrodialysis reach higher values than during the first hours of operation after the system reaches a steady state. However, it was noted that when the membrane continues to be used, the flux of components through the MA-41 membrane decreases. What is more, this change is pronounced with a high current density.

This decrease in mass transport, an increased voltage drop on the MB-2 and MA-41 membranes, and lower values for the effective OH⁻ ion transport number for the MA-41 membrane are associated with the phenomenon of organic fouling confirmed by revealed structural changes in the ion-exchange material, which become significant after a prolonged contact (more than 60 hours) with a mixed solution of tyrosine and sucrose. These changes are associated with the accumulation of an amino acid and its oxidation product, 3,4-dihydroxyphenylalanine, in the membrane phase, as well as with a decrease in the content of sucrose absorbed by the membrane.

Keywords: Electrodialysis, Separation, Ion-exchange membrane, Tyrosine, Sucrose, Organic fouling

Funding: The study was supported by the Russian Science Foundation, project No. 22-29-01480.

The IR spectra of the membrane samples were obtained using the equipment of the Centre for Collective Use of Scientific Equipment of Voronezh State University. URL: <http://ckp.vsu.ru>.

For citation: Kharina A. Yu., Charushina O. E., Eliseeva T. V. Organic fouling of anion-exchange and bipolar membranes during the separation of amino acid and sucrose by electrodialysis. *Condensed Matter and Interphases*. 2023;25(2): 268–276. <https://doi.org/10.17308/kcmf.2023.25/11107>

Для цитирования: Харина А. Ю., Чарушина О. Е., Елисеева Т. В. Органическое отравление анионообменной и биполярной мембран при разделении аминокислоты и сахарозы методом электродиализа. *Конденсированные среды и межфазные границы*. 2023;25(2): 268–276. <https://doi.org/10.17308/kcmf.2023.25/11107>

✉ Anastasiia Yu. Kharina, e-mail: aukharina@gmail.com
© Kharina A. Yu., Charushina O. E., Eliseeva T. V., 2023



1. Introduction

Amino acids in the form of pure compounds are in great demand in the food, medical, pharmaceutical, and biotechnology industries. They are used as nutrient additives, such as seasonings and flavourings, growth feed supplements, and pharmaceutical preparations to treat various diseases. The demand for amino acids continues to grow. Currently, L-amino acids are produced by microorganisms (by fermentation). However, their processing and extraction from fermentation broths can be challenging and inefficient [1, 2].

Membrane technologies offer a promising solution to the extraction of amino acids. Their implementation is attractive due to the fact that there is a wide range of materials that can be used to produce membranes with certain required properties and there are various ways of controlling the parameters of membrane processes. Electromembrane technologies use ion-exchange membranes and the electrical potential gradient as the driving force of mass transport of charged particles. These technologies have such important advantages as the possibility of separating components with different charges, they require no reagents, are environmentally friendly, and relatively inexpensive [3–5]. Electrodialysis with ion-exchange membranes provides a tool for the separation of electrolytes and non-electrolytes, desalination, and concentration of electrolyte solutions. This method is often used in food industry for the deionisation of various intermediates and food products and for demineralisation of wastewater, sea and brackish water, desalination of tobacco leaf extract, extraction of lactic acid and amino acids from the juice of grass silage, etc. [6–12]. Bipolar membrane electrodialysis is used to obtain acids and bases from salts, to perform other chemical transformations, to separate electrolytes and non-electrolytes, to deoxidise certain foods, to separate mixtures of organic and inorganic acids, and to produce highly purified water [13–15]. Some works consider the separation of amino acids and their isolation from impurities remaining after synthesis, mineral salts and carbohydrates [16–19].

Ion-exchange membranes are modern materials and have a wide range of applications

[20–23]. To effectively use bipolar and monopolar membranes for amino acids extraction from solutions, it is important to understand changes in the structural, transport, and current-voltage characteristics of these polymer materials since when ion-exchange membranes come into contact with organic substances, there might appear undesirable side interactions.

The long-term use of ion-exchange materials in solutions of amino acids and a number of other organic substances can complicate electromembrane processes due to organic fouling, which causes changes in the electrochemical, transport, and structural characteristics of membranes [24–26]. Biological fouling is also a possibility [27].

The study of the properties of membranes used in electromembrane systems for a long time is very important since currently there is not enough data on the characteristics of ion-exchange membranes that come in durable contact with aromatic amino acid solutions.

Therefore, the purpose of this study was to assess changes in the current-voltage, transport, and structural characteristics of anion-exchange and bipolar membranes during prolonged electrodialysis of a solution of an aromatic amino acid (tyrosine) and disaccharide (sucrose).

2. Experimental

Changes in the current-voltage and transport characteristics of ion-exchange membranes were studied during a prolonged electrodialysis of model solutions of an aromatic amino acid, i.e. tyrosine (Sigma-Aldrich, Burlington, USA) ($C = 0.0025M$) and sucrose (Sigma-Aldrich, Burlington, USA) ($C = 0.02M$) in a seven-compartment laboratory apparatus (Fig. 1) for 60 hours. We used the L-optical isomer of tyrosine, an amino acid that contains a para-hydroxyphenylmethyl side radical in its structure. Some physicochemical properties of tyrosine are given in Table 1.

Electrodialysis compartment 4 had an anion-exchange and bipolar membrane. The anion-exchange layer of the bipolar membrane faced section 4. The working area of the membranes was 20 cm^2 . The height of the apparatus was 20 cm, the intermembrane distance was 10 mm, and the linear fluid flow rate was $0.05\text{ cm}\cdot\text{s}^{-1}$. The anode

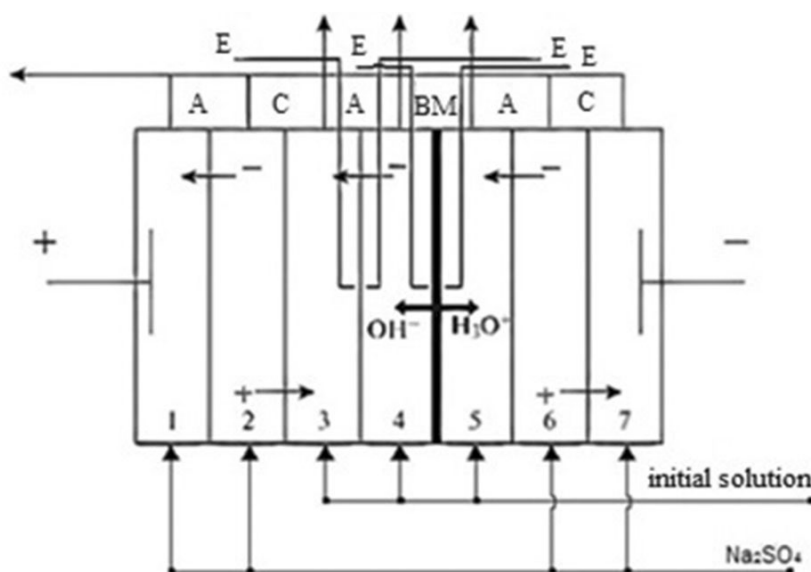
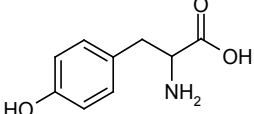


Fig. 1. Seven-compartment electro dialysis cell with alternating cation (C)- and anion (A)-exchange membranes, BM – bipolar ion-exchange membrane, ‘+’ – cation, ‘-’ – anion, E – Pt electrodes

Table 1. Physicochemical properties of the amino acid studied [28–30]

Amino Acid	Structure	pI	pK			Molecular Weight	Solubility, g/100 mL H ₂ O, 25 °C	Side Radical Volume, nm ³
			pK ₁	pK ₂	pK ₃			
Tyrosine (Tyr)		5.63	2.20	9.11	10.07	181.19	0.045	0.1388

was made of platinum, while the cathode was made of stainless steel.

We used an MA-41 heterogeneous anion-exchange membrane, an MK-40 cation-exchange membrane, and an MB-2 bipolar membrane manufactured by LLC *Shchekinoazot*. These heterogeneous membranes have a styrene-divinylbenzene matrix. The structure of the MA-41 anion-exchange membrane includes quaternary ammonium base groups, whereas the MK-40 membrane has sulpho groups. The MB-2 bipolar membrane is manufactured using the MA-41 and MK-40 membranes [31].

A mixed solution of tyrosine (Tyr) and sucrose (Suc) entered compartments 3, 4, and 5 of the electro dialysis apparatus. A sodium sulphate solution ($C = 0.1\text{M}$) (ZAO *Vekton*, Saint Petersburg, Russia) was supplied to compartments 1, 2, 6, and 7 of the apparatus. The analysis was performed for solutions flowing from sections 3, 4.

The changes in current-voltage characteristics (CVC) of bipolar and anion-exchange membranes during electro dialysis were detected using a V7-26 voltmeter. Platinum electrodes were placed near the studied membrane surfaces at a distance of 0.2 mm on each side.

The UV spectroscopy was used for the quantitative determination of Tyr [32], while Suc was analysed by a photometric method based on the sucrose oxidation in acidic medium with potassium dichromate to CO₂ applying the calibration curve procedure [33].

The substance flux through the ion-exchange membrane was calculated according to formula (1) [22]:

$$J = C \cdot V \cdot \tau^{-1} \cdot S^{-1}, \quad (1)$$

where J is the flux through the ion-exchange membrane, mol·cm⁻²·s⁻¹; C is the concentration of the solution, mol·dm⁻³; V is the sample volume, dm³; τ is the sampling time, s; and S is the working area of the ion-exchange membrane, cm².

The effective hydroxyl ion transport number was determined by equation (2) [22]:

$$T = z \cdot F \cdot J \cdot i^{-1}, \quad (2)$$

where T is the effective transport number; F is the Faraday constant, $\text{C} \cdot \text{mol}^{-1}$; z is the ion charge; i is the current density, $\text{A} \cdot \text{cm}^{-2}$; and J is the flux of OH^- ions, $\text{mol} \cdot \text{cm}^{-2} \cdot \text{s}^{-1}$.

The pH of the studied solutions was measured using an I-160MI electronic pH-meter which had been calibrated by buffer solutions (pH = 1.65, pH = 9.18). The pH of the solutions supplied to compartment 4 was within 5.5–5.9, which was close to the isoelectric point of tyrosine.

The structural changes in the ion-exchange membranes which came in contact with solutions containing an aromatic amino acid were investigated by IR spectroscopy. The membrane samples were pre-dried at 50°C , crushed, and compressed with KBr into tablets at a ratio of 1 to 100. The spectra were obtained using a Vertex 70 IR-Fourier spectrometer, Bruker Optik GmbH (Germany).

3. Results and discussion

To assess the effect of the interactions of an aromatic amino acid, sucrose, and ion-exchange material under the action of the electrical potential gradient, we studied the changes in transport characteristics of the MA-41 membrane during the prolonged bipolar

membrane electro dialysis of a solution containing tyrosine and sucrose (Fig. 2a, b). Figure 2 shows the dependences of the component fluxes through the MA-41 membrane on the current density for the “pristine” membrane after the steady state was reached and for the samples of membranes after they had been used for 50 and 60 hours without washing.

At the initial section of the obtained dependencies, there was a gradual increase in tyrosine flux with increasing current density followed by a “plateau” at a current density of $i = 1.0\text{--}2.3 \text{ mA} \cdot \text{cm}^{-2}$. Then, the amino acid mass transport continued to grow with a higher current density (Fig. 2a). The absence of decreasing fluxes through the MA-41 membrane in the area of the “barrier effect” observed in a system with alternating monopolar membranes was due to the intensive generation of hydrogen and hydroxyl ions by the bipolar membrane, which led to the conversion of tyrosine bipolar ions into anions in the compartment 4 even with a low current. At a higher current density, there was an increase in the slope angle of the considered dependencies $J - i$, which is associated with an increased electrical convection contributions and an increased effect of facilitated electromigration [34, 35]. There was a slight increase in the disaccharide flux with an increase in current density (Fig. 2b) since sucrose

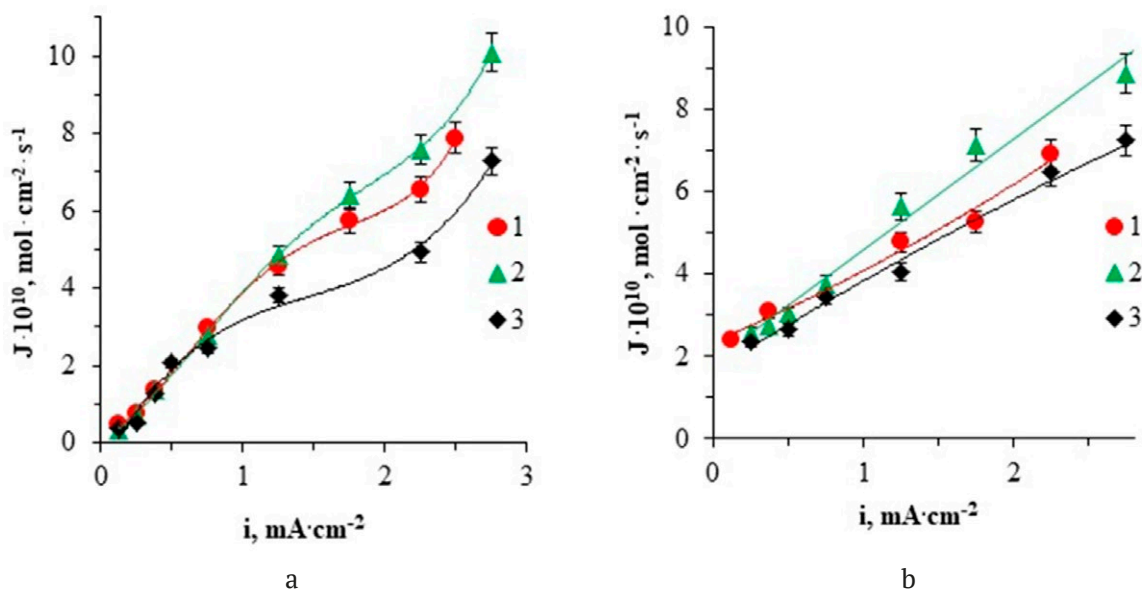


Fig. 2. Dependence of Tyr (a) and Suc (b) fluxes through the MA-41 membrane on the current density in electro dialysis of Tyr + Suc solution: 1 – membrane after establishment of a steady state (“pristine” membrane), 2 – membrane after 50 hours of operation, 3 – membrane after 60 hours of operation

is a weak electrolyte with an acid dissociation constant of about 10^{-15} [30].

These dependencies mean that the tyrosine and sucrose fluxes through the anion-exchange membrane, which has been used for 50 hours, reach higher values as compared to the “pristine” membrane sample (Fig. 2a, b). These changes are due to the mass transport of quite large hydrated organic substances which changes the porosity of the membrane: pores of a larger radius appear in the membrane as compared to a “new” membrane [36].

However, if membranes continued to be used with a high current density, the fluxes of these components through the MA-41 membrane decreased. The dependences of the amino acid flux through the MA-41 membrane on the electro dialysis duration with different values of current density are shown in Fig. 3. It was obvious that with a high current density, the tyrosine flow through the membrane, which had been used for a long time in a solution containing an amino acid and disaccharide, started to decrease after 50 hours of operation.

This may be due to the gradual organic fouling of ion-exchange membranes that were in contact with a solution of tyrosine and sucrose during the electro dialysis.

We also recorded changes in the current-voltage characteristics of ion-exchange

membranes during a prolonged electro dialysis of the Tyr + Suc solution. There was an increased voltage drop for both MA-41 and MB-2 membranes after 50 hours of operation. CVCs for MB-2 membranes at different operating times are shown in Fig. 4a. The changes may be explained by the shielding of the functional groups of the studied membranes with amino acid and sucrose molecules that block the membrane pores which impede the reaction of water dissociation due

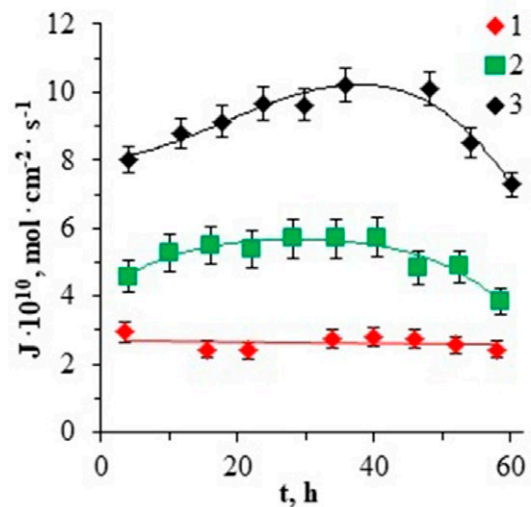


Fig. 3. Dependence of Tyr fluxes through the MA-41 membrane on time in electro dialysis of Tyr + Suc solution: 1 – at $0.75 \text{ mA} \cdot \text{cm}^{-2}$, 2 – $1.25 \text{ mA} \cdot \text{cm}^{-2}$, 3 – $2.75 \text{ mA} \cdot \text{cm}^{-2}$

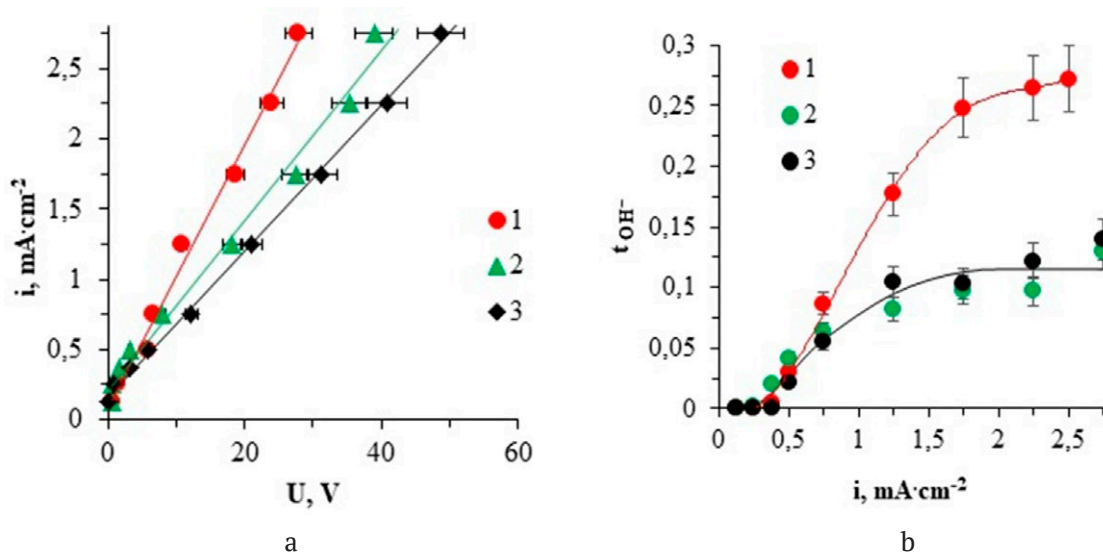


Fig. 4. Current-voltage characteristics of MB-2 (a) membranes and dependence of the effective transport numbers of OH^- ions for the MA-41 membrane on the current density (b) in long-term electro dialysis of Tyr + Suc solution: 1 – «pristine» membrane, 2 – membrane after 50 hours of operation; 3 – membrane after 60 hours of operation

to a decrease in the catalytic activity of the functional groups of the membranes in relation to the reaction of water dissociation. In case of the MA-41 anion-exchange membrane used for a long time during electro dialysis, this fact was confirmed by a decrease in the effective hydroxyl ion transport number (Fig. 4b).

The CVC of the MB-2 membrane (Fig. 4a) did not show the presence of three traditional sections characteristic of the MA-41 monopolar membrane [22]. This is due to the fact that when any current flows through the bipolar membrane, water molecules dissociate at the inner boundary separating the cation-exchange and anion-exchange parts of the membrane.

In addition, we recorded a change in the total cell voltage during a prolonged electro dialysis without washing (regeneration) of ion-exchange membranes. As the time of the membranes' contact with a solution containing an aromatic amino acid and a carbohydrate increased, the total voltage in the system increased at the same value of the current.

Figure 5 shows the recorded dependences of the pH of the solution in the compartment 4 on the operation time of the membranes. The obtained results show that after 50 hours of the membranes' operation without regeneration, lower pH values of the solution in the compartment 4 were achieved. This is due to a decrease in

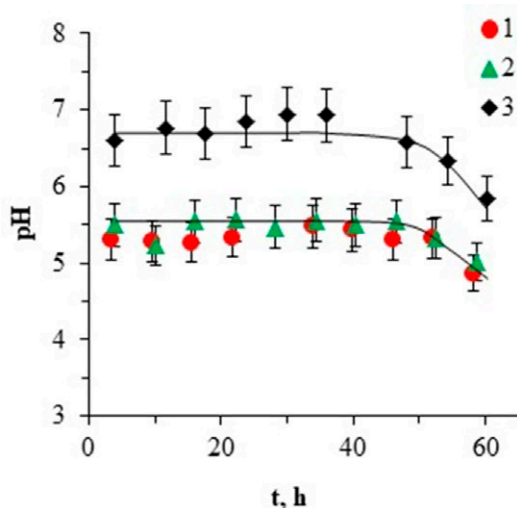


Fig. 5. Time dependence of pH for the compartment 4 output in long-term electro dialysis of Tyr + Suc solution: 1 – at $0.75 \text{ mA}\cdot\text{cm}^{-2}$, 2 – $1.25 \text{ mA}\cdot\text{cm}^{-2}$, 3 – $2.75 \text{ mA}\cdot\text{cm}^{-2}$

the generation of hydroxyl ions by the MB-2 membrane over time and indicates fouling of the anion-exchange layer of the bipolar membrane.

The study revealed that the changes in the transport and current-voltage characteristics of the membranes were accompanied by changes in their structure. We studied samples of the MA-41 anion-exchange membrane, whose structure was identical to the anion-exchange layer of the MB-2 bipolar membrane: in the basic form, in the form that adsorbed the components from the Tyr + Suc solution, and the “fouled” membrane after its prolonged contact with the solution for 10 days.

On the IR spectra of the MA-41 membrane, the presence of tyrosine in the membrane phase after sorption from the Tyr + Suc solution was confirmed by the absorption bands at 1157 cm^{-1} (Tyr phenolate ion), 1573 , and 1257 cm^{-1} (carboxylate ion). An increase in the intensity of these maxima after 10 days of the membrane's contact with a solution containing an amino acid and sucrose indicates the accumulation of tyrosine in the membrane phase. In addition, on the IR spectrum of the membrane which was in a prolonged contact with a Tyr + Suc solution for 10 days, there was a new peak of 1595 cm^{-1} , which may indicate the appearance of 3,4-dihydroxyphenylalanine, the product of tyrosine oxidation, in the membrane phase.

After the membrane adsorbed Suc from a mixed solution of amino acid and carbohydrate, there were bands on the spectra at 1635 cm^{-1} (C-O) and at 1307 , 1257 , and 1089 cm^{-1} (C-O-C group). In addition, the intensity of the band increased at 3425 cm^{-1} (OH group). These changes indicate the presence of disaccharide in the membrane phase. After 10 days of contact with the studied solution, on the IR spectrum, there was a decrease in the intensity of the bands at 1635 cm^{-1} (C-O), and 1307 , 1257 , and 1089 cm^{-1} (C-O-C group), which indirectly indicates a decrease in the content of disaccharide in the phase of the ion-exchange membrane.

4. Conclusions

The article presents the study of the behaviour of the MA-41 anion-exchange membrane and MB-2 bipolar membrane during the electro dialysis of a solution containing tyrosine and sucrose.

The study revealed an increased voltage drop on the membranes during a prolonged electro dialysis. These changes can be due to the shielding of the functional groups of the MB-2 membrane with an amino acid and sucrose, as well as blocking of the membrane pores, which impede the reaction of water dissociation.

It was found that the flux of tyrosine and sucrose during electro dialysis reaches higher values when it passes through the MA-41 membrane, which has been used for 50 hours rather than through the “pristine” membrane. The transport characteristics of the membrane increase due to changes in the porosity and moisture content of the membrane during its contact with highly hydrated organic substances. However, further usage of membranes leads to a reduction in the flux of amino acids and sucrose through the MA-41 membrane with a high current density. A reduction in the mass transport of components through the MA-41 membrane, an increase in the resistance of the MB-2 membrane, as well as the detected decrease in the achieved values of the effective OH⁻ ion transport number for the studied membranes during their operation are associated with the phenomenon of organic fouling accompanied by detected structural changes that occur after a prolonged contact (over 50 hours) with a mixed solution of tyrosine and sucrose and that manifest themselves in the retention of an amino acid and its oxidation product, 3,4-dihydroxyphenylalanine, in the membrane phase, and in a decrease in the sucrose content in the membrane phase.

Contribution of the authors

A. Yu. Kharina – preparation of the review, discussion of the results, writing and editing the text. O. E. Charushina – conducting research, writing the text. T. V. Eliseeva – scientific guidance, concept of the study, discussion of the results.

Conflict of interests

The authors declare that they have no known competing financial interests or personal relationships that could have influenced the work reported in this paper.

References

1. Samonina A. S. Obtaining amino acids by the biotechnological method. Production stages.

Application in medical practice*. In: *Actual issues of pharmaceutical and natural sciences: Collection of articles of the All-Russian student scientific and practical conference with international participation, May 17–21, 2021, Irkutsk*. Irkutsk: Irkutsk State Medical University Publ.; 2021, p. 313–316. (In Russ.). Available at: <https://elibrary.ru/item.asp?id=46592328>

2. Suwal Sh. Doyen A., Bazinet L. Characterization of protein, peptide and amino acid fouling on ion-exchange and filtration membranes: review of current and recently developed methods. *Journal of Membrane Science*. 2015;496: 267–283. <https://doi.org/10.1016/j.memsci.2015.08.056>

3. Bykov V. I., Ilyina S. I., Loginov V. Ya., Ravi-chev L. V., Svitzov A. A. Electro dialysis: history and development prospects. *Bulletin of the Technological University*. 2021;24(7): 5–10. (In Russ., abstract in Eng.). Available at: <https://elibrary.ru/item.asp?id=46423712>

4. Xu T., Huang C. Electro dialysis-based separation technologies: a critical review. *AIChE Journal*. 2008;54: 3147–3159. <https://doi.org/10.1002/aic.11643>

5. Lazarova Z., Beschkov V., Velizarov S. Electro-membrane separations in biotechnology. *Physical Sciences Reviews*. 2020;5: 1–11. <https://doi.org/10.1515/psr-2018-0063>

6. Wang M., Kuang S., Wang X., ... Zhang Y. Transport of amino acids in soy sauce desalination process by electro dialysis. *Membranes*. 2021;11(6): 408. <https://doi.org/10.3390/membranes11060408>

7. Zeppenfeld S., van Pinxteren M., Engel A. A protocol for quantifying mono- and polysaccharides in seawater and related saline matrices by electro-dialysis (ED) – combined with HPAEC-PAD. *Ocean Science*. 2020;16: 817–830. <https://doi.org/10.5194/os-2020-2>

8. Ge S., Zhang Z., Yan H., ... Wang Y. Electro dialytic desalination of tobacco sheet extract: membrane fouling mechanism and mitigation strategies. *Membranes*. 2020;11: 14. <https://doi.org/10.3390/membranes10090245>

9. Thang V. H., Koschuh W., Kulbe K. D. Desalination of high salt content mixture by two-stage electro dialysis as the first step of separating valuable substances from grass silage. *Desalination*. 2004;162(1-3): 343–353. [https://doi.org/10.1016/S0011-9164\(04\)00068-2](https://doi.org/10.1016/S0011-9164(04)00068-2)

10. Bazinet L., Geoffroy T. R. Electro dialytic processes: market overview, membrane phenomena, recent developments and sustainable strategies. *Membranes*. 2020;10: 221. <https://doi.org/10.3390/membranes10090221>

11. Campione A., Gurreri L., Ciofalo M., Micale G., Tamburini A., Cipollina A. Electro dialysis for water desalination: a critical assessment of recent developments on process fundamentals, models and applications. *Desalination*. 2018;434: 121–160. <https://doi.org/10.1016/j.desal.2017.12.044>

12. Gurreri L., Tamburini A., Cipollina A., Micale G. Electrodialysis applications in wastewater treatment for environmental protection and resources recovery: a systematic review on progress and perspectives. *Membranes*. 2020;10: 146. <https://doi.org/10.3390/membranes10070146>
13. Pourcelly G. Electrodialysis with bipolar membranes: principles, optimization, and applications. *Russian Journal of Electrochemistry*. 2002;38(8): 919–926. <https://doi.org/10.1023/A:1016882216287>
14. Mani K. N. Electrodialysis water splitting technology. *Journal of Membrane Science*. 1991;58(2): 117–138. [https://doi.org/10.1016/s0376-7388\(00\)82450-3](https://doi.org/10.1016/s0376-7388(00)82450-3)
15. Medina-Collana J. T., Rosales-Huamani J. A., Franco-Gonzales E. J., Montaña-Pisfil J. A. Factors influencing the formation of salicylic acid by bipolar membranes electrodialysis. *Membranes*. 2022;12(2): 149. <https://doi.org/10.3390/membranes12020149>
16. Pelletier S., Serre E., Mikhaylin S., Bazinet L. Optimization of cranberry juice deacidification by electrodialysis with bipolar membrane: impact of pulsed electric field conditions. *Separation and Purification Technology*. 2017;186: 106–116. <https://doi.org/10.1016/j.seppur.2017.04.054>
17. Kharina A. Y., Charushina O. E., Eliseeva T. V. Specific features of the mass transport of the components during electrodialysis of an aromatic amino acid–mineral salt–sucrose solution. *Membranes and Membrane Technologies*. 2021;4: 127–132. <https://doi.org/10.1134/S2517751622020068>
18. Eliseeva T. V., Krisilova E. V., Shaposhnik V. A., Bukhovets A. E. Recovery and concentration of basic amino acids by electrodialysis with bipolar membranes. *Desalination and Water Treatment*. 2010;14(1-3): 196–200. <https://doi.org/10.5004/dwt.2010.1028>
19. Eliseeva T. V., Tekuchev A. Yu., Shaposhnik V. A., Lushchik I. G. Electrodialysis of amino acid solutions with bipolar ion-exchange membranes. *Russian Journal of Electrochemistry*. 2001;37(4): 423–426. <https://doi.org/10.1023/A:1016642510229>
20. Sheldeshov N. V., Zabolotsky V. I. *Bipolar ion-exchange membranes. Receipt. Properties. Application. Membranes and membrane technologies*^{*}. Moscow: Nauchnyi mir Publ.; 2013. 70–115. (In Russ.)
21. Strathmann H. *Ion-exchange membrane separation processes*. Amsterdam: Elsevier; 2004. 348 p. [https://doi.org/10.1016/s0927-5193\(04\)80031-7](https://doi.org/10.1016/s0927-5193(04)80031-7)
22. Zabolotsky V. I., Nikonenko V. V. *Ion transport in membranes*^{*}. Moscow: Nauka Publ.; 1996. 392 p. (In Russ.)
23. Tanaka Y. *Ion exchange membranes*. Amsterdam: Elsevier Science; 2015. 522 p.
24. Apel P. Y., Velizarov S., Volkov A. V., ... Yaroslavtsev A. B. Fouling and membrane degradation in electromembrane and baromembrane processes. *Membranes and Membrane Technologies*. 2022;4: 69–92. <https://doi.org/10.1134/S2517751622020032>
25. Kharina A. Yu., Eliseeva T. V. Cation-exchange membrane MK-40 characteristics in electrodialysis of mixed solutions of mineral salt and amino acid. *Sorption and chromatography processes*. 2017;17(1): 148–155. (In Russ., abstract in Eng.). <https://doi.org/10.17308/sorpchrom.2017.17/364>
26. Eliseeva T. V., Kharina A. Y. Voltammetric and transport characteristics of anion-exchange membranes during electrodialysis of solutions containing alkylaromatic amino acid and a mineral salt. *Russian Journal of Electrochemistry*. 2015;51(1): 63–69. <https://doi.org/10.1134/S1023193515010048>
27. Mikhaylin S., Bazinet L. Fouling on ion-exchange membranes: classification, characterization and strategies of prevention and control. *Advances in Colloid and Interface Science*. 2016;229: 34–56. <https://doi.org/10.1016/j.cis.2015.12.006>
28. Meister A. *Biochemistry of the amino acids*. New York: Academic Press; 1957. 485 p.
29. Jakubke H.-D., Jeschkeit H. *Aminosäuren, Peptide, Proteine*. Berlin: 1982.
30. *Chemical encyclopedia: in five volumes*. N. S. Zefirov (ed.) Moscow: “Great Russian Encyclopedia”, 1995. V. 4. p. 295. (In Russ.)
31. Berezina N. P., Kononenko N. A., Dvorkina G. A., Sheldeshov N. V. *Physicochemical properties of ion-exchange materials*^{*}. Krasnodar: Kuban. Gos. Univ. Publ.; 1999. 82 p. (In Russ.)
32. Kotova D. L., Krysanova, T. A., Eliseeva, T. V. Spectrophotometric determination of amino acids in aqueous solutions^{*}. Voronezh: Voronezh State University Publ.; 2004. 115 p. (In Russ.)
33. Lur'e I. S. *Guidance on technical control in the confectionery industry*^{*}. Moscow: Pishchevaya promyshlennost' Publ.; 1978. p. 56–59.
34. Nikonenko V. V., Pismenskaya N. D., Belova E. I.; Sistas P., Huguet P., Pourcelly G., Larchet C. Intensive current transfer in membrane systems: modelling, mechanisms and application in electrodialysis. *Advances in Colloid and Interface Science*. 2010;160: 101–123. <https://doi.org/10.1016/j.cis.2010.08.001>
35. Eliseeva T. V., Shaposhnik V. A. Effects of circulation and facilitated electromigration of amino acids in electrodialysis with ion-exchange membranes. *Russian Journal of Electrochemistry*. 2000;36(1): 64–67. <https://doi.org/10.1007/BF02757798>
36. Dobrevsky J., Zvezdov A. Investigation of pore structure of ion exchange membranes. *Desalination*. 1979;28(3): 283–289. [https://doi.org/10.1016/s0011-9164\(00\)82235-3](https://doi.org/10.1016/s0011-9164(00)82235-3)

* Translated by an author of the article

Information about the authors

Anastasiia Yu. Kharina, Cand. Sci. (Chem.), Research Fellow, Senior Engineer at the Department of Analytical Chemistry, Voronezh State University, (Voronezh, Russian Federation).

<https://orcid.org/0000-0003-3050-8684>
aukharina@gmail.com

Olga E. Charushina, Junior Researcher at the Department of Analytical Chemistry, Voronezh State University, (Voronezh, Russian Federation).

<https://orcid.org/0009-0008-9568-9088>
charushinaoe@gmail.com

Tatiana V. Eliseeva, Cand. Sci. (Chem.), Associate Professor, Head of the Department of Analytical Chemistry, Voronezh State University, (Voronezh, Russian Federation).

<https://orcid.org/0000-0003-2391-8415>
tatyanaeliseeva@yandex.ru

Received 01.11.2022; approved after reviewing 24.11.2022; accepted for publication 02.12.2022; published online 25.06.2023.

Translated by Irina Charychanskaya
Edited and proofread by Simon Cox



Original articles

Research article

<https://doi.org/10.17308/kcmf.2023.25/11108>

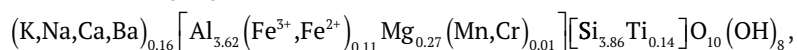
Specifying the structural formula of kaolinite from the Orenburg Region by means of spectroscopic methods

A. G. Chetverikova¹✉, V. N. Makarov¹, O. N. Kanygina¹, M. M. Seregin², E. A. Stroganova¹¹Orenburg State University,
13 Prospect Pobedy, Orenburg 460018, Russian Federation²LLC “Lumex-Centrum”
28A Varshavskoe sh., Moscow 117105, Russian Federation**Abstract**

Kaolinite certification is necessary when using it as a raw material in the ceramic industry. The kaolin clay deposit discovered in the Orenburg Region in 2018 is presumably the largest in the country. Within the Koskolskaya area, 5 mineral deposits have been described. Three of them are particularly promising deposits of high-quality kaolin clay. Previously, studies of the technological and physical characteristics of clay from this deposit were carried out. The purpose of our study was to derive and specify the structural formula of kaolinite contained in the clays.

After elutriation and grinding in a ball mill, natural clay was sifted through a sieve with meshes of 40 μm. The conducted IR, Raman, and EPR spectroscopy, as well as DTA allowed us to monitor the process of metakaolinisation, which occurs as a result of dehydration of kaolinite (i.e. the process of transformation of kaolinite into metakaolinite). Spectroscopic methods made it possible to analyse the parameters of the fine structure, in particular, the degree of crystallinity of kaolinite particles and the occurrence of iron and magnesium ions in hydroxyl sheets.

Conducting a series of experiments, we managed to specify the structural formula of the kaolinite of the Koskolsky deposit of the Orenburg region:



The square brackets indicate the cationic compositions of the hydroxyl and siloxane sheets that formed the surface charge of the mineral particles. Compensator ions remain outside the square brackets. Thus, in our study we assessed the substance used as a raw material in the ceramic industry and determined the role of elutriation and mechanical treatment of kaolin clay.

Keywords: Structure, Kaolinite, XRF spectroscopy, Differential thermal analysis, FTIR spectroscopy, Raman spectroscopy, EPR spectroscopy

Funding: This study was supported by the Russian Foundation for Basic Research and the government of the Orenburg Region (project No. 9-43-560001 r_a “Physicochemical processes of microwave consolidation of kaolinites”).

Acknowledgments: the XRF spectroscopy and the Raman spectroscopy were performed using the equipment of the Engineering Centre of Orenburg State University.

For citation: Chetverikova A. G., Makarov V. N., Kanygina O. N., Seregin M. M., Stroganova E. A. Specifying the structural formula of kaolinite from the Orenburg Region by means of spectroscopic methods. *Condensed Matter and Interphases*. 2023;25(2): 277–291. <https://doi.org/10.17308/kcmf.2023.25/11108>

Для цитирования: Четверикова А. Г., Макаров В. Н., Каныгина О. Н., Серегин М. М., Строганова Е. А. Коррекция структурной формулы каолинита Оренбургской области спектроскопическими методами. *Конденсированные среды и межфазные границы*. 2023;25(2): 277–291. <https://doi.org/10.17308/kcmf.2023.25/11108>

✉ Chetverikova Anna Gennadievna, e-mail: kr-727@mail.ru

© Chetverikova A. G., Makarov V. N., Kanygina O. N., Seregin M. M., Stroganova E. A., 2023



The content is available under Creative Commons Attribution 4.0 License.

1. Introduction

Over 3/4 of the Earth's crust consists of silicate rocks whose finely dispersed powders are used to synthesise technical ceramics [1]. Following the current trends in physical materials science, the potential of clays is determined by their key parameters, namely their chemical, mineralogical, and phase compositions. Kaolinite has long been used in ceramics, coatings, paper, and oil industries. It is now largely considered to be a promising material for the production of more valuable products that can be widely used for industrial purposes [2, 3]. Kaolinite is reported to be used for the production of materials with new physical and chemical properties [4, 5]. The phase composition of kaolin clays is important for determining their functional properties including the sorption process [6], catalysis [7], sintering [8], etc.

The main method used to identify the phases of crystalline minerals is X-ray diffraction. However, it does not always register poorly crystallized minerals, even when they are present in significant quantities. X-ray diffraction analysis is not sensitive enough to register small distortions in the crystal lattice caused by isomorphic substitutions, especially when their number is insignificant. Impurity phases, even in small quantities, can lead to incorrect conclusions regarding the structure of the mineral. Therefore, aluminosilicate minerals have mainly been analysed by means of spectroscopic methods, including infrared (IR) spectroscopy and electron paramagnetic resonance (EPR) spectroscopy [9, 5, 10]. Kaolin clays contain a relatively small number of paramagnetic ions. Therefore, EPR spectroscopy [11] can provide valuable information regarding the nature and distribution of paramagnetic ions in transition metals, free radicals, and structural defects [12–14], which can be important for determining the degree of conductivity.

The Orenburg Region is rich in kaolin clays. Within the Koskolskaya area, 5 mineral deposits have been described. The kaolin clay deposits found in the Orenburg Region in 2018 are presumably the largest in the Russian Federation and are of a high quality [15]. Kaolin clay mining is currently of economic strategic importance for Russia. It provides valuable information that

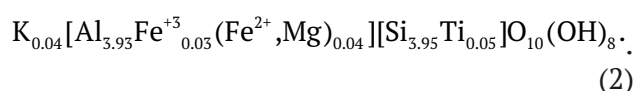
can be used to build a database of eluvial mineral deposits. Therefore, the exploration and material studies of kaolin clays in the Svetlinsky area are of utmost importance [16, 17].

Samples of kaolin were analysed in much detail in [8, 18, 19] by means of colorimetric gradation, X-ray diffraction analysis, and fractal analysis. This article presents the results of further studies of enriched kaolin and provides new information obtained by means of spectroscopic methods and derivative thermal analysis.

Kaolinite, being the main component of kaolin clay, is a layered clay mineral which belongs to the aluminosilicate group. Each layer consists of a tetrahedral (T) sheet composed of silicon and oxygen ions and an octahedral (O) sheet composed of oxygen, aluminium, and hydroxyl ions linked by hydrogen and molecular bonds (Fig. 1). The mineral has a triclinic structure (space group aP13). When the crustal lattice deteriorates, the structure can transform into monoclinic. Ideally, kaolinite does not show any isomorphism, and the structural formula is presented as follows:



The averaged structural formula of kaolinite taking into account isomorphism is presented as follows [20]:



The square brackets indicate cationic compositions of the hydroxyl (octahedral) and siloxane (tetrahedral) sheets (Fig. 1) forming the surface charge of the particles. Deriving the structural formula of the Orenburg natural kaolinite – is a difficult but important task required for the certification of the material used in industrial production.

The purpose of our study was to derive and specify the structural formula of kaolinite by means of a comprehensive analysis of enriched eluvial kaolin from the Orenburg Region deposits.

2. Experimental

2.1. Materials

In our study, we analysed samples of natural clay mined in the Orenburg Region. X-ray phase analysis demonstrated [18] that the

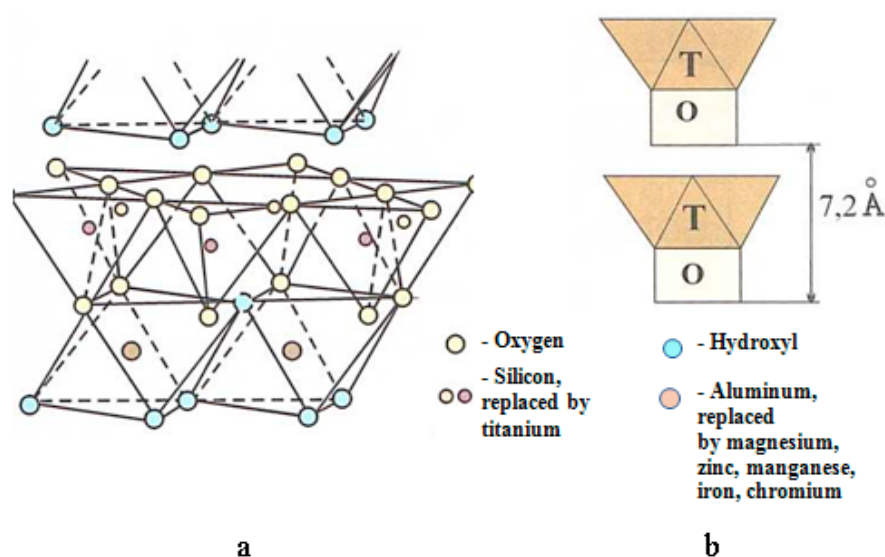
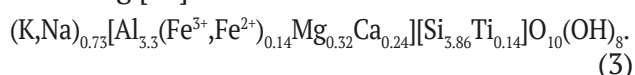


Fig. 1. Kaolinite structure: a – atomic, b – schematic [20]

clay contained about 40% (vol.) of amorphous and 60% (vol.) of crystalline modifications. Of the crystalline phases, kaolinite substituted 73.2 wt.%, corundum – 15.4 wt.%, and free silica – 11.4 wt.%. Finely dispersed clay materials have a low degree of crystallinity, i.e. they are X-ray amorphous. Therefore, the validity of the complete phase analysis of the sample is not very high.

The elemental composition of kaolin, expressed in form of oxides, was determined by means of chemical analysis according to [21]. The resulting preliminary structural formula was the following [22]:



The comparison of the structural formula (3) with the averaged formula (2) and the ideal formula (1) demonstrated that kaolinite from the studied deposit includes a large number of isomorphous substitutions and is far from ideal.

Further in the article we describe the results of the analysis of kaolin clay after mechanical treatment, namely after it was grounded in an iMold milling machine and subjected to sieve analysis with the mesh size of 40 μm .

The isoelectric point of mechanically treated kaolin clay ($d \leq 40 \mu\text{m}$) determined according to [23] is close to $\text{pH} = 2$, since the ζ -potential decreases from +5 to –20 mV, when pH decreases from 1.5 to 3.3 [24]. In proximity to the isoelectric point of the mineral cleavages, the dissociation of

silanol (Si–OH) and aluminium (Al–OH) groups was minimum, and the insignificant numbers of positive and negative charges formed on the cleavages were equal. As a result, when $\text{pH} = 2$, we managed to determine the granulometric composition of the clay by means of photon correlation spectroscopy [25]. The size of the particles is represented by three modal peaks: (0.14 ± 0.05) ; (1.13 ± 0.40) ; $(23.4 \pm 2.7) \mu\text{m}$.

To study the structural state of kaolinite in mechanically treated clay in more detail we used methods which helped us to assess both mineralogical parameters (2.2–2.3) and the fine structure (methods 2.4–2.6).

2.1. X-ray fluorescence analysis (XRF)

X-ray fluorescence analysis helped us to specify the elemental composition of the kaolin clay. X-ray fluorescence spectra were recorded using a Spectroscan MAX-GVM vacuum energy-dispersive X-ray spectrometer in the wavelength range from 800 to 14000 mÅ. The analysing crystals were PET, LiF, KAP, and C002. Powder samples were pressed into 20 mm tablets on a boric acid substrate at a ratio of 5:4.

2.2. Differential thermal analysis (DTA)

Differential thermal analysis (DTA) was used to monitor structural transformations in the mechanically treated kaolin clay sample. Derivatograms were recorded using a Thermoscan-2 unit with a heating rate of 10 $^{\circ}\text{C}/\text{min}$ according to [26]. The sample was

heated from room temperature to 900 °C. The error for temperature measurement was ± 1 °C. Aluminium oxide powder (Al_2O_3) with a weight of 0.5 g and sealed in a quartz container was used as a reference. The weight of the analysed sample was 0.50 ± 0.01 g.

2.3 Optical microscopy

The morphological analysis of kaolinite particles (their size, shape, and surface properties) was conducted. The images were obtained using a Bresser optical microscope, with a CELESTRON digital camera with a resolution of 5 MP.

2.4. Infrared (IR) spectroscopy

The IR spectra of the initial and annealed (after DTA) samples were registered using an InfraLum FT-08 spectrometer (Lumex) with a potassium bromate optical system. The spectrometer had an attachment for disturbed total internal reflection (DTIR) with a zinc selenide crystal. The measurement cycle time was 120 seconds. The spectral range was from 525 to 8000 cm^{-1} with a step of 4 cm^{-1} . Before each measurement, the background spectrum of the attachment was assessed. Powder sample was then placed on the surface of the crystal under a high pressure. After each measurement the crystal was cleaned with cotton wool wetted with acetone.

2.5. Raman spectroscopy

Raman spectroscopy is used to analyse a large number of chemical substances whose molecules are active in the Raman spectra (the substance can be a solution, a solid, or in a multi-phase state) and their concentration does not exceed 0.1%. This approach is important for studying clay materials. The Raman spectra of the initial sample were registered using a RamMix M532 spectrometer. The spectral range was from 120 to 4000 cm^{-1} with a step of 4 cm^{-1} . Before each measurement, the background spectrum of the attachment was assessed. The IR spectroscopy and the Raman spectroscopy – complement each other and demonstrate bond vibrations of various intensity [27].

2.6. Electron paramagnetic resonance (EPR) spectroscopy

The sensitivity of the EPR spectroscopy depending on the type of paramagnetic centres

during a qualitative mineralogical analysis is up to $0.08 \div 0.10\%$. Some ions including Fe^{3+} , Fe^{2+} , Cu^{2+} , Mn^{2+} , and Ti^{4+} , which have unpaired electrons on *d*-sheaths, have non-zero electron spins and magnetic moments. This makes it possible to analyse the minerals containing these ions by means of electron paramagnetic resonance spectroscopy. The EPR method is gaining popularity and is used to study the fine structure of clay materials. A large number of studies are fully or partially dedicated to the interpretation of EPR spectra created by paramagnetic ions or radicals in clays [28, 29].

Besides the lines of metal ions, EPR spectra of aluminosilicates often demonstrate narrow lines of paramagnetic defects of the electron structure, namely localised unpaired electrons and holes. Both types of centres – electron and hole – have *g*-factors close to $g \approx 2.00$. It is believed [28, 30] that electron centres have $g \leq 2.00$ and hole centres have $g \geq 2.00$. Therefore, EPR spectra can provide accurate data regarding their localisation.

The EPR spectra of the initial samples and samples after DTA were registered using a CMS8400 compact automatic controlled spectrometer at room temperature. The spectra were registered under the following conditions: frequency of 9.86 GHz, magnetic field of $1 \div 7$ kOe, magnetic field modulation frequency of 100 kHz and amplitude of 6 Hz.

3. Results and discussion

3.1. Specifying the elemental composition by means of XRF

X-ray fluorescence analysis of mechanically treated kaolin clay from the Svetlinsky area of the Orenburg Region has not yet been described in literature. Table 1 presents the chemical composition of the clay expressed in form of oxides. The compositions are listed from the largest to the smallest quantitative content. The legend is given below the table. Elements whose content increased or decreased after the processing are shown in pink and blue. Trace amounts of barium, sulphur, and chromium registered by the XRF are tinted yellow. The content of paramagnetic centres (Fe_2O_3 and MnO) did not change after mechanical treatment within the experimental error. The concentration of the following oxides increased significantly: SiO_2 – by 10%, Al_2O_3 – by 20%, and MgO – by

Table 1. Composition of the enriched kaolin clay obtained by means of X-ray fluorescence analysis

SiO ₂	Al ₂ O ₃	K ₂ O	TiO ₂	MgO	Fe ₂ O ₃	BaO	SO ₂	CuO	CaO	P ₂ O ₅	MnO	Cr ₂ O ₃
59.13	27.35	7.04	2.43	2.23	1.84	0.19	0.13	0.08	0.07	0.04	0.03	0.02
Z	increased		Z	decreased		Z	hasn't changed		Z	discovered		

2 times. The concentration of CuO – decreased by 3 times, and the concentration of CaO decreased by 30 times [21].

Table 1 demonstrates that the chemical composition of the sample includes the following oxides: SiO₂ (silica), Al₂O₃ (alumina), Na₂O and K₂O (alkali oxides), Fe₂O₃ and TiO₂ (colouring oxides), as well as CaO (lime), and MgO (magnesia). Silica was found in the clays in bound (in clay minerals) and free states (in sand and quartz dust impurities). Its total content is usually about 60÷65% in clays, and up to 85% in oversanded clays. Therefore, the analysed sample was not oversanded.

The silica was found in the clay mainly in a bound state (clay minerals and mica impurities). It is a highly refractory oxide ensuring the refractoriness of clays. Based on the content of silica and titanium dioxide (%) the analysed clay was classified as semiacid [26].

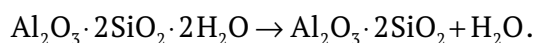
Iron oxide (1.84%) in the form of isomorphic substitutions of the ions of the hydroxyl layer practically did not have any colouring effect. Titanium dioxide (2.43%) was present in the form of isomorphic impurities in the siloxane sheet of the kaolinite lattice.

Alkali oxides, which reduce the colouring effect of iron and titanium oxides by reducing the melting point of clay, were present in the clay minerals and impurities in the isomorphic form. Their content was below 8%. High concentrations of these compounds enabled us to perform chemical processing – elutriation, i.e. removal of water-soluble salts. As a result, their concentration in the sample was below 1.5%. The percentage of crystalline kaolinite in mechanically and chemically treated clays exceeded 77% (vol.) [21].

[17] pointed out that the composition of elutriated finely dispersed kaolin clay (with low concentrations of Na and K oxides) is close to monokaolinite, which makes it a promising material for obtaining metakaolinite - an intermediate product whose areas of application are constantly extending.

3.1. Differential thermal analysis of kaolin clay

In order to study the physico-chemical processes occurring in the clay, the sample was subjected to thermal treatment at 900 °C. At this temperature, the calcination of kaolinite is usually complete and it transforms into metakaolinite [31]. The thermogram presented in Fig. 2 demonstrates an endothermic effect in the said temperature range, which started at a temperature of about 520 °C and ended at 680 °C. Maximum energy absorption corresponded to a temperature of about 590 °C. According to [32], in this temperature range ideal kaolinite begins transforming into metakaolinite with the water of crystallization being removed:



The thermogram presented in Fig. 3 shows an asymmetric peak with an inflection at a temperature of about 620 °C. Such a double peak can be interpreted as an increase in the structural disorder of kaolinite following a decrease in the size of its crystallographic planes, which is characteristic of the formation of metakaolinite. In certain situations, this effect is explained by the presence in the clay of a mineral that is difficult to identify – dickite, whose mineralogical properties are close to those of kaolinite [33]. Thus [34, 35] present a differential thermal analysis of kaolin clay from the Novoorsky deposit, which did not demonstrate asymmetric peaks. At temperatures above 680 °C, no thermal processes were observed, which is characteristic of the state of transformation of kaolinite into metakaolinite [36].

3.3. Morphology of kaolinite particles

Optical images of the particles in transmitted light are given in Fig. 4. In their initial state, the particles are translucent, inhomogeneous, and lamellar (Fig. 4a); their size does not exceed 10 μm. At larger magnification (Fig. 4b), 10±5 μm particles were observed to have kaolinite-like faceting (a hexagon at the end of the crystal).

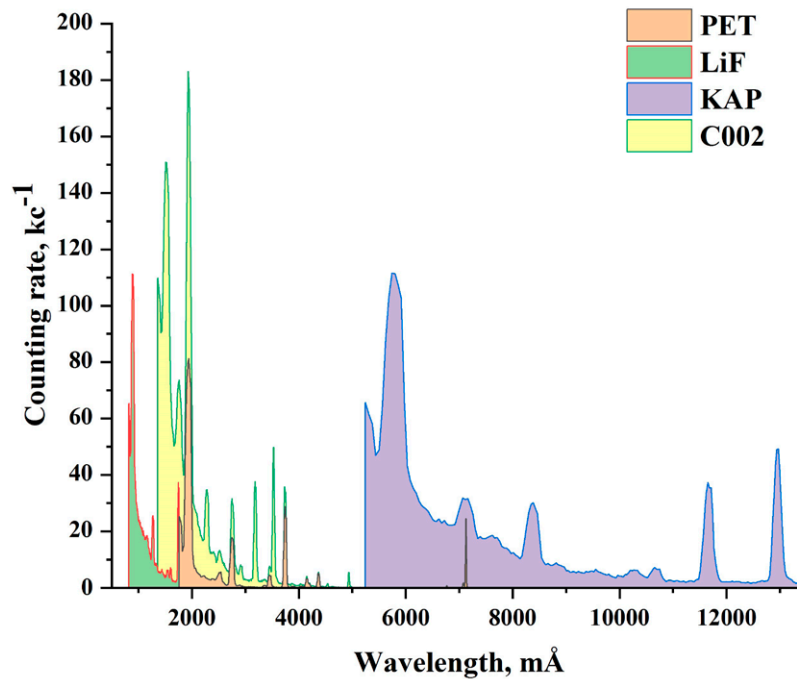


Fig. 2. Integral XRF spectrum of the enriched kaolin clay; PET, LiF, KAP, and C002 are analysing crystals

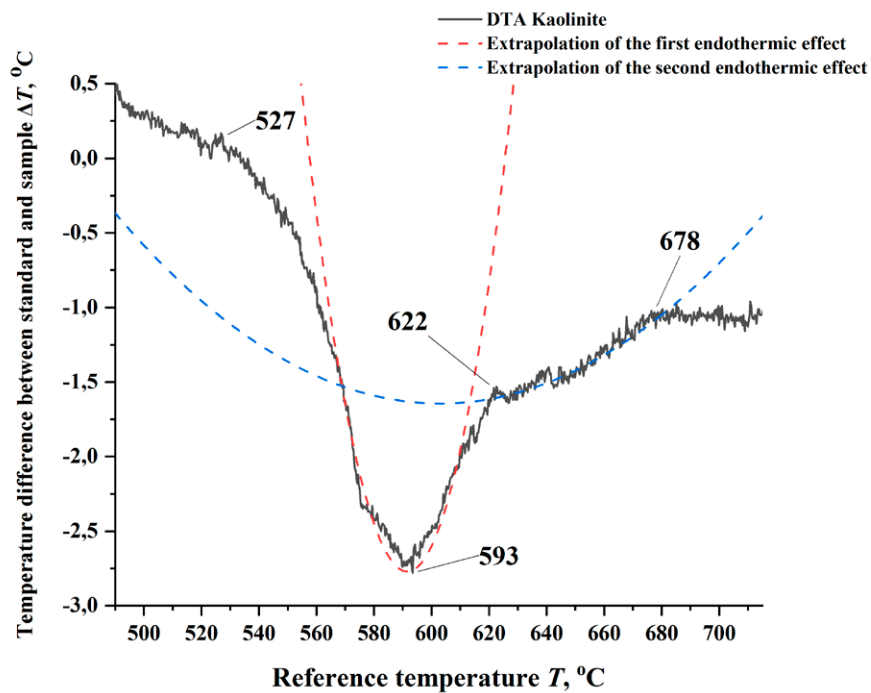


Fig. 3. Derivatogram (thermogram) of the enriched kaolin clay

There were also cleavage planes in certain crystals. According to the modern classification, the analysed clay can be attributed to the 1st class, which corresponds to the presence of minerals with the least defective structures and the least physico-chemical activity [20].

We also performed a comparative morphometric study of kaolinite particles before and after the DTA. After the first endothermic effect of annealing at 620 °C we observed aggregations of particles (Fig. 4c), their partial agglomeration and cluster wafers of up to 30 μm with hexagonal

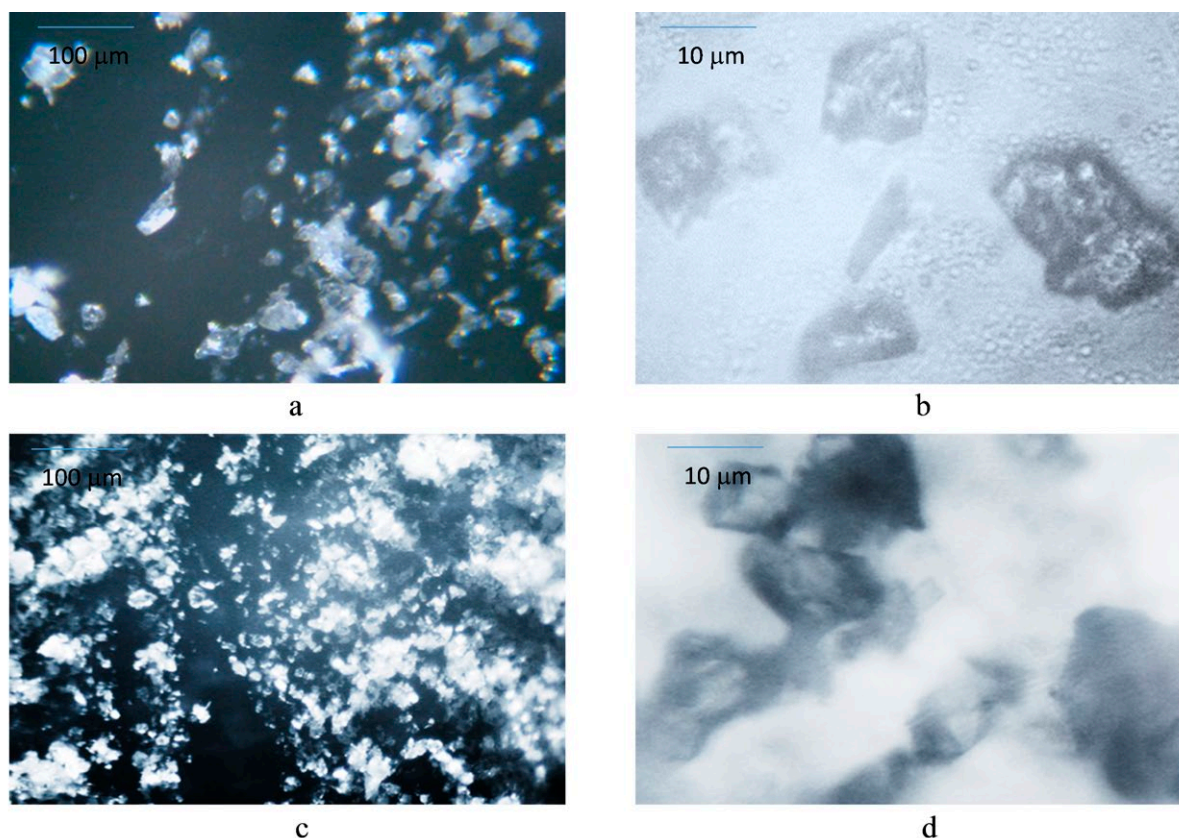


Fig. 4. Lamellar kaolinite particles: a – before thermal treatment (1 cm = 50 μm); b – before thermal treatment (1 cm = 5 μm); c – after thermal treatment (1 cm = 50 μm); d – after thermal treatment (1 cm = 5 μm)

symmetry (Fig. 4d). The formation of point and phase contacts was confirmed by a slight increase in the number of crystalline phases, according to the X-ray phase analysis [8, 18, 19]. A similar microstructure of the products of heating of kaolin clay of the Novoorsky deposit obtained in reflected light is described in [34].

3.4. Interpretation of the IR and Raman spectra (specifying the chemical bonds)

The main purpose the IR spectroscopy was to specify the chemical bonds in the clay sample and the presence of dickite. In order to do this, we obtained the IR and Raman spectra of the samples of enriched kaolin clay (Fig. 5, 6).

The results of the analysis of the IR spectra are given in Table 2. The spectra of the kaolin samples before and after the DTA demonstrate (Fig. 5) that the IR radiation was mainly absorbed in two regions: from 3600 to 3700 cm^{-1} and from 800 to 1200 cm^{-1} . The region near 1000 cm^{-1} in both cases corresponded to asymmetric Si-O vibrations in the structure of aluminosilicates [42]. The

spectrum of the initial kaolin clay demonstrated four intense absorption bands corresponding to O-Si-O and O-Al-O vibrations at 1164, 1113, 1025, and 999 cm^{-1} , as well as two absorption bands corresponding to Al-OH vibrations at 935 and 909 cm^{-1} [37]. Two Si-O-Al bending vibrations in the kaolinite structure were observed at 788 and 750 cm^{-1} [37]. The mode at 687 cm^{-1} is explained by Si-O-Al vibrations where the aluminium ion was replaced by a magnesium ion [37, 39]. In the range from 3600 to 4000 cm^{-1} four peaks were registered at 3690, 3670, 3650, and 3619 cm^{-1} corresponding to the vibrations of OH groups in the kaolinite structure [37, 38]. The above presented data led us to the conclusion that the clay sample contained mainly kaolinite with an insignificant amount of free silica impurities.

The Raman spectra of the enriched kaolin clay are presented in Fig. 6 and Table 3. The Raman spectra of the kaolin clay demonstrated two main regions explained by the absorption by hydroxyl groups in the range from 3000 to 4000 cm^{-1} and by crystalline vibrations in the

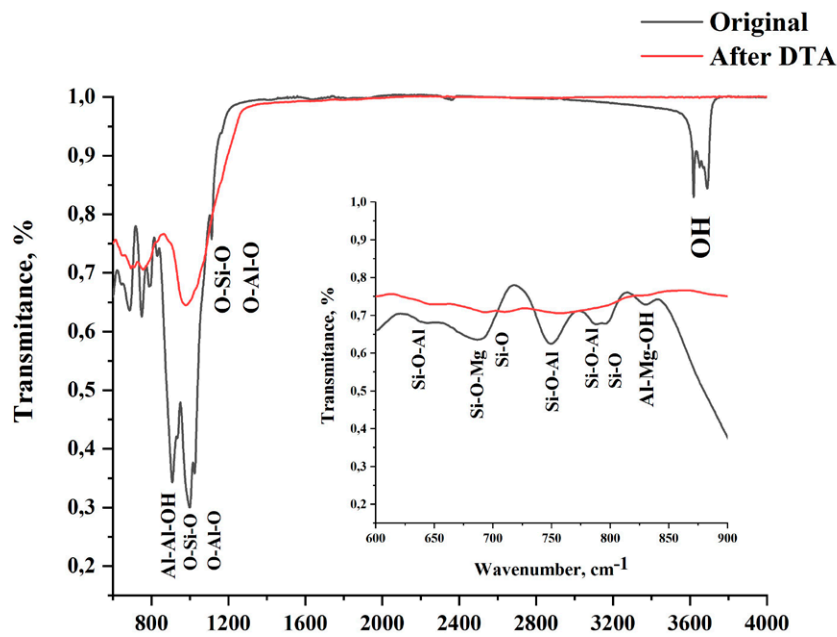


Fig. 5. IR spectra of the samples of enriched kaolin clay before and after DTA

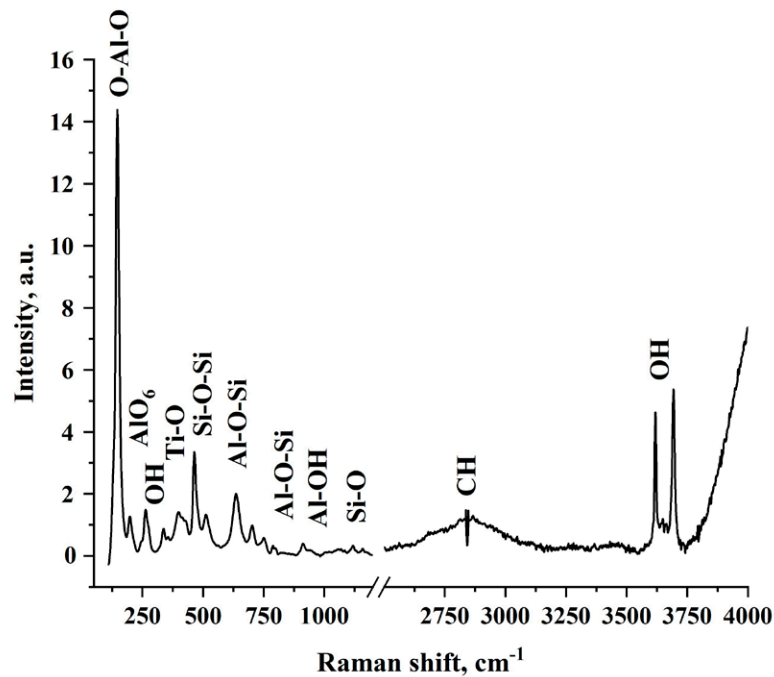


Fig. 6. Raman spectrum of the initial enriched kaolin clay

range of up to 1200 cm^{-1} . The vibration region of hydroxyl groups demonstrated four absorption bands: at $3619, 3648, 3661,$ and 3693 cm^{-1} . These modes were responsible for the vibrations of constitutional water (OH groups of kaolinite) [46].

In the range from 140 to 1000 cm^{-1} there were a large number of intense absorption bands corresponding to the vibrations of the

crystal structure of kaolinite [43–46]. The Raman spectrum also demonstrated weak absorption bands of quartz [43] and Ti-O chemical bonds [43]. Unfortunately, the intense absorption of kaolinite and partial overlap of the bands makes the identification process rather problematic. The presence of dickite was excluded based on the absence of characteristic Si-O vibration

Table 2. Characteristic modes of interatomic bonds in the samples of enriched kaolin clay in the initial state obtained by means of IR spectroscopy

Wavenumber starting material, cm ⁻¹	Wavenumber after DTA, cm ⁻¹	Oscillation type	Mineral
643	645	Si-O-Al [37, 38]	Kaolinite
687	–	Si-O-Mg [37 - 39]	Kaolinite
-	694	Si-O [40]	Silica
750	760	Si-O-Al [37, 38]	Kaolinite
790	–	Si-O-Al [37, 38]	Kaolinite
797	795	Si-O-Si [40, 19]	Kaolinite
830	830	Al-Mg-OH [37, 38]	Kaolinite
909, 935	–	Al-Al-OH [37, 38, 19]	Kaolinite
1164, 1113, 1025, 999	1164, 1036, 979	O-Si-O, O-Al-O [37, 38, 41]	Kaolinite
3620	–	Constitutional water (OH-group) [37, 38, 19, 41]	Kaolinite
3652, 3670, 3690	–	Constitutional water (OH-group) [37, 38, 41]	Kaolinite

Table 3. Characteristic modes of interatomic bonds in the samples of enriched kaolin clay in the initial state obtained by means of Raman spectroscopy

Raman shift, cm ⁻¹	Oscillation type	Mineral
146,2	O-Al-O [43]	Kaolinite
198	AlO ₆ octahedron [44]	Kaolinite
263	Конституционная вода (OH-группа) [44]	Kaolinite
337	Constitutional water (OH-group) [43]	Kaolinite
355	SiO ₄ tetrahedron [44]	Kaolinite / Silica
413	Ti-O [43]	Substitutional ion in kaolinite
428	Si-O-Si [44]	Kaolinite / Silica
464	Si-O-Si [43]	Silica
512	Al-O-Si [44]	Kaolinite
702	Al-OH [44]	Kaolinite
750	Al-O-Si [44, 43]	Kaolinite
788	Al-O-Si [44, 43]	Kaolinite
800	Al-O-Si [45]	Dickite
911	Al-OH [44, 43]	Kaolinite
1070	Si-O [45]	Dickite
1118	Si-O [45]	Dickite
2836	CH [27]	Organic compounds
3619	Constitutional water (OH-group)	Kaolinite
3648	Constitutional water (OH-group)	Kaolinite
3661	Constitutional water (OH-group)	Kaolinite
3693	Constitutional water (OH-group)	Kaolinite

bands with the peaks at 1070 and 1118 cm^{-1} [45]. A broad weak absorption band with a peak at 2836 cm^{-1} corresponds to C-H vibrations of organic compounds in the clay [27].

After the DTA the clay underwent structural transformations and the IR spectrum did not register the absorption bands corresponding to the vibrations of OH groups (Fig. 4, Table 2). The absence of absorption bands at 3600 cm^{-1} indicates complete dehydration of the crystal structure of kaolinite, i.e. its transformation into metakaolinite. The identification of the spectra of the studied structures was hindered by the partial amorphisation of silicon oxide whose absorption bands overlapped with the absorption bands of anhydrous aluminosilicates. To specify the fine structure, other methods should be used, for instance EPR spectroscopy.

3.5. Paramagnetic centres in the structure of enriched kaolin clay

EPR spectroscopy of soils and nonmetallic minerals is often used to study their structural features [47, 48]. The EPR spectra of mechanically and chemically treated kaolin clay in the initial state and after annealing at 620 °C (for a detailed study of structural transformations) and 900 °C are given in Fig. 7.

The EPR spectrum of the initial clay (Fig. 7A) contained characteristic groups of resonances: the first group of low field lines with the central g -factor of about 4.2 and the second group of overlapping lines in a strong magnetic field with $g \approx 2.0$. Similar to standard kaolinites, the analysed sample demonstrated the following lines: the so-called A-line with $g \approx 4.2$ and three symmetric B-lines of various intensity with $g_{B1} = 4.6790$, $g_{B2} = 4.3173$, and $g_{B3} = 3.7986$. The A-line in a weak magnetic field with $g \approx 4.2$ belonged to Fe^{3+} ions in the crystal lattice with strong trigonal distortions. It is known that Fe^{3+} ions can replace Al^{3+} ions in an octahedral system of phyllosilicates and do not replace Si atoms in the tetrahedral system (Fig. 1) [49]. B-lines are often allowed in the EPR spectra of powders [28]. Their presence indicated that the layers were regularly packed and the mineral had good crystallinity. According to [50] in this triplet, the side lines with $g_{B1} = 4.6790$ and $g_{B3} = 3.7986$ are explained by the replacement of the Fe^{3+} ion, located in the surface layers of kaolinite. It

is known [28, 51] that the ratio of the intensity of lines of the B/A spectrum helps to determine the degree of structural perfection of kaolinite crystals, i.e. the Hinckley crystallinity index. In our study it was close to 0.2.

A broad intense line with $g \approx 2.0$ was identified as a line of magnetic resonance of Fe_3O_4 superparamagnetic particles. Such spectra are also called superparamagnetic resonance (SPR) spectra [52, 53]. The line usually overlaps with signals connected with local defects: narrow lines close to $g \approx 2.0$ [30]. Lines with $g = 2.0016$ and $g = 1.9789$ are explained by electron-hole centres formed as a result of isomorphic substitutions of cations in the octahedral sheet. These are O-centres of the substitution stabilisers $\text{Mg}^{2+} \rightarrow \text{Al}^{3+}$. They are relatively poorly connected with the structure of the mineral and served as indicators of the external influence on the structural order of the mineral.

Annealing of the enriched kaolin clay at 620 °C practically did not change the location, width, or shape of the magnetic resonance line with the g -factor of 2.0018 (Fig. 6b). Therefore, the annealing did not change the concentration of Fe^{3+} ions inside the distorted crystallographic cells, and Fe^{3+} ions did not transform into unobserved Fe^{2+} ions and did not leave the distorted octahedral cell. The width of the low field line with the g -factor of 4.2085 decreased to about 14 mT, and the amplitude increased by three times similar to [53]. A significant increase in the intensity of the isotropic signal with $g = 4.2085$ indicated a decrease in the Hinckley crystallinity index almost to zero and formation of metakaolinite. A prominent connection between the resonance and the degree of perfection of crystals agrees well with the interpretation of the results of the DTA. During the formation of metakaolinite the environment of the Fe^{3+} ions in the kaolinite lattice changed following the modification of Al^{3+} coordination in the octahedral layer of the lattice.

The signal explained by the hole defects (vacancies) caused by the replacement of Al^{3+} ions with double charge ions (in this case, Mg^{2+} , Mn^{2+} , and Fe^{2+}) disappeared. The position and amplitude of the second signal remained the same.

The end of the transformation of the enriched kaolin clay processed at 900 °C into metakaolinite

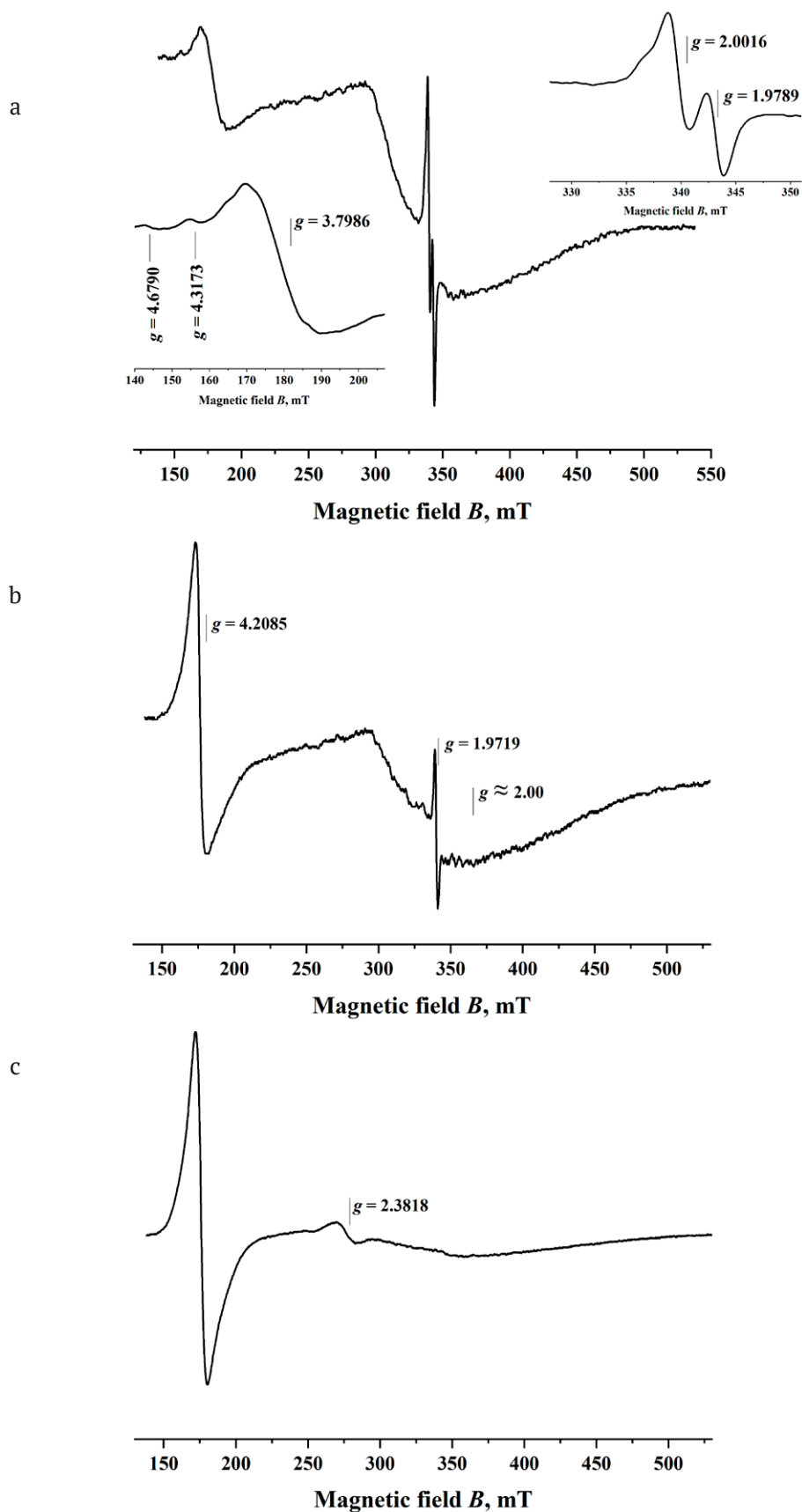
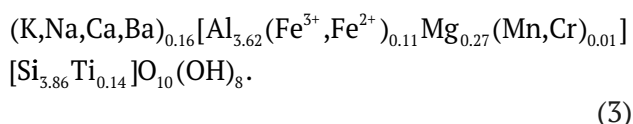


Fig. 7. EPR spectrum of the enriched kaolin clay: a – initial; b – after 620 °C; c – after 900 °C

resulted in a slight expansion of the line with $g \approx 2.00$ and a significant decrease in the amplitude (Fig. 7c). It is possible that, when the crystal lattice was destroyed, the diffusion of Fe^{3+} ions caused the depletion of supermagnetic domains rich in iron, which resulted in a decrease in the concentration of diluted Fe^{3+} [53]. This explains the signal with $g = 2.3819$ which is attributed to the release of aggregated iron Fe^{3+} as a cluster previously contained in ferrihydrite impurities which are not clay minerals [54]. As a rule, the signal is not observed in elutriated clays. Therefore, the analysed sample of enriched kaolin clay requires longer and more thorough chemical treatment in order to extract weakly bound iron ions from the surface layers of kaolinite particles and from impurities.

Manganese and copper lines are indiscernible, presumably due to a low concentration of paramagnetic centres in the sample (less than 0.03%). Titanium lines are also indiscernible, same as in [55, 56], due to correct substitution of $\text{Si}^{4+} \rightarrow \text{Ti}^{4+}$ in the tetrahedral layer. Ca^{2+} , Na^+ , K^+ , and Ba^{2+} cations are usually described as compensator cations and located outside the hydroxyl and siloxane sheets. Al^{3+} cations together with substituting Mg^{2+} , Fe^{3+} , Fe^{2+} , and Mn^{2+} ions are attributed to octahedral positions.

Based on the obtained results, we specified the formula of kaolinite after the mechanical and chemical treatment of the sample:



The corrections in the structural formula agree with the changes in the quantitative and qualitative compositions of the hydroxyl and siloxane sheets of the kaolinite lattice as compared to the averaged formula (1).

4. Conclusions

The XRF determined that the chemical composition of the analysed kaolin clay includes the following oxides: SiO_2 (silica), Al_2O_3 (alumina), Na_2O and K_2O (alkali oxides), Fe_2O_3 and TiO_2 (colouring oxides), as well as CaO (lime), and MgO (magnesia). Trace amounts of barium, sulphur, and chromium registered by the XRF were also registered.

The results of the IR and Raman spectroscopy led us to the conclusion that the clay sample contained mainly kaolinite with an insignificant amount of free silica impurities. The disappearance of the absorption band connected with the vibrations of the OH groups on the IR spectrum of the clay after DTA indicates complete dehydration of the crystal structure of kaolinite, i.e. its transformation into metakaolinite. The EPR spectroscopy registered the introduction of iron ions into the octahedral sheet of the kaolinite lattice.

The study specified the structural formula of kaolinite from the Koskolsky deposit in the Orenburg Region using a series of experiments. Thus, we assessed the substance used as a raw material in ceramics industry. The study determined that spectroscopic methods can be used to analyse fine structural parameters, namely the degree of crystallinity and the mechanism of introduction of iron ions. We also monitored the process of metakaolinitisation as a result of dehydration of kaolinite by means of IR, Raman, and EPR spectroscopy and the DTA.

Author contributions

A. G. Chetverikova – research concept, analysis of the results, analysis of the EPR spectroscopy, deriving the structural formula, text writing and editing. V. N. Makarov – analysis of the results, DTA analysis, graphs plotting, text writing and editing. O. N. Kanygina – analysis of the results, methodology development, analysis of the particles morphology, text writing and editing. M. M. Seregin – analysis of the IR and Raman spectroscopy. E. A. Stroganova – X-ray fluorescence analysis and Raman spectroscopy.

Conflict of interests

The authors declare that they have no known competing financial interests or personal relationships that could have influenced the work reported in this paper.

References

1. Grevtsev V. A., Lygina T. Z. Morphological and structural features of natural, activated and synthesized substances*. *Bulletin of the Kazan Technological University*. 2010;(8): 236–249. (in Russ.). Available at: <https://www.elibrary.ru/item.asp?id=15240366>
2. Klepikov M. S. *Study of the physicochemical properties of kaolins from the Poletaevsky deposit of the*

*Chelyabinsk region and ceramic materials based on them**. Cand. chem. sci. diss. Abstr. Chelyabinsk: 2012. 23 p. (in Russ.). Available at: <https://www.dissercat.com/content/issledovanie-fiziko-khimicheskikh-svoystv-kaolinov-poletaevskogo-mestorozhdeniya-chelyabinsk>

3. Vereshchagin V. I., Shatalov P. I., Mogilevskaya N. V. Speckless technology of diopside ceramic dielectrics based on iron-free diopside raw materials from the Slyudyanskoye deposit*. *Refractories and Industrial Ceramics*. 2006;(8): 33–35. (in Russ.). Available at: <https://www.elibrary.ru/item.asp?id=16501015>

4. Worasith N., Goodman B. A., Neampan J., Jeyachoke N., Thiravetyan P. Characterization of modified kaolin from the Ranong deposit Thailand by XRD, XRF, SEM, FTIR and EPR techniques. *Clay Minerals*. 2011;46(4): 539–559. <https://doi.org/10.1180/claymin.2011.046.4.539>

5. García-Tojal J., Iriarte E., Palmero S., ... Muñoz P. Phyllosilicate-content influence on the spectroscopic properties and antioxidant capacity of Iberian Cretaceous clays. *Spectrochimica Acta Part A: Molecular and Biomolecular Spectroscopy*. 2021;(251): 119472. <https://doi.org/10.1016/j.saa.2021.119472>

6. Chen J., Min Fan-fei, Liu Ling-yun, Jia Fei-fei. Adsorption of methylamine cations on kaolinite basal surfaces: A DFT study. *Physicochemical Problems of Mineral Processing*. 2020;56(2): 338–349. <https://doi.org/10.37190/ppmp/117769>

7. Worasith N., Ninlaphurk S. Mungpayaban H., Wen D., Goodman B. Characterization of paramagnetic centres in clay minerals and free radical surface reactions by EPR spectroscopy. 2014. Available at: <https://www.researchgate.net/publication/292536710>

8. Chetverikova A. G., Kanygina O. N., Filyak M. M. *Structural transformations in oxides constituting natural clays under the influence of a microwave field**. Orenburg: OGU Publ.; 2021. 204 p. (in Russ.)

9. Nasirov R. N., Samatov I. B., Slyussarev A. P., Nasirov A. R. Complex mineralogical and lithological study of sedimentary oil and gas bearing rocks of the precaspian region by EPR, IR-spectroscopy, X-ray diffractometry and thermal analysis*. *News of the national academy of sciences of the republic of Kazakhstan series of geology and technical sciences*. 2018;(4): 174–185. (In Russ.). Available at: <http://geolog-technical.kz/images/pdf/g20184/174-185.pdf>

10. Rutherford D. W., Chiou C. T., Eberl D. D. Effects of exchanged cation on the microporosity of montmorillonite. *Clays and Clay Minerals*. 1997;45(4): 534–543. <https://doi.org/10.1346/ccmn.1997.0450405>

11. Balan E., Allard T., Boizot B., Morin G., Muller J. P. Quantitative measurement of paramagnetic Fe³⁺ in kaolinite. *Clays and Clay Minerals*. 2000;48(4): 439–445. <https://doi.org/10.1346/ccmn.2000.0480404>

12. Gaité J. M., Ermakoff P., Allard T., Müller J. P. Paramagnetic Fe³⁺: a sensitive probe for disorder in kaolinite. *Clays and Clay Minerals*. 1997;45(4): 496–505. <https://doi.org/10.1346/CCMN.1997.0450402>

13. Dobosz B., Krzymiński R. Characteristic of paramagnetic centres in burnt clay and pottery by the EPR method. *Radiation measurements*. 2007;42(2): 213–219. <https://doi.org/10.1016/j.radmeas.2006.11.003>

14. Goodman B. A., Worasith N., Deng W. EPR spectra of a new radiation-induced paramagnetic centre in kaolins. *Clay Minerals*. 2016;51(5): 707–714. <https://doi.org/10.1180/claymin.2016.051.5.01>

15. Chibilev A. A., Petrishchev V. P., Klimentiev A. I., ... Rychko O. K. *Geographical atlas of the Orenburg region**. Moscow: DIK Publ.; 1999. 96 p. (in Russ.)

16. Kadyrbakov I. Kh., Isinbaev A. V., Zubairov R. R. Structural features of eluvial kaolin deposits of the Kovylnoe deposit in the Orenburg region (according to exploration results)*. *Practice of geologists in production. Proceedings of the VI All-Russian Student Scientific and Practical Conference dedicated to the Year of Science and Technology. Rostov-on-Don – Taganrog, 2021*. Rostov-on-Don: Southern Federal University Publ.; 2021. p. 36–38. (in Russ.)

17. Vasyanov G. P., Gorbachev B. F., Chechulina Yu. V., Shmelkov N. T. Deposit eluvial kaolin Kovylny in the east of the Orenburg region. *National Geology (Otechestvennaya Geologiya)*. 2012;(4):11–19. (in Russ., abstract in Eng.). Available at: <https://www.elibrary.ru/item.asp?id=17789124>

18. Kanygina O. N., Chetverikova A. G., Alpysbaeva G. Zh., ... Gun'kov, V. V. Characteristics of kaolin clay from the deposit in the svetlinskii area of Orenburg oblast. *Glass and Ceramics*. 2021;77(9-10): 355–360. <https://doi.org/10.1007/s10717-021-00306-y>

19. Chetverikova A. G., Kanygina O. N., Alpysbaeva G. Z., Yudin A. A., Sokabayeva S. S. Infrared spectroscopy as the method for determining structural responses of natural clays to microwave exposure. *Condensed Matter and Interphases*. 2019;21(3): 446–454. <https://doi.org/10.17308/kcmf.2019.21/1155>

20. Osipov V. I., Sokolov V. N. *Clays and their properties. Composition, structure and formation of properties**. Moscow: Geos Publ.; 2013. 578 p. (In Russ.)

21. GOST 21216-2014. Clay material. Test methods: approved and put into effect by the Interstate Council for Standardization, Metrology and Certification (minutes of May 25, 2014 No. 45-2014): introduction date 2015-07-01. (in Russ.) Available at: <https://docs.cntd.ru/document/1200115068>

22. Chetverikova A. G., Chetverikova D. K. Transduction of crystal chemistry methods into the physics of materials*. *University complex as a regional center of education, science and culture. Collection of*

materials of the All-Russian Scientific and Methodological Conference, Orenburg, January 26–27, 2022. Orenburg: Orenburg State University Publ.; 2022. p. 2939–2942. (In Russ.)

23. ISO 21822:2019(en). Fine ceramics (advanced ceramics, advanced technical ceramics). Measurement of iso-electric point of ceramic powder*. This document was prepared by Technical Committee ISO/TC 206, Fine ceramics. Available at: <https://www.iso.org/obp/ui>

24. Chetverikova A. G. Determination of particle size distribution and electrokinetic potential of phyllosilicate powders by photon correlation spectroscopy. *Measurement Techniques*. 2022;64(11): 936–941. <https://doi.org/10.1007/s11018-022-02024-5>

25. ISO 24235:2007(en). Fine ceramics (advanced ceramics, advanced technical ceramics). Determination of particle size distribution of ceramic powders by laser diffraction method. ISO 24235 was prepared by Technical Committee ISO/TC 206, Fine ceramics. Available at: <https://www.iso.org/obp/ui>

26. GOST 9169-2021. Clay raw materials for the ceramic industry. Classification: adopted by the Interstate Scientific and Technical Commission for Standardization, Technical Regulation and Conformity Assessment in Construction (MNTKS) (Minutes of June 30, 2021 № 141-P): introduction date 2022-04-01. (In Russ.) Available at: https://allgosts.ru/81/060/gost_9169-2021

27. Becker Yu. *Spectroscopy*. Moscow: Technosphere Publ.; 2009. 528 p. (in Russ.)

28. Hall P. L. The application of electron spin resonance spectroscopy to studies of clay minerals: I. Isomorphous substitutions and external surface properties. *Clay Minerals*. 1980;15(4): 321–335. <https://doi.org/10.1180/claymin.1980.015.4.01>

29. Bortnikov N. S., Mineeva R. M., Savko A. D., ... Speransky A. V. Kaolinite history in the weathering crust and associated clay deposits: EPR data. *Doklady Earth Sciences*. 2010;433: 927–930. <https://doi.org/10.1134/S1028334X10070184>

30. Babinska J., Dyrek K., Wyszomirski P. EPR study of paramagnetic defects in clay minerals. *Mineralogia*. 2007;38(2): 125. <https://doi.org/10.2478/v10002-007-0021-x>

31. Liu Y., Huang Q., Zhao L., Lei S. Influence of kaolinite crystallinity and calcination conditions on the pozzolanic activity of metakaolin. *Gospodarka Surowcami Mineralnymi-Mineral Resources Management*. 2021: 39–56. <https://doi.org/10.24425/gsm.2021.136295>

32. Escalera E., Antti M.L., Odén M. Thermal treatment and phase formation in kaolinite and illite based clays from tropical regions of Bolivia. *IOP Conference Series: Materials Science and Engineering*. IOP Publishing. 2012;31(1): <https://doi.org/10.1088/1757-899X/31/1/012017>

33. Stoch L. Significance of structural factors in dehydroxylation of kaolinite polytypes. *Journal of Thermal Analysis and Calorimetry*. 1984;29(5): 919–931. <https://doi.org/10.1007/bf02188838>

34. Guryeva V.A. Physico-chemical studies of the use of dunites in decorative and finishing ceramics. Orenburg: IPK GOU OGU: 2007. 129 p. (in Russ.)

35. Rakhimov R.Z., Rakhimova N.R., Gaifullin A.R., Morozov V.P. Dehydration of clays of different mineral composition during calcination. *Izvestiya KGASU*. 2016;4(38): 388–394. (in Russ.)

36. Janotka I., Puertas F., Palacios M., Kuliffayová M., Varga C. Metakaolin sand-blended-cement pastes: Rheology, hydration process and mechanical properties. *Construction and Building Materials*. 2010;24(5): 791–802. <https://doi.org/10.1016/j.conbuildmat.2009.10.028>

37. Tironi A., Trezza M.A., Irassar E.F., Scian A.N. Thermal treatment of kaolin: effect on the pozzolanic activity. *Procedia Materials Science*. 2012;(1): 343–350. <https://doi.org/10.1016/j.mspro.2012.06.046>

38. Khang V.C., Korovkin M.V., Ananyeva L.G. Identification of clay minerals in reservoir rocks by FTIR spectroscopy. *IOP Conference Series: Earth and Environmental Science*. IOP Publishing. 2016;43(1): 012004.

39. Rosa M.S.L., Silva R.A.O., Sousa P.E., do Nascimento R.T., Knoerzer T., Santos M.R.M.C. Doxazosin adsorption in natural, expanded, and organophilized vermiculite-rich clays. *Cerâmica*. 2022;68(385): 75–83. <https://doi.org/10.1590/0366-69132022683853175>

40. Fricke H.H., Mattenklott M., Parlar H., Hartwig A. Method for the determination of quartz and cristobalite [Air Monitoring Methods, 2015]. *The MAK – Collection for Occupational Health and Safety: Annual Thresholds and Classifications for the Workplace*. 2002;1(1): 401–436. <https://doi.org/10.1002/3527600418.am0sio2fste2015>

41. Tosoni S., Doll K., Ugliengo P. Hydrogen bond in layered materials: structural and vibrational properties of kaolinite by a periodic B3LYP approach. *Chemistry of Materials*. 2006;18(8): 2135–2143.

42. Jovanovski G., Makreski P. Minerals from macedonia. XXX. Complementary use of vibrational spectroscopy and x-ray powder diffraction for spectro-structural study of some cyclo-, phyllo- and tectosilicate minerals. A review. *Macedonian Journal of Chemistry and Chemical Engineering*. 2016;35(2): 125–155. <https://doi.org/10.20450/mjcc.2016.1047>

43. Saikia B.J., Parthasarathy G., Borah, R.R., Borthakur R. Raman and FTIR spectroscopic evaluation of clay minerals and estimation of metal contaminations in natural deposition of surface sediments from Brahmaputra river. *International Journal of Geosciences*, 2016;7(7): 873–883.

44. Samyn, P., Schoukens, G., Stanssens, D. Kaolinite nanocomposite platelets synthesized by intercalation and imidization of poly (styrene-co-maleic anhydride). *Materials*. 2015;8(7): 4363–4388. <https://doi.org/10.3390/ma8074363>
45. Johnston C.T., Helsen J., Schoonheydt R.A., Bish D.L., Agnew S.F. Single-crystal Raman spectroscopy study of dickite. *American Mineralogist*. 1998;83(1-2): 75–84. <https://doi.org/10.2138/am-1998-1-208>
46. Basu A., Mookherjee M. Intercalation of Water in Kaolinite ($\text{Al}_2\text{Si}_2\text{O}_5(\text{OH})_4$) at Subduction Zone Conditions: Insights from Raman Spectroscopy. *ACS Earth and Space Chemistry*. 2021;5(4): 834–848. <https://doi.org/10.1021/acsearthspacechem.0c00349>
47. Vasilevich R. S., Beznosikov V. A., Lodygin E. D. Molecular structure of humic substances in permafrost hilly peatlands of the forest-tundra. *Soil science*. 2019;(3): 317–329. (in Russ.) <https://doi.org/10.1134/S0032180X19010167>
48. Kurochkina G. N., Kerzhentsev A. S., Sokolov O. A. Physico-chemical study of soils contaminated with rocket fuel components. *Soil science*. 1999;(3): 359–369. (in Russ.)
49. Calas G. Electron paramagnetic resonance. In *Spectroscopic Methods in Mineralogy and Geology* (F.C. Hawthorne, Eds.). *Reviews in Mineralogy*. 1988;(1): 513–571.
50. Savko A. D., Krainov A. V., Ovchinnikova M. Yu., Milash A. V., Novikov V. M. Ages of formation of weathering crusts and connection with them of deposits of secondary kaolins and ceramic clays in the Phanerozoic of the Voronezh anticline. *Bulletin of the Voronezh State University. Series: Geology*. 2019;(3):23–34. (in Russ.)
51. Grevtsev V.A., Lygina T.Z. Aspects of application of the method of electron paramagnetic resonance in the study of non-metallic raw materials. *Exploration and protection of mineral resources*. 2010;(8): 34–39. (in Russ.)
52. Slay D., Cao D., Ferré E.C., Charilaou M. Ferromagnetic resonance of superparamagnetic nanoparticles: The effect of dipole–dipole interactions. *Journal of Applied Physics*. 2021;130(11): 113902. <https://doi.org/10.1063/5.0060769>
53. Bertolino L.C., Rossi A.M., Scorzelli R.B., Torem M.L. Influence of iron on kaolin whiteness: An electron paramagnetic resonance study. *Applied Clay Science*. 2010;49(3): 170–175. <https://doi.org/10.1016/j.clay.2010.04.022>
54. Lyutoev V.P., Burtsev I.N., Saldin V.A., Golovataya O.S. EPR and IR spectroscopy of oil shale: material composition and forms of localization of heavy metals (Chim-Loptyugskoye deposit, Komi Republic). *Mineralogy of technogenesis*. 2012;(13): 115–132. (in Russ.)
55. Gaite J. M., Ermakoff P., Muller J. P. Characterization and origin of two Fe^{3+} EPR spectra in kaolinite. *Physics and Chemistry of Minerals*. 1993;20(4): 242–247.
56. Djemai A., Balan E., Morin G., Hernandez G., Labbe J.C., Muller J.P. Behavior of paramagnetic iron during the thermal transformations of kaolinite. *Journal of the American Ceramic Society*. 2001;84(5): 1017–1024. <https://doi.org/10.1111/j.1151-2916.2001.tb00784.x>

* Translated by author of the article.

Information about the authors

Anna G. Chetverikova, Cand. Sci. (Phys.-Math.), Associate Professor, Dean of the Physics Faculty, Orenburg State University (Orenburg, Russian Federation).

<https://orcid.org/0000-0002-7045-3588>
kr-727@mail.ru

Valery N. Makarov, Cand. Sci. (Phys.-Math.), Senior Lecturer, Department at Physics and Methods of Teaching Physics, Orenburg State University (Orenburg, Russian Federation).

<https://orcid.org/0000-0001-5749-1427>
makarsvet13@gmail.com

Olga N. Kanygina, Dr. Sci. (Phys.-Math.), Full Professor, Department of Chemistry, Orenburg State University (Orenburg, Russian Federation)

<https://orcid.org/0000-0001-6501-900X>
onkan@mail.ru

Mikhail M. Seregin, Analytical Chemist, Lumex-Centrum LLC (Moscow, Russian Federation).

<https://orcid.org/0000-0002-2263-9679>
Sereginmm@lumex.ru

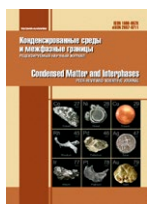
Elena A. Stroganova, Cand. Sci. (Chem.), Associate Professor of the Department of Chemistry, Orenburg State University (Orenburg, Russian Federation).

<https://orcid.org/0000-0002-6583-516X>
stroganova_helen@mail.ru

Received 21.10.2022; approved after reviewing 20.12.2022; accepted for publication 15.01.2023; published online 25.06.2023.

Translated by Yulia Dymant

Edited and proofread by Simon Cox



Original articles

Research article

<https://doi.org/10.17308/kcmf.2023.25/11168>**Phase equilibria in the $\text{Ag}_2\text{S}-\text{Ag}_8\text{GeS}_6-\text{Ag}_8\text{SiS}_6$ system and some properties of solid solutions**G. M. Ashirov¹, K. N. Babanly¹, L. F. Mashadiyeva¹, Y. A. Yusibov², M. B. Babanly¹✉¹*Institute of Catalysis and Inorganic Chemistry n.a. M. Nagiyev
113 H. Javid av., Baku Az1143, Azerbaijan*²*Ganja State University,
Heydar Aliyev, 187, Ganja AZ2000, Ganja, Azerbaijan***Abstract**

Phase equilibria in the $\text{Ag}_2\text{S}-\text{Ag}_8\text{SiS}_6-\text{Ag}_8\text{GeS}_6$ system were studied using differential thermal analysis and powder X-ray diffraction technique. Boundary section $\text{Ag}_8\text{SiS}_6-\text{Ag}_8\text{GeS}_6$, liquidus surface projection, an isothermal section of the phase diagram at 300 K, and some polythermal sections of the studied system were constructed.

The formation of continuous series of solid solutions between both crystalline modifications of the starting compounds was determined in the $\text{Ag}_8\text{SiS}_6-\text{Ag}_8\text{GeS}_6$ system. The liquidus surface of the $\text{Ag}_2\text{S}-\text{Ag}_8\text{SiS}_6-\text{Ag}_8\text{GeS}_6$ system consists of two fields corresponding to the primary crystallization of the high-temperature modifications of the HT- $\text{Ag}_8\text{Si}_{1-x}\text{Ge}_x\text{S}_6$ and HT- Ag_2S phases. Lattice parameters for both modification of solid solutions were calculated based on powder X-ray diffraction data. The concentration dependence of lattice parameters obeys Vegard's rule.

The obtained new phases are of interest as environmentally safe materials with thermoelectric properties and mixed ion-electron conductivity.

Keywords: Argyrodite family compounds, Silver-germanium sulfide, Silver-silicon sulfide, Phase equilibria, Solid solutions, $T-x$ diagram, Crystal structure

Acknowledgment: The work was financially supported by the Azerbaijan Science Foundation – Grant No AEF-MCG-2022-1(42)-12/10/4-M-10.

For citation: Ashirov G. M., Babanly K. N., Mashadiyeva L. F., Yusibov Y. A., Babanly M. B. Phase equilibria in the $\text{Ag}_2\text{S}-\text{Ag}_8\text{GeS}_6-\text{Ag}_8\text{SiS}_6$ system and some properties of solid solutions. *Condensed Matter and Interphases*. 2023;25(2): 292–301. <https://doi.org/10.17308/kcmf.2023.25/11168>

Для цитирования: Аширов Г. М., Бабанлы К. Н., Машадиева Л. Ф., Юсубов Ю. А., Бабанлы М. Б. Фазовые равновесия в системе $\text{Ag}_2\text{S}-\text{Ag}_8\text{GeS}_6-\text{Ag}_8\text{SiS}_6$ и некоторые свойства твердых растворов. *Конденсированные среды и межфазные границы*. 2023;25(2): 292–301. <https://doi.org/10.17308/kcmf.2023.25/11168>

✉ Mahammad Babanly; email: babanlymb@gmail.com

© Ashirov G. M., Babanly K. N., Mashadiyeva L. F., Yusibov Y. A., Babanly M. B., 2023



The content is available under Creative Commons Attribution 4.0 License.

1. Introduction

Binary and more complex chalcogenides of copper and silver are valuable functional materials [1–3]. Among these compounds, synthetic analogs of the argyrodite mineral with formula $\text{A}_8\text{B}^{\text{IV}}\text{X}_6$ (A – Cu, Ag; B^{IV} – Si, Ge, Sn; X – S, Se, Te) have high thermoelectric performance at low temperatures and are of special interest because they are environmentally safe [4–12]. At the same time, these compounds have semiconductor, photovoltaic, and optical properties [13–18]. On the other hand, the presence of highly concentrated and highly mobile Ag^+/Cu^+ ions distributed in a rigid anionic framework is ensured in the crystal structure of this class of compounds. Due to this feature of the crystal structure, some of the argyrodite compounds have high ionic conductivity for $\text{Cu}^+(\text{Ag}^+)$ cations, which makes them very promising for use in the preparation of photoelectrode materials, electrochemical solar energy converters, ion-selective sensors, etc. [19–22].

Study of new multicomponent materials is based on information about the phase equilibrium of the corresponding systems and the thermodynamic properties of the phases formed in them [23–26]. As the argyrodite family compounds are isostructural, there is a high probability of the formation of solid solutions in systems composed of these compounds. In [27–34], phase equilibria were studied in several systems consisting of argyrodite phases, and continuous series of solid solutions were found.

The present study aimed to obtain a complete picture of the phase equilibrium of the $\text{Ag}_2\text{S}-\text{Ag}_8\text{GeS}_6-\text{Ag}_8\text{SiS}_6$ composition area of the $\text{Ag}_2\text{S}-\text{GeS}_2-\text{SiS}_2$ quaternary system.

The primary compounds of the $\text{Ag}_2\text{S}-\text{Ag}_8\text{GeS}_6-\text{Ag}_8\text{SiS}_6$ system have been sufficiently studied. Ag_2S compound melts congruently at 1113 K and undergoes polymorphic transitions at 449 and 844 K [35]. Ag_8SiS_6 compound melts congruently at 1231 K and has a polymorphic transformation at 526 K [36]. Ag_8GeS_6 compound melts congruently at 1221 K [36] or 1223 K [37]. The polymorphic transition temperature of this compound is 488 K [36] or 496 K [37]. Both Ag_8SiS_6 and Ag_8GeS_6 low-temperature modifications crystallize in orthorhombic system (phase group $\text{Pna}2_1$) and the lattice parameters are as follows:

Ag_8SiS_6 : $a = 15.024$, $b = 7.428$, $c = 10.533$ Å [38];
 Ag_8GeS_6 : $a = 15.149$, $b = 7.476$, $c = 10.589$ Å [39].

High-temperature modifications of the ternary compounds have a cubic structure (phase group $F-43m$) with parameters: Ag_8SiS_6 : $a = 10.63$ Å [38]; Ag_8GeS_6 : $a = 10.7$ Å [40].

$\text{Ag}_2\text{S}-\text{Ag}_8\text{GeS}_6$ and $\text{Ag}_2\text{S}-\text{Ag}_8\text{SiS}_6$ quasi-binary boundary sections were reported in [35, 46]. Both systems form a eutectic-type diagram. Eutectic mixtures crystallize at 1080 K (20 mol% Ag_8GeS_6) [35] and 1085 K (24 mol % Ag_8SiS_6) [36].

The $\text{Ag}_8\text{GeS}_6-\text{Ag}_8\text{SiS}_6$ system has not been studied.

2. Experimental

2.1. Synthesis

Ag_2S , Ag_8SiS_6 , and Ag_8GeS_6 compounds were synthesized by melting stoichiometric mixtures of the corresponding elements with high purity (no less 99.9999 %) in quartz ampoules under vacuum conditions (10^{-2} Pa). As the saturated vapor pressure of sulfur ($T_{\text{boiling}} = 717$ K) is high at the melting temperature of all three compounds, their synthesis was carried out in a two-zone furnace. The furnace was gradually heated to a temperature of 40–50 K above the melting point of the synthesized compound. The part of the ampoule outside the oven is constantly cooled. Due to the process of cooling with water for 2–3 hours, the sulfur accumulated in the form of vapor at the end of the ampoule was condensed and sent to the reaction zone, and after absorbing most of the sulfur, the ampoule was completely inserted into the furnace. After keeping the ampoule in the furnace for 4–5 hours, they were gradually in the off-furnace mode.

The synthesized compounds were identified by differential thermal analysis (DTA) and X-ray diffraction (XRD) technique. Thus, the DTA results of Ag_2S , Ag_8SiS_6 , and Ag_8GeS_6 compounds showed that their polymorphic transition and melting temperatures agree well with the literature data given above. X-ray diffraction analysis confirmed the homogeneity of the synthesized samples and the diffraction patterns of all three compounds agree with the literature data [19–28]. DTA and XRD results of the synthesized compounds are listed in the Table 1.

Alloys of the $\text{Ag}_2\text{S}-\text{Ag}_8\text{GeS}_6-\text{Ag}_8\text{SiS}_6$ system were prepared by melting mixtures of the

obtained starting compounds in different proportions in vacuumed quartz ampoules. To bring the samples to the equilibrium state, they were thermally treated for a long time (500 h) at 900 K. Two samples were prepared for each composition in the $\text{Ag}_8\text{GeS}_6-\text{Ag}_8\text{SiS}_6$ system, one of which was gradually cooled in a switched-off furnace after thermal treatment, and the other one was quenched by dropping the ampoule in cold water at 900 K.

2.2. Research methods

All the alloys were analyzed using powder XRD and DTA techniques. Powder XRD analysis was performed in a Bruker D2 PHASER diffractometer using $\text{CuK}\alpha 1$ radiation within the scanning range of $2\theta = 5\div 75$. DTA measurements were recorded with a “Netzsch 404 F1 Pegasus system” differential scanning calorimeter (under flowing argon atmosphere) and a multichannel device based on the electronic “TC-08 thermocouple data logger” (in sealed quartz tubes). The measurement results were processed using the NETZSCH Proteus Software. The temperature measurement accuracy was within ± 2 K.

3. Results and discussion

From the present experimental data and published reports on the $\text{Ag}_2\text{S}-\text{Ag}_8\text{GeS}_6$ and $\text{Ag}_2\text{S}-\text{Ag}_8\text{SiS}_6$ constituent binaries, we obtained a detailed picture of phase equilibria in the $\text{Ag}_2\text{S}-\text{Ag}_8\text{GeS}_6-\text{Ag}_8\text{SiS}_6$ system.

3.1. The border section $\text{Ag}_8\text{SiS}_6-\text{Ag}_8\text{GeS}_6$

Based on the DTA and XRD results, the phase diagram of the $\text{Ag}_8\text{SiS}_6-\text{Ag}_8\text{GeS}_6$ system was constructed. As can be seen from Fig. 1, continuous series of solid solutions are formed between both low (γ -phase) and high-temperature modifications (δ -phase) of the initial compounds. A special point of interest is that even though the melting temperatures (1231 and 1218 K) and polymorphic transformation temperatures (512 and 491 K) of the primary compounds are very close to each other, the extreme points on both the liquidus and solidus and $\delta \leftrightarrow \gamma$ phase transition curves not observed.

The lattice parameters of both ternary compounds and solid solutions were calculated using the TOPAS3.0 computer program and the results are listed in Table 1.

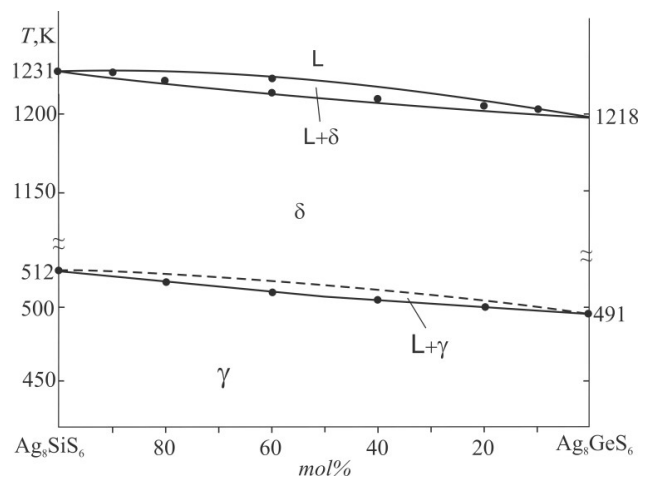


Fig. 1. Phase diagram of the $\text{Ag}_8\text{SiS}_6-\text{Ag}_8\text{GeS}_6$ system

Table 1. DTA and XRD results for $\text{Ag}_8\text{SiS}_6 - \text{Ag}_8\text{GeS}_6$ system

Composition, Mol % Ag_8GeS_6	Effect temperatures according to DTA data, K	Lattice parameters, Å ; low-temperature phase obtained by slow cooling to 298 K, (Sp. gr. $Pna2_1$)			Lattice parameters, Å ; high temperature phase obtained by quenching from 900 K (Sp. gr. $F-43m$)
		<i>a</i>	<i>b</i>	<i>c</i>	<i>a</i>
0 (Ag_8SiS_6)	512 ; 1231	15.0264	7.4384	10.5311	10.6225
10	510 ; 1229	15.0524	7.4439	10.5411	10.6348
20	506 ; 1227	15.0751	7.4412	10.5429	10.6436
40	503 ; 1225-1228	15.0926	7.4523	10.5562	10.6552
60	499 ; 1223	15.0962	7.4601	10.5626	10.6785
80	497 ; 1121	15.1265	7.4694	10.5774	10.6935
90	494 ; 1219	15.1345	7.4705	10.5823	10.7026
100	491 ; 1218	15.1442	7.4713	10.5912	10.7124

Ag_8GeS_6 and Ag_8SiS_6 compounds both have orthorhombic structure under room conditions (space group- Pna_21). The high-temperature modifications of both compounds are cubic (phase group F-43m). Table 1 lists the thermal effects and crystal lattice parameters of the starting compounds and solid solutions.

Graphs of the dependence of crystal lattice parameters on concentration were constructed (Fig. 2). As can be seen, the lattice parameters of both modifications of solid solutions increase linearly with Ge substitution, i.e., they follow Vegard's rule.

Fig. 3 shows powder diffraction patterns of thermally treated and slowly cooled alloys. As can be seen, all intermediate alloys have the same diffraction pattern as the starting compounds. This indicates the formation of continuous series of solid solutions in the $\text{Ag}_8\text{SiS}_6-\text{Ag}_8\text{GeS}_6$ system between room temperature modifications of the starting compounds over the entire concentration range. A slight shift of the diffraction lines towards small angles is observed because of $\text{Si} \rightarrow \text{Ge}$ substitution. This is because the ionic radius of germanium is larger than silicon.

Fig. 4 shows powder XRD patterns of $\text{Ag}_8\text{SiS}_6-\text{Ag}_8\text{GeS}_6$ alloys quenched at 900 K. Analysis of the

XRD patterns of the quenched alloys shows the formation of continuous series of solid solutions between high-temperature modifications in the entire range. As can be seen, the diffraction patterns of high-temperature alloys have a

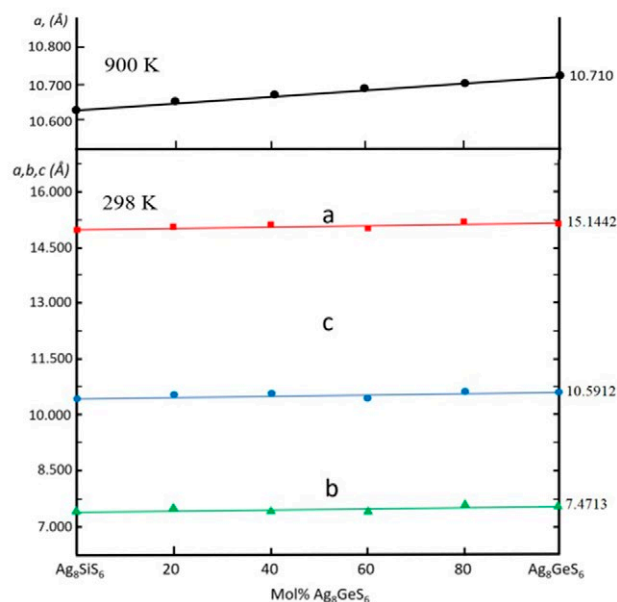


Fig. 2. Dependences of lattice parameters of the low-temperature (stable at room temperature) and high-temperature modifications of $\text{Ag}_8\text{SiS}_6-\text{Ag}_8\text{GeS}_6$ solid solutions on composition

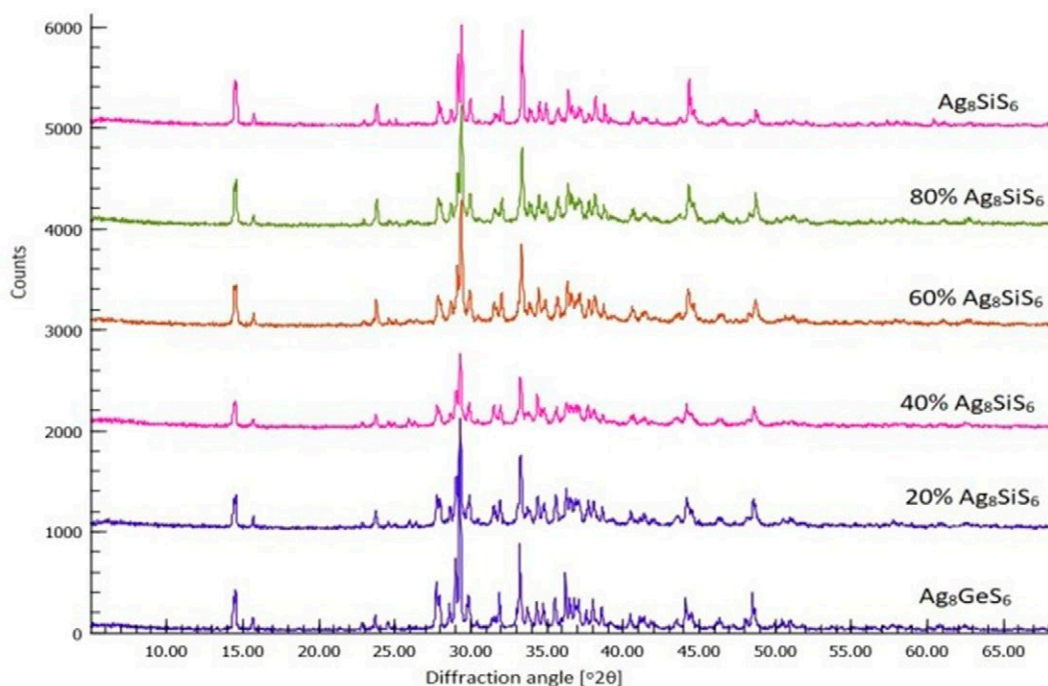


Fig. 3. Powder XRD patterns of the $\text{Ag}_8\text{SiS}_6-\text{Ag}_8\text{GeS}_6$ alloys (slowly cooled to room temperature samples)

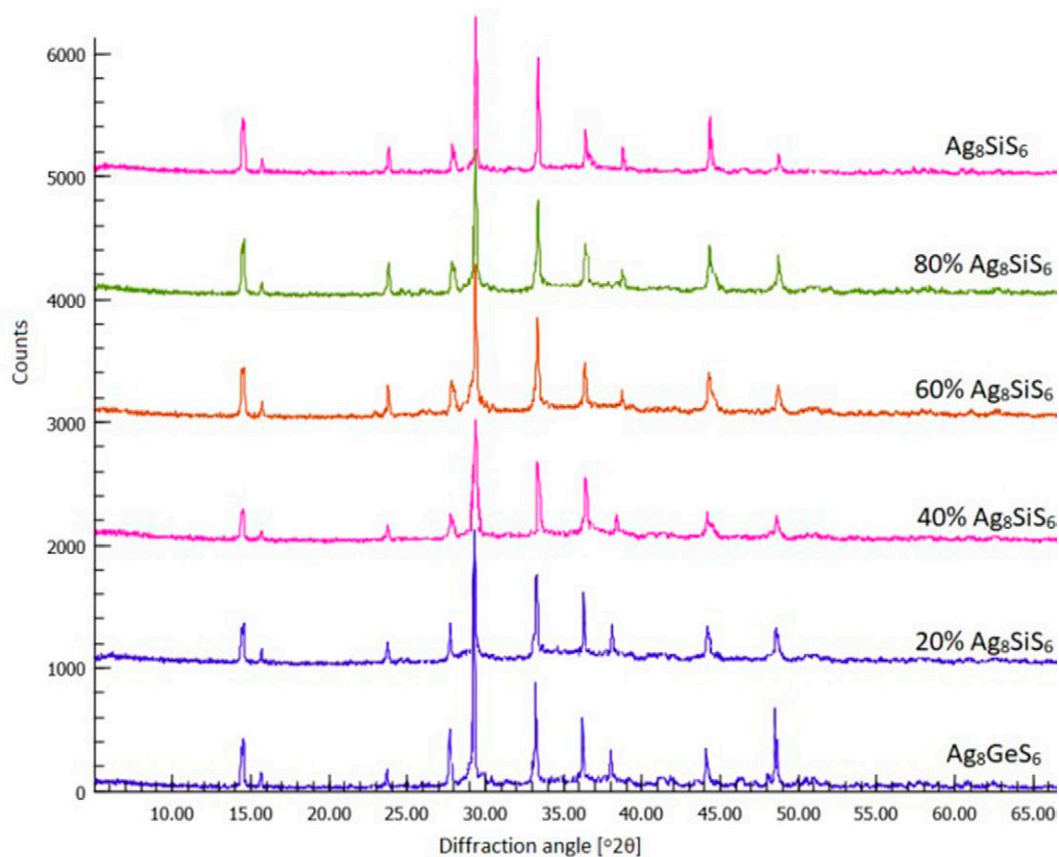


Fig. 4. Powder XRD patterns of $\text{Ag}_8\text{SiS}_6 - \text{Ag}_8\text{GeS}_6$ alloys (quenched at 900 K samples)

diffraction pattern characteristic of a cubic structure.

3.2. Solid phase equilibria in the $\text{Ag}_2\text{S}-\text{Ag}_8\text{GeS}_6-\text{Ag}_8\text{SiS}_6$ system at 300 K

Based on the XRD results of a number of equilibrium alloys within the $\text{Ag}_2\text{S}-\text{Ag}_8\text{GeS}_6-\text{Ag}_8\text{SiS}_6$ concentration triangle and the phase diagrams of boundary quasi-binary systems, a solid phase equilibria diagram of this system at 300 K was constructed (Fig. 5). The formation of the γ -phase in the $\text{Ag}_8\text{GeS}_6-\text{Ag}_8\text{SiS}_6$ boundary system, and the absence of other phases in the concentration triangle lead to the formation of a two-phase $\alpha'+\gamma$ field (where α' is a solid solution formed on the basis of low-temperature Ag_2S). Connate lines are formed between α' and γ -phases. The phase composition of room temperature alloys of the $\text{Ag}_2\text{S}-\text{Ag}_8\text{GeS}_6-\text{Ag}_8\text{SiS}_6$ system was determined by XRD. Fig. 5 shows the studied vertical sections and the composition of the alloys. For example, the diffraction patterns and phase compositions of alloys 1 and 2 from

Fig. 5 are shown in Fig. 6. As can be seen, the diffraction patterns of both alloys consist of the sum of the diffraction lines of the low-temperature modification of Ag_2S and the γ -phase.

3.3. Liquidus surface projection of the $\text{Ag}_2\text{S}-\text{Ag}_8\text{GeS}_6-\text{Ag}_8\text{SiS}_6$ system

The liquidus surface projection of this system consists of two fields, which correspond to the primary crystallization of the δ -phase and α solid solutions based on the high-temperature modification of the Ag_2S compound (Fig. 7). These fields are bounded by the e1e2 monovariant eutectic curve:



3.4. Some polythermal sections of the phase diagram

The $\text{Ag}_2\text{S}-[\text{A}]$ section ($[\text{A}] - \text{Ag}_8\text{Si}_{0.5}\text{Ge}_{0.5}\text{Se}_6$ solid solution). The liquidus of this section (Figure 8) consists of two curves of primary crystallization fields of α and δ solid solutions.

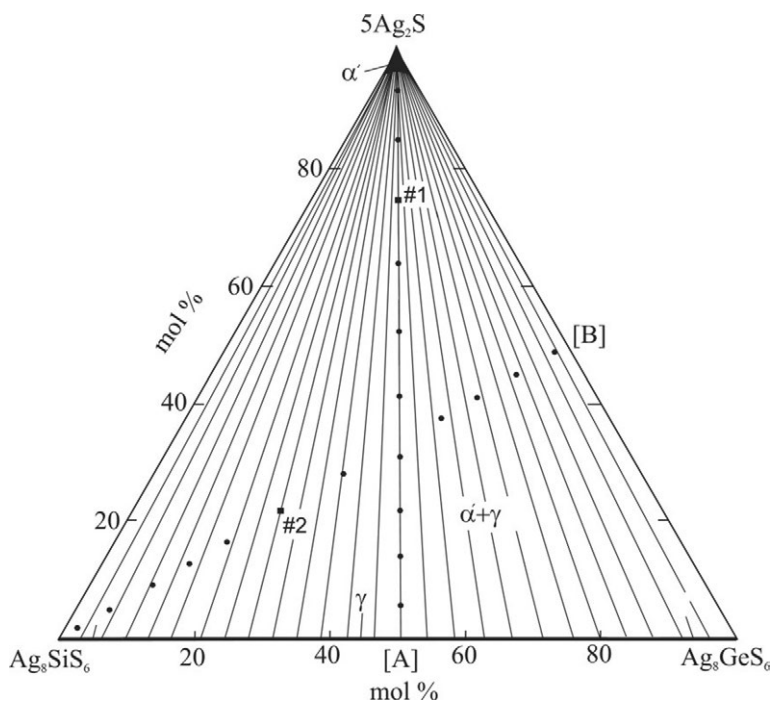


Fig. 5. Isothermal section of the $\text{Ag}_2\text{S}-\text{Ag}_8\text{SiS}_6-\text{Ag}_8\text{GeS}_6$ system at 300 K

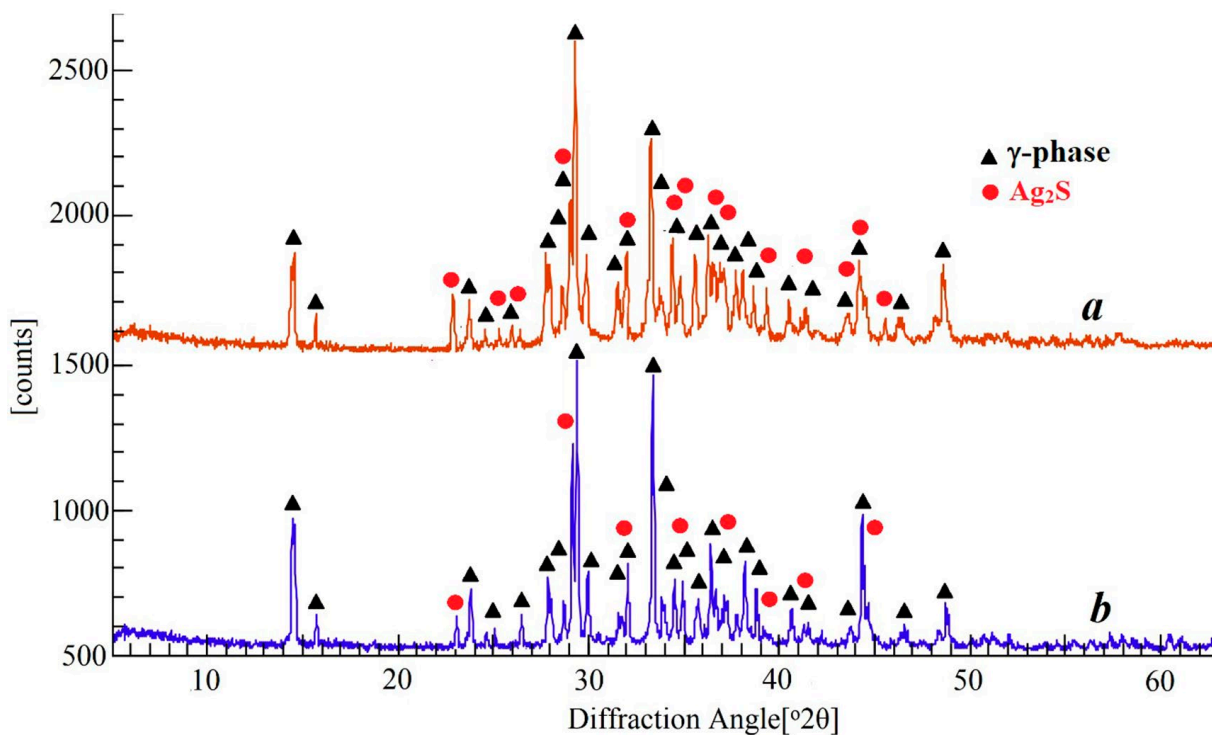


Fig. 6. Powder XRD patterns (300 K) of $\text{Ag}_2\text{S}-\text{Ag}_8\text{SiS}_6-\text{Ag}_8\text{GeS}_6$ alloys: (a) alloy – #1 and (b) alloy – #2 in Fig. 5

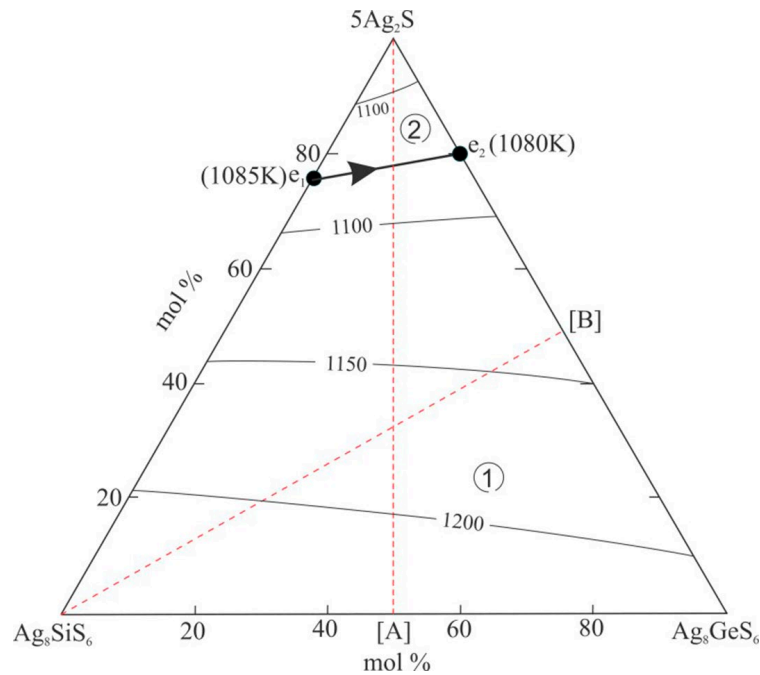


Fig. 7. The liquidus surface projection of the $\text{Ag}_2\text{S}-\text{Ag}_8\text{GeS}_6-\text{Ag}_8\text{SiS}_6$ system. Primary crystallization fields: 1 (δ), 2 (α). Dashed lines indicate studied sections

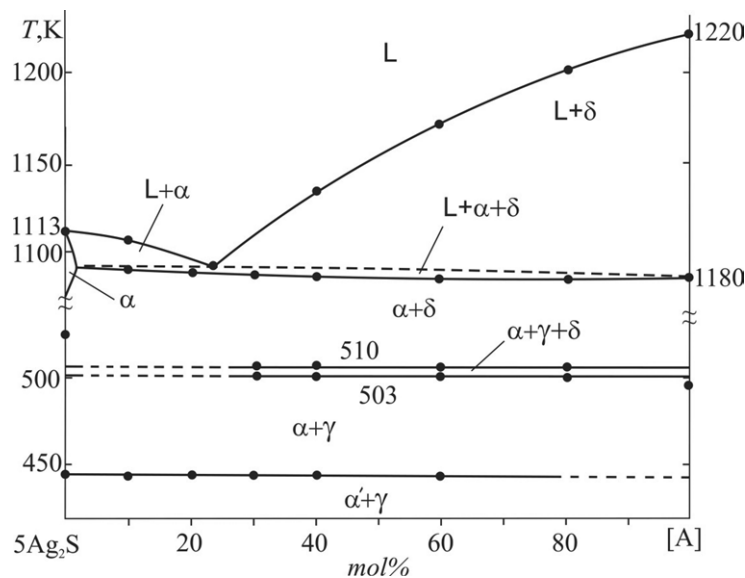


Fig. 8. Polythermal section $\text{Ag}_2\text{S}-[\text{A}]$ ($[\text{A}] - \text{Ag}_8\text{Si}_{0.5}\text{Ge}_{0.5}\text{S}_6$ solid solution)

The crystallization process ends with the formation of the two-phase field $\alpha + \delta$. Below the liquidus, crystallization proceeds according to the eutectic reaction (1). Since the temperatures of e_1 and e_2 eutectic equilibria on $\text{Ag}_2\text{S}-\text{Ag}_8\text{SiS}_6$ and $\text{Ag}_2\text{S}-\text{Ag}_8\text{GeS}_6$ boundary systems differ little (Fig. 7), the temperature interval of this monovariant eutectic equilibrium is very small (2–3°). Therefore, in Figure 8, the $L + \alpha + \delta$ three-phase field is delimited by a dotted line. Thermal

effects at the 503–510 K range correspond to monovariant equilibrium $\delta \leftrightarrow \alpha + \gamma$. There is no more than 5% solubility area based on the high-temperature modification of Ag_2S . The horizontal line at 443K corresponds to the polymorph transformation $\alpha \leftrightarrow \alpha'$.

The $\text{Ag}_8\text{SiS}_6-[\text{B}]\text{Ag}_2\text{S}-[\text{A}]$ section ($[\text{B}]$ is alloy of the $5\text{Ag}_2\text{S}-\text{Ag}_8\text{GeS}_6$ system containing 50 mol % Ag_8GeS_6). This section is entirely located in the primary crystallization field of the δ -phase (Fig. 9)

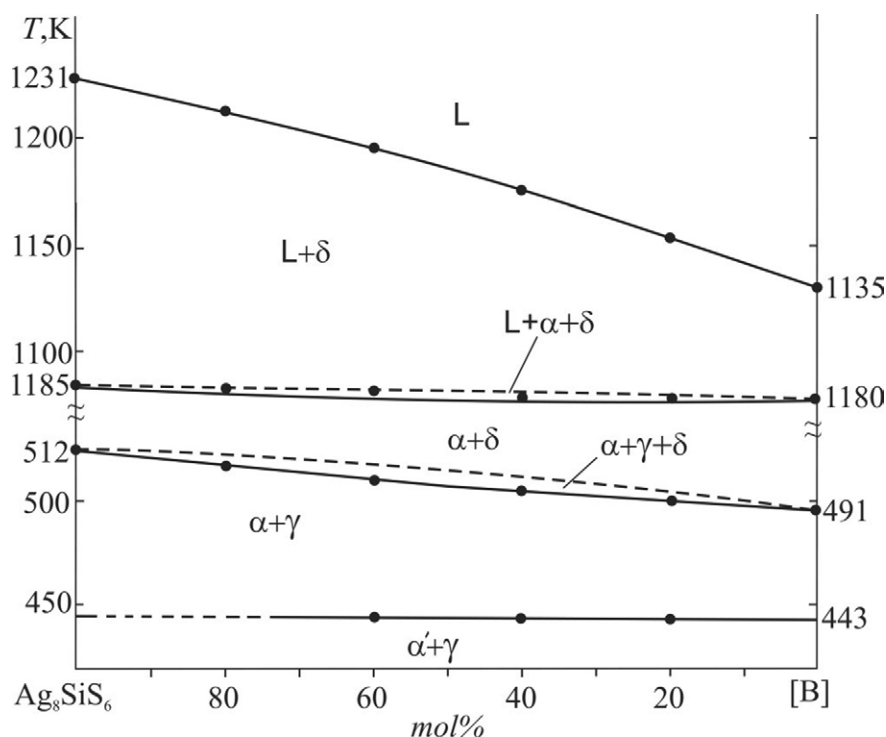


Fig. 9. Polythermal section Ag_8SiS_6 -[B] section. ([B] – is alloy of the $5\text{Ag}_2\text{S}-\text{Ag}_8\text{GeS}_6$ system containing 50%mol Ag_8GeS_6)

and firstly δ -solid solutions crystallize from the liquid phase. Crystallization continues according to the monovariant eutectic reaction (1) and ends with the formation of two-phase mixtures $\alpha + \delta$. Then $\delta \leftrightarrow \alpha + \gamma$ monovariant eutectoid reaction (512–491) and polymorphic transformation of Ag_2S (443 K) take place.

3. Conclusion

The phase equilibria of the $\text{Ag}_2\text{S}-\text{Ag}_8\text{SiS}_6-\text{Ag}_8\text{GeS}_6$ plane of the Ag–Si–Ge–S system were studied. The liquidus surface projection of the mentioned subsystem, solid phase equilibria diagram at 300 K, as well as two polythermal sections of the phase diagram were constructed. It was determined that continuous series of solid solutions are formed between both crystallographic modifications of the starting compounds in the boundary $\text{Ag}_8\text{SiS}_6-\text{Ag}_8\text{GeS}_6$ system. Based on powder diffractograms, the homogeneity of both solid solutions was confirmed, and their crystal lattice types and parameters were determined. It is shown that the dependence of the lattice parameters on the composition obeys Vegard's rule. The obtained new non-stoichiometric phases are of particular interest as environmentally

safe, thermoelectric, and mixed ion-electron conducting materials.

Author contributions

G. M. Ashirov – research concept, conducting research, synthesis of compounds, article writing, discussion of results. L. F. Mashadiyeva – analysis of scientific literature, discussion of results. K. N. Babanly – discussion of results. Y. A. Yusibov – discussion of results. M. B. Babanly – research concept, final conclusions.

Conflict of interests

The authors declare that they have no known competing financial interests or personal relationships that could have influenced the work reported in this paper.

References

1. Sanghoon X. L., Tengfei L. J., Zhang L. Y. *Chalcogenides: From 3D to 2D and beyond*. Elsevier; 2019. 398 p.
2. Ahluwalia G. K. *Applications of chalcogenides: S, Se, and Te*. Springer; 2016. 461 p.
3. Fujikane M., Kurosaki K., Muta H., Yamanaka S.. Thermoelectric properties of α - and β - Ag_2Te . *Journal of Alloys and Compounds*. 2005;393(1-2): 299–301. <https://doi.org/10.1016/j.jallcom.2004.10.002>

4. Schwarzmüller S., Souchay D., Günther D., ... Oeckler O. Argyrodite-type $\text{Cu}_8\text{GeSe}_6-x\text{Te}_x$ ($0 \leq x \leq 2$): temperature-dependent crystal structure and thermoelectric properties. *Zeitschrift für anorganische und allgemeine Chemie*. 2018;644(24): 1915–1922. <https://doi.org/10.1002/zaac.201800453>
5. Acharya S., Soni A. High thermoelectric power factor in *p*-type Cu_8GeSe_6 . *DAE Solid State Physics Symposium 2018*. 2019;2115(1): 1–3. <https://doi.org/10.1063/1.5113463>
6. Li W., Lin S., Ge B., Yang J., Zhang W., Pei Y. Low sound velocity contributing to the high thermoelectric performance of Ag_8SnSe_6 . *Advanced Science*. 2016;3(11): 1600196. <https://doi.org/10.1002/advs.201600196>
7. Ghrib T., Al-Otaibi A. L., Almessiere M. A., Assaker I. B., Chtourou R. High thermoelectric figure of merit of Ag_8SnS_6 component prepared by electrodeposition technique. *Chinese Physics Letters*. 2015;32(12): 127402. <https://doi.org/10.1088/0256-307x/32/12/127402>
8. Jin M., Lin S., Li W., ... Pei Y. Fabrication and thermoelectric properties of single-crystal argyrodite Ag_8SnSe_6 . *Chemistry of Materials*. 2019;31(7): 2603–2610. <https://doi.org/10.1021/acs.chemmater.9b00393>
9. Shen X., Yang C.-C., Liu Y., Wang G., Tan H., Tung Y.-H., Zhou X.. High-temperature structural and thermoelectric study of argyrodite Ag_8GeSe_6 . *ACS Applied Materials & Interfaces*. 2018;11(2): 2168–2176. <https://doi.org/10.1021/acsami.8b19819>
10. Charoenphakdee A., Kurosaki K., Muta H., Uno M., Yamanaka S. Ag_8SiTe_6 : A new thermoelectric material with low thermal conductivity. *Japanese Journal of Applied Physics*. 2009;48(1): 01160–01169. <https://doi.org/10.1143/jjap.48.011603>
11. Jiang Q., Li S., Luo Y., Xin J., Li S., Li W., Yang J. Ecofriendly highly robust Ag_8SiSe_6 -based thermoelectric composites with excellent performance near room temperature. *ACS Applied Materials & Interfaces*. 2020;12(49): 54653–54661. <https://doi.org/10.1021/acsami.0c15877>
12. Fujikane M., Kurosaki K., Muta H., Yamanaka S. Thermoelectric properties of Ag_8GeTe_6 . *Journal of Alloys and Compounds*. 2005;396(1-2): 280–282. <https://doi.org/10.1016/j.jallcom.2004.12.038>
13. Semkiv I., Ilchuk H., Pawlowski M., Kusnezh V. Ag_8SnSe_6 argyrodite synthesis and optical properties. *Opto-Electronics Review*. 2017;25(1): 37–40. <https://doi.org/10.1016/j.opelre.2017.04.002>
14. Lu C.-L., Zhang L., Zhang Y.-W., Liu S.-Y., Mei Y. Electronic, optical properties, surface energies and work functions of Ag_8SnS_6 : First-principles method. *Chinese Physics B*. 2015;24(1): 017501. <https://doi.org/10.1088/1674-1056/24/1/017501>
15. Boon-on P., Aragaw B. A., Lee C.-Y., Shi J.-B., Lee M.-W. Ag_8SnS_6 : a new IR solar absorber material with a near optimal bandgap. *RSC Advances*. 2018;8(69): 39470–39476. <https://doi.org/10.1039/c8ra08734b>
16. Brammertz G., Vermang B., ElAnzeery H., Sahayaraj S., Ranjbar, S., Meuris M., Poortmans J. Fabrication and characterization of ternary Cu_8SiSe_6 and Cu_8SiS_6 thin film layers for optoelectronic applications. *Thin Solid Films*. 2016;616: 649–654. <https://doi.org/10.1016/j.tsf.2016.09.049>
17. Acharya S., Pandey J., Soni A. Enhancement of power factor for inherently poor thermal conductor Ag_8GeSe_6 by replacing Ge with Sn. *ACS Applied Energy Materials*. 2019;2(1): 654–660. <https://doi.org/10.1021/acsaem.8b01660>
18. Tim B., Riley H., Bjoern W., ... Wolfgang G. Z. Considering the role of ion transport in diffuson-dominated thermal conductivity. *Advanced Energy Materials*. 2022;12: 2200717. <https://doi.org/10.1002/aenm.202200717>
19. Hull S., Berastegui P., Grippa A. Ag^+ diffusion within the rock-salt structured superionic conductor $\text{Ag}_4\text{Sn}_3\text{S}_8$. *Journal of Physics: Condensed Matter*. 2005;17(7): 1067–1084. <https://doi.org/10.1088/0953-8984/17/7/002>
20. Heep B. K., Weldert K. S., Krysiak Y., ... Tremel W. High electron mobility and disorder induced by silver ion migration lead to good thermoelectric performance in the argyrodite Ag_8SiSe_6 . *Chemistry of Materials*. 2017;29(11): 4833–4839. <https://doi.org/10.1021/acs.chemmater.7b00767>
21. Boucher F., Evain M., Brec R. Distribution and ionic diffusion path of silver in $\gamma\text{-Ag}_8\text{GeTe}_6$: A temperature dependent anharmonic single crystal structure study. *Journal of Solid State Chemistry*. 1993;107(2): 332–346. <https://doi.org/10.1006/jssc.1993.1356>
22. Sardarly R. M., Ashirov G. M., Mashadiyeva L. F., ... Babanly M. B. Ionic conductivity of the Ag_8GeSe_6 compound. *Modern Physics Letters B*. 2023;36(32): 2250171. <https://doi.org/10.1142/S0217984922501718>
23. West D. R. F. *Ternary phase diagrams in materials science*. 3rd edition. CRC Press; 2019. 236 p.
24. Saka Hiroyasu. *Introduction to phase diagrams in materials science and engineering*. World Scientific Publishing Company; 2020. 188 p. <https://doi.org/10.1142/11368>
25. Babanly M. B., Mashadiyeva L. F., Babanly D. M., Imamaliyeva S. Z., Taghiyev D. B., Yusibov Y. A. Some issues of complex investigation of the phase equilibria and thermodynamic properties of the ternary chalcogenide systems by the EMF method. *Russian Journal of Inorganic Chemistry*. 2019;64(13): 1649–1671. <https://doi.org/10.1134/s0036023619130035>
26. Imamaliyeva S. Z., Babanly D. M., Tagiev D. B., Babanly M. B. Physicochemical aspects of development of multicomponent chalcogenide phases having the

Ti_5Te_3 structure: A Review. *Russian Journal of Inorganic Chemistry*. 2018;63(13): 1703–1730. <https://doi.org/10.1134/s0036023618130041>

27. Mashadiyeva L. F., Alieva Z. M., Mirzoeva R. D., Yusibov Yu. A. A., Shevel'kov V., Babanly M. B. Phase equilibria in the $\text{Cu}_2\text{Se}-\text{GeSe}_2-\text{SnSe}_2$ system. *Journal of Inorganic Chemistry*. 2022;67: 670–682. <https://doi.org/10.1134/S0036023622050126>

28. Alverdiyev I. J., Aliev Z. S., Bagheri S. M., Mashadiyeva L. F., Yusibov Y. A., Babanly M. B. Study of the $2\text{Cu}_2\text{S}+\text{GeSe}_2 \leftrightarrow \text{Cu}_2\text{Se}+\text{GeS}_2$ reciprocal system and thermodynamic properties of the $\text{Cu}_8\text{GeS}_6-x\text{Sex}$ solid solutions. *Journal of Alloys and Compounds*. 2017;691: 255–262. <https://doi.org/10.1016/j.jallcom.2016.08.251>

29. Alverdiyev I. J., Bagheri S. M., Aliyeva Z. M., Yusibov Y. A., Babanly M. B. Phase equilibria in the $\text{Ag}_2\text{Se}-\text{GeSe}_2-\text{SnSe}_2$ system and thermodynamic properties of $\text{Ag}_8\text{Ge}_{1-x}\text{Sn}_x\text{Se}_6$ solid solutions. *Inorganic Materials*. 2017;53(8), 786–796. <https://doi.org/10.1134/s0020168517080027>

30. Aliyeva Z. M., Bagheri S. M., Aliev Z. S., Alverdiyev I. J., Yusibov Y. A., Babanly M. B. The phase equilibria in the $\text{Ag}_2\text{S}-\text{Ag}_8\text{GeS}_6-\text{Ag}_8\text{SnS}_6$ system. *Journal of Alloys and Compounds*. 2014;611: 395–400. <https://doi.org/10.1016/j.jallcom.2014.05.112>

31. Bagheri S. M., Imamaliyeva S. Z., Mashadiyeva L. F., Babanly M. B. Phase equilibria in the $\text{Ag}_8\text{SnS}_6-\text{Ag}_8\text{SnSe}_6$ system. *International Journal of Advanced Scientific and technical Research (India)*. 2014;4(2): 291–296.

32. Bayramova U. R., Poladova A. N., Mashadiyeva L. F. Synthesis and X-RAY study of the $\text{Cu}_8\text{Ge}_{(1-x)}\text{Si}_x\text{S}_6$ solid solutions. *New Materials, Compounds & Applications*. 2022;6(3): 276–281.

33. Alieva Z. M., Bagheri S. M., Alverdiyev I. J., Yusibov Y. A., Babanly M. B. Phase equilibria in the pseudoternary system $\text{Ag}_2\text{Se}-\text{Ag}_8\text{GeSe}_6-\text{Ag}_8\text{SnSe}_6$. *Inorganic Materials*. 2014;50(10): 981–986. <https://doi.org/10.1134/s002016851410001x>

34. Ashirov G. M. Phase equilibria in the $\text{Ag}_8\text{SiTe}_6-\text{Ag}_8\text{GeTe}_6$ system. *Azerbaijan Chemical Journal*. 2022;1: 89–93. <https://doi.org/10.32737/0005-2531-2022-1-89-93>

35. Olekseyuk I. D., Kogut Y. M., Fedorchuk A. O., Piskach L. V., Gorgut G. P., Parasyuk O. V. The $\text{Ag}_2\text{S}-\text{GeS}_2$ system and Ag_2GeS_5 crystal structure. *Naukovyi visnyk Volyn's'koho Natsional'noho Universytetu im. Lesi Ukrainky. Neorhanichna Khimiia*. 2010;16: 25–33.

36. Venkatraman M., Blachnik R., Schlieper A. The phase diagrams of $\text{M}_2\text{X}-\text{SiX}_2$ (M is Cu, Ag; X is S, Se). *Thermochimica Acta*. 1995;249: 13–20. [https://doi.org/10.1016/0040-6031\(95\)90666-5](https://doi.org/10.1016/0040-6031(95)90666-5)

37. Mikolaichuk A. G., Moroz N. V. T-x diagram of the Ag-Ge-S system in the $\text{Ag}-\text{Ge}-\text{GeS}_2-\text{Ag}_8\text{GeS}_6-\text{Ag}$ region: The glassy crystalline state of alloys. *Russian Journal of Inorganic Chemistry*. 2010;55(1): 87–92. <https://doi.org/10.1134/S0036023610010171>

38. Krebs B., Mandt J. Zur Kenntnis des argyrodit-strukturtyps: die kristallstruktur von Ag_8SiS_6 / The argyrodite structure type : The crystal structure of Ag_8SiS_6 . *Zeitschrift Für Naturforschung B*. 1977;32(4): 373–379. <https://doi.org/10.1515/znb-1977-0404>

39. Eulenberger G. Die kristallstruktur der tiefemperatormodifikation von Ag_8GeS_6 – synthetischer argyrodit. *Monatshefte für Chemie*. 1977;108: 901–913. <https://doi.org/10.1007/BF00898056>

40. Gorochov O. Les composés Ag_8MX_6 (M= Si, Ge, Sn et X= S, Se, Te). *Bull. Soc. Chim. France*. 1968;6: 2263–2275

Information about of authors

Garay M. Ashirov, PhD student, Researcher, Institute of Catalysis and Inorganic Chemistry named after academician Murtuza Naghiyev (Baku, Azerbaijan).

<https://orcid.org/0000-0001-5050-9858>
garayasirov@gmail.com

Kamala N. Babanly, PhD in Chemistry, Senior Researcher, Institute of Catalysis and Inorganic Chemistry named after academician Murtuza Naghiyev (Baku, Azerbaijan).

<https://orcid.org/0000-0002-3275-5833>
leylafm@rambler.ru

Leyla F. Mashadiyeva, PhD in Chemistry, Senior Researcher, Institute of Catalysis and Inorganic Chemistry named after academician Murtuza Naghiyev (Baku, Azerbaijan).

<https://orcid.org/0000-0003-2357-6195>
leylafm76@gmail.com

Yusif A. Yusibov, DSc in Chemistry, Professor, Rector of the Ganja State University

<https://orcid.org/0000-0003-4081-6170>
babanlymb@gmail.com

Mahammad B. Babanly, DSc in Chemistry, Professor, Associate Member of the Azerbaijan National Academy of Sciences, Executive Director of the Institute of Catalysis and Inorganic Chemistry named after academician Murtuza Naghiyev (Baku, Azerbaijan).

<https://orcid.org/0000-0001-5962-3710>
babanlymb@gmail.com

Received 05.10.2022; approved after reviewing 24.11.2022; accepted for publication 15.15.2022; published online 25.06.2023.

Translated by author